Dynamic instabilities of model granular materials

Thi Thu Tra Nguyen

N°d'ordre NNT : **2019LYSET007**

THESE de DOCTORAT DE L'UNIVERSITE DE LYON
opérée au sein de
Ecole Nationale de Travaux Publics de l'Etat

Ecole Doctorale N° 162
MEGA
Mécanique – Energétique – Génie Civil - Acoustique

Spécialité : Génie Civil

Soutenue publiquement le 17/07/2019, par :

NGUYEN Thi Thu Tra

Les instabilitiés dynamiques des matériaux granulaires modèles

---

Devant le jury composé de :

Jérôme Crassous, Professeur, Université de Rennes 1	Rapporteur
François Nicot, Directeur de Recherche, IRSTEA - Grenoble	Rapporteur
Gaël Combe, Professeur, Université Grenoble Alpes	Président
Irini Djeran-Maigre, Professeure, Insa Lyon	Examinatrice
Valérie Vidal, Chercheur, Ens Lyon	Examinatrice
Davy Dalmas, Chercheur, LTDS Lyon	Co-encadrant
Alain Le Bot, Directeur de Recherche, LTDS Lyon	Co-directeur de thèse
Thiep Doanh, Chercheur, LTDS Lyon	Co-directeur de thèse

Thesis National Number : **2019LYSET007**

A THESIS OF THE UNIVERSITY OF LYON
prepared at
Ecole Nationale de Travaux Publics de l'Etat

Doctoral School N° 162
MEGA
Mechanics – Energy – Civil Engineering – Acoustic

Speciality : Civil Engineering

Defended on July 17, 2019 by:

NGUYEN Thi Thu Tra

Dynamic instabilities of model granular materials

In front of the following examination committee:

Jérôme Crassous, Prof., Rennes University 1	Reviewer
François Nicot, Prof., IRSTEA - Grenoble	Reviewer
Gaël Combe, Prof., Grenoble Alpes University	Committee chair
Irini Djeran-Maigre, Prof., Insa Lyon	Examiner
Valérie Vidal, Dr., Ens Lyon	Examiner
Davy Dalmas, Dr., LTDS Lyon	Co-supervisor
Alain Le Bot, Prof., LTDS Lyon	Co-director
Thiep Doanh, Dr., LTDS Lyon	Co-director

This thesis has been supervised equally by Davy Dalmas, Thiep Doanh and Alain Le Bot. Unfortunately, for some administrative reasons of Doctoral School ED MEGA, we deeply regret that Davy cannot be on the front-page as co-director.

Acknowledgements

Although by these few lines, I hope people addressed here could understand how much they have meant to me. Foremost I am indebted to my supervisors. Dr. T. Doanh was so strict but actually kind, patient, thoughtful and insightful in all detailed works within the research even the administrative works for a non-French-speaking PhD student like me. Without him, I could have not finished the thesis. I am grateful to Prof. A. Le Bot, who always gave invaluable advice as the key orientation as well as his sincere encouragement to me. I am so fortunate to have Dr. D. Dalmas as the co-advisor with the extreme dedication, very sharp and precious discussions to revise my work resulting in significant improvements.

I would also like to thank the committee members for their time to examine my thesis, especially Prof. J. Crassous and Prof. F. Nicot. They indeed broadened my view and gave valuable comments.

Indispensably, I deeply appreciate my family during these years. My parents, sisters and brother, my husband and daughter have been so strong to finish my responsibility for so many years. This thesis is a small gift to their expectation.

Throughout this long journey, I have been also accompanied by my best friends in Vietnam- the great friend who stimulated my abroad studying, a group of close friends always sharing both the delightful and stressful moments of daily life. Thanks you all.

Finally, I would like to pay gratitude to the staff of ENTPE and LTDS due to their special helps for a foreign student. All of you represent a beautiful France in my heart. I indeed had a good fortune of having an unforgettable period of life in this excellent country. Merci beaucoup !

Abstract

This thesis reports a laboratory study on the dynamic instabilities of model saturated granular material using a triaxial apparatus. The term instability consists of isotropic collapse and liquefaction under isotropic compression and of stick-slip under triaxial compression in drained condition. The instabilities spontaneously occur at unpredictable effective stress with unexpected buildup of excess pore pressure irrespective of fully drained condition, contrasting with the instability-free behaviour of natural granular materials. In isotropic compression, instantaneous local collapse happens and in triaxial compression, very large and quasi-periodic stick-slip occurs with sudden volumetric compaction and axial contraction. Sometimes, these local failures (collapse and stick-slip) can develop into total liquefaction failure, destroying completely the granular structure.

High time-resolved data permit the discovery of a new family of dynamic and static liquefaction. Passive acoustic measurements allow the identification of typical spectral signature. For stick-slip phenomenon, the slip phase with constant duration of stress drop can be interpreted as dynamic consolidation at constant deviatoric stress, limited by a unique boundary inside the critical state line in the effective stress plane. The precise temporal sequence of mechanical measurements excludes the generated pore pressure as the main cause of the instabilities. However, the role of pore pressure is emphasised by consistent quantitative relations between the amplitude of incremental stresses, incremental strains and the ephemeral stabilised excess pore pressure developed during the dynamic event, leading to the quasi-deterministic nature of granular instabilities. These empirical relations are based only on the short-lived maximum vertical acceleration and governed separately by the confining pressure and the initial void ratio. The

similarity of pore pressure evolution for different kinds of instability strongly suggests some common speculative triggering mechanisms, probably originated from different rearrangements of the granular micro-structure.

Résumé

Cette thèse étudie les instabilités dynamiques des milieux granulaires modèles saturés à l'aide d'un appareil triaxial classique. Les instabilités englobent la liquéfaction et les effondrements en compression isotrope drainée, les frottements saccadés en compression triaxiale drainée. Ces instabilités apparaissent spontanément à des contraintes effectives de confinement imprévisibles. Elles sont accompagnées de très rapides et très fortes surpressions interstitielles, malgré un drainage approprié; ce que ne présentent pas les milieux granulaires naturels. En compression isotrope drainée (consolidation), des effondrements locaux naissent instantanément. En compression triaxiale drainée, on observe de larges frottements saccadés quasi-périodiques caractérisés par des déformations volumiques et axiales contractantes. De temps en temps, ces effondrements et frottements saccadés locaux peuvent se développer en liquéfaction menant à une destruction complète de la structure granulaire.

Les données à haute résolution temporelle issues de ce travail ont permis la découverte d'une nouvelle famille de liquéfaction dynamique et statique. L'étude des émissions acoustiques passives a permis l'identification de signature spectrale caractéristique. Pour les frottements saccadés, la phase de glissement peut être interprétée comme une consolidation dynamique, limitée par l'unique surface en dessous de la ligne critique de rupture dans le plan des contraintes effectives. La séquence temporelle précise des événements exclut que la pression interstitielle soit la cause principale des instabilités. Cependant, le rôle important de la surpression interstitielle est démontré dans des relations quantitatives entre les incréments de contraintes, et de déformations et l'éphémère surpression interstitielle stabilisée développée pendant la phase de glissement. Cela montre finalement la nature quasi-déterministique de ces instabilités dynamiques. Ces relations empiriques sont basées uniquement sur l'amplitude maximale de l'accélération verticale de très courte durée et sont gouvernées indépendamment par la pression de confinement et par l'indice des vides. La similarité de la surpression interstitielle entre différentes instabilités suggère

fortement quelques mécanismes similaires de déclenchement, probablement à partir de ré-arrangements de la micro-structure granulaire.

L'annexe E offre un résumé plus étendu de cette thèse.

Contents

List of Figures

List of Tables

1

Introduction

Studying earthquake mechanism is sometime based on the relative movements of rock surfaces forming complex interfacial fault zone. These tectonic fault zones contain granular media showing a dynamic stick-slip behavior under shear loading. Understanding this stick-slip behavior provides insights to find out the earthquake mechanism. Stick-slip is believed to be a frictional instability with frictional dynamics at microscopic scale governing the macroscopic force fluctuations. The development in 2D and 3D exhibits more complex processes in bulk behaviours. However, model experiments in 3D and saturated condition are still very rare. Consequently we carry out research to survey new aspects in stick-slip behavior with high time-resolved data.

With the initial objective to study stick-slip instability, two new types of instability are found including isotropic liquefaction and isotropic collapse. Among them, liquefaction is peculiar due to its dramatic consequences to human life. After the spectacular Niigata earthquake in 1964, tremendous liquefactions induce consequences such as building sinking into the ground, damages of foundation and superstructure of bridge. Thus liquefaction phenomenon has been extensively and intensively studied throughout the latest decades. This provided fundamental knowledge on the complex term liquefaction often associated with saturated cohesionless soils under undrained conditions. The related external disturbances causing these devastating events are either cyclic or monotonic static shearing. Our recent discovery (31, 34) of a new mode of liquefaction under quasi-static isotropic loading and in drained condition exposed more challenges in finding the physics of these failures. From point of view of soil mechanics, liquefaction is characterised by the buildup of pore pressure leading to an assessment

that pore pressure is the indicator of the phenomenon. However the mechanism of this generation of pore pressure is still not well understood except for the case of static liquefaction.

Previous works (30, 89) preliminarily revealed the similarities between three types of instability (isotropic collapse, isotropic liquefaction and drained compression stick-slip) in the response of unexpected excess pore fluid pressure. This motivates us to conduct this in-depth experimental work on model granular materials to give more insights into the detailed behaviours with the expectation to discover the elusive triggering mechanisms of these instabilities. Within this study, traditional stress and strain are measured with a new set of static and dynamic pressure sensors, complemented by a set of passive acoustic transducers comprising vertical top cap acceleration, lateral sound pressure and lateral vibration.

The thesis is divided in five chapters as follows:

In chapter 2, the scientific context is presented. The overall complex behaviour of granular materials as solid and fluid is described by numerous studies both at macro and microscopic scales and by various approaches. Among the remaining challenges of the granular mechanics, instability is still an open problem. This thesis focuses on three kinds of dynamic instability on model granular materials.

In chapter 3, the studied material is described together with the apparatus and accompanying measuring devices. The fabrication process, the testing procedure, and the post-test measuring are also described.

In chapter 4, stick-slip is investigated in global and detailed behaviour. Global behaviour of generated stick-slip is impacted by confining pressure and initial void ratio. High time-resolved data showed the precise time sequence of measurements to exclude pore fluid pressure as the cause of the instability. The mechanical measurements are characterised and related to each other by empirical relations with decoupling effects of confining pressure and initial void ratio.

In chapter 5, isotropic liquefaction and some other new subtypes of liquefaction and collapse are investigated and characterised. The evolution from collapse to liquefaction is established.

In chapter 6, complementary passive acoustic emission measurements are exploited. The amplitude, frequency content and time sequences are analysed to relate together

mechanical and acoustical measurements. Acoustic measurements emphasise the strong links between the three types of instability.

Finally, essential conclusions are reported and the links between the three kinds of instability are highlighted. The drawbacks are pointed out and further recommendations are suggested.

2

Literature

2.1 Global view on the solid-liquid behaviour of granular materials

Granular materials are found everywhere as one of the most ubiquitous matters constituted this world. It attracts the interests in many fields of civil engineering, industry, geophysics, etc. Its diverse responses make it more and more intriguing as it can perform and transform between solid, liquid, gas and vice versa under different conditions (56). The failures of powder or cereal silo, the separation of granular mixture such as graded stones for pavement when transporting, the rate of rotating drum when mixing the material, the strength when compressing, etc in industry and numerous unexpected failures in natural systems as erosion, earthquake, snow/rock avalanche, soil liquefaction, have motivated the scientists to describe the state of a granular system in order to accurately predict its future behaviour.

As an unusual solid, for example a sand pile or grains in a cylindrical container, contact forces and static friction emerged as the factors controlling the different response compared to homogeneous continuum medium. The contact force network was early investigated and showed the strong inhomogeneity of force chains both in 3-D model (3, 36, 71, 119) and in 2-D system (54, 74, 83, 98, 128). Those studies reported the strong spatial variation of contact forces within the medium by direct observation, the clear fluctuation of force amplitude compared to the mean, the difference between strong force distribution (exponential) and that of weak force (power law), and the independence of force distribution and grain size. The formation of force chains, the

variation of geometry contact network (representative geometry as one particle in contact with several grains or a loop of touching particles, etc) and the nature of the contact point are key issues at microscopic scale for the grain to grain interaction. The force network is also a characteristic resulting in anisotropic structure under external loading beside the intrinsic anisotropy texture of the material. These matters of static granular solid are essentially governed by the inherent disorder state of grain, the volume fraction (relevant to number of coordination (44)), compaction (50) and history dependence of force chains (121)).

Along timeline of history, one of the first community to work early with granular materials is soil mechanics. The macroscopic approach based on continuum mechanics was applied to derive very simple plastic criteria such as Mohr-Coulomb or Drucker-Prager in describing soil failure, taking into account only the solid frictional behaviour. However these criteria ignored the initial variation of volume fraction before reaching the critical state at very large strain. The coupled volume fraction in the early stage of shearing behaviour is considered by Reynolds dilatancy (103) through the concept of dilatancy angle. This concept is introduced in a model for coupled frictional-dilatant material (105) with three elements (i) the scalar definition of macroscopic friction threshold with presence of dilatancy, (ii) the evolution of volume fraction during shearing and (iii) the linear relation between dilatancy angle and the difference of volume fraction at critical state. Beyond this scalar description for the case of plane strain, more sophisticated and complex models were suggested for stress-strain behaviours (109) with the combination of elasticity before transiting to plasticity, contributing a powerful framework to the static behaviour of both cohesive and cohesionless soils under monotonic static shearing, as Cam Clay model based on Critical State Theory. Since these fundamental elasto-plastic models are insufficient to describe the structural changes of the packing to capture some novel behaviours under more complex stress paths (creep, unloading, cyclic load), the link between continuum mechanics and microscopic processes at grain contacts is still challenging. This actuates the micro mechanical approach (18, 20). The contact force network controls the anisotropy which evolves during plastic deformation. One of the attempts is the association of anisotropy variable on the constitutive equation (105) conducted with the support of discrete element method (DEM).

DEM emerges as a robust tool to access the microscopic information which are difficult to measure experimentally for example contact forces, angular force distribu-

tion (fabric), coordination number of a single bead (97). The most popular method is based on Newton's law of motion, pioneered by Cundall and Strack (23), in which the movements of particle resulting from external disturbances are propagated from the boundary through the medium. Time step must be constrained smaller than the characteristic time (time scale) of the propagation over one grain. The equilibrium equation of one grain complies with Newton's laws; normal contact force is reproduced by spring-dashpot representing the inelastic collision, tangential force modelled by sliding block and spring representing friction. This fundamental framework combined with further modifications helps to simulate various configurations, particle sizes, physical properties of grain, etc and various processes at grain scale as well as mesoscale. The power of DEM in micro-mechanical approach makes several advanced steps in describing the granular fabric. Due to the diverse configurations of grain to grain or a group of grains, the internal variables manifesting the skeleton structure are constructed by upscaling (micro, meso, macro) estimation of the probability density function of microscale parameters at the contacts (number of contacts, force, angular, branch vector). The common internal variables, such as fabric tensor, are introduced in many simulations (96, 99). Also other equivalent quantities representing fabric anisotropy are exploited as number of contacts or characteristic orientations of void shape (15, 62, 108). These complex variables are significantly accessible with the numerical support of DEM. As a result, DEM extends the studies of contact force network which used to be investigated by photoelastic disks or carbon paper. They confirmed the heterogeneity of force network (71, 98, 101), the difference on distributions of strong and weak force chains (5, 101), the oriented organisation of strong force chain in the direction of major stress and weak force chains support the strong ones in orthogonal direction. DEM also opens the potential to study the position, rotation, movement (62, 63), velocity field of the grains during quasi-static shearing and formation of local failure (100).

In coexistence with the micro-mechanical approach, macroscopic modelling still keeps the pace on the development of classical concept. Among numerous studies, they could be categorised into some striking directions. For example, the energetic approach to overcome the basis of dissipative processes between grains due to inelastic collision and friction, or the concept of free energy and dissipation function to explain classical macroscale elastoplastic models (21, 102). One other approach is to modify classical constitutive relation in critical state theory with increasingly sophisticated

anisotropy such as anisotropic critical state theory (40, 70). Beyond the quasi-static and rate-independent regime of granular assembly, many attempts are spent to improve models in dense flowing regime at large strain and large scale as avalanches using the inertial number $I = \dot{\gamma} d \sqrt{\frac{\rho}{p}}$, with grain size d, grain density ρ, shear rate $\dot{\gamma}$ and confining pressure p (42). Empirical friction relations $\mu(I)$ and volume fraction relations $\Phi(I)$ can predict the stress and velocity in several configurations of dense granular flows. More complicated geometry configurations are developed by this I-based approach such as phenomena in mixing, coating-like problems, dragging and instabilities. Unfortunately, no theoretical foundations have been found for these empirical relations.

In that immense overall picture of granular behaviour, our work is a small puzzle piece focusing on instability, happening well before failure. In granular mechanics, instability can be understood as the inability to have continuous and quasi-static loading, either in strain or stress prescribed conditions.

2.2 Instability

2.2.1 Stick-slip motion under shear

From the earthquake engineering point of view, over at least three recent decades, stick-slip attracted the interests of researchers in multidisciplinary field due to the analogy between stick-slip and strong ground motion in fault gouge during earthquake (8) but it is still not completely understood. This phenomenon exhibits various behaviours under different loadings (isotropic or shear, monotonic or cyclic), boundaries, historical stress states but basically characterised by (i) a very fast phase in which a sudden release of stress and concurrent contraction strain take place, subsequently (ii) a quasi-static phase in which the stress of granular media recovers with dilatancy behaviour.

Initially, frictional failure is considered as the basic law for the macroscopic slipping in classical granular models. Granular friction is important for understanding the stick-slip motion in earthquake faults. In physics, by simple fundamental configuration of a sliding solid block, stick-slip motion is explored as an aspect of solid friction (94) associated with contact ageing (51). At this fundamental level, one of the early high time-resolved observations on stick-slip is contributed by Nasuno et al. (87). Figure 2.1 shows regular and irregular stick-slips of thin layer of 0.09 mm spherical beads being sheared by a moving transparent solid plate with fast (top) and slow (bottom) pushing

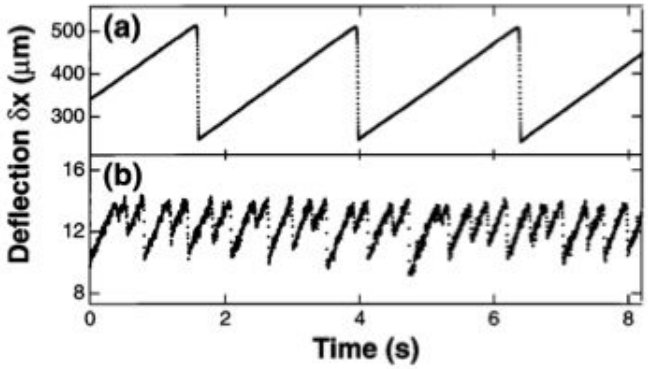

Figure 2.1: Regular and irregular stick-slips of thin layer of 0.09 mm beads in slider frictional machine (87).

velocity. This cover plate is pushed by a normal force, the shear force is imposed on the granular layer through a spring connected to the plate. The controlling parameters of the system are translation velocity, stiffness and normal force. The slip dynamics at sufficient time resolution are exhibited including temporal evolution of displacement, velocity, vertical acceleration and frictional force. The evolution of frictional force during a slip phase lasting within 40 ms is revealed as a multivalued function of velocity. The vertical displacement of the cover plate is used to estimate the volumetric dilation. Small creep before slip events is detected, accompanied by visual evidence of the arrangement of the grain contact. This study concludes that fluidization and displacement (local motion of particles) cause the decline of frictional force and the localised precursors before major slip event. Geminard et al. (43) likewise investigated a thin layer of mono size glass beads under shear force in similar designed system but in immersed condition to find the macroscopic friction dynamics, confirmed the velocity dependent friction law. They suggested an empirical dynamic equation with the introduction of dilatancy rate of granular media. It was in agreement with the friction law by Marone et al. (76) taking into account the state variable describing the transient dilatancy. But horizontal stick-slip motions are observed at only very low driving velocity below 0.1 μm/s. The presence of water and very low normal force as well as negligible confining pressure appear to affect the transition to stick-slip motions in this study. The configuration of thin layer is quite common in the interest of rock mechanics to imitate the fault gouge being sheared between two sliding blocks of a geological

system. Friction is believed to be the essential physical process governing stick-slip motion. Thus, the time, velocity and state dependent characteristics of friction are studied to better understand the fault dynamics (28, 75, 106).

In other configurations like 2D plane, 3D bulk rather than simplest thin layer represented by 1D spring-rigid sliding block, more complex processes are involved to control the stick-slip behaviour since the interaction and motion between grains are not only frictional, but also rotational, buckling, arrangement, collision, etc. Due to the complicated behaviour of granular material, so far no completely satisfactory constitutive relationships can satisfy all general loading conditions. Laboratory tests are still necessary to discover new relations, new aspects and to validate the existing ones. Many useful techniques are developed to measure the strain of discrete grain such as X-ray photography but not for the stress inside the sample. One has to estimate the force from the boundary. One idea is that model system including disks or spheres should be employed for the simplification of geometry, the idealisation of the contact area of grains, etc. Various parameters reflecting the real characteristics of soil are introduced and compared with the model materials to expand this simplest case. With model materials, beyond the displacement, the rotation and contact force are measured by photoelastic disks (74), the fluctuations of these stress-strain measurements are captured and associated with stick-slip behaviour by photo-elastics disks (27), by X-ray (92), by IRM tomography (85).

In an annular shear cell, Cain et al. (14) investigated the effects of shearing velocity and applied normal force, confirming previous observations in thin layer. Dilation behaviour is captured by the vertical displacement of the top plate with the assumption on the constant cross section of the whole packing inside the cell.

In a configuration of 3D cylindrical sample using triaxial machine, Adjemian et al. (1) presented a comprehensive testing program of dry loose glass beads and Hostun sand at low confining pressure from 30 to 60 kPa with crescent strain rate (figure 2.2). In this study, many parameters are examined including confining pressure, strain rate, dimension of the sample, then two main parameters controlling stick-slip phenomenon are identified: the ratio of sample size and diameter of glass beads and the strain rate. The authors also studied the velocity weakening effect of the strain rate that large strain rate leads to small and scarce stick-slips. Moreover stick-slip characteristics depend on

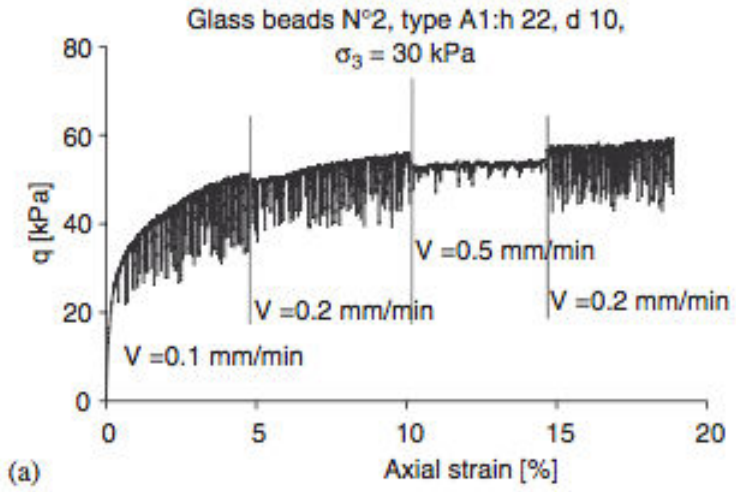

Figure 2.2: Stick-slip behaviour on dry sample of 0.7 mm glass beads under 30 kPa of confining pressure with crescent strain rate (1).

strain rate history. Nevertheless, the low sampling rate of 3 seconds of this study does not allow to detect the variation of volume during stick-slip (compaction and dilation).

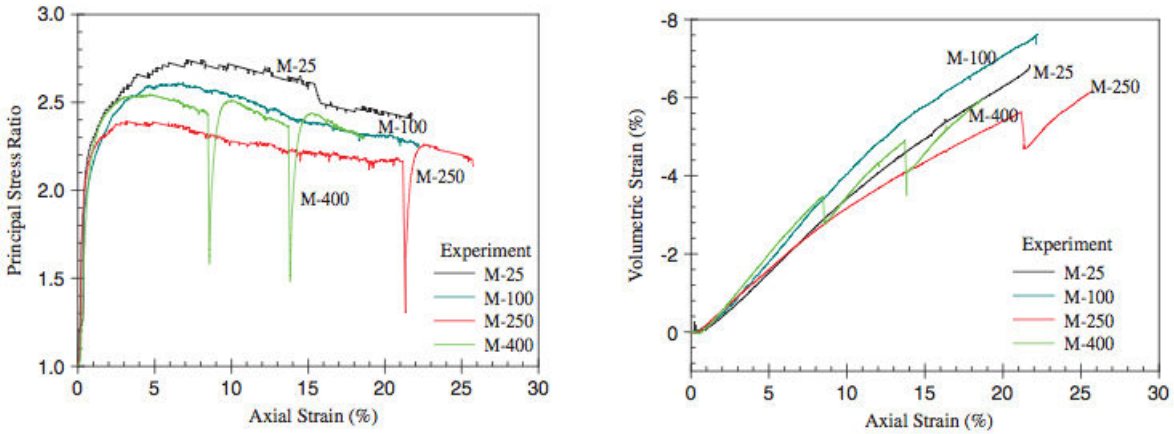

Figure 2.3: Stick-slip behaviour (stress-strain and volumetric) for medium 1.7 mm beads under 25 to 400 kPa of confining pressure (2).

At higher confining pressure up to 400 kPa, Alshibli et al. (2) considered further parameters as particle size, gradation and large density. Surprising large stick-slips were detected, together with volumetric variation for medium dense 1.7 mm beads beyond

Figure 2.4: Absence of localised sheardband on axial cross-sections of computer tomography images on medium 1.7 mm beads (2).

250 kPa of confining pressure (figure 2.3). Global shearing behaviour of dense granular media should obey the transient dilatancy in early stage of shear, then approach critical void ratio with the formation of shear band, but contrastingly, the computer tomography images show no localised shear band for a dilative behaviour (figure 2.4).

On the application for geological systems in which soil is possibly frequently immersed in fluid, the simplest case with full saturation is considered. Doanh et al. (32) presented the coupled volumetric strain behaviour in stick-slip events and analysed the effect of confining pressure and strain rate on axial strain, stress drop and volumetric strain in slip phase. In figure 2.5 shows very large and quasi-regular drained compression stick-slips at 400 kPa of confining pressure, with deviatoric stress drop down to isotropic level. A unique relation of dilatancy characteristic and stress ratio also was established in quasi-static stick phase. During the slip phase, it is sometimes accompanied by surprising sudden generation of fluid pore pressure despite adequate drainage system.

Wu et al. (124, 125) conducted both experimental and numerical works to reproduce stick-slip phenomenon in conventional triaxial test in both dry and saturated monosized large glass beads. Neither testing results nor DEM simulation can reproduce the

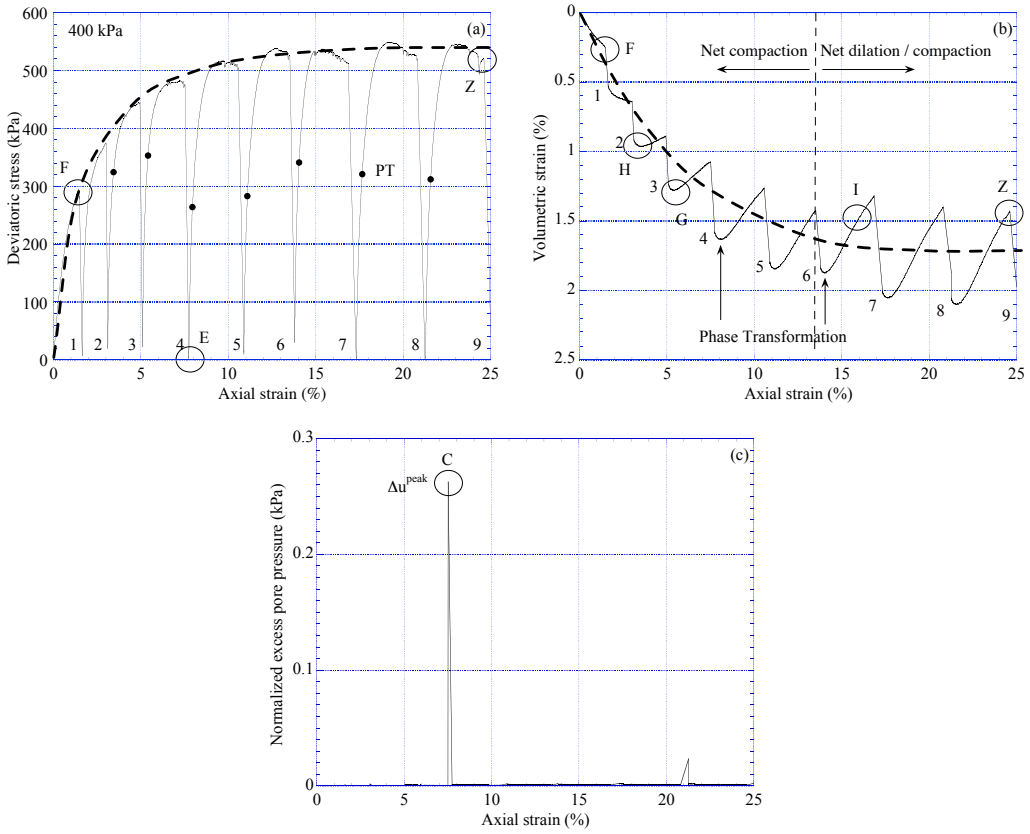

Figure 2.5: Stick-slip behaviour (stress-strain and volumetric) for 0.7 mm beads under 400 kPa of confining pressure (32).

coupled volumetric strain oscillation. The parameter impacting the global shearing behaviour is the surface characteristics of the beads, since Teflon treated beads show lower peak stress and frictional angle. But the differences in the occurrence and amplitude of stick-slip events in case of dry material, saturated and Teflon treated beads are ignored. Only global dilatancy behaviour is exploited.

Scuderi et al. (110) observed pore pressure increases and porosity (correspondingly volumetric strain is estimated) during dynamic stick-slip of drained and undrained saturated glass beads at very high confining pressure. The study added the influence of drainage boundary to stress, strain, global characteristics of stick-slip separately and qualitatively assessed the effect of pore pressure to stress and strain. It verified the effect of confining pressure, strain rate at the range of very high pressure up to 5-10 MPa (figure 2.6). Small excess pore pressure of about only 20 kPa was observed despite

high confining pressure and saturated condition.

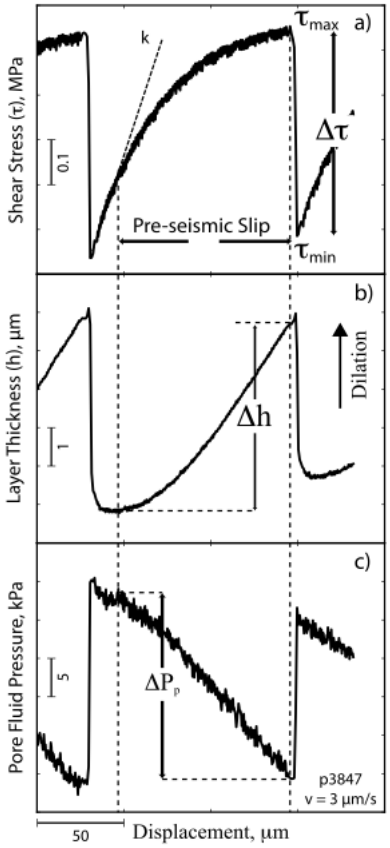

Figure 2.6: Stick-slip behaviour (stress-strain, thickness and pore pressure) in double shear testing for medium 0.125 mm beads under 1.5 MPa of confining pressure (110).

The presence of pore fluid in a fully saturated system excludes the emergence of capillary forces between particles so diminishes the complexity of the interphase stress state inside the sample. Microstructural observations by SEM images (110) highlighted the role of pore pressure in enhancing the time-dependent gouge strengthening, meaning increasing the recurrence time of stick-slip events by promoting the contact area at grain junctions. Note that this is only valid at very high pressure of 5-10 MPa with nontrivial plastic deformation at grain contact (110) including wearing effect, crushing of particle and grain fracture. Fluid is also reported to significantly enhance the magnitude of the stick-slip behaviour compared to the sparse and small amplitude stick-slip in dry granular materials (35). In a different way, fluid amplifies stick-slip phenomenon

hence facilitates the acquiring and decomposing data. The effects of amplifying the stress drop of stick-slip in saturated condition compared to the dry one are reported by Cain et al. (13) but no further analysis has been carried on the detailed coupling behaviour of pore fluid. Even the detailed response of volumetric strain within individual stick-slip event has been not captured. The presence of humidity in the media indeed plays a fundamental role in the time-dependent deformation at contacts by modification of the stress-strain behaviour and friction (29). Particularly, they found that friction coefficient decreased and larger stick-slip instability occurred in the presence of humidity compared to dry condition. Scuderi et al. (111) also found that water acts like a lubricant which enhances the frictional healing; meaning it facilitates the stick-slip occurrence. Specifically, highest stress drop occurred at humidity of 100 %.

Another advantage of studying on saturated granular media is that on the classical triaxial compression test, the variation of volume can be estimated by the volume of water expelling or moving into the sample. It also allows to study the coupled behaviour of volumetric strain and real dilatancy of the bulk medium (32).

Though, stick-slip behaviour is still significantly affected by pore fluid and has not been sufficiently understood. More specifically in isotropic collapse the role of water is still an open question. Very few experimental researches depicted the evolution of pore pressure during instabilities. Two early representative studies (in laboratory and on site) have exhibited basic features of pore pressure fluctuation (figure 2.7). The upper subfigure is the fluctuation of pore pressure located at some distances from the shearing plane of a media constituted of fiberglass rods. The dashed line is the reference hydrostatic pressure at the location of transducer numbered as 1 in the figure of cross section of testing column. The amplitude of pore pressure intermittently exceeds the normal stress, meaning the pore pressure supports the weight of the rod system above the reference surface. Associated with fast photographs at the plateau of pore pressure evolution, it was shown the separation of upper and lower part of testing rods, hence grain contacts are released. It implies the possibility that slip event can grow to a liquefaction. The lower subfigure is the development of pore pressure ratio at several locations in Christchurch, New Zealand, during earthquake describing a sudden surge of pore pressure followed by a long dissipation process. The differences in the dissipation phase are due to the geological conditions of subsoil (drained, undrained or

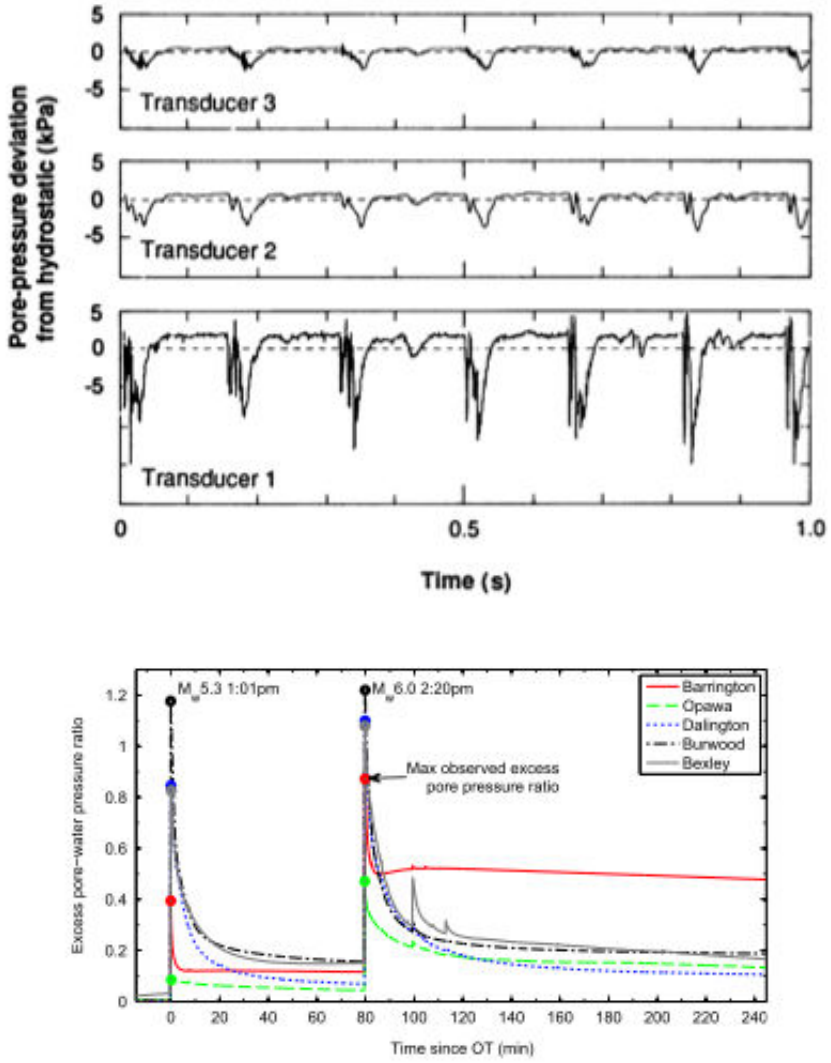

Figure 2.7: Time evolution of pore pressure from (a) laboratory test by Iverson (55), (b) realistic measurement of Christchurch earthquake (9).

partially drained).

Abrupt and sharp surge of pore pressure during stick-slip event has been detected no matter what fills the void space like air (22), de-aired water (32), sugar-water solutions, silicon oil (17), but no sufficient detailed data have been obtained to capture the dynamics of the behaviour. Small amplitude of pore pressure detected in small scale specimen in laboratory restricts the sufficiently detailed data.

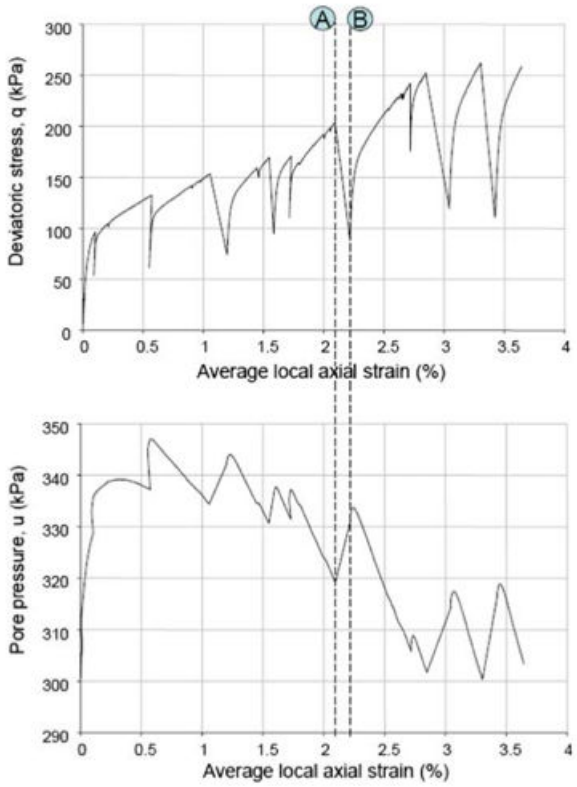

Figure 2.8: Deviatoric stress and pore-pressure in undrained triaxial compression stick-slip experiment of Leighton Buzzard sand with sugar-water solutions (17).

In saturated medium with de-aired water (32), the response of pore water pressure is like a pulse with significant large amplitude even under drained condition. With different viscosity fluid like sugar-water solutions or silicon oil (17), global undrained shearing behaviour with high viscosity pore fluid is drastically modified with the decline of shear strength compared to pore de-aired water. Figure 2.8 shows the effects of pore fluid viscosity on the stick-slip behaviour of Leighton Buzzard sand in sugar-water solutions with stress drop, jump of axial strain and pore pressure increase from slip phase of A to B. Interestingly, high viscosity pore fluid increased the occurrence of stick-slip events as well as stick-slip amplitudes. All cases exhibited the fluctuations of pore fluid pressure but no sufficient detailed data have been obtained to capture the stick-slip dynamics.

So far, no stick-slip motions are detected in realistic granular material (sands), however, in figure 2.9, the presence of only 5% of tiny 0.044 mm glass beads in Fujian

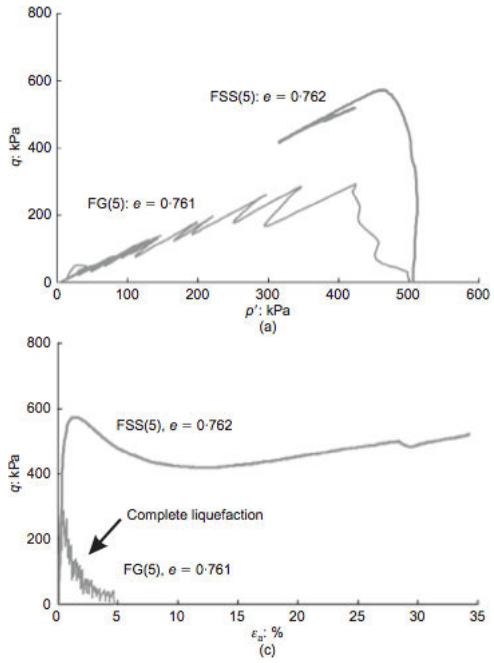

Figure 2.9: Undrained triaxial shear behaviour of Fujian sand modified by addition of 1.7 mm beads (126).

sand (FG) is enough to create undrained stick-slips accompanying by strong fluctuations of pore pressure and final static liquefaction in conventional triaxial testings (126). The usual steady-state of deformation is attained with crushed silica (FSS). Nevertheless, the presence of stick-slip instabilities in both dry (1, 22, 124) and saturated condition for model granular materials (2, 32, 125) means that pore pressure is not the cause of stick-slip.

Measuring the internal microscopic stress and strain in triaxial test requires high cost equipment, for example computer tomography (CT), thus simulations of triaxial test by DEM are needed as useful alternative. Many advances are achieved from the basic triaxial drained tests taking into account the rolling resistance (6), or other improved modifications to investigate the effect of grain size distribution (64), or various sophisticated lateral boundary condition (61, 69, 91, 125) on the attempt to capture the observed behaviour in laboratory tests.

Within the scope of the saturated granular media due to its relevance to mimic devastating disasters like liquefaction during earthquake, analytical and numerical methods

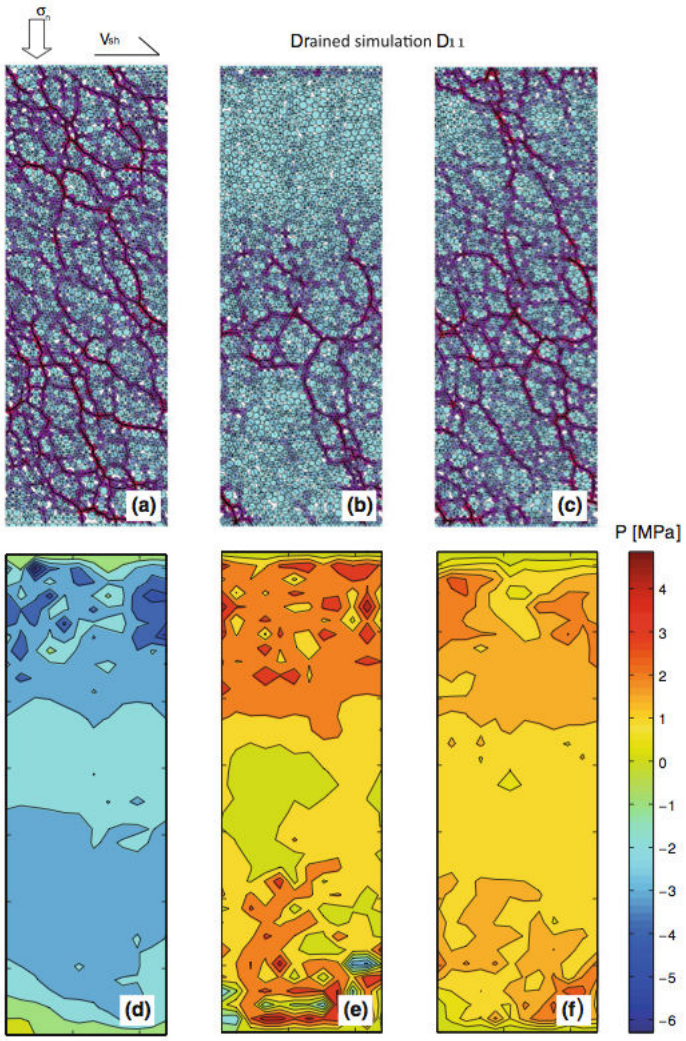

Figure 2.10: Liquefaction potential in drained numerical experiment with granular configuration (top) and pore pressure map (bottom) under 2.4 MPa of confining pressure (46).

also have been employed to reproduce the evolution of pore fluid pressure. Goren et al. (45, 46) considered the pore pressure evolution as the response to the deformation of the solid matrix. They applied a stiffness approximation assuming that the pore pressure gradient exerts a force back on the grain skeleton to relieve the effects of the void space deformation. General equations originated from continuum mechanics incorporated with Darcy's law can reproduce the generation of pore pressure in loose granular media even in drained boundary. Figure 2.10 (middle top) indicates a brief absence of stress chains due to an equally brief liquefaction state (middle bottom) when

the excess pore pressure (red) overcomes the confining pressure in drained triaxial numerical experiment. However the behaviour of pore pressure in this simulation did not reproduce the oscillations of pore pressure as in experimental evidences and the very large deformation in liquefaction case.

2.2.2 Isotropic instabilities

While stick-slip phenomenon on model granular materials still remains not fully understood, recently during the first drained isotropic consolidation stage of the same procedure of triaxial compression testing, isotropic liquefaction (31) and isotropic collapse (30) have been reported. These new phenomena happen instantaneously in a dynamic regime under isotropic loading. Liquefaction is a total failure with extremely large deformation whereas isotropic collapse still maintains the geometry after the event with limited deformation. These new types of failure increase the complexity in granular problems but question the possibility of a relation between stick-slip and these isotropic failures. The essential difference between those three instabilities is the external loading (shearing and isotropic compression).

Conceptually, liquefaction has been conventionally believed as the separation of grains from their neighbours, they loose contact, move freely, behave like fluid and stop carrying external load. From soil mechanics point of view, this phenomenon can be qualitatively explained by the lack of granular skeleton when granular particles are separated from each other; equivalent to a null effective contact stress σ' between grains. From the effective stress principle (figure 2.11 left), $\sigma' = \sigma - U$ formulated by Terzaghi (116) for totally saturated medium, σ being the total stress of the only two-phase (grains and water) element and U the pore fluid pressure, liquefaction can be best understood as the vanishing of σ' or the equalisation of σ and U (figure 2.11 middle) with a total destruction of the granular structure. Consequently, (figure 2.11 right) shows a new compacted granular structure rapidly formed at the bottom of sample with a totally separated water volume on top after liquefaction failure. Liquefaction is observed in laboratory shearing test only under **deviatoric shearing loading** and **undrained** condition.

To this day, to reproduce the liquefaction in laboratory, only two modes of liquefaction failures are introduced including (i) static liquefaction with monotonic quasi-static

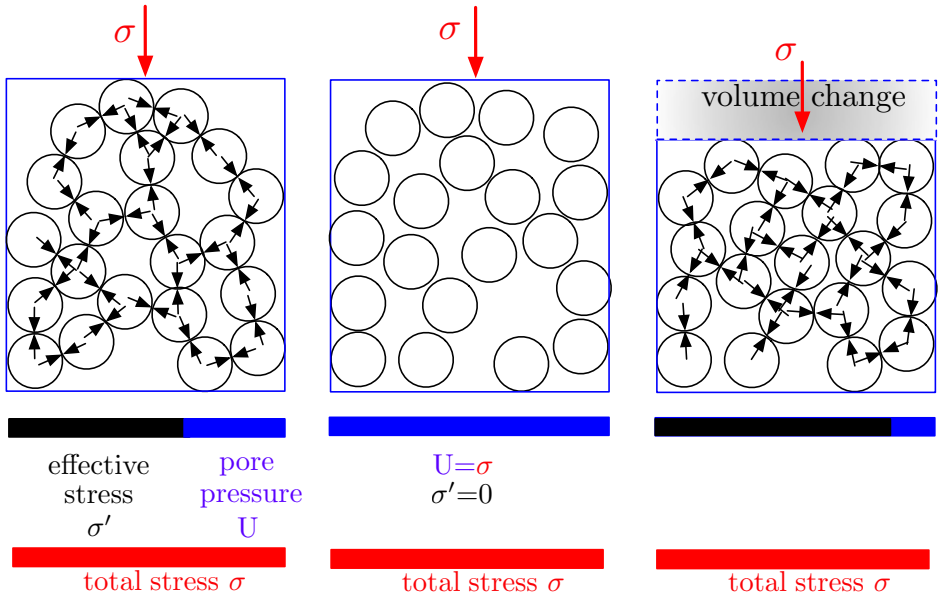

Figure 2.11: Schematic diagram of the stress composition of saturated medium including two phases, solid and liquid.

shearing load and (ii) cyclic liquefaction under cyclic shearing load. Cyclic or pseudo-dynamic liquefaction was first investigated using conventional and dynamic triaxial and torsional shear machines, due to the similarity with liquefaction induced by seismic waves during earthquakes.

Static liquefaction was rapidly followed in undrained or partially drained loading conditions. The pore pressure evolution was determined with great precision; although it was slowly and progressively generated by a quasi-static loading condition. However, the physical significance behind the pore pressure generation is far from being fully understood, excepting the soil dilatancy mechanism, Schofield et al. (109). Under undrained condition, meaning the water cannot escape, the total volume of the two phases (solid grains and water) is constant. Under static monotonic loading, the granular packing also compacts, the packing volume of the grain skeleton reduces due to the decrease of the void volume. The decline of pore fluid volume is compensated by the rising of pore pressure since pore water is incompressible. The complexity of liquefaction has risen when many field and experimental evidences of this phenomenon happen in **drained** shearing conditions, contrasting the traditional belief that no excess pore pressure can emerge in well drainage medium.

Observations on site encounter the limit of instrumentation, causing the incomplete understanding on pore pressure and acceleration of ground motions. Therefore laboratory experiments are useful and economical to learn about this phenomenon. Centrifuge and 1-g shaking table testings complete the laboratory investigation as a useful step towards the understanding of the dynamic character of earthquake. Recently in-situ instrumentation has shed new light on the real time history of excess pore pressure on liquefied soils and discovered the difficulty of measuring the pore pressure on-site. These tests point out the dynamic aspect of pore pressure by a sudden increase of pore pressure shortly after the beginning of shaking period, either in laboratory or on-site.

Figure 2.12 shows the unexpected spontaneous instabilities under drained isotropic compression and the temporal development of normalised excess pore pressure during isotropic collapse and isotropic liquefaction (31). Three events (two precursory collapses and one final catastrophic liquefaction) happen with sudden and simultaneous drop of void ratio in the compressibility behaviour; and three narrow and surprising sharp peaks of pore pressure are clearly related to these events, despite a complete drained system.

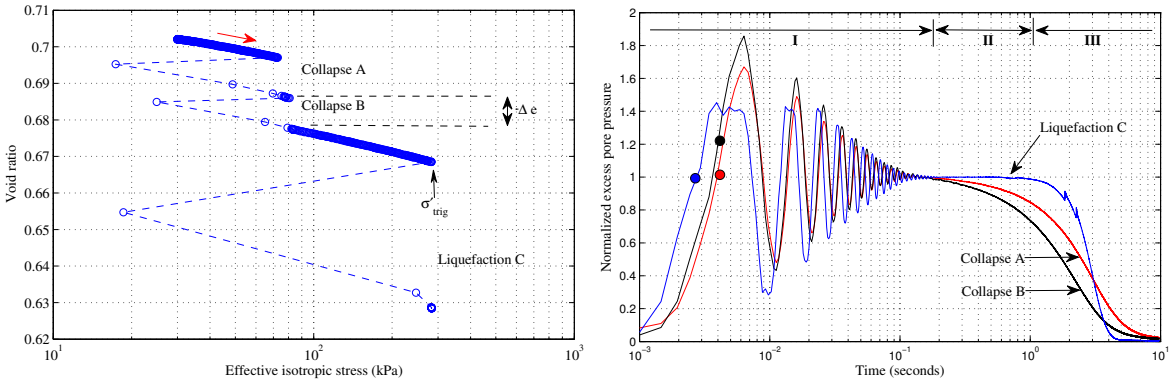

Figure 2.12: (left) Spontaneous instabilities under drained isotropic compression, (right) Time evolution of normalised pore pressure during isotropic collapse and isotropic liquefaction (31).

In the semi-logarithmic representation, excess pore pressure is normalised by its stabilised value (the absolute value after the decaying vibration) to see the similarity features of various events independently of stabilised excess pore pressure and triggering stress. This synthetic representation shows a clear temporal evolution of pore pressure from the initial steady-state of back pressure in 3 phases: (i) first, a transient phase I

lasting only 200 ms with very fast rising time to reach the peak of excess pore pressure. The excess pore pressure vibrates like an oscillating underdamped system with a same dominant frequency, irrespective of event type, (ii) second, an intermediate phase II for liquefaction case only, characterised by a constant excess pore pressure for more than one second, (iii) third, a longest dissipation phase III in which the pore pressure returns to the initial equilibrium state. The solid circles indicate the liquefaction level with vanishing effective stress. The duration of phase II was not long enough for collapses A and B to sustain a full liquefaction.

Isotropic collapses or local failures are characterised by limited axial and volumetric deformations, and the possibility to resume the compressibility behaviour, while isotropic liquefaction or total failure refers to very large strains with total destruction of the granular skeleton.

In this study, the appearance conditions for instantaneous liquefaction were also identified in figure 2.13: (i) the usual vanishing of the effective stress $\sigma^{'}$, (ii) the duration of this effective stress should extend beyond one second, and (iii) the granular assembly should be loose enough above the void ratio threshold e_{30}^{thres} at 30 kPa of confining pressure.

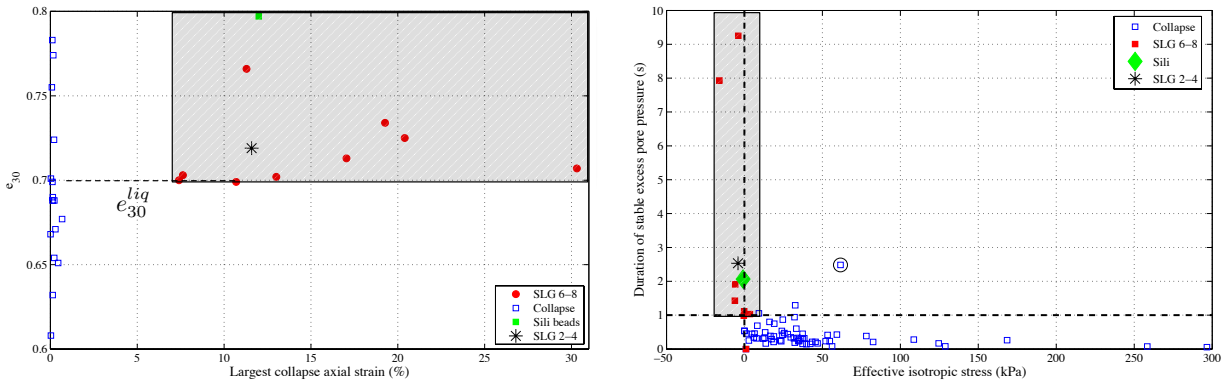

Figure 2.13: Conditions for isotropic liquefaction (left) Void ratio threshold, (right) Duration of stabilised excess pore pressure (31).

The important role of pore fluid pressure on amplifying the stick-slips was noticed, as in isotropic liquefaction and collapse. So far, isotropic collapse and compression stick-slip are also detected in dry granular medium (30, 125). However, the pore air pressure generated during stick-slip in dry glass beads (22) is too small below 1 kPa

under confining pressure of 1 MPa. This low pore air pressure cannot vanish the effective stress of the grain skeleton, as a result dry sample cannot liquefy. Therefore, the presence of pore fluid is one necessary condition to liquefy, but whether pore fluid is the cause of liquefaction needs to be explored.

In civil engineering and nature, numerous collapses take place without external loading causing devastating settlement even total failure of the ground. This phenomenon is more dominant for loose and collapsible soil. El Korchi et al. (38) found that the suction stress variation as the cause triggering the collapse. The question is again raised here that if the modification of water pressure happens before the release of the skeleton stress.

2.3 Acoustic technique

In 3D system it is difficult to access the stress-strain measurements at grain scale, hence sound wave is introduced as a useful tool to probe the information from contact force networks.

Useful effective technique as visualised photo-elastic disks, successfully applied in 1D-2D system, is no longer effective for 3D system. In that situation, acoustic emission (AE) technique seems to be an appropriate solution. Remind that the force fluctuation of granular medium is a multi-scale issue, but there is no clear separation of spatial-temporal scale, thus to some extents AE could overcome this obstacle. It offers the access to further information relevant to the grain scale behaviour that is not efficiently obtained by macro-measuring instruments. It is more popularly applied in monitoring and diagnosing the civil structures and materials. Some crucial advanced contributions of AE technique is briefly presented in this paragraph.

At microscopic scale the interaction between grains is very complicated; each particle slide, rotate, collide with chaotic trajectories. The following mechanisms are possible sources for acoustic signal: motion at grain contact, collision between grains, abrupt release of contact force, buckling of force chain column, rupture of capillary bridge, rearrangement of grain contact network, breakage of cementation contact, motion of fluid (hydroacoustic), and so on. Corresponding to each mechanical response at micro/mesoscale, a characteristic range of frequency or energy is estimated (80). Those referenced values can be theoretically, experimentally or numerically evaluated. Note

that AE signals are generally generated as the combination of multiple sources, thus it often requires more localised techniques to separate the underlying mechanisms.

In physics, within the solid-like behaviour, Hidalgo et al. (52) measured acoustic waves during microscopic rearrangement of a uniaxial compressed cylindrical granular sample and linked the statistics of AE signals to macro constitutive model (continuous damage model of finer composite). AE distribution showed a good agreement with the suggested novel approach, meaning that the dominant failure mechanism is the rupture of force chains. Gardel et al. (41) considered the characteristics of dense flow using piezoelectric sensor directly attached on the container of glass beads to capture the force and velocity fluctuations during the flowing regime until almost jamming state. Rich information are presented to recognise the dominant interactions at grain scale which are collisions or frictional motions with distinctive frequency contents. It also showed the soft transition from collision in flowing regime to frictional dynamics near jamming threshold. Furthermore, the spatial correlations of force and velocity were identified averagely across the cross section of the container. Acoustic activity before the failure is associated to precursors and is diagnosed to be the reorganisation of the weak force chains in the bulk media (25, 37, 127).

In geoscience and geotechnical engineering, the AE originated during continuous deformation of soil is used to probe the movement of slope (12). The characteristic frequencies of AE measurements corresponding to various rainfall amount during the failure are also identified (104) and help to link with the potential of imminent landslide. Qualitative assessments are obtained to recognise the impending failure such as the increase of AE rate or AE energy release during static deformation prior to major failure (26, 39, 59, 81) or the drop of elastic wave velocity in soil slope during rainfall being the indicator of an ongoing landslide (19). As an improvement, high temporal resolution AE measurements produced a quantitative good direct linear relation between generated AE rate and velocity of the slope movement (114) which exposed the promising potential in early warning applications.

One of the statistical models using AE measurements to qualitatively describe the process of micro-scale failure is Fiber Bundle Model (FBM) (48, 81). The change in power-law distribution of AE burst energy before a failure associated with the statistics of event amplitude can be detected. These studies tried to link the distribution of AE energy release to the distribution of event magnitude. Figure 2.14 shows the

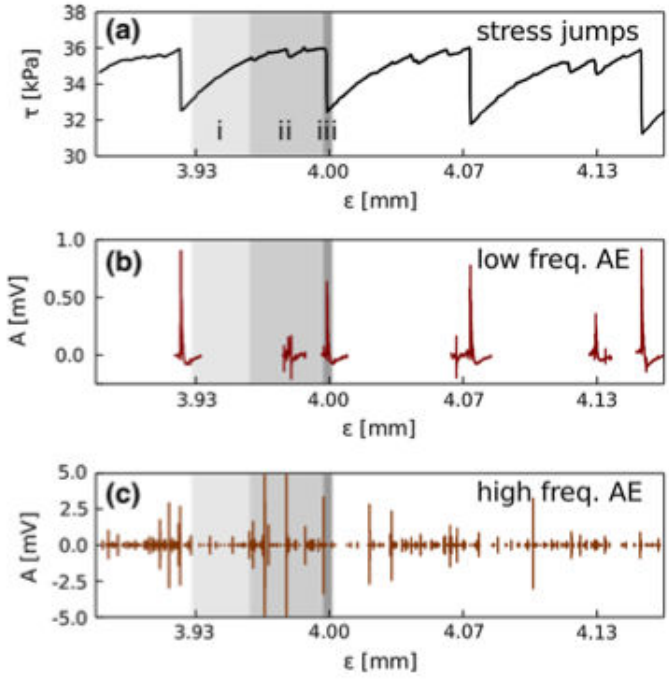

Figure 2.14: Stick-slip and acoustic measurements in direct shear stick-slip experiment of 4 mm beads under 60 kPa of confining pressure (81).

synchronous record of low and high-frequency acoustic signals with stick-slip in direct shear experiment of 4 mm beads under 60 kPa of confining pressure. These mechanical and acoustical measurements were highly correlated. Nevertheless, the empirical relation between stress jump and AE event amplitude is still unclear (81).

2.4 Objectives of the research

In the aforementioned context, instability is of great interest in granular materials science. While the undrained instability and the diffuse failure on sands have been successfully simulated (24, 90), the recent unexpected instabilities on model granular materials, i.e. the stick-slip, especially the coupled volumetric stick-slip and the fast transition from solid-like to liquid-like behaviour has not been fully predicted theoretically, despite a large number of advanced constitutive models for geomaterials at macro scale (24, 47, 65, 68, 82, 90, 123), nor detected in advanced numerous numerical DEM experiments for spherical particles (77, 78, 95, 112), even including a full solid-liquid

coupling formulation (45, 46).

These unknown instabilities (isotropic collapse, isotropic liquefaction and compression stick-slip) on model granular materials in their simplest possible shapes with very simple isotropic compression experiments can enhance the current understandings and modelling of real granular soils. The experimental work in this thesis has a threefold objective:

First, following the discovery of a third liquefaction type under drained isotropic compression, is it possible to discover additional liquefactions under other conditions? What are the appearance conditions? What are the factors controlling the evolution of axial and volumetric strain, as well as that of excess pore pressure in these instabilities? What are the links between stick-slip, isotropic collapse as well as isotropic liquefaction? This first set of questions is the staring point of this work.

Second, the role of pore pressure in the saturated granular assembly is of paramount importance. However, its dynamic response has been often overlooked, especially in stick-slip phenomenon. The existence of the surprising excess pore pressure peak is unambiguously detected in experimental studies in drained and in undrained conditions, and triggers a new set of questions: What are the physical triggering mechanisms? Can we explain the unexpected pore pressure outburst? Can we relate this outburst to other stress and strain measurements by quantitative relationships? Why the strong oscillations pore pressure of the transient phase I, and not on strains? And more importantly, what are the reasons for keeping stabilised excess pore pressure for more than one second in phase II in order to liquefy? The partial answers to this second set of questions should rely on an in-depth verification of the pore pressure measurements and on high-time resolved data. The exploration of stick-slip phenomenon, especially the dynamic slip phase, with new observations on well designed experiments using new set of up-to-date sensors is one of the objectives of this work.

Third, the primary goal of this work still concerns the elusive physical triggering mechanisms, especially in the case of isotropic instabilities. The literature review suggest the use of passive acoustic measurements in low frequency range with easy-to-use small submersible accelerometer inside the travail chamber, complemented by external

microphones and laser vibrometer. Can we relate the mechanical and acoustical measurements during isotropic and triaxial loading, i.e. the macroscopic stress and strain parameters and the magnitude and acoustic energy on the level of individual events? Can we find the distinctive spectral signature of these dynamic instabilities? Answering this set of questions is equally one of the goals.

3

Experimental work

3.1 Introdution

This experimental study is conducted at the Laboratoire de Tribologie et Dynamique des Systèmes (LTDS, Tribology and Systems Dynamics Laboratory) of l'École Nationale des Travaux Publics de l'État (ENTPE, National School of Publics Works). Classical isotropic and triaxial compression tests are performed, using high resolution data acquisition system and high precision sensors to investigate the detailed behaviour of saturated granular materials under medium range of effective confining pressure, from 50 up to 500 kPa. Model granular materials are successively submitted to a drained isotropic compression (isotropic consolidation), followed by a triaxial compression under drained or undrained conditions. This chapter describes the material, the apparatus, the sensors, the system and the procedure of the test. The testing programme is also presented.

3.2 Material descriptions

The soda lime spherical glass beads "Sil-glass" used in this study are supplied by CVP Linselles, France. The chemical compositions of glass beads in table 3.1 indicates a sensitive component, 15-20% calcium oxide (CaO), implying the possibility of chemical reaction with the surrounding substance.

Figure 3.1 shows an Scanning Electron Microscope (SEM) image of a virgin glass beads SLG 6-8 (around 0.7 mm of diameter) with smooth texture of the surface and spherical shape. These beads have a static friction coefficient of 0.24 on glass according

SiO_2	Na_2O	CaO	MgO	Al_2O_3	Others
60-70%	12-18%	15-20%	1-4%	1-5%	± 2 %

Table 3.1: Chemical compositions of CVP soda lime glass beads

to CVP. Although such model granular material is of different shape compared to real ones, it provides the simplest description of the shape of real sands to test in laboratory. In the other hand, numerous numerical studies are based on spherical particles to allow fundamental understandings on the complex behaviour of granular materials. Thus laboratory experiments on spherical glass beads can complement and validate these simulated works.

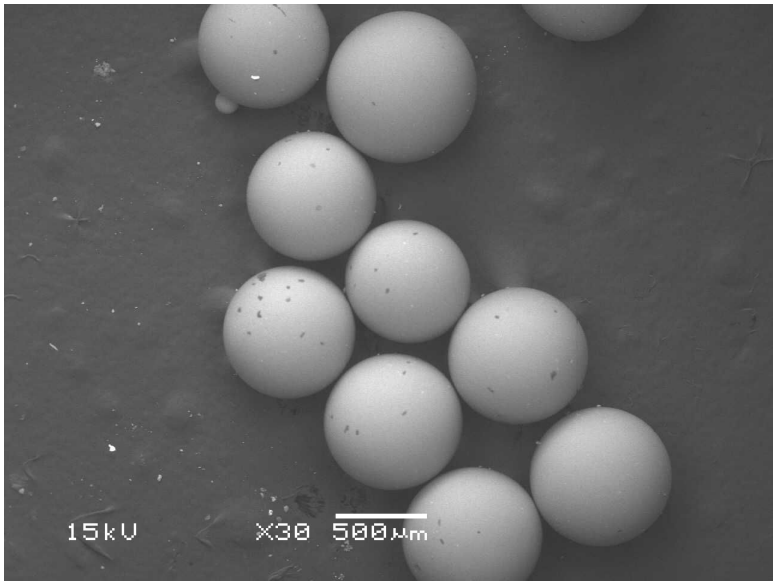

Figure 3.1: SEM picture of CVP glass beads

The particle size analysis is performed to determine the aggregate characteristic of material by laser diffraction method. The gradation curve in figure 3.2 representing the percent of particles finer than a given size has a very steep slope of uniform grain size. The frequency histogram shows an almost symmetric distribution with average diameter D_{50} of 0.723 mm. This characteristic is quantitatively measured by two coefficients based on the distribution of particles: uniformity coefficient $C_u = \frac{D_{60}}{D_{10}}$ and curvature

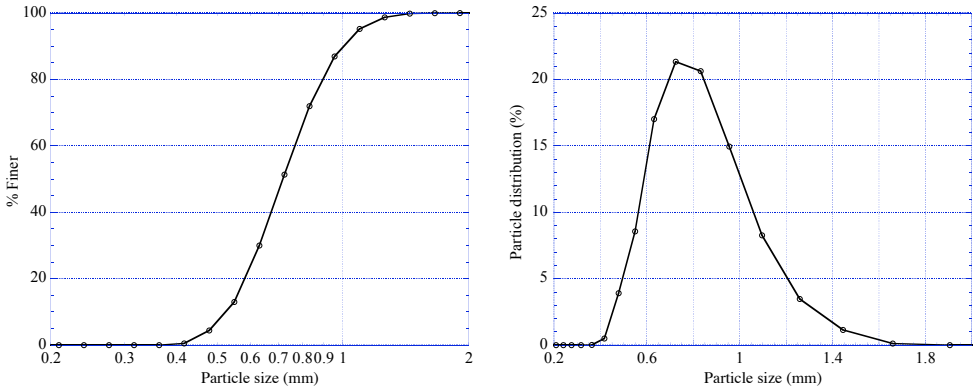

Figure 3.2: Gradation curve and grain size distribution of CVP glass beads

Property	D_{10} mm	D_{30} mm	D_{60} mm	D_{50} mm	e_{max}	e_{min}	C_u	C_c
Value	0.523	0.630	0.776	0.723	0.686	0.574	1.463	0.989

Table 3.2: Properties of CVP glass beads

coefficient $C_c = \frac{D_{30}^2}{D_{10} * D_{60}}$ (10). D_{10} (D_{30}, D_{60}) is the diameter of particles having 10% (30%, 60%) of particles finer. In table 3.2, C_u is very close to the minimum value of 1, corresponding to a mono-sized assembly. Additionally C_c, also close to 1 without any gap in gradation curve, confirms the uniformity characteristic of glass beads. This material can be considered as ideal spherical monosized and correspondingly classified as clean poorly graded and fine-grained sand (SP) according to the United Soil Classification System.

3.3 Triaxial test apparatus

The conventional triaxial test apparatus, Figure 3.3, normally consists of basic components as follows: the loading frame, the pressure control system, the triaxial cell, the sensors and the data acquisition system.

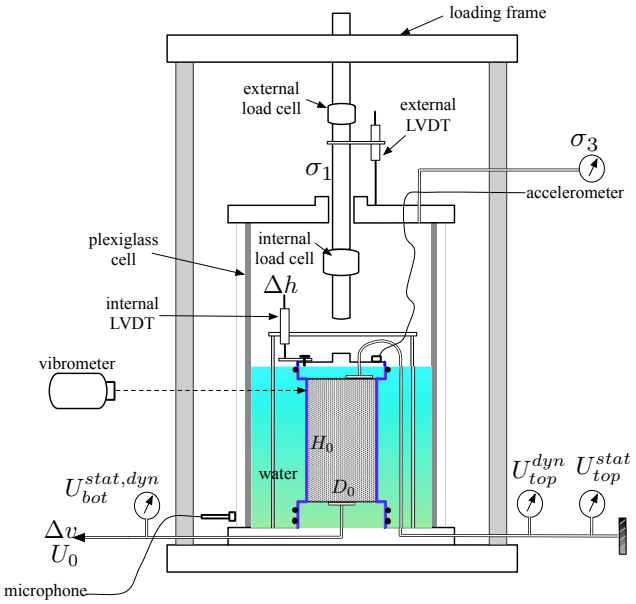

Figure 3.3: Scheme of the triaxial test apparatus

3.3.1 Loading frame

The loading frame is 2-column type, from Farnell, with top beam clamping. It is capable of handling compression testing up to 50 kN which is much higher than the axial stress σ_1 required in this study and allows both monotonic and cyclic loading with additional control system. It is built with precision gear to ensure smooth and reliable operation. It is also versatile due to the mixed electro-mechanical actuation type which is useful when adjusting or connecting the vertical loading ram. It provides a manual strain rate gauge to operate the strain-controlled regime of vertical loading. The applied constant axial strain rate is between 0.001 mm/min to 4 mm/min. One auxiliary external load cell is attached on the loading frame and connected to the slow data acquisition system. Its maximum capacity is 20 kN.

3.3.2 Pressure controller

Two pressure control systems are designed independently. The first system controls the confining pressure of the triaxial chamber which includes air pressure regulators and pneumatic system connected directly to the space inside the chamber through a tube at the top cap of chamber. The confining pressure is added manually and

displayed in pressure gauge with the precision of 1 kPa and the capacity of 700 kPa. The second system controls the back pressure which also consists of air pressure regulators, pneumatic system and water tank. Air pressure, manually regulated, is transmitted to the sample by compressing de-aireated water through thick plastic tube at the pedestal of the triaxial chamber.

3.3.3 Triaxial cell

The triaxial cell is a usual transparent plexiglass (axisymmetric) cylinder reinforced by five equal-spaced carbon bands along the height. The cell wall is installed before the top plate, then the top plate is fastened by 8 columns screwed tightly to the pedestal and the loading ram is assembled to the loading frame. The triaxial cell partially contains water to transmit isotropic pressure to the sample.

3.3.4 Measurements

An **external linear variable differential transformer** (LVDT) is fixed outside the triaxial chamber to monitor the axial displacement of loading ram, figure 3.3. This sensor L50 has a measuring range of 50 mm. Since this outside measurements of axial deformation are affected by numerous errors (alignment of loading ram, gaps between loading piston and sample top cap ...), this external displacement sensor is just a global backup axial measurement.

A waterproof **internal LVDT**, type L20, is mounted on a fixed frame inside the cell and directly touches the specimen top cap to record the actual axial displacement Δh of the sample. Its measuring range is 20 mm while the investigated axial strain of sample is set to 25%, approximately 18 mm of displacement. The LVDT was calibrated within the range of 30 mm by steps of 0.2 mm. The sensitivity of the device is 0.1 V/cm. Since local strain sensors are too heavy for loose glass bead sample, this internal LVDT is a small improvement over outside LVDT (1, 17, 22, 124).

A **pressure transducer**, Sedeme MD20, monitors the confining pressure with the resolution of ± 0.05 kPa.

An **external load cell** outside the triaxial chamber, type BD20 of Sedeme, measuring the axial force at the interacted position with load frame, is directly attached on the press frame. The maximum load is 20 kN. Due to the non-alignment of loading ram and press frame or friction, this external force sensor is used as backup measurement.

A submersible **internal load cell**, of Wykeham Farrance, is assembled nearly at the end of the loading ram. This load cell is close to the contact position of the ram and the specimen top cap. The precision of force measurement is high due to the exclusion of piston friction.

The **pore pressure** is detected by two different techniques using 4 sensors, 2 at the top and 2 at the bottom of the sample. The location scheme of pore pressure sensor is in figure 3.3. A piezoresistive transducer (Sedeme, MD20) with unknown resonant frequency is mounted at a distance of 60 cm from the top cap and outside the chamber to acquire static pore pressure. A piezoelectric transducer (PCB S112A21) is 10 cm from the piezoresistive transducer. This one is of high resonant frequency of 250 kHz and used to get dynamic pore pressure at sample top. At the distance of 10 cm from the specimen bottom and also outside the chamber, a static sensor (Kistler, 4053A10) with natural frequency of 120 kHz and a dynamic sensor (PCB S112A21) are combined in one box to measure static and dynamic pore pressures at the sample bottom. The capacity of sensors is up to 2 MPa and accuracy is $\pm$ 0.05 kPa.

A **volumetric sensor** measures the volume variation of specimen by water entering and expelling from the sample while deforming. This volume change measuring device, of Wykeham Farrance, is installed in one parallel branch of a bifurcated system to supply and control the pore fluid pressure. The volume change sensor and the applied back pressure are connected to the bottom of sample by the same small tube.

An **accelerometer** (PCB 607A11 SN 140952), is a piezoelectric sensor measuring the vertical acceleration of the sample top cap. The sensitivity is 9 mV/g. The acceleration range is 100 g. This sensor provides a broad useable frequency response of 0-10000 Hz. It has small dimensions around $1.5 * 1.5 * 2.0$ cm and light weight of about 50 gr.

A **vibrometer**, Ometron OH-100-D, used in this study is of non-contact single point laser vibrometer. It measures the amount of vibration at a single point on the object's surface. More specifically, a laser vibrometer measures the projected component of the object's surface vibration vector along the direction of the incident laser beam. The vibrometer is installed outside the triaxial chamber, of about 0.7 m from the specimen's membrane. Surface vibration in velocity and displacement are measured with high precision and low noise with a bandwidth of 3.2 MHz at 10 m/s maximum velocity.

A **microphone**, PCB 377B02 class A, is fixed on the bottom base plate to acquire the lateral sound pressure outside the triaxial chamber. To avoid the unwanted noise of the surrounding structure component where the microphone is installed, it is wrapped by rubber sheet and isolated sheet.

3.3.5 Acquisition system

All signals of sensors (voltage changes) are measured by a synchronised dynamic data acquisition system NI4472B of National Instruments with 14 channels. Some sensors need to be amplified before being collected by acquisition box: internal axial load, external axial load, cell pressure, axial strain, volumetric strain, and four pore pressure sensors. Moreover, we keep in parallel two data acquisition systems: one old slow system HP3852 with the sampling frequency of 0.5 Hz and one new faster system operated at 10 kHz. The slow system only records permanently the external and internal vertical load, cell pressure, static pore pressure at the top of sample, internal axial strain and volumetric strain. Since the number of acquiring channels has been extended gradually in the testing period so not all tests have acquired all those measurements. Then the data are transferred to a computer via an acquisition HPIB card. LabView software is customarily composed to control and graphically display the data during test.

3.4 Sample preparation

The sample is constructed directly on the base fixed to the pedestal of machine at the center of chamber. The diameter of the sample base is 9 cm, larger than the sample diameter of 7 cm. These enlarged top and bottom platens are used throughout this study to ensure the uniform radial deformation of sample along its height (115). On the same purpose to lubricate the interfaces of sample and platen to freely deform at large strain during shearing, only a small filter paper is put at the bottom platen.

The porous stone of 20 mm in diameter is installed in both the bottom and top platen of specimen. The bottom and top cap platens were made of polished duralumin to minimize the weight of the top cap on loose specimen.

A 0.3 mm thickness membrane is stretched over the bottom platen, figure 3.4. To preliminarily hold the membrane, a small amount of water is placed on the inner surface

of membrane in contact with the bottom platen. A small rubber O-ring is placed on the higher groove and a large ring is moved downward to keep the membrane in place.

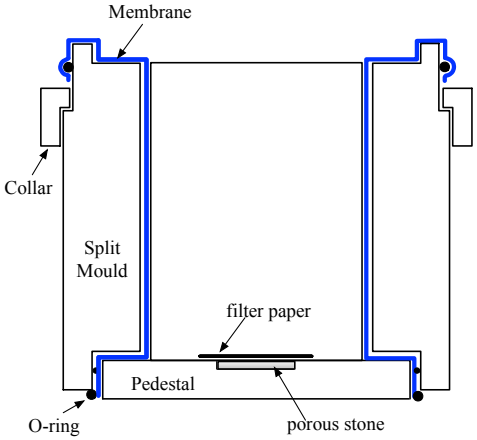

Figure 3.4: Accessories for sample fabrication

A thin layer of grease is spread along the vertical cross section of the split mould to support the vacuum condition and to stick two halves of them together. The mould is placed on the base to cover the platen and membrane. The mould collar is assembled and two cramps below the collar are tightened to fit the mould. Another rubber O-ring is put around the top collar to close the membrane and top platen subsequently. A proper amount of vacuum pressure is applied through three holes in the body of split mould. The upper extended part of membrane is stretched and folded out to cover the mould top as well as the O-ring. Vacuum pressure is used to attach the membrane to the inner wall of the mould and to keep identical diameter of sample during deposition of granular material. Note that the dimension mark on the membrane should be adjusted to match the mouth of the mould thus the membrane is not twisted or stretched or loose resulting in the unanticipated initial stress state of material when dismounting the mould. A filter paper in circle shape of 30 mm diameter is placed on top of the porous stone. Figure 3.5 shows the final step of mould preparation.

The sample is fabricated by moist tamping method to create the loose initial state (66). Glass beads are weighed and mixed with 2% of distilled water in weight. This mixture must be covered to keep the moisture constant. The material is divided into 5 equal amounts for 5 layers. The material is gradually transferred to the mould by small spoon with no drop height. Only 1-2 grams of material is placed on the mould each

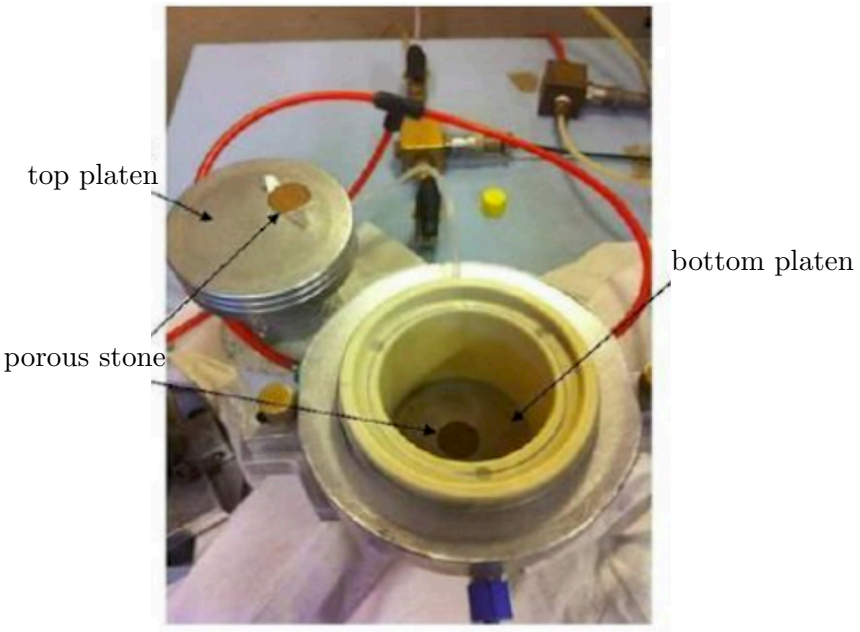

Figure 3.5: Scheme and picture of available mould for deposition of material

time. The order of location of material in the circular section of the mould is complied with the spiral locus from the outside circumference to inside. The upper surface of the deposited material should be flat before tamping. Each layer is compacted by circular rod of 20 mm in diameter to reach the predetermined equal thickness. The motion of tamping rod is also spiral from outside to the center. Approximately 10-12 gentle impacts are applied for each layer. The surface of deposited layer is slightly scratched by a brush before adding another layer. The indentation is carried out in only 1-2 mm depth to avoid the artificial sliding surface between layers. The cycle of action is repeated until the top layer. The pre-compacted thickness of the top layer always exceeds the height of mould, therefore a stainless ring is used to extend the wall of mould for the purpose of avoiding the formation of narrow neck at the specimen top. The ring is removed after compacting the top layer. No indentation is needed for this layer. It should be ensured that no glass beads are left on the horizontal surface of the mould collar prior to put the top platen to enclose the sample. The top platen is pressed and the folded membrane is gently rolled up around the side of top platen. The rubber O-ring is moved up to the groove to tighten the membrane. The tube at the pedestal connected with bottom platen is closed to apply a vacuum pressure of

around -10 kPa inside the sample to hold it and carry the top platen while separating the mould. The mould collar is removed before the installation of internal LVDT and vertical accelerometer. The altitude of the top platen is noted before dismounting the mould. The split mould is carefully disassembled without modifying this altitude. Any altitude variation is taken to deduce the void ratio of sample at the beginning of test. The large O-ring at the bottom platen is moved to the groove. The diameter of sample is measured at the bottom, half and top position by measuring tape, then the average diameter is identified.

Figure 3.6: Deposition of material, top layer and finished sample

3.5 Apparatus preparation

A circular frame is erected around the specimen to mount the internal LVDT. The availability of the sensor is always carefully checked. From now on, the value of LVDT is always measured to estimate the void ratio of sample. The triaxial chamber and the top cap of cell are assembled without disturbance of the specimen and keep a good alignment of vertical loading ram. The loading ram is fixed to the rod of loading frame. The cell is filled with water up to level of top platen of sample. The pneumatic system

is connected to the chamber through the tube on the cell top and all possible sensors are checked at this stage (except for volume change sensor and four pore pressure sensors). The axial deformation is noted before the application of initial cell pressure. The vacuum pressure inside the sample is now replaced by the cell pressure. The transferring process is manipulated to keep the effective stress of the granular medium constant. Hence the vacuum pressure is released with the simultaneous application of confining cell pressure at 20 kPa. Axial deformation is always recorded during this process and should be constant.

3.6 CO_2 percolation and saturation

CO_2 is injected at low pressure of 0.02 - 0.03 kPa through the bottom drainage system at pedestal. The air occupying the void of the granular assembly is pushed out and replaced by this soluble gas to facilitate the saturation of sample. This process lasts within 2 hours (at least 30 min depending on kinds of material). A tube connected with the top specimen is put in a bowl of water to check the speed of CO_2 percolation of about 2 bubbles per second.

The tank of back pressure controller is filled by distilled de-aired water. The water supply system is connected to the bottom platen. At this step static and dynamic pore pressure sensors at the bottom are also installed. De-aired water is pushed to the bottom of sample under 3-5 kPa and constant rate. Depending on the type of material, the imbibition rate is different. In this study with bead diameter of about 0.7 mm, the rate is 400 ml of water in 14 hours (28.6 ml/hr for clean sand specimens). The effectiveness of the saturation process is subsequently verified by Skempton coefficient. Note that the axial deformation is always acquired continuously before and after saturation process.

3.7 Application of back pressure

Back pressure technique is necessary to support the saturation condition of sample. The target of this step is to create a back pressure of 200 kPa and keep the sample intact regarding stress state and deformation. The detailed manipulation is the following:

The bottom valve is closed to stop supplying water, then the static and dynamic pore pressure sensors are connected to the top of specimen. The bottom valve is open again and wait until the pore pressure equals the pressure of the water tank (3-5 kPa). The volume change sensor is connected, checked and set the initial value. An intermediate step is carried out in which the cell pressure is increased to 40 kPa simultaneously with an imposed pore pressure at 20 kPa to keep the effective pressure constant at 20 kPa. Next, simultaneously the cell pressure is manually increased up to 220 kPa and the pore pressure up to 200 kPa at the same rate. This step must prevent the sample from any additional stress state or deformation and keep the effective stress constant at 20 kPa.

3.8 Estimation of Skempton coefficient

Once the pore pressure stabilized, the bottom valve of drainage system is closed to isolate the sample. The cell pressure is increased from 220 kPa to 320 kPa to have an incremental cell pressure in loading of $\Delta\sigma_3 = 100$ kPa. The excess pore pressure is measured and the Skempton's coefficient (113) in loading estimated by:

$$\Delta u = B[\Delta\sigma_3 + A(\Delta\sigma_1 + \Delta\sigma_3)] \tag{3.1}$$

where A, B are pore pressure coefficients measured experimentally and $\Delta\sigma_3$, $\Delta\sigma_1$ are incremental radial and vertical stress.

Due to isotropic condition then A = 0 thus Δu = B $*\Delta\sigma_3$ and B = $\frac{\Delta u}{\Delta\sigma_3}$.

The inverse process to decrease cell pressure from 320 kPa to 220 kPa is also conducted to have B in unloading. The lowest value of B is taken as Skempton's coefficient. The state can be considered as saturated when B is larger than 0.95.

3.9 Testing procedures

A classical triaxial test consists of two successive loading steps: isotropic drained compression or isotropic consolidation followed by drained triaxial compression or vertical shearing only if the sample is still geometrically stable. The first step is stress-controlled while the second is axial strain-controlled.

3.9.1 Drained isotropic compression

In this first mandatory stage, the drainage is allowed with opened bottom valve. Since the drainage of the sample top cap is connected to a closed-end, the water can only expel from the sample bottom. The cell pressure is increased manually at mostly constant stress rate until reaching the desired level. The cell pressure is slowly increased by step of 2-3 kPa followed by a waiting time for the pore pressure to return to a stable back pressure level.

3.9.2 Drained triaxial compression shearing

After the isotropic consolidation phase, if the sample still maintains its cylindrical geometry, the triaxial compression shearing phase is started by adding an axial load and allowing the drainage. The presence of axial stress creates a deviatoric stress q. In this research, fixed axial strain rate of 0.02 mm/min was used to conduct CID (isotropically consolidated and drained) triaxial test. This rate was selected to ensure a proper dissipation of pore pressure on glass beads and on usual sands. The test completes when the sample reaches an axial strain of 25 %.

3.9.3 Undrained triaxial compression shearing

For undrained shearing, the same procedures as drained shearing phase are performed excepting that the drainage system is not allowed.

In summary, a drained (or undrained) triaxial testing includes the following steps in two distinct phases:

- Preparation phase
  - Sample preparation
  - Sensors preparation
  - CO_2 percolation and water saturation
  - Application of back pressure
  - Estimation of Skempton coefficient
- Testing phase

– Prerequisite drained isotropic compression (isotropic consolidation)

– Drained (or undrained) triaxial compression (vertical shearing)

3.10 Determination of void ratio

3.10.1 Determination of void ratio by weighing method after test

To identify the void ratio of sample at the end of each test, in case of drained shearing phase, the bottom valve is closed immediately to isolate the remaining water inside the sample. In undrained shearing test, this step is skipped because the valve is already closed. The testing devices are dismantled in this order: back pressure and cell pressure are simultaneously released to 0 and 100 kPa, energy sources of sensors disconnected, water inside the chamber pushed out due to the remaining cell pressure of 100 kPa, then remaining pressure of 100 kPa completely released, cell top cap removed, all internal sensors and cell finally disassembled.

The outside surface including membrane, O-ring, top-bottom platen and platen are dried totally by paper towels. The O-ring placed at top platen is removed first, the top platen is separated and dried by towels. The O-rings at bottom platen are removed, the whole of membrane and materials inside carefully transferred to an aluminium tray without loosing water and grains. This tray together with all used towels is weighed (m_{final}) with accuracy of ± 0.1g and dried out in oven at 100^{o}C until the mass is constant (m_{dry}).

The mass of water at the final state of test is:

$$m_{water} = m_{final} - m_{dry} \tag{3.2}$$

The void ratio at the final state of test (e_{final}) is:

$$e_{final} = \frac{m_{water} \cdot \rho_s}{m_s \cdot \rho_{water}} \tag{3.3}$$

in which, ρ_s is density of grains, ρ_{water} density of water and m_s mass of grains.

Based on this final void ratio e_{final} and on continuous measurements of volumetric variation and axial displacement, the void ratio and cylinder dimensions of sample at each fabrication stage are determined. A backward calculation procedure is established as below:

The void ratio at the beginning of drained shearing phase e_{shear}:

$$e_{shear} = \frac{\rho_s V_{shear}}{m_s} - 1 \tag{3.4}$$

V_{shear} is the total volume of sample at the beginning of shearing stage. In case of undrained shearing, $e_{shear} = e_{final}$. V_{shear} is deduced from the final weighing by:

$$V_{shear} = \frac{m_s}{\rho_s} + V_{water} + \Delta V_{shear} \tag{3.5}$$

ΔV_{shear} is the volume change of the drained shearing stage which is read by volumetric sensor.

The height of sample at the beginning of shearing phase H_{shear} is estimated from the initial height of the sample H_0, the displacement during initial fabrication Δh_{ini} counted from the beginning until setting up the volume change sensor, the displacement during intermediate steps, Δh_{int}, such as application of back pressure or measuring Skempton's coefficient and displacement of the whole stage of isotropic consolidation Δh_{cons}. All displacements are acquired by internal axial LVDT during testing procedure.

$$H_{shear} = H_0 - \Delta h_{ini} - \Delta h_{int} - \Delta h_{cons} \tag{3.6}$$

From V_{shear} and H_{shear}, the diameter of sample at the beginning of shearing phase can be determined:

$$D_{shear} = \sqrt{\frac{4V_{shear}}{\pi H_{shear}}} \tag{3.7}$$

Similarly the void ratio and diameter at the beginning of isotropic consolidation is also identified.

3.10.2 Determination of void ratio according to the initial geometry measurements

From the initial geometric measurements of the sample when dismantling the mould, the vertical displacement of the sample is continuously measured by internal LVDT throughout the test. As the volume change sensor is only connected after saturation process before the step of application of initial 20 kPa confining pressure, there is an initial duration in which the volumetric strain needs to be estimated according to hypothesis that strain behavior of the media complies the anisotropic characteristics during isotropic consolidation. This characteristic is represented by the experimental anisotropic coefficient $i = \frac{\varepsilon_v}{\varepsilon_1}$.

The volume change in initial duration is

$$\Delta V_{ini} = \frac{\pi D_0^2 H_0}{4}\varepsilon_v = \frac{\pi D_0^2 H_0}{4} * i * \varepsilon_1 = \frac{\pi D_0^2}{4} * i * \Delta h_{ini} \tag{3.8}$$

The void ratio at the beginning of drained shearing phase is e_{shear}. V_{shear} is deduced from the initial geometry measurements by:

$$V_{shear} = \frac{\pi D_0^2 H_0}{4} - \Delta V_{ini} - \Delta V_{int} - \Delta V_{cons} \tag{3.9}$$

The height of sample at the beginning of shearing phase H_{shear} is estimated similarly in equation 3.6. From V_{shear} and H_{shear}, the diameter of sample at the beginning of shearing phase, D_{shear}, can be determined by equation 3.7.

These two ways of calculation of void ratio and diameter of sample has been compared and the method of weighing is more reliable then is applied throughout the testing program (122).

3.11 Testing program

The experimental work of the thesis includes three core series and some supplementary series/tests in table 3.3. All tests used glass beads of 0.7 mm of diameter, excepting two specific tests with the notices in the last column.

The first core series, CIDNC series, contains 5 tests, using virgin glass beads with N being the number of re-use of glass beads, N = 1 for virgin material, N = 2 for material experienced liquefaction or shearing once. These 5 tests correspond to 5 different confining pressures p_0 from 50 to 500 kPa. B is the Skempton's saturation coefficient. Each test in this CIDNC series includes numerous stick-slips occurring under drained shearing (CID). This series will be analysed in chapter 4.

The second, Liquefaction series, consists of 17 rare isotropic liquefaction events (IL_{01}-IL_{17}) under isotropic consolidation, 2 stick-slip liquefactions under drained shearing (CID), 2 static liquefactions under undrained shearing (CIU) and other types of new liquefactions subsequently under various loading conditions. This series will be presented in detail in chapter 5.

The third, Collapse series, contains 56 collapse events under isotropic consolidation spanning a wide range of triggering stress σ'_{trig} from 32 to 476 kPa. One additional series B is introduced with 13 CID tests having a wide range of Skempton coefficient B to investigate the effect of saturation on the frequency of pore pressure (section 4.4.2.1). Two tests $Dmix_{01}$ and $Dmix_{02}$, structured by a mixture of granular, are added to study the effect of grain size to the signature frequency of the granular structure (chapter 6); and special test HD2 with double slenderness of the sample to explore the factors affecting the frequency of pore pressure (chapter 5).

Table 3.3: Testing program within the thesis.

Test	N	p_0, σ'_{trig} (kPa)	Loading	B	
CIDNC Series					
N500	1	500	CID	0.98	
N400	1	400	CID	0.86	
N200	1	200	CID	0.99	
N120	1	120	CID	0.97	
N50	1	50	CID	0.95	
Liquefaction Series					
IL_{01}-IL_{17}	1-2	30-418	isotropic	0.88-1.00	IL_{03} (d=0.4 mm)
SL_{01}-SL_{02}	1-2	50-200	CID	0.89-0.97	
UL_{01}-UL_{02}	1	50-100	CIU	0.97-0.98	
BL_{01}-BL_{02}	1	32-42	application of back pressure		
WL_{01}	1	30	water imbibition		
FL_{01}	1	12	water flushing		
Collapse Series					
$Coll_{01}$-$Coll_{56}$	1	32-476	isotropic	0.86-1.00	
Additional Series					
B_{01}-B_{13}	1-3	50-500	CID	0.71-1.00	
$Dmix_{01}$	1	500	CID	0.95	50% $d_{0.4}$+50% $d_{0.7}$
$Dmix_{02}$	1	500	CID	0.82	50% $d_{0.4}$+50% $d_{0.7}$
HD2	1	500	CID	0.98	slenderness H/D=2

In addition to these main series, an in-depth verification of the pore fluid pressure is performed with a new set of static and dynamic pore pressure sensors. The unexpected

pore pressure outburst in isotropic and triaxial compressions under drained condition is measured synchronously at sample top and bottom. The results and their analyses are in the appendix.

4

Time-resolved study of drained compression stick-slip on normally consolidated state

4.1 Introduction

Following the unexpected presence of pore fluid development in isotropic collapse and isotropic liquefaction, and the discovery of very large and regular stick-slip in drained triaxial compression on model granular materials, the main objective of this chapter is triple. First, obtain a precise description of the stick-slip instability in triaxial compression including an unambiguous response of pore fluid pressure with the help of additional static and dynamic pore pressure sensors. Second, understand the dynamics of granular stick-slip, especially the still unknown slip phase and help clarify as far as possible the physical triggering mechanisms using high time-resolved data. Third, identify the common parameters underlying the three kinds of granular instability since the compression stick-slip is not the only one in granular mechanics; we need to include isotropic collapse as well as isotropic liquefaction.

This chapter is based on a comprehensive series of drained triaxial compression on loose and fully saturated model granular materials under constant confining pressure from 50 kPa up to 500 kPa, and under constant prescribed axial strain rate of 0.0048 %/s. This series is designed to probe finely the stick-slip dynamics on triax-

ial machine, without forgetting the mandatory and often overlooked drained isotropic compression prior to the drained triaxial compression. Specifically, this chapter will explore the stress-strain relationships, including the volumetric counterpart, the combined effects of initial void ratio at the beginning of compression shearing and confining pressure.

4.2 Experimental information and notations

This study report a series, named CIDNC for drained triaxial compression on isotropically and normally consolidated sample, conducted under drained condition with confining pressure of 50, 120, 200, 400 and 500 kPa, using virgin CVP beads whose average diameter, d_{50}, is 0.723 mm (see figure 3.2). All tests are under fully saturated condition verified by Skempton coefficient B$\geq$0.95 (67), except for test N400 having a lower B of 0.86. During the isotropic consolidation phase, the cell pressure is applied at constant stress rate around 1 kPa/s. In the next triaxial compression, the axial force is imposed at constant axial strain rate of 0.0048 %/s (0.2 mm/min) to respect the full drainage during shearing phase. In table 4.1, SS is abbreviated to stick-slip, e_{20} is void ratio at the beginning of isotropic consolidation phase at 20 kPa, e_c void ratio at the beginning of shearing phase, Dr_{20} (Dr_c) the relative density at the beginning of isotropic consolidation phase (at the beginning of shearing phase), ϕ the internal frictional angle of the material estimated averagely at the plateau of stress-strain curve. Void ratio e is popular in soil mechanics which is defined by the volume of void divided by the volume of solid while relative density Dr is related to void ratio e by $Dr = \frac{e_{max} - e}{e_{max} - e_{min}}$, e_{max} and e_{min} are the maximum and minimum void ratio of a cohesionless soil in its loosest and densest states.

The parameters used in this study are described on figure 4.1 and defined as:

$\sigma'_3 = p'_0$: constant effective confining pressure (kPa)

σ_1 : vertical stress (kPa)

$q = \sigma_1$ - σ_3 : deviatoric stress (kPa)

q_{trig} : triggering deviatoric stress at the beginning of slip event (kPa)

q_{vib} : minimum deviatoric stress of the slip phase (kPa)

q_{stable} : stabilised deviatoric stress after the slip phase (kPa)

Table 4.1: Summarized characteristics of studying tests.

Test	$\sigma_3^{'}$ (kPa)	B	Number of isotropic collapse	Number of SS	e_{20} ($D_{r_{20}}$,%)	e_c (D_{r_c},%)	ϕ (∘)	Brief description
N500	500	0.98	1	44	0.676 (9.26)	0.651 (31.25)	30.77 ±0.99	wide range of SS amplitude, 2 very large SS
N400	400	0.86	3	18	0.687 (-0.78)	0.643 (38.64)	30.88 ±0.44	periodic large SS
N200	200	0.99	2	57	0.685 (1.19)	0.656 (26.79)	28.99 ±0.49	wide range of SS amplitude
N120	120	0.97	0	80	0.684 (1.45)	0.677 (8.04)	31.57 ±2.71	wide range of SS amplitude
N50	50	0.95	0	114	0.680 (5.59)	0.680 (5.36)	29.43 ±0.53	small to medium amplitude SS

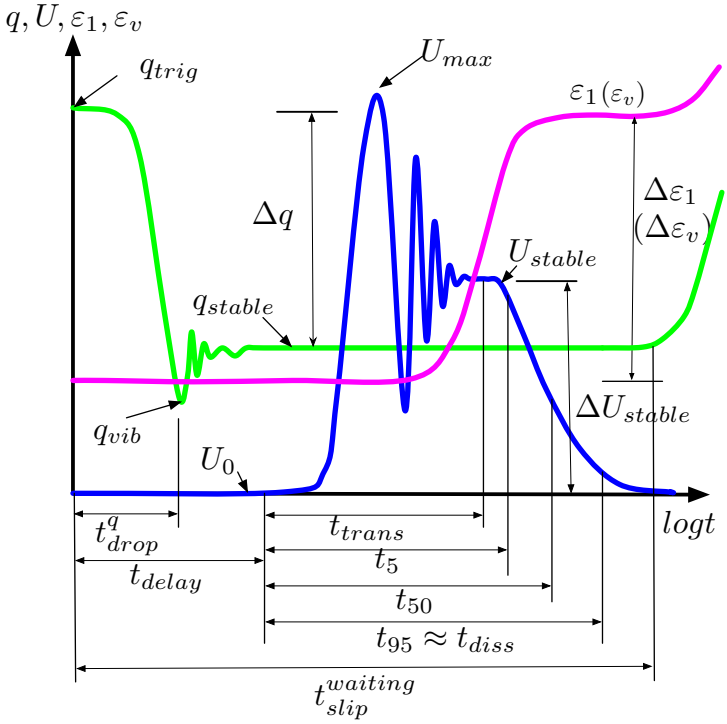

Figure 4.1: Schematic diagram of measurements of typical isotropic collapse and triaxial compression stick-slip.

$\Delta q =$ q_{trig} - q_{stable} : deviatoric stress drop (kPa)

$\Delta q^{norm} = \frac{\Delta q}{q_{trig}}$: normalised deviatoric stress drop or normalised amplitude of SS

$q^{norm} = \frac{q}{q_{trig}}$: normalised deviatoric stress

U_0 : constant back pressure (kPa)

U_{max} : pore pressure at the peak of vibration phase (kPa)

U_{stable} : stabilised pore pressure (kPa)

$\Delta U_{stable} = U_{stable}$ - U_0 : stabilised excess pore pressure (kPa)

$\Delta U_{max} = U_{max}$ - U_0 : maximum excess pore pressure (kPa)

$\Delta U^{norm} = \frac{\Delta U}{\Delta U_{stable}}$: normalised excess pore pressure

$\Delta U^{norm}_{stable} = \frac{\Delta U_{stable}}{p_0}$: normalised stabilised excess pore pressure

$\Delta U^{norm}_{max} = \frac{\Delta U_{max}}{p_0}$: normalised maximum excess pore pressure

$\Delta\varepsilon_1$: incremental axial strain (%)

$\Delta\varepsilon_v$: incremental volumetric strain (%)

t_{trans} : duration of the transient vibration phase of pore pressure counted from the origin of pore pressure development (s)

t_{05}, t_{50}, t_{95} : duration from the origin of pore pressure to the moment when excess pore pressure dissipates the amount of 5%, 50%, 95% of ΔU_{stable} (s). The amount of 5%, 95% are recommended due to their acceptable errors while at 1%, 99% are difficult to identify.

$t_{100} = t_{diss}$: duration of excess pore pressure to totally dissipate (s), in soil mechanics $t_{diss} \approx t_{95}$

$t^{waiting}_{slip}$: duration from the drop of deviatoric stress q_{trig} until the beginning of stick phase (s), or the slip duration revealed by low sampling rate data.

t^{delay} : time delay between deviatoric stress q and excess pore pressure ΔU (ms)

t^{q}_{drop} : drop time of deviatoric stress q from q_{trig} to q_{vib} (ms)

p' : effective mean pressure (kPa)

$p'_{stable} = p'_0 + \frac{q_{stable}}{3}$ - ΔU_{stable} : effective mean pressure at stabilised state of U (kPa)

p'_{crit}, q_{crit} : effective mean pressure and deviatotric stress at the plateau of stress-strain relation q-ε_1 (kPa), in which $p'_{crit} = p'_0 + \frac{q_{crit}}{3}$

$p'^{norm}_{stable} = \frac{p'_{stable}}{p'_{crit}}$: normalised effective mean pressure at stabilised state

$q^{norm}_{stable} = \frac{q_{stable}}{q_{crit}}$: normalised deviatoric stress at stabilised state

4.3 Experimental results

The core series, CIDNC, will be presented in this section. First, the global behaviours including isotropic phase and drained shearing phase are introduced with low sampling rate confirming the results of previous work (32). Then, a time-resolved study of a typical SS event is shown which reveals details and new aspects of the behaviour. Following one SS event, detailed mechanical measurements at high temporal resolution of all SSs at different confining pressures p'_0 are shown. The observations of these global behaviours provide useful qualitative assessments which direct the quantitative analysis in the next section.

In this work, **isotropic collapse and triaxial compression stick-slip** are defined as local failure with limited strains, while preserving the geometrical sample shape and the continuity of the test. In contrast, **liquefaction** is global failure with extreme large strains, associated with a complete destruction of the grain structure and of the cylindrical shape of the sample. The test simply stops.

The definition of a stick-slip (SS) event is introduced in figure 4.2. In granular literature, each SS in stress-strain plane (q-ε_1) consists of an abrupt deviatoric stress drop Δq (called as slip phase from A to B) from an uncontrolled triggering stress q_{trig} and a gradual hardening (stick phase) up to the previous level (from B to C). Accompaniying with the stress drop is the jump of both volumetric strain $\Delta\varepsilon_{vol}$ and axial strain $\Delta\varepsilon_1$. Furthermore, sudden generation of pore pressure is detected simultaneously within the stress drop and strain jump AB. These portions AB are marked by dashed line since they are constructed by only two data points (A and B). This description results from low sampling rate data which is not sufficient to describe the real slip phase and its dynamics.

4.3.1 Global behaviour

This section describes the global behaviour of 5 tests within the series to introduce the isotropic collapses and stick-slip events which interrupt the traditional behaviour of granular soils in figures 4.3 and 4.4. Remind that the isotropic consolidation of traditional granular soil in soil mechanics is just the packing evolution in porous media

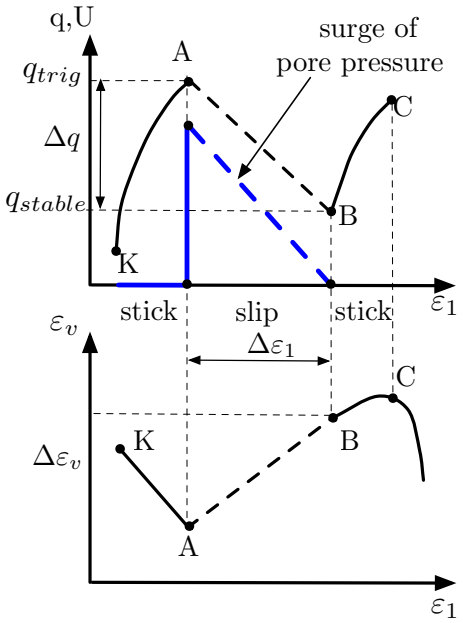

Figure 4.2: Definition of triaxial compression stick-slip event in schematic diagram.

community. That is a continuous evolution of void ratio e with the imposed pressure p', illustrated by red curve in figure 4.3a. It is characterised by a constant, compressibility coefficient C_c, which is the slope of the curve. It is necessary to show all 5 tests to see the uncontrollability and unrepeatability of the dynamic events within one test and between tests.

4.3.1.1 Drained isotropic compression collapse

Figure 4.3 presents the compressibility behaviour of the void ratio e as function of the mean effective pressure p' for five samples of the series. The logarithm of p' is commonly used in soil mechanics to emphasise low confining range below 100 kPa. The sample is isotropically compressed from 20 kPa to the targeted effective confining pressure p'_0. The compressibility starts at uncontrolled void ratio, e_{20}, which cannot be fully controlled as in the case of sands. This is due to the unexpected collapses during the imbibition and saturation phase of the sample preparation (appendix A). Instead of a smooth packing evolution of real geomaterial as the expected red curve in figure 4.3a, the behaviour is interrupted by many collapses occurring at unanticipated triggering stress σ'_{trig}. Each collapse is characterised by an unexpected drop of void

ratio Δe and a synchronous outburst of excess pore pressure revealed as in the insets of figure 4.3a to c. The release of the effective stress σ' of grain skeleton is deduced by Terzaghi's principle $\sigma' = \sigma$ - U, σ is the total confining pressure, U the recorded pore pressure. Under drained condition with appropriate constant axial strain rate, the pore pressure should dissipate correctly with no excess value. In our study, systematic and unexpected surge of pore pressure U is measured at the top and bottom of sample. After the drop Δe and the loss of effective stress, the stress recovers gradually its level prior to the collapse event. The isotropic stage of test is completed at uncontrollable e_c, due to the unpredictable number of isotropic collapses.

The maximum number of collapses is fairly small, only 3, within the studied range of confining pressure, only up to 500 kPa. In case of no collapse, the compressibility of test N500 would have been smooth and characterised by a compressibility coefficient $C_c = 0.01815$, and finished at point A with slightly higher void ratio, $e_A = 0.657$ ($D_r = 25.9\%$) instead of 0.651 ($D_r = 31.25\%$). The isotropic compression of tests N120 and N50 without any collapse does not mean no collapse occurring below 120 kPa. Isotropic collapse do happen below 120 kPa as for tests N200, N400 and N500. Both the arbitrary number of collapses and arbitrary triggering stress underlie the uncontrollability nature of isotropic collapse phenomenon. This observation means the exact repeatability with identical results of isotropic and triaxial compression can not be guaranteed.

These above global responses of collapses confirmed already known information (30), briefly reminded here, that cell pressure is not the cause of the instabilities since it is constant within $\pm$ 0.1 kPa for the whole duration of the event. High sampling rate data also showed the negative mean effective pressure p' and multiple collapse events (double, triple, quintuple ones). Audible crackling noise was detected accompanying the collapses which led to the acoustic investigation in this current study. During collapse, the geometry shape of the specimen still maintains contrary to liquefaction event which will be studied in chapter 5. Unloading collapse (collapse during isotropic unloading for overconsolidated materials) was also acknowledged and thickened the mysteriousness of the mechanisms. Dry collapses of our previous work (30) at the same designed isotropic compression test can give a good reference and comparison to saturated case of this study.

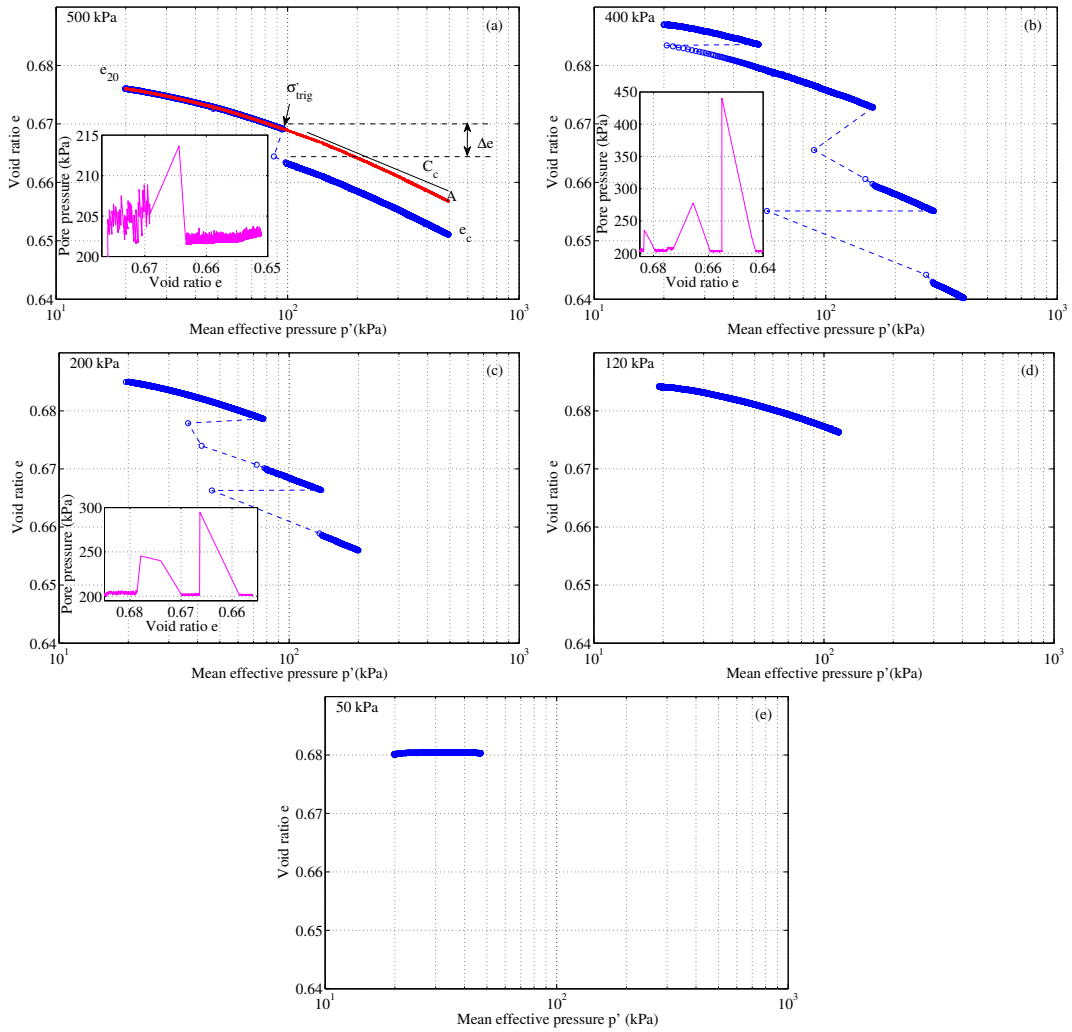

Figure 4.3: Global behaviour in isotropic consolidation phase to reach different effective confining pressure p'_0 from 50 up to 500 kPa.

4.3.1.2 Drained triaxial compression stick-slip

Now the global behaviour of the CIDNC series during the subsequent shearing phase is presented. Starting at the targeted confining pressure p'_0, the sample undergoes drained triaxial compression test (i.e. axial compression shearing with the addition of deviatoric stress). The shearing response is described by the stress-strain relation (q-ε_1) and the additional volumetric strain-axial strain (ε_{vol}-ε_1) in figure 4.4. Basically the CIDNC series shows the globally contractive stress-strain behaviour equivalent to the high e_c of loose material obtained at the end of previous isotropic phase (left column

of figures 4.4). Again, instead of a smooth conventional shearing behavior like the dashed red curve in figure 4.4a until deviatoric stress q reaches the plateau at large strain as the usual behavior of loose granular materials, the behavior is interrupted by SS events occurring irregularly. Each SS, for instance the SS_{25} in the rectangular region, includes two phases as previously defined in figure 4.2. Coupled with the stress-strain behavior is the volumetric strain behavior (the right column of figures 4.4) with strong corresponding stick-slip characterized by a volumetric contraction in slip phase and a dilation in stick phase. Some large SSs make noticeable jumps of volumetric strain. Ignoring the SS during volumetric strain behavior, the mean curve (red dashed curve) conforms to the conventional contractant behavior of loose material towards the constant critical state of void ratio. Once again, similar to collapse event, during SS events, the buildups of pore pressure, represented by magenta curve, are also detected and reminded in the inset of figure 4.4b. Since the inset exhibits low sampling rate data as in previous works then it only captures the major outbursts of pore pressure. This study will show the whole detailed coupled behaviour to improve the results and fulfill the missing gap in the understanding in section 4.3.2.2.

Among 5 tests, only test N500 begins the compression shearing stage as medium dense ($D_r = 31.25\%$), thus a strain softening between large stick-slip events (SS_{10}, SS_{16}, SS_{25}, SS_{33}, SS_{42}) in figure 4.4a and a lightly dilatancy globally of volumetric strain ε_{vol} by dashed red envelop in figure 4.4b. It still remains coherent with the conventional shearing behaviour of initially loose cohesionless soils. The global shearing behaviour is divided into two stages consisting of (i) an initial stage during which stress-strain curve (q-ε_1) gradually moves up approaching a plateau and (ii) a critical stage during which stress-strain curve stabilises. In the critical stage, the average of maximum amplitudes of SSs seems to decrease with decreasing confining pressure p'_0. The amplitude of volumetric strain, ε_v, also shares similar decreasing features as those of deviatoric stress drop Δq when confining pressure p'_0 gets lower.

Neglecting the first SSs with Δq dropping down to isotropic stress level, the occurrence of SS appears to be quasi-periodic for the group of largest SSs in each test. The number of generated SS events within the range of 25% axial strain exhibits the basic trend that the lower the confining pressure p'_0 is, the more SS events occur. Test N400 (fig 4.4c) does not comply this trend with particularly few number of SSs. Thus, the occurrence of SS seems to depend not only on the confining pressure p'_0, but also on

4. TIME-RESOLVED STUDY OF DRAINED COMPRESSION STICK-SLIP ON NORMALLY CONSOLIDATED STATE

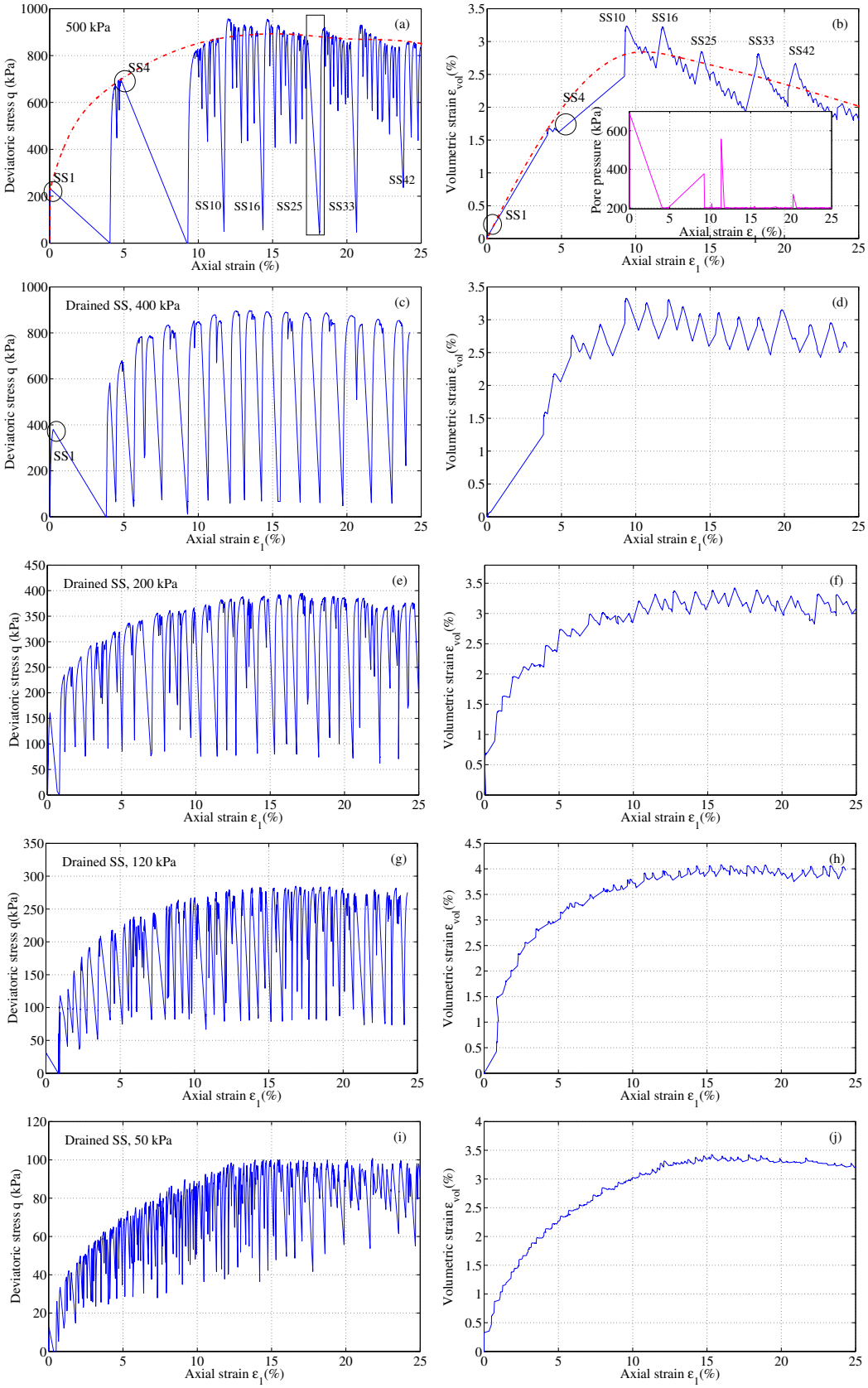

Figure 4.4: Global drained compression stick-slip behaviour in drained shearing phase at different confining pressure p'_0.

additional parameters such as void ratio e. This observation will be taken into account in section 4.4.1.

In all cases, the first SS often is the largest SS in terms of axial and volumetric strains. In the rare case of test N500, two very large SSs marked as SS_{01} and SS_{04} in figure 4.4a are detected, associated with two very large contractive volumetric strains in figure 4.4b. Test N500 is the only test having two very large SSs in our collection and we still ignore the reason of their appearance. Remind the first SSs with null deviatoric stress q at the end of slip phase, leading to some rare liquefactions, named as stick-slip liquefaction. Within 120 tests of this thesis even including past work, stick-slip liquefaction has never been observed beyond the first SS. Furthermore, very large SS with axial strain jump of more than 5% also has never been occurred in the plateau of stress-strain curve. It can be inferred that the largest SS has much probability to occur only at a void ratio lower than the critical void ratio during the plateau and only the first SS has the potential to liquefy.

So far, the global view of collapses and SSs under isotropic compression and drained shearing has been introduced. The way they appear is unexpected and unanticipated in each test. The confining pressure p'_0 qualitatively impacts on the amplitude and the occurrence of SS events as concluded in previous studies. The uncontrolled void ratios e_{20} and e_c can contribute some effects together with p'_0.

In summary, there are 5 features needed to be considered: (i) the amplitude of SS, (ii) the recurrence of SS, (iii) the existence of first very large SSs potentially liquefied, (iv) the coupled volumetric behaviour, (v) the uncontrolled initial void ratio e_c. Points (i), (ii) and (v) are going to be analysed in section 4.4.1, point (iv) in section 4.4.4.1 and point (iii) in section 5.5.1.

4.3.2 Detailed behaviour

The global view of SS phenomenon, shown in previous subsection, revealed the coupling volumetric behaviour and raised one logical question concerning the surge of pore pressure in drained condition. This counter-intuitive pore pressure measurement should not exist for complete free drainage when sheared axially in a constant axial strain rate of 0.2 mm/sec. We will now explore the slip dynamics of SS events.

4.3.2.1 Anatomy of typical stick-slip behaviour

The first single stick-slip event (SS_{01}) of test N500 in figure 4.4a is going to be inspected as a typical behavior. Figure 4.5 gives the temporal evolution of the relevant measuring parameters including additional passive acoustic measurements, over five time decades. From top to bottom, this figure gives successively the deviatoric stress q, vertical top cap acceleration, lateral sound pressure, lateral vibration, normalised excess pore pressure ΔU^{norm}, incremental axial strain ε_{vol} and incremental volumetric strain ε_{vol} for this SS_{01}. In isotropic collapses, without local device to capture the stress of the grain skeleton, the buildup of pore pressure might be attributed to the local failure of the granular structure. This led to the idea of using vertical accelerometer on the sample top cap to acquire some signals happening before the pore pressure changes. The structural anisotropy during isotropic drained compression led to additional lateral acoustic sensors.

The origin of time is shifted to the beginning of deviatoric changes ± 0.1 ms, which is the current time resolution. A logarithmic scale of time is employed to emphasise the fast change of these parameters below one second in the transient phase. The additional mechanical measurement in this stick-slip study, compared to previous works on isotropic collapses, is the deviatoric stress q which suddenly drops from q_{trig} to a residual stable value q_{stable} at 0 kPa. A transient phase of q is noticed with a small number of oscillations with small magnitude during 10 ms before attaining the constant q_{stable}. It remains at the constant level of q_{stable} for more than 10 seconds. The deviatoric stress evolves abruptly from a steady state of q_{trig} to another steady state of q_{stable}. The triggering stress q_{trig} is identified manually since the automatic identification is far more difficult than expected. The drop duration of stress t^q_{drop} is defined as the time difference between the beginning of q_{trig} and the occurring of the minimum of q, q_{vib} in the transient phase as shown schematically in figure 4.1. In this case, t^q_{drop} of the first SS_{01} of test N500 equals 1.7 ms. This reveals an extremely short drop duration compared to previous works (32, 57, 110).

The problematic pore pressure evolution is shown below the deviatoric stress q using the same time scale. Similar to our previous works (30), the parameter $\Delta U^{norm} = \frac{\Delta U}{\Delta U_{stable}}$ was introduced to remove the potential dependency on the short-lived ΔU_{stable}. In this study, under **drained triaxial compression shearing**, the pore pressure of SS_{01}

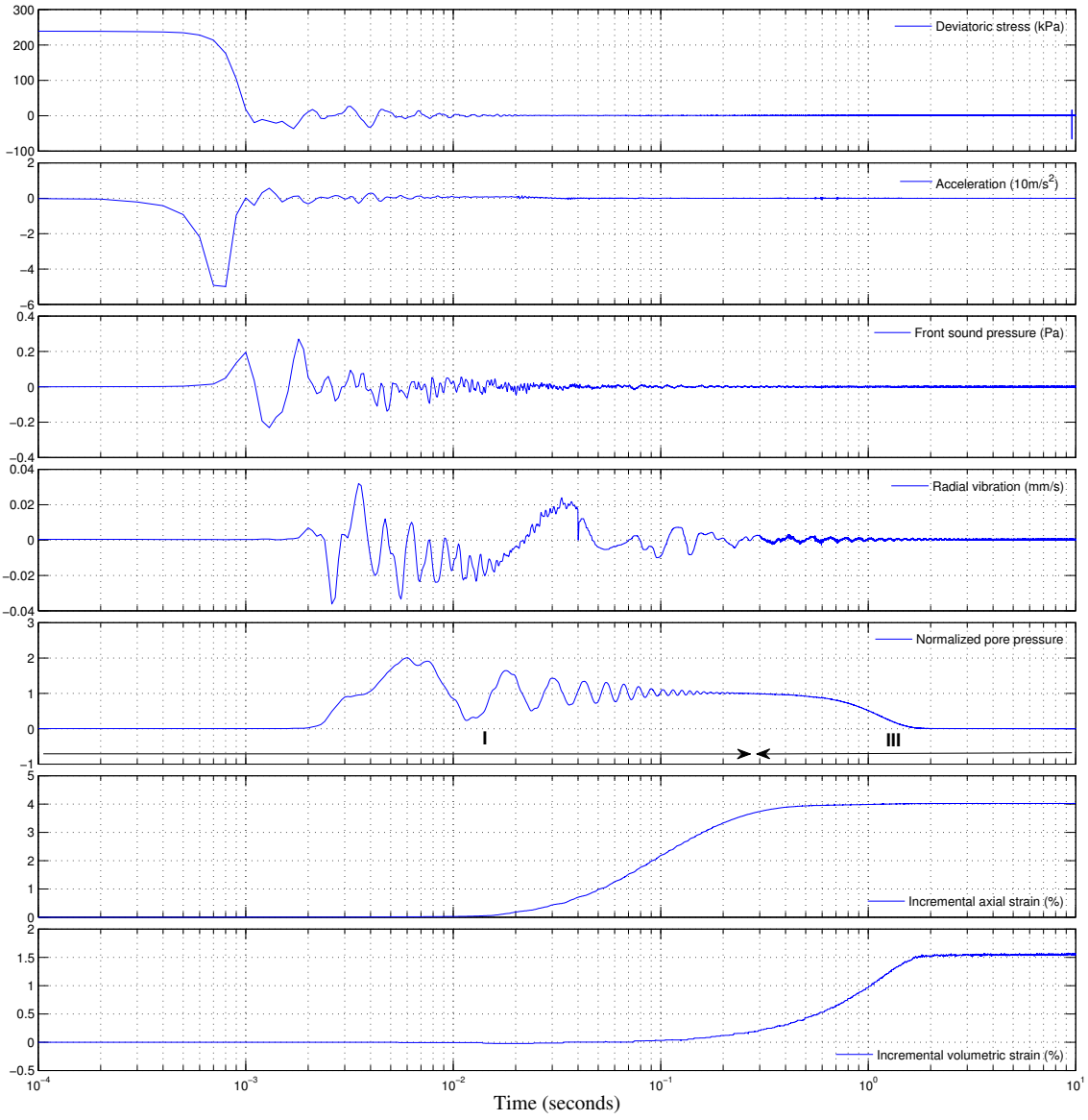

Figure 4.5: Temporal evolution inside a typical stick-slip SS_{01} at 500 kPa (test N500) : Deviatoric stress q, vertical top cap acceleration, lateral sound pressure, lateral vibration, normalised pore pressure U^{norm}, incremental axial strain $\Delta\varepsilon_1$, incremental volumetric strain $\Delta\varepsilon_{vol}$.

shows the same dynamic characteristics to isotropic collapses which includes only 2 phases. The first phase I is an underdamped free oscillation at the same frequency regardless of ΔU_{stable}. That first transient phase is very brief within 200 ms and followed by a relatively longer dissipation phase III at the order of second. The stabilised phase

II of ΔU is only valid in case of liquefaction (30). During the event due to the difference between pore pressure at the top and bottom of the sample, a brief non homogeneous stress state remains in the granular medium (88). The measured deviatoric stress drop of this study always finishes the drop before the surge of pore pressure.

Similarly to collapse in isotropic loading, the axial strain ε_1 and volumetric strain ε_{vol} develop nearly as the last consequences and rapidly during only some seconds. ε_1 freely develops from an initial stable state to another stable state without any kinematic constraints. Both ε_1 and ε_{vol} do not show the transient phase that are not physically consistent to the vibration of deviatoric stress q and of excess pore pressure.

The complementary measurements in this work consisting of acoustic measurement in lateral sound pressure, lateral vibration and top cap vertical acceleration are also presented in the appearance order in this figure. The top cap vertical acceleration changes very rapidly, nearly at the same time as the change of q, then vibrates and settles down quickly within the first transient phase I of U. The amplitude of acceleration is up to 50 m/s^2 = 5 g for less than 1 ms. Identically, the lateral sound pressure and the lateral vibration show some vibrational changes prior to the pore pressure development and slightly later than the vertical top cap acceleration. Other acoustic characteristics will be exploited in chapter 6. These synchronised passive acoustic measurements strongly suggest some modifications occurring inside the granular body prior to the generation of pore pressure in the following temporal order in table 4.2.

Table 4.2: Time delay (± 0.1 ms) of essential measurements counted from the origin of deviatoric stress drop of stick-slip SS_{01} of test N500.

Deviatoric stress q	Acceleration G	Sound pressure M	Lateral vibration V	Excess pore pressure ΔU	Axial strain ε_1	Volumetric strain ε_{vol}
0 ms	0 ms	0.4 ms	1.3 ms	1.6 ms	13 ms	41 ms

With high time-resolved data inside one single stick-slip event, the triggering time of different measurements helped to reach one conclusion that **the excess of pore pressure U is not the cause of the stick-slip instability**. The deviatoric stress drop Δq and the vertical top cap acceleration always precede the pore pressure development, by 1.6 ms in this first SS_{01}. This conclusion is equally valid for all drained stick-slips

in this study. The existence of stick-slip in dry and wet conditions also supports this assessment.

4.3.2.2 Temporal behaviour at different confining pressures

To examine the systematic repetition and possible distinctions of the whole CIDNC series, all stick-slip events at different confining pressure p'_0 are exploited. The temporal evolution of q^{norm}, ΔU^{norm}, $\Delta\varepsilon_v$, $\Delta\varepsilon_1$ respectively of the whole stick-slip events are exhibited in figures 4.6 to 4.9, in which deviatoric stress q is normalised by q_{trig} to join all SSs at the beginning of the drop. The index of studied SS is denoted by colour bar in the right of each subfigure. This index is approximately proportional to the increasing axial strain ε_1 at the beginning of stick-slip event.

The temporal development of deviatoric stress q of around 300 SS events of all tests within CIDNC series in figure 4.6 exhibits the same features of the typical SS_{01} in figure 4.5 with very averagely brief dynamic slip time t^q_{drop} less than 3 ms. Instead of the monotonic drop of deviatoric stress q reported in previous works due to low resolution data as illustrated by black curve in figure 4.2, the drop of stress actually consists of two stages in this study. The first stage is an extremely brief dynamic slip time, as the duration counted from the beginning of the stress drop to the first local extremum of q^{norm}, and this slip time seems to depend on the normalised amplitude of stick-slip. It can be conjectured that smaller SSs favour the mode of gradual deformation of grain skeleton with longer slip time while larger ones are relevant to the sudden failure of grain contacts. The second stage is a stable phase in which q^{norm} vibrates and approaches a constant value. The transient phase of q almost occurs within 10 ms at all confining pressure p'_0. The first SSs represented by the darkest blue curves always maintain the longest stable stage at zero effective stress (isotropic effective stress state) in all tests for more than 10 seconds. It means a separation of the loading ram from the top platen of the specimen and a different nature of deformation. The axial strain for these SSs must be very large. In all tests there are two largest normalised drops of q (dark blue curves), excepting test N400 with only one large first stick-slip at the lowest void ratio among the series (densest sample). Note that these largest normalised drops of q have the potential to liquefy. This leads to a conjecture that initial void ratio affects the possibility of liquefaction.

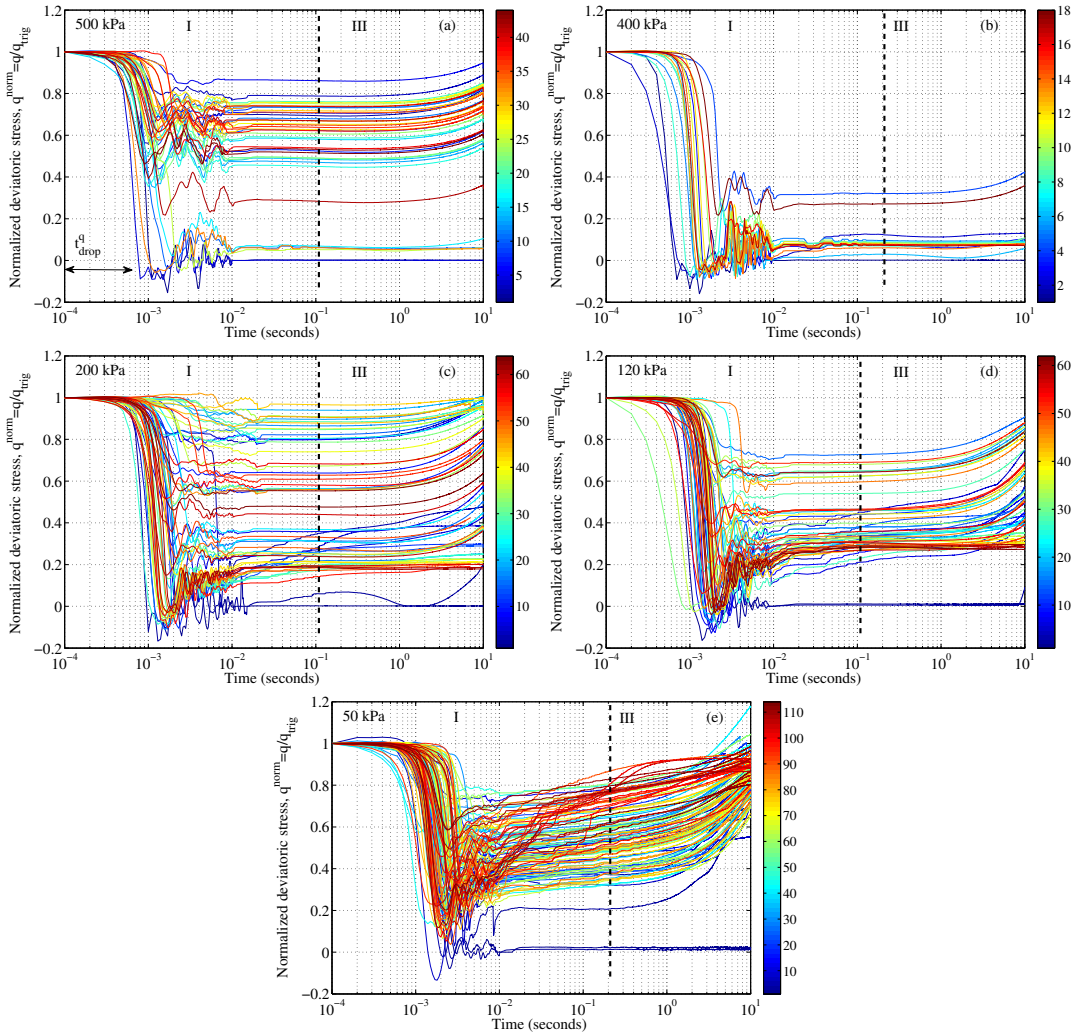

Figure 4.6: Time evolution of normalised deviatoric stress q^{norm} during stick-slip events at (a) 500 kPa of confining pressure, (b) 400 kPa, (c) 200 kPa, (d) 120 kPa and (e) 50 kPa.

ΔU^{norm} in figure 4.7 behaves consistently following two phases like isotropic collapse without any stabilised phase. The phase II of liquefaction in which ΔU_{stable} remains constant for more than 1 s is completely absent. Hence the stick-slip response, like collapse, can be considered as a local instability. In the first transient phase I, it fluctuates at almost the same frequency in each test. Two tests N400 and N50 with abnormal low frequency of pore pressure are explored in section 4.4.2.1. One noticeable feature of ΔU^{norm} is the negative ΔU^{norm} after the dissipation phase of test N200 (figure 4.7c). Though some specific ΔU^{norm} decline to almost -3 but the magnitude

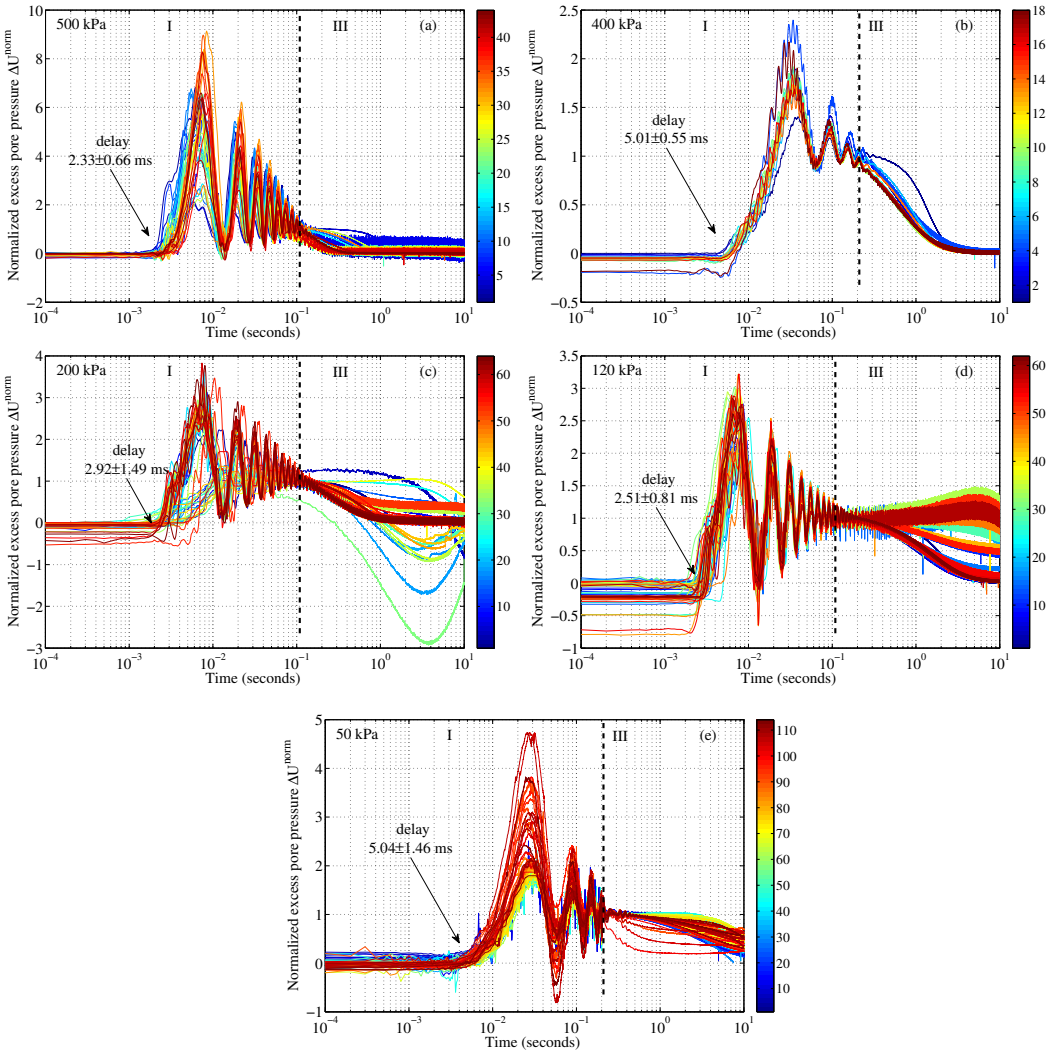

Figure 4.7: Time evolution of normalised excess pore pressure ΔU^{norm} during stick-slip events at (a) 500 kPa of confining pressure, (b) 400 kPa, (c) 200 kPa, (d) 120 kPa and (e) 50 kPa.

without normalisation (in kPa) is only -2 kPa equivalent to back pressure of 198 kPa. This apparently large reduction of ΔU^{norm} is due to the normalisation of relatively low value of stabilised excess pore pressure. This negligible loss of pressure compared to permanent back pressure $U_0 = 200$ kPa still ensures the condition of fully saturation for the granular assembly.

The evolution of axial strains in figure 4.8 reveals the extensions at the beginning of slip phase termed as intermediate extension, which are quite common in all tests.

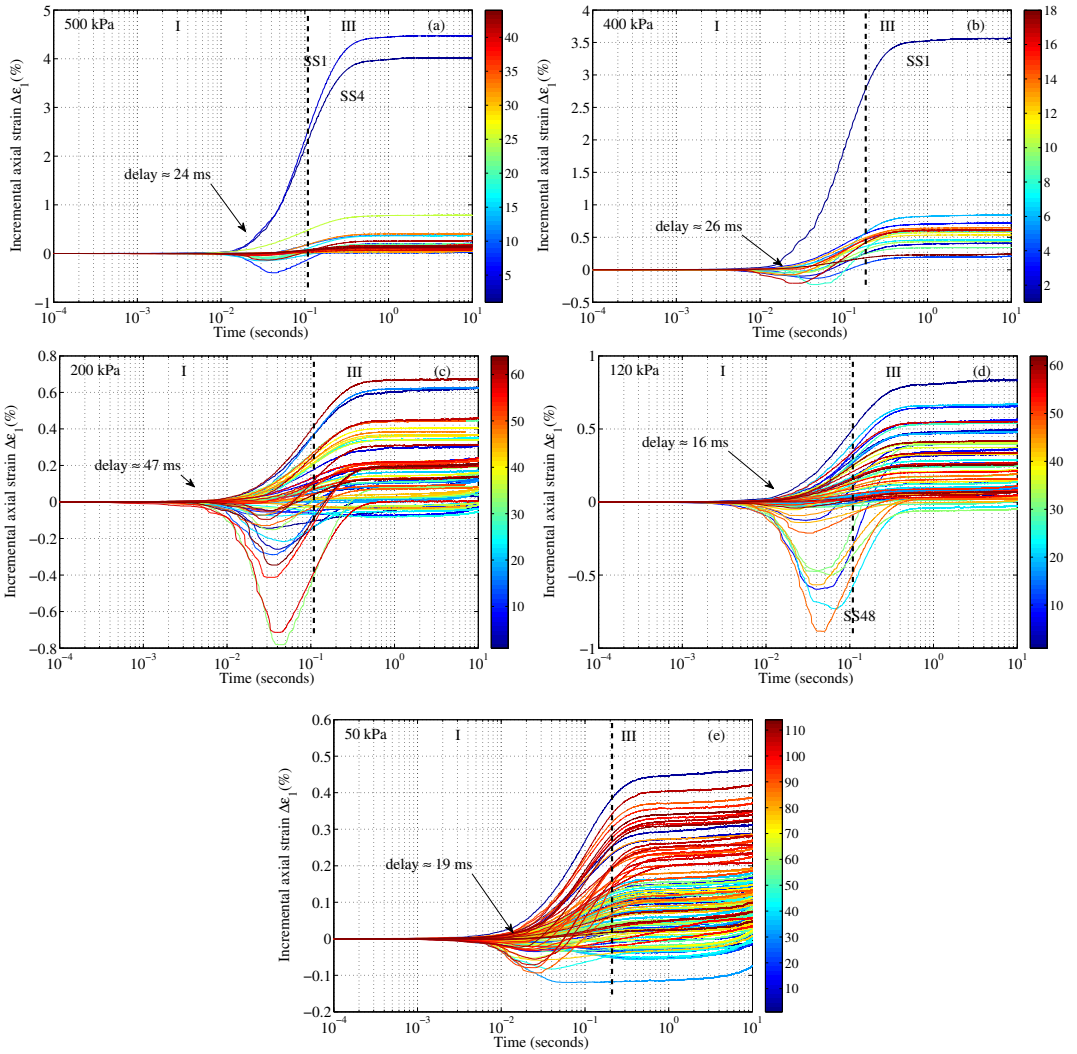

Figure 4.8: Time evolution of incremental axial strain $\Delta\varepsilon_1$ during stick-slip events at (a) 500 kPa of confining pressure, (b) 400 kPa, (c) 200 kPa, (d) 120 kPa and (e) 50 kPa.

The remarkable amplitude of extension $\Delta\varepsilon_1$ especially in the case that deviatoric stress does not drop to zero meaning that the loading ram still contacts with the top plate of the specimen and plays as a constraint. Consequently the maximum upward axial strain of SS_{48} in test N120 at 0.88% (figure 4.8d) is impossible because it exceeds the elastic strain of the loading ram. One plausible explanation has been obtained for these extension strains that the top cap is tilted due to the inhomogeneous deformation of the media resulting in an upward movement of top cap at the installed position of LVDT. The overall $\Delta\varepsilon_1$ is still in the contraction side with some exceptions for intermediate

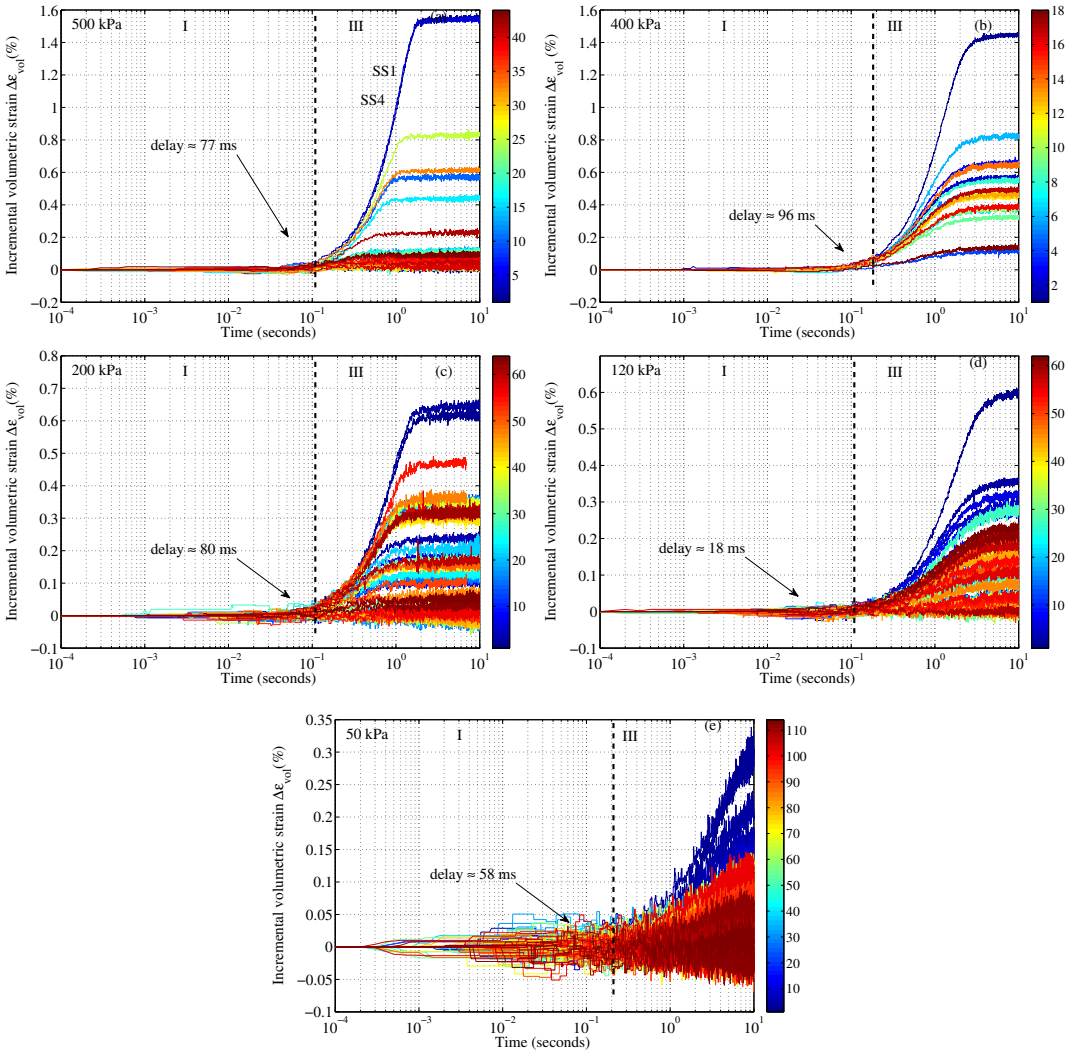

Figure 4.9: Time evolution of incremental axial strain $\Delta\varepsilon_{vol}$ during stick-slip events at (a) 500 kPa of confining pressure, (b) 400 kPa, (c) 200 kPa, (d) 120 kPa and (e) 50 kPa.

extension as in SS_{48}. While the incremental volumetric strain $\Delta\varepsilon_v$ (figure 4.9) is always in contraction and the largest $\Delta\varepsilon_v$ corresponds to the largest $\Delta\varepsilon_1$. Both axial and volumetric strain do not exhibit the transient phase of vibration.

The magnitude of all peak of normalised stabilised excess pore pressure ΔU_{max}^{norm}, incremental volumetric strain $\Delta\varepsilon_v$, and incremental axial strain$\Delta\varepsilon_1$ declines with decreasing confining pressure. Within this each test, the largest incremental strains are always obtained at the first stick-slip.

Concerning the time delay of measurements referenced to the time origin of devi-

atoric stress q, irrespective of confining pressure p'_0 in the range of 50-500 kPa, the sudden generation of pore pressure is 2-5 ms later than the drop of q (see the time delay denoted in figure 4.7). Subsequently, the axial strain ε_1 begins to develop at 16-47 ms (figure 4.8) within the transient phase of U long before the gradual development of volumetric strain ε_{vol} which is the latest modification (figure 4.9). Since these features are very similar to those of isotropic collapse, they point to the same triggering mechanisms inside the granular body; termed as the structural instability hypothesis (4, 58, 73). The late development of the axial strain ε_1 after the deviatoric stress q exposed a problem on the estimated modulus during dynamic slip phase, in which modulus is the fraction of Δq and ε_1. But $\varepsilon_1 = 0$ during dynamic drop of q means infinite modulus. Associated with foregoing noticeable large extension axial strains, it can be seen that LVDT technology should be taken with caution in this kind of instabilities.

In brief, the detailed behaviour of all SSs at different confining pressure p'_0 has raised some preliminary conclusions as (i) very short slip time is independent of confining pressure p'_0, (ii) coupled SSs in axial strain and volumetric strain are consistent to SSs in stress drop, (iii) the first SS always drops to zero with largest strains, (iv) the existence of extension axial strains implies the inhomogeneous strain state in the granular media during dynamic instabilities, (iv) the difference in the frequency of pore pressure needs to be explored.

4.4 Analysis and discussion

The view on the global and detailed behaviour of stick-slips contributed qualitative aforementioned assessments. This section is devoted to a quantitative analysis of the obtained data to establish some empirical relations between key parameters.

4.4.1 Effect of confining pressure and void ratio on global behaviour of stick-slip

As the preliminary observations aforementioned, it can be stated that the means of stick-slip amplitude (both $< \Delta q^{norm} >$ and $< \Delta q >$) have no clear relation to p'_0 as demonstrated in appendix B. The mean $< \Delta q >$ of test N400 which is out of linearly increasing trend, can be linked to additional observation of void ratio e_c in table 4.1.

This test, N400, has the lowest e_c among the series. So, the confining pressure p'_0 is not the only factor affecting maximum SS amplitude as stated by many previous studies (2, 22, 93, 125). Therefore, the role of e_c is investigated to explore its effect on the amplitude of stick-slip.

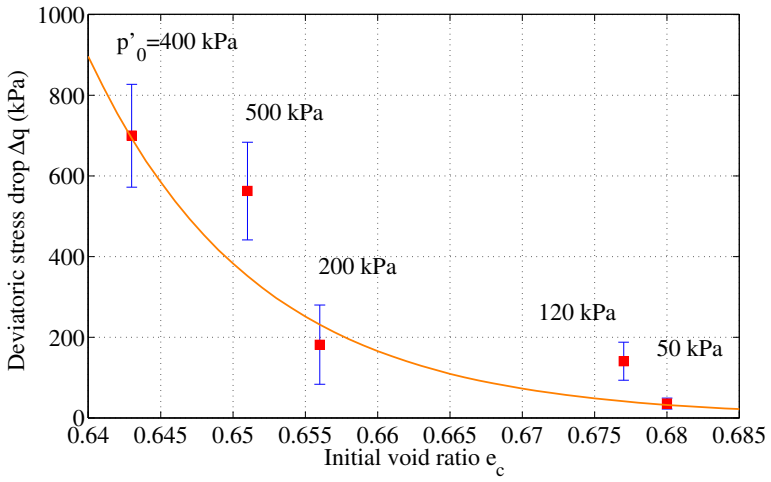

Figure 4.10: Effect of void ratio e_c at the beginning of shearing phase on the magnitude of deviatoric stress drop Δq.

Figures 4.10 confirms the empirical relation with high correlation coefficient $R^2 = 0.96$ that the looser the granular, the smaller the magnitude of stick-slip Δq. It is well known in soil mechanics that the final e_c decreases with increasing p'_0 (fig 4.3) but here the impact of void ratio e_c is greater which can be interpreted by many unexpected collapses occurring before shearing state. Actually both e_c and p'_0 are supposed to govern on stick-slip amplitude.

Normalised deviatoric stress drop $\Delta q^{norm} = \frac{\Delta q}{q_{trig}}$ is introduced in this study to remove the possible dependency of q_{trig} and to facilitate the graphical exploration of SS, independently of q_{trig}. It will be presented in most relations in subsequent sections. Since $<\Delta q^{norm}>$ does not exhibit a clear relation to e_c, the importance and representativeness of this parameter need to be examined. Additionally, it should be reminded that the maximum possible amplitudes Δq^{max} are affected by p'_0 and all these maximum amplitudes belong to the plateau of stress strain curve when the SS behavior is quasi-periodic and stable. For instance in test N500 (figure 4.4a) the maximum amplitude is the SS event numbered by SS_{10}. For this reason, it is more appropriate

to only investigate the maximum Δq^{norm} in the plateau in relevance to p'_0 and e_c. As illustrated for test N500, the group of largest SSs in the plateau is SSs marked as SS_{10}, SS_{16}, SS_{25}, SS_{33}, SS_{42} in figure 4.4a. In two following subfigures 4.11a,b, only the collections of largest SSs within the plateau are taken into account.

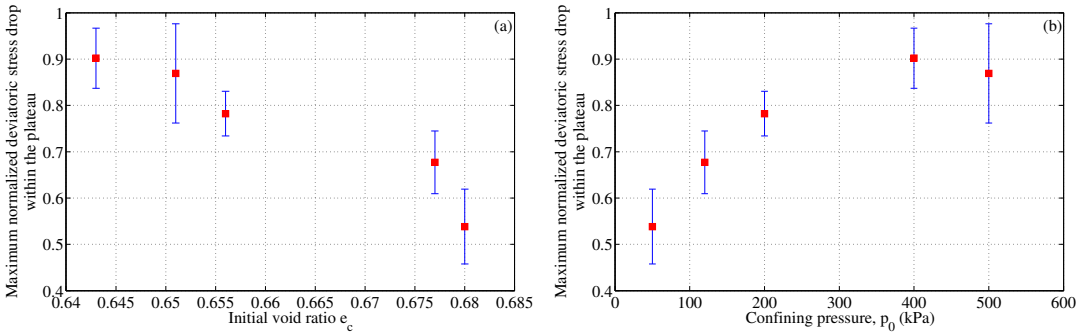

Figure 4.11: Effect of void ratio and confining pressure on the global behaviour of stick-slip.

Now, the $< \Delta q^{norm} >$ exhibits strong relation both to p'_0 and e_c (figure 4.11). Lower void ratio e_c generates larger normalised amplitude $< \Delta q^{norm} >$. Conversely, lower confining pressure p'_0 leads to smaller $< \Delta q^{norm} >$. Therefore p'_0 still impacts on normalised amplitude of SS and it proves that Δq^{norm} is a comprehensive quantity representing the size of SS event instead of the usual amplitude Δq as in most previous studies. The inverse impacts of p'_0 and e_c are understandable since it complies with their traditional relation in compressibility of isotropic consolidation phase for soil. This relation describes the smooth red curve in figure 4.3a by the equation $e = f(e_{20}, p')$. Increasing p'_0 always results in denser state of material. But in case of model granular material, the combined effects of p'_0 and e_c are missing due to the unexpected collapses occurring during the isotropic consolidation step and during the fabrication phase.

The density of SS during shearing, e_c, is the key parameter that influences the occurrence of SSs implying that the looser the media, the more SSs experienced during axial shearing (figure 4.12). The recurrence of SS is evaluated by the average number of events happening within a unit interval of axial strain of 1% for the whole testing range of $\varepsilon_1 = 25\%$. This quantity is estimated by the number of all SS events generated within the studied range of $\varepsilon_1 = 25\%$ divided by the total ε_1. The relation of e_c and recurrence of SS can be considered as linear with high correlation coefficient R^2. It may be partially explained by our hypothesis (34) on the ejection of particles to the

possible surrounding void space, thus the denser state corresponds to a less possibility of ejection of particles equivalent to less SS events.

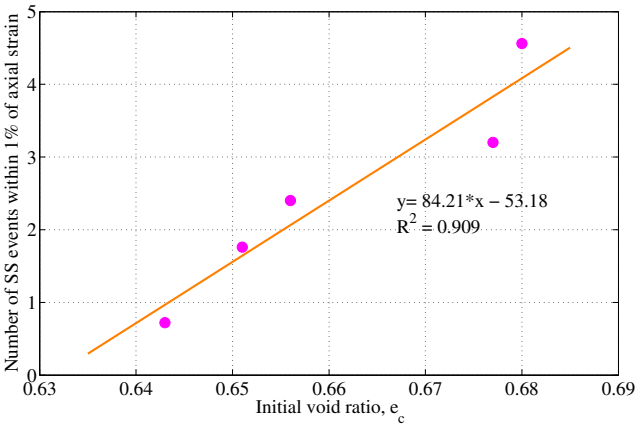

Figure 4.12: Effect of void ratio e_c and confining pressure p'_0 on the global behaviour of stick-slip.

To summarise, some conclusions can be drawn below:

(i) both e_c and p'_0 (2, 13, 22, 32, 93), impact on the global SS behaviour due to the unpredictable isotropic collapse,

(ii) e_c has more significant influences on the magnitude of stress drop Δq, on the normalised amplitude Δq^{norm} and on the occurrence of SS, particularly for loose materials,

(iii) p'_0 still maintains its key role in controlling the maximum amplitude which can be generated within the plateau of stress-strain behaviour.

4.4.2 Characterization of pore pressure behaviour

In saturated granular assembly, previous works (30) show the presence of sudden excess pore pressure ΔU during collapse and stick-slip events, and the behaviour was also depicted with two phases. Our detailed measurement shows similarity to realistic measurement on site during an earthquake (9), especially the stabilised state. Moreover, our data depicts a vibration not observed in these field measurements probably due to too low sampling frequency. In this section, the response of pore pressure will be successively characterised by the first transient phase associated with the dominant frequency f_U, by the amplitude at stabilised state ΔU_{stable} and at the first peak ΔU_{max}. The

response of pore pressure in the second phase will be characterised by the traditional dissipation process.

4.4.2.1 Frequency of pore pressure

The first transient phase I of pore pressure is characterised by a dominant frequency, extracted by Fast Fourier Transformation (FFT). Figure 4.13 shows the vibration frequency of pore pressure during both stick-slip and collapse events gathering in two highly separate groups: one at 81.13 ± 3.57 Hz for 120, 200, 500 kPa and a second one at 16.50 ± 0.41 Hz of confining pressure of 50 and 400 kPa.

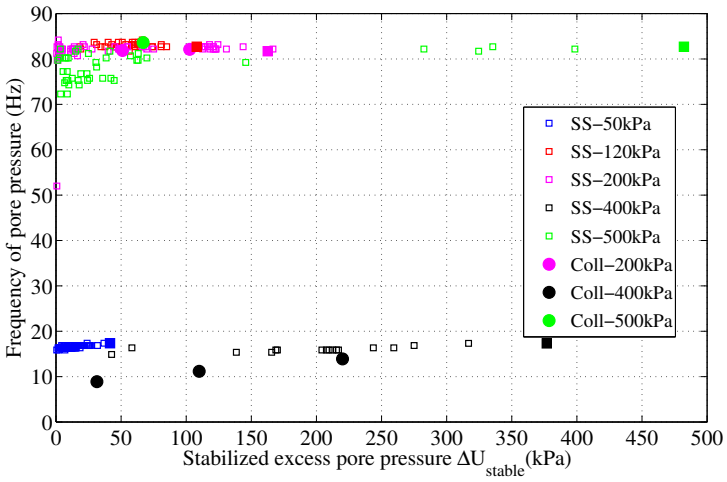

Figure 4.13: Effect of stabilised excess pore pressure ΔU_{stable} on the frequency of pore pressure.

During collapse event, the frequency of U also consistently distributes in two similar groups in the whole CIDNC series and exhibits a slightly increasing tendency of frequency belonging on ΔU_{stable}. This reveals that the effect of confining pressure on the frequency actually exists. Its significance needs to be examined further. The agreement of frequency in both stick-slips and collapses in each individual test of the whole series means that the frequency is not dominantly impacted by the confining pressure but depends on the initial parameter as saturation or void ratio. Note that test N400 has a low Skempton's coefficient B = 0.86, representing the saturation of granular assembly, and test N50, having high Skempton's coefficient B of 0.95.

Therefore, an investigation to explore the effect of saturation represented by Skempton's coefficient B and confining pressure p'_0 is conducted. A set of 13 tests is added and combined with current CIDNC series. In table 4.3, N is the number of re-use of glass beads, N = 1 means virgin material, N = 2 material which was liquefied or sheared once before, B the Skempton's coefficient, CID the standard drained shearing test, CIDOC the drained shearing test with the material at overconsolidated state, CIUOC the undrained shearing test with the overconsolidated materials, f_U the estimated frequency of U in the first transient phase.

Table 4.3: Summarized characteristics of additional tests on the effects of B on the frequency of pore pressure.

	Test	N	p'_0 (kPa)	Loading	B	f_U (Hz)
Additional Series						
1	P50B1	2	50	CID	0.97	19.45
2	P400B2	2	400	CID	0.98	83
3	P400B3	1	400	CID	0.91	9.42
4	P100B4	1	100	CIDOC	0.71	21.1
5	P200B5	1	200	CIDOC	0.89	17.65
6	P50B6	1	50	CIU	0.92	12
7	P100B7	2	100	CIU	0.90	16.9
8	P100B8	3	100	CIU	0.99	75
9	P200B9	2	200	CIU	0.91	17.48
10	P400B10	3	400	CIU	0.98	82.87
12	P200B11	1	200	CIU	0.95	18.8
11	P50B12	1	50	CIUOC	1	85
13	P400B13	1	400	CIUOC	0.95	86
CIDNC Series						
14	N500	1	500	CID	0.98	81.68
15	N400	1	400	CID	0.86	16.34
16	N200	1	200	CID	0.99	82.18
17	N120	1	120	CID	0.97	83.17
18	N50	1	50	CID	0.95	16.84

These tests are under various conditions for the material (virgin beads or reused beads), the loading history (normally consolidated or overconsolidated), and the

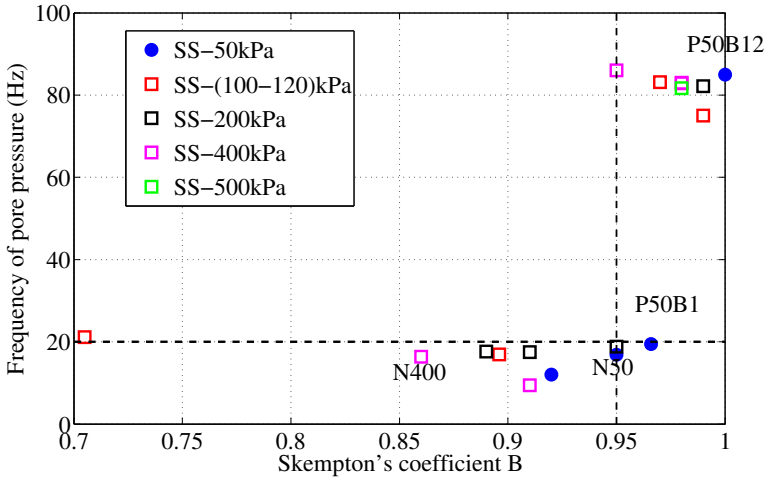

Figure 4.14: Variation of frequentcy of pore pressure in relevance to Skempton's coefficient B.

drainage (drained or undrained) with different initial saturations (B) resulting in different frequencies of pore pressure. From this table, it can be seen that the dominant frequency of pore pressure is independent on the time of re-use of material or drainage condition as well as the overconsolidated state of material. Figure 4.14 presents the evolution of the pore pressure frequency as function of B for different p'_0 represented by different colors. Solid circles are special tests at the lowest $p'_0 = 50$ kPa. The results show two distinct groups of frequency. A threshold is achieved for B = 0.95, lower than this threshold, irrespective of confining pressure p'_0 pore pressure vibrates in low frequency less than 20 Hz, excepting for the tests at low $p'_0 = 50$ kPa, specifically test P50B1. B is the stronger factor controlling the frequency of U since a special blue dot P50B12 at B = 1 with $p'_0 = 50$ kPa and $f_U = 85$ Hz proves that B is the prerequisite condition to ensure the consistency of frequency. With low B, there is the presence of a certain amount of gas resulting in air-water mixture.

In the literature, many relations between saturation S_r and measured Skempton's coefficient B were suggested (84, 118). At constant back pressure $U_0 = 200$ kPa, the variation of surveyed B from 0.86 to 1 corresponds to saturation S_r from 0.997 to 0.999 estimated for average sands with void ratio around 0.6 (67). Additionally that study pointed out that higher B results in higher S_r. Associated with studies on the speed of sound in two-phase mixture, they showed that the presence of air bubbles

in water can have a dramatic effect on the speed of sound compared to individual constituent phase, gas or liquid (16, 60, 72, 79). In particular, the speed of sound in fresh water is around 1480 m/s, in air about 331 m/s but in the mixture of air-liquid phase the speed sharply drops to 50 m/s with the void fraction only at 1%, corresponding to S_r= 0.99. This can explain the drop of frequency of pore pressure depending on Skempton's coefficient B in figure 4.14. Furthermore, the slight effect of confining pressure on the increasing frequency of pore pressure in figure 4.13 can be explained, since stabilised excess pore pressure ΔU_{stable} is almost linearly correlated to confining pressure (figure 5.39a). For example test N400 (black squares and circles) exhibits the obvious increasing tendency in the frequency with the increase of ΔU_{stable}. Furthermore, both Kieffer (60) and McWilliam (79) stated that gas-liquid mixture is strongly dependent on the pressure. More specifically, the depression of vibration speed is much less if the pressure is increased. Hence at the same saturation within a single test, larger ΔU_{stable} leads to higher sound speed, meaning higher frequency.

Besides, at confining pressure larger than 50 kPa, among 120 tests conducted throughout 3 years only approximately 5.8% has low frequency of pore pressure. Thus the predominated frequency within the testing program on saturated granular medium is around 80 Hz. The effect of the group of low frequency will be noticed in subsequent analysis on the time characteristics of U.

4.4.2.2 Relation between ΔU_{stable} and ΔU_{max}

ΔU_{stable} and ΔU_{max}, normalised by confining pressure p'_0, are presented in figure 4.15. The first stick-slips represented by solid squares located on the upper right corner of the plot, their abscissae $\Delta U^{norm}_{stable} = \frac{\Delta U_{stable}}{p_0}$ cannot exceed 1. When $\Delta U^{norm}_{stable} = 1$, it is possible to reach the liquefaction for the first stick-slip. All tests present a linear relation between the peak and the stabilised excess pore pressure that can be fitted by the following equation:

$$\Delta U^{norm}_{max} \;=\; 2.262\ \Delta U^{norm}_{stable} \tag{4.1}$$

This strong linear relation means that ΔU_{max}, the first local peak of U in the transient phase I, seems to govern the magnitude of ΔU_{stable}. Even though test N400 and N50 are at low frequency of U (20 Hz), the correlation coefficient R^2 remains high. That indicates the independence of amplitude of pore pressure irrespective of the vibration in

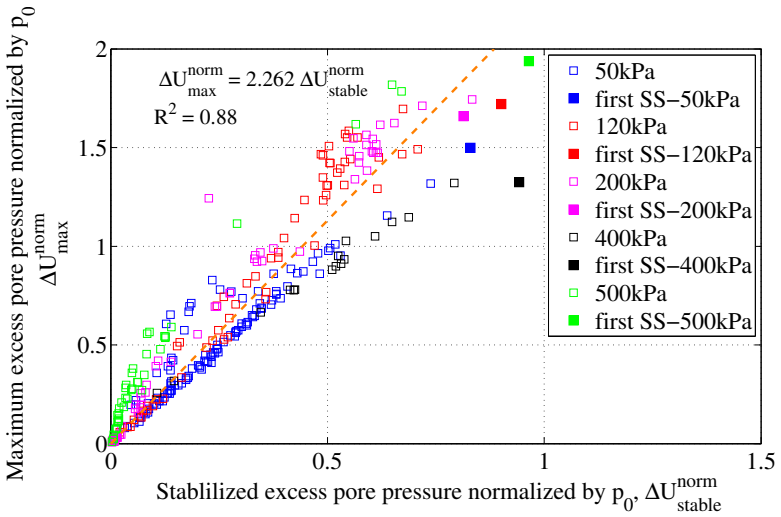

Figure 4.15: Maximum and stabilised excess pore pressure normalised by p'_0 in a linear relation.

the first transient phase I. Further measures of the decaying vibration of pore pressure need to be conducted to capture the full behaviour of the transient phase.

4.4.2.3 Dissipation phase

After the first transient phase I, the dissipation phase III is characterized. Upon ignoring the lateral deformation, the observed excess pore pressure can be approximately governed by one dimensional (vertical) consolidation, equation (4.2), originally developed by Terzaghi (116):

$$\frac{\partial U}{\partial z} = C_v \frac{\partial^2 U}{\partial t^2} \tag{4.2}$$

with the vertical consolidation coefficient $C_v = \frac{k}{m_v \gamma_w}$, k the permeability, m_v the oedometric compressibility, γ_w the fluid unit weight. With the boundary conditions of no pore pressure at drainage surface ($z = H$) and $U = U_m$ at the impermeable surface, this consolidation equation has an analytical solution in a Fourier series:

$$U(z,t) = U_m \sum_{m=0} \frac{2}{M} \sin(M \frac{z}{H}) \exp(-M^2 T_v) \tag{4.3}$$

with $M = \pi(2m+1)/2$ and the dimensionless time factor $T_v = \frac{C_v t}{H^2}$. An approximated solution consists of using only the first term of this Fourier series, equation (4.4), giving a straight line having slope $(\frac{-\pi^2 C_v}{4H^2})$ in the logarithmic plot of U versus time:

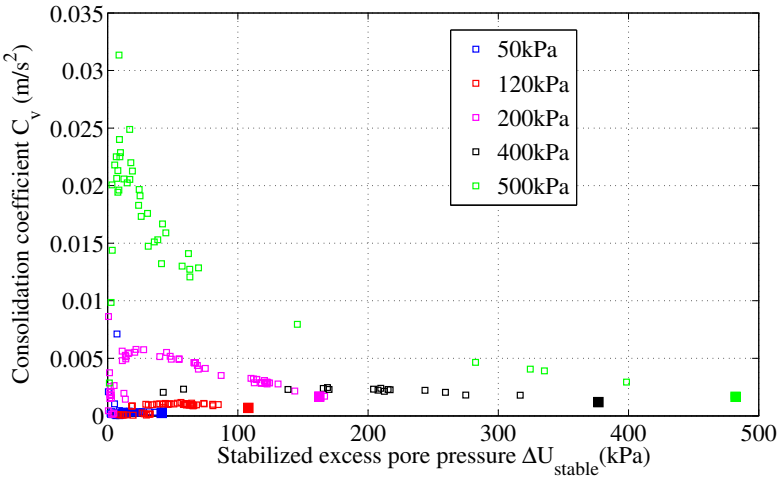

Figure 4.16: Consolidation coefficient C_v in relation to ΔU^{norm}_{stable}.

$$U(z,t) \;=\; U_m \frac{4}{\pi} \sin(\frac{\pi z}{2H}) \exp(\frac{-\pi^2 C_v}{4H^2} t) \tag{4.4}$$

Alternatively, C_v can be determined by the traditional Casagrande logarithm of time (Taylor square root of time) method using the theoretical time factor $T_v = 0.197$ (0.848) at 50 (90)% of pore pressure dissipation. Figure 4.16 shows the effects of normalised stabilized excess pore pressure ΔU^{norm}_{stable} on C_v using Casagrande method. At low p'_0, C_v appears to be a constant at a specific p'_0. While at larger confining pressure p'_0 of 500 kPa, a strong evolution is observed.

Ignoring the evolution of C_v with ΔU_{stable} at high confining pressure p'_0, C_v at each p'_0 is represented by the mean value. Figure 4.17 presents the variation of C_v with increasing confining pressure p'_0. Basically larger confining pressure p'_0 leads to higher C_v. However test N400 is out of the increasing trend.

Globally this nonlinear evolution complied the nonlinear relationships between permeability k, the compressibility m_v and consolidation coefficient C_v (107) as the extensive modification of Terzaghi's consolidation theory. In which, instead of Terzaghi's assumption of constant permeability k and compressibility m_v, Samarasinghe (107) suggested that permeability k is a power law function of void ratio e, $k = k_0(1+e)^{\kappa}$. κ is identified by experiment dependent on specific soil. For normally consolidated soil, void ratio e can be written as the function of compressibility m_v and pressure p as $e = e_0$ - $m_v.p$, in which e_0 is the initial void ratio. Equivalently, C_v can be rewritten as

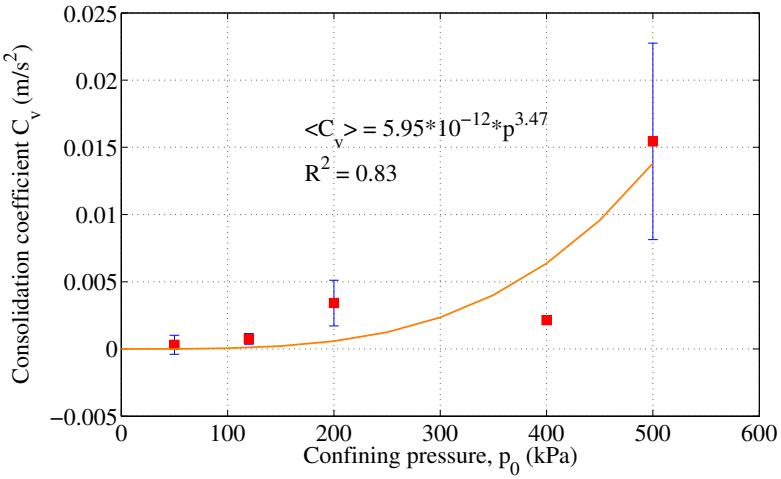

Figure 4.17: Mean of consolidation coefficient $< C_v >$ in relation to confining pressure p'_0.

$C_v = \frac{k_0(1+e_0-m_v.p)^\kappa}{m_v\gamma_w}$ which is a nonlinear monotonic increasing function of pressure. This explains the power law function of the fitting curve, $C_v = 5.95{*}10^{-12}{*}p'^{3.47}_0$. But for model granular material, the compressibility curve under shear of material is interrupted by uncontrolled stick-slips and the evolution of void ratio e is unpredictable from the effective pressure. Thus C_v is affected by both pressure p and void ratio e. It explains the low value of $< C_v >$ although at high pressure of 400 kPa. This is due to the particularly low void ratio e_c of test N400.

So far, the pressure p'_0 still maintains the nonlinear influence on consolidation coefficient C_v of model granular material as previous study for soils. The combined effects of confining pressure p'_0 and void ratio e_c on C_v have not been established. However this qualitative analysis gives a direction for further study.

4.4.3 Time-resolved analysis

One of the advantages of this study is to have high resolution data. Figure 4.18a shows one single stick-slip event, including a dynamic slip phase and a quasi-static stick phase, for two sampling rates of 0.2 Hz and 10 kHz. It shows a conventional fast slip phase from point A to C in stress-strain curve (blue) in which the granular structure looses the strength. The loss of stress coincides with a contraction of volumetric strain from point A' to C' (red). After the slip phase, the skeleton gradually supports additional

loading after the rearrangement of the contact network and accumulates energy in a quasi-static stick phase from C to further stress.

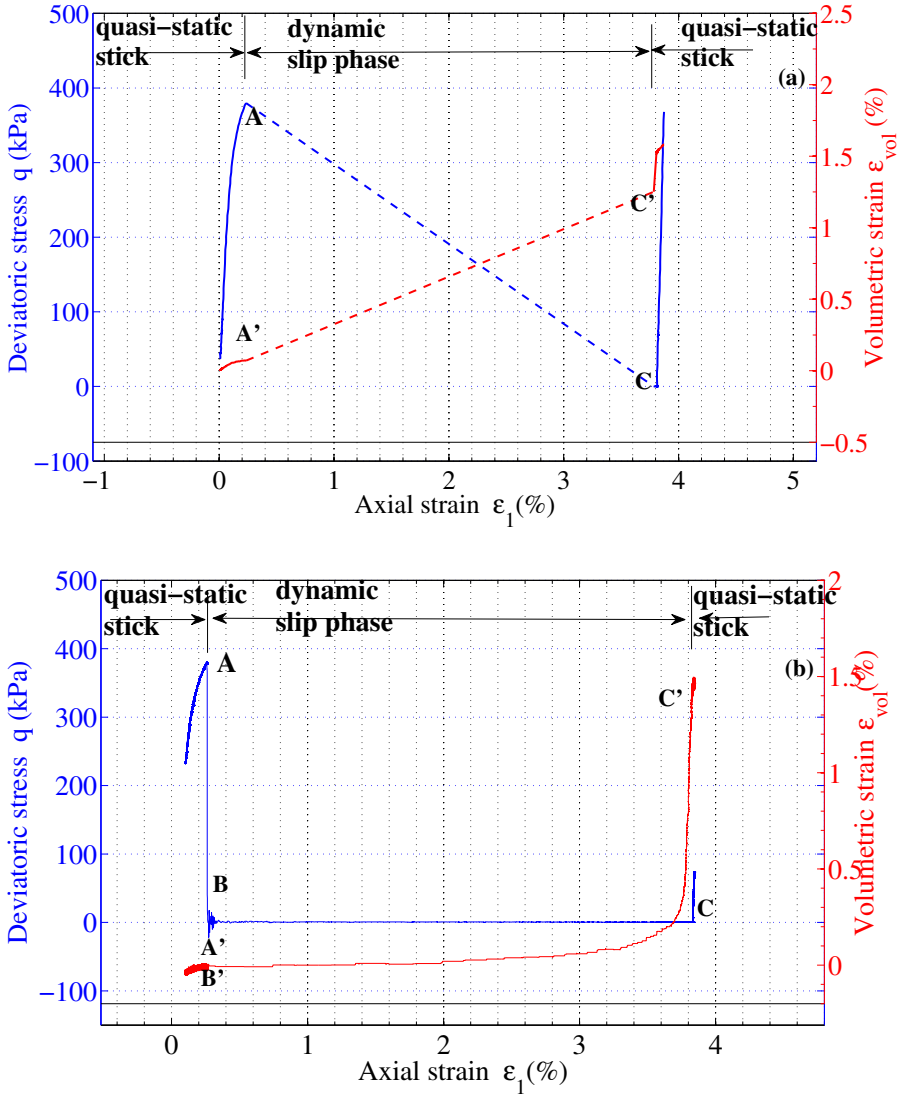

Figure 4.18: Typical stick-slip behaviour in drained triaxial compression at 400 kPa with stress-strain and volumetric strain behaviours acquiring of (a) 0.2 Hz and (b) 10 kHz.

At higher sampling rate of 10 kHz, a significant distinction in behaviour of slip phase is revealed in figure 4.18b. Instead of jumping directly from A to C, the drop of deviatoric stress suddenly takes place from A to B while the axial strain has not yet responded. Therefore the modulus of the slip process can be considered as infinite.

This raises a question concerning the capability of LVDT in capturing the dynamic strain during the stress drop AB. After dropping, the deviatoric stress q maintains a stable state at constant level from B to C before moving up in the next stick phase.

All possible time characteristics of deviatoric stress q and excess pore pressure U are going to be analysed in this section including drop duration of q, t^q_{drop}, duration of the transition phase I t_{trans} and other characteristic times of dissipation phase III t_{05}, t_{50}, t_{diss}.

4.4.3.1 Duration of deviatoric stress drop t^q_{drop}

One of the most useful information to depict the dynamics of stress drop is the drop duration of q, t^q_{drop} (figure 4.1). Under isotropic loading the effective stress of the skeleton is inferred from the pore pressure buildup by the equation $\sigma' = \sigma$ - U. The actual temporal evolution of the effective stress release is the subtraction of a constant total stress σ and a function of time U(t). Under shearing, the drop of deviatoric stress q showed a short duration t^q_{drop} which is investigated in the relation to normalised deviatoric stress drop Δq^{norm} in figure 4.19. It seems that the drop duration is a constant of around 2 ms, consistent to other works (86). At very few particular small SSs with low Δq^{norm}, the drop duration t^q_{drop} increases up to 8 ms.

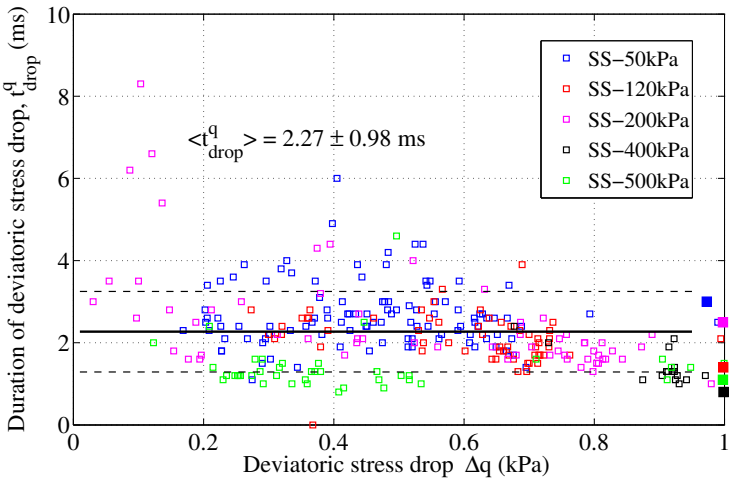

Figure 4.19: Duration of deviatoric stress drop t^q_{drop} in relevance with normalised deviatoric stress drop Δq^{norm}.

Moreover, since deviatoric stress q always finishes the drop before the pore pressure

buildup ΔU thus the dynamic drop duration t^q_{drop} is not impacted by the subsequent response of U. The magnitude of stabilised excess pore pressure ΔU_{stable} is also explored and has no effect on the drop duration t^q_{drop}. The remaining parameter, the frequency of U, is controlled by the saturation.

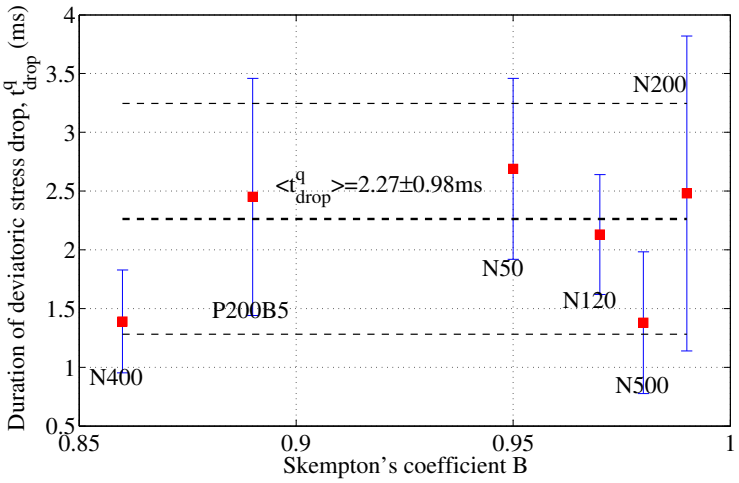

Figure 4.20: Duration of deviatoric stress drop t^q_{drop} in relevance with Skempton's coefficient B.

Figure 4.20 presents an investigation of t^q_{drop} of CIDNC series with the variation of saturation represented by Skempton's coefficient B. The difference of their means are not significant; they fluctuate around the unique mean value of 2.07±0.74 ms. t^q_{drop} is independent of saturation S_r and confining pressure p'_0. It only depends on the way of rearrangement of grain contacts. The conclusions are also enhanced and verified by the addition of test P200B5 on overconsolidated sample. It seems that t^q_{drop} is independent of loading history.

4.4.3.2 Time delay between deviatoric stress and excess pore pressure t_{delay}

In presence of pore fluid, the time delay between deviatoric stress and pore pressure t_{delay} (defined in figure 4.1) appears to be impacted by the own response of U resulting in two distinct groups irrespective of the magnitude of the stress drop Δq (figure 4.21).

One group includes tests N50 and N400 (blue and black squares) at low saturation and the other group is the remaining tests with high saturation. The mean of the former

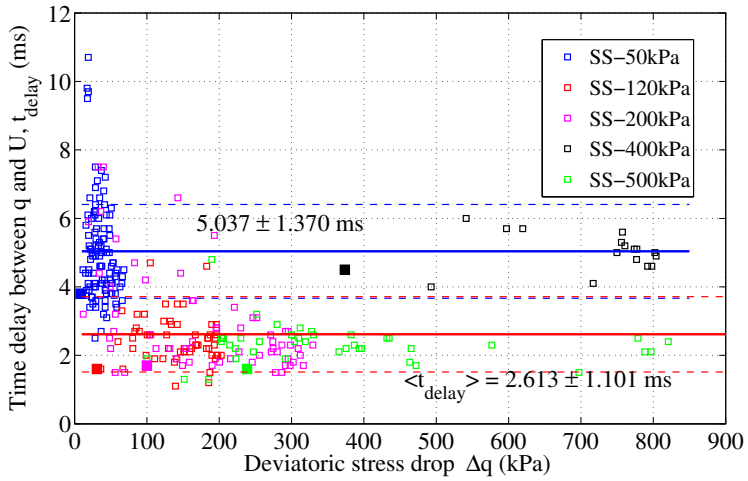

Figure 4.21: Time delay between deviatoric stress q and the buildup of pore pressure ΔU in relevance with deviatoric stress drop Δq.

group is 5.036 ± 1.370 ms and the one of the latter is lower of 2.613 ± 1.101 ms. Their means and standard deviations are statistical significant. It can be conjectured that the saturation condition influences the propagation of vibration from the stress drop of the grains to the pore fluid, resulting in the buildup of pore pressure at different speeds. It is suspected that pore pressure can initiate the instabilities. Indeed, in dry granular media, small fluctuations were found as the probable consequences of the rearrangement of the force chains (117). This systematic time delay between ΔU and Δq is another strong proof that excess pore pressure always occurs after the stress drop, thus it is not the cause of SS instability in saturated media.

4.4.3.3 Duration of the transient phase I t_{trans}

Here we explore the dependency of t_{trans} on the stabilised effective mean stress p'_{stable}. In figure 4.22, t_{trans} is plotted as function of the amplitude of stabilised effective mean pressure p'_{stable}.

This function approaches and crosses the ordinate axis at a specific representative t_{trans} of a dynamic instability having $p'_{stable} = 0$. That is equivalent to liquefaction under shear (named SSLiq in chapter 5). Increasing p'_{stable} corresponds to smaller SS event and diminished t_{trans}. Orange diamond represents the average t_{trans} of all collapse events at any frequency of U which is $< t^{Coll}_{trans} > = 0.1835 \pm 0.0918$ seconds

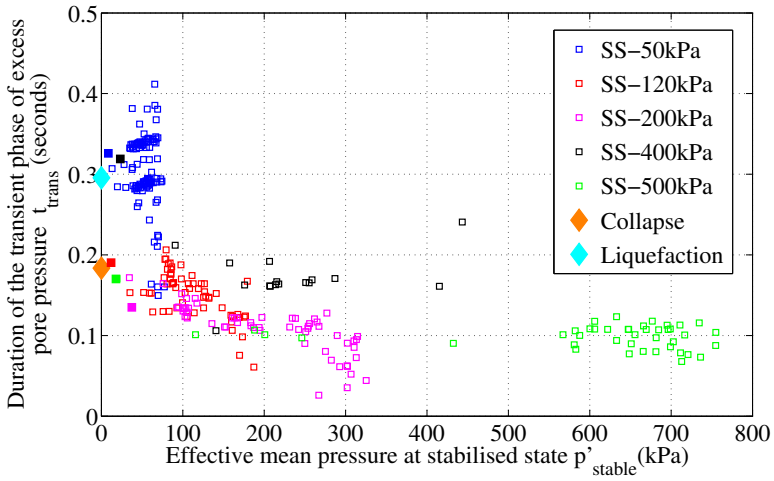

Figure 4.22: Relation between duration of the first transient phase of U, t_{trans}, and stabilised effective mean pressure p'_{stable}.

and cyan diamond the mean t_{trans} for all isotropic liquefaction events at any frequency of U which is $< t^{Liq}_{trans} > = 0.2956 \pm 0.1705$ seconds. It is observed a separation of test N400 from the main trend of the series and test N50 showing the considerably extended t_{trans} compared to the one of liquefaction t^{Liq}_{trans}. Both these two distinct tests are at lower saturation (low B). Targeting only full saturated media, the group of test N120, N200, N500 at high B and high dominant frequency of U around 80 Hz is separately investigated.

The most interesting finding of this chapter is the evolution from stick-slip to liquefaction indicated by the comparison of measurements of stick-slip to those of liquefaction. In other chapters the evolution of most parameters from collapse to liquefaction is established. Finally key parameters of liquefaction are measured and characterised. From the referenced measurements of liquefaction it is deduced all related parameters of stick-slip and collapse. Thus the parameters of stick-slip and collapse are normalised by those of liquefaction and are used throughout this study.

On the main stream of exploitation of normalised parameters to see the evolution from stick-slip to liquefaction, figure 4.23 shows the relation of normalised duration of the transient phase of stick-slip and the normalised stabilised effective mean pressure p'^{norm}_{stable}. This quantity points out the position of stabilised stress state on surface boundary (section 4.4.7). The evolution is a nonlinear monotonic curve crossing two

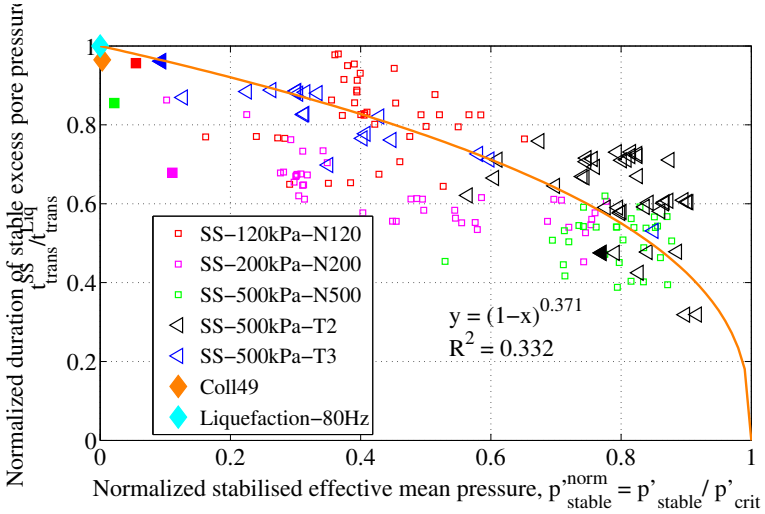

Figure 4.23: Relation between normalised duration of the first transient phase of U, t^{norm}_{trans}, and the normalised stabilised effective mean pressure p'^{norm}_{stable}.

mandatory points (1,0) and (0,1). At point (1,0), $p'_{stable} = p'_{crit}$ there is no SS then $t_{trans} = 0$ and $t^{norm}_{trans} = 0$. Within the range that $p'_{stable} < p'_{crit}$, low p'_{stable} equivalent to large SS, it is shown that pore pressure vibrates in longer transient phase. Until $p'_{stable} = 0$ corresponding to the largest SS with the largest drop to $q = 0$ (isotropic state) so t_{trans} approaches exactly the mean $< t^{Liq}_{trans} >$ of isotropic liquefaction. The accuracy of data is enhanced by a special rare collapse event which almost liquefied, named test Coll_{49} in chapter 5, having measured $t^{Coll}_{trans} = 0.192$ seconds. In the other hand $< t^{Liq}_{trans}(80\text{Hz}) > = 0.199$ s (figure 5.27), thus $t^{norm}_{trans} = 0.192/0.199 = 0.997$. As presented, this orange diamond of Coll_{49} very close to cyan diamond represented liquefaction, appreciably improves the quality of data. This fitting curve is suggested by following equation:

$$t^{norm}_{trans} = \frac{t^{SS}_{trans}}{< t^{Liq}_{trans} >} = (1 - \frac{p'_{stable}}{p'_{crit}})^{0.371} \tag{4.5}$$

with

$$p'^{norm}_{stable} = \frac{p'_{stable}}{p'_{crit}} = \frac{p_0 + \frac{(q_{trig} - \Delta q)}{3} - p_0 * \Delta U^{norm}_{stable}}{M * p_0}$$

Since only tests N500, N200, N120 having high Skempton's coefficient B are investigated, to enhance the reliability of data, two additional tests T2, T3 on 500 kPa of

effective confining pressure are explored (black and blue triangles). Although the correlation coefficient R^2 is quite low, the addition of tests T2 and T3 greatly confirmed the tendency of evolution. By this equation, t_{trans} could be predicted from p'_{stable}.

4.4.3.4 The intermediate duration between phase I and III

The next time characteristic is the starting point of dissipation phase of U (phase III), t_5. As illustrated in figure 4.1, there is a difference between t_{trans} and t_{05}, $\Delta t_{05} = t_{05}$ - t_{trans} that is the phase II where U maintains at stabilised state. In case of stick-slip events, Δt_{05} is small hence the lack of phase II.

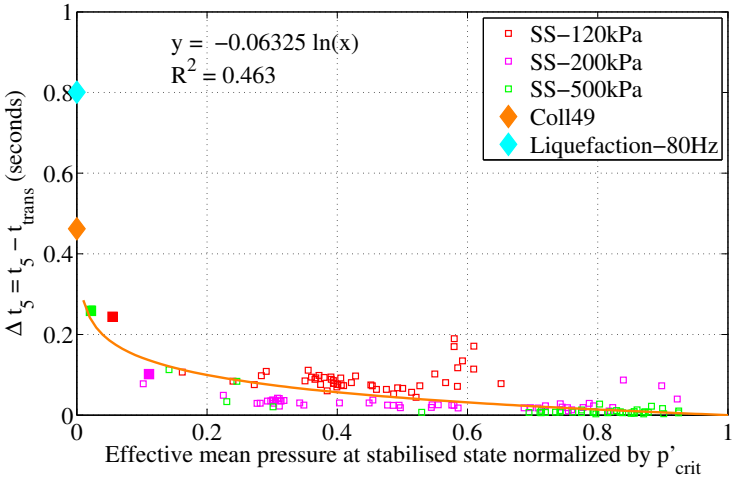

Figure 4.24: Duration between phase I and phase III of pore pressure, Δt_{05}, in relevance with $\frac{p'_{stable}}{p'_{crit}}$.

Large stick-slip can keep the stabilised pore pressure longer to approach the isotropic state of collapse (orange diamond) and if this duration expands sufficiently to reach the threshold of liquefaction (cyan diamond) the stick-slip event can liquefy. In figure 4.24 this intermediate duration is fitted by following equation :

$$\Delta t_{05} = -0.06186 \ln(\frac{p'_{stable}}{p'_{crit}}) \tag{4.6}$$

This equation successfully describes the intercept condition, at $\frac{p'_{stable}}{p'_{crit}} = 1$ meaning no drop of q, no stick-slip, no Δt_{05}. At very large stick-slip event with $\frac{p'_{stable}}{p'_{crit}}$ moving to 0, q totally drops to 0 moving the stress state to isotropic state. The intermediate

phase Δt_{05} extends to the value of extremely large isotropic collapse represented by orange diamond of test Coll_{49} (chapter 5). This rare mostly liquefied collapse of appreciably importance with $\Delta U_{stable}^{norm} = 0.9968$, $\Delta t_{05} = 0.424$ seconds whose the detail is shown in chapter 5. This special collapse proved the good fitting equation despite the low correlation coefficient R^2 due to the noise in small SSs. The evidence of the good fitting equation 4.6 at the intercept (represented by orange diamond) is proved in section 5.5.8. The cyan diamond represents the threshold Δt_{05}^{thres}, exceeding this threshold the collapse evolves to a liquefaction. As published in our previous work (34), the threshold to occur liquefaction is $t_{05}^{Liq,thres} = 1$ second, Δt_{05}^{thres} is estimated as $t_{05}^{Liq,thres}$ - $< t_{trans}^{Liq}(80\text{Hz}) >$ = 1 - 0.199 = 0.801 seconds.

4.4.4 Role of stabilised pore pressure

The interest of this study is saturated granular material in which the presence of pore fluid plays the key role in controlling other stress or strain measurements. Hence, the importance of pore pressure is quantitatively analysed in this section.

4.4.4.1 Relation of ΔU_{stable}^{norm} and $\Delta\varepsilon_{vol}$

The volumetric strain has not been appropriately considered in some lately researches (35, 125), only global volumetric strain of the whole shearing phase was captured (2), the evolution of $\Delta\varepsilon_{vol}$ inside SS events has been missed. The pore pressure has just been estimated qualitatively in relevant to stress drop and to the dilation in the slip phase under undrained boundary (111). The role of pore pressure in drained stick-slip so far is still missing. This shortcoming is fulfilled in this study.

As a function of normalised ΔU_{stable} in figures 4.25a to e, $\Delta\varepsilon_{vol}$, for all confining pressure p'_0, evolves according to the same law $\Delta\varepsilon_{vol} = m.\ln(1\text{-}\Delta U_{stable}^{norm})$. The presence of large $\Delta\varepsilon_{vol}$ in case of first SSs and large quasi-periodic SSs fills advantageously the domain of high ΔU_{stable}. The discrepancy between curves is significant in figure 4.25f due to the difference in parameter m. The addition of cyan diamond symboled for the mean of $\Delta\varepsilon_{vol}$ of liquefaction cases enhanced the meaning of fitting equation. It describes the smooth transition from SS event as a local instability to the global failure at very large $\Delta\varepsilon_{vol}$ and the null state of effective pressure when excess pore pressure equals confining pressure, $\Delta U_{stable}^{norm} = 1$.

This parameter represents different amplitudes of generated $\Delta\varepsilon_{vol}$ even in case of

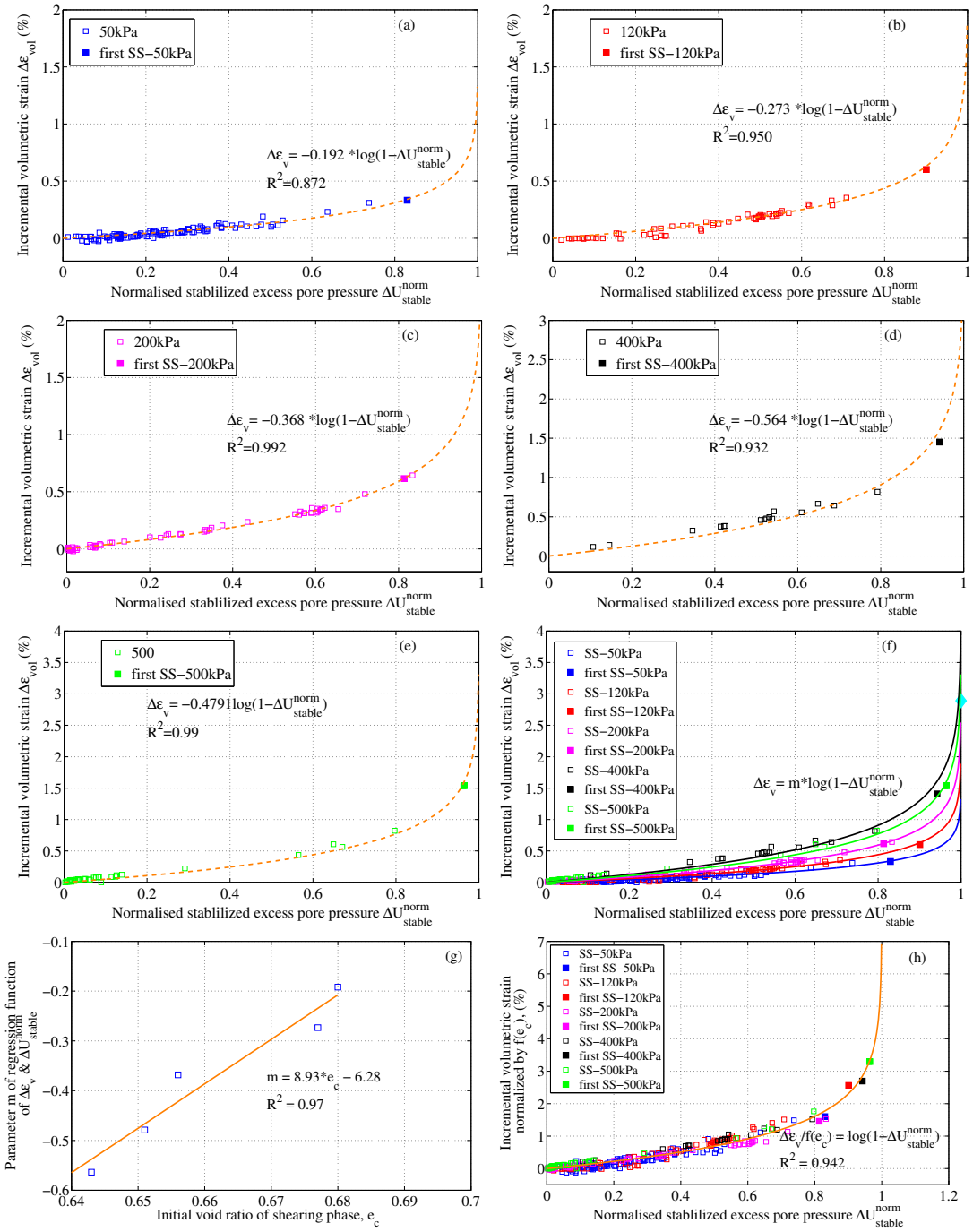

Figure 4.25: Normalised stabilised excess pore pressure ΔU^{norm}_{stable} and incremental volumetric strain $\Delta\varepsilon_{vol}$ incorporating with the effect void ratio e_c at the beginning of shearing.

same confining pressure. Among the unknown factors affecting the shearing behaviour of granular materials, the void ratio at the beginning of shearing e_c is one of the most significant impact on the macroscopic behaviour such as the small strain stiffness. Thus, the void ratio e_c is investigated in relevance with parameter m of fitting equation in figure 4.25g showing a highly linear correlation as

$$m \;=\; f(e_c) \;=\; 8.93\, e_c - 6.28 \tag{4.7}$$

With high correlation coefficient $R^2 = 0.97$, the correction based on $f(e_c)$ can be used to collapse all different relationships of figure 4.25f into one single master curve. Figure 4.25h demonstrates the uniqueness of relation of $\Delta\varepsilon_{vol}$ and ΔU^{norm}_{stable} independent of confining pressure p'_0 and of void ratio e_c with very high correlation coefficient $R^2 = 0.942$.

$$\frac{\Delta\varepsilon_{vol}}{f(e_c)} \;=\; \ln(1 - \Delta U^{norm}_{stable}) \tag{4.8}$$

The quantity $\frac{\Delta\varepsilon_{vol}}{f(e_c)}$ can account for the variation of void ratio e_c at the beginning of compressive shearing, regardless of the number of collapses occurring in the isotropic consolidation phase. Equation 4.8 also shows the uncoupling effects of void ratio e_c and confining pressure p'_0.

4.4.4.2 Relation between ΔU^{norm}_{stable} and $\Delta\varepsilon_1$

At low confining pressure, $\Delta\varepsilon_1$ seems to be constant, irrespective of ΔU^{norm}_{stable} (figures 4.26a,b,c). However very large SS events in test N500 and N400 in figures 4.26d,e reveal the nonlinear evolution of $\Delta\varepsilon_1$. Combined with the cyan diamond representing the mean $<\Delta\varepsilon_1>$ of isotropic liquefaction cases, it depicts the whole evolution of $\Delta\varepsilon_1$ by the same trend as $\Delta\varepsilon_{vol}$. The regression equation and correlation coefficient R^2 in the figure are estimated for compressive $\Delta\varepsilon_1$ only, since negative $\Delta\varepsilon_1$ has no physical meaning at current knowledge.

$$\Delta\varepsilon_1 \;=\; -0.689\,[\ln(1 - \Delta U^{norm}_{stable})] \tag{4.9}$$

In case of $\Delta\varepsilon_1$, the master curve obtains very high $R^2 = 0.961$ even without the incorporation of e_c. Although there is a gap from the maximum $\Delta\varepsilon_1 = 4.4\%$ of SS_4 in test N500 to the mean $<\Delta\varepsilon_1> = 24.14\%$ of isotropic liquefaction, the basis and relation of $\Delta\varepsilon_1$ and $\Delta\varepsilon_{vol}$ still support similar fitting equation for $\Delta\varepsilon_1$.

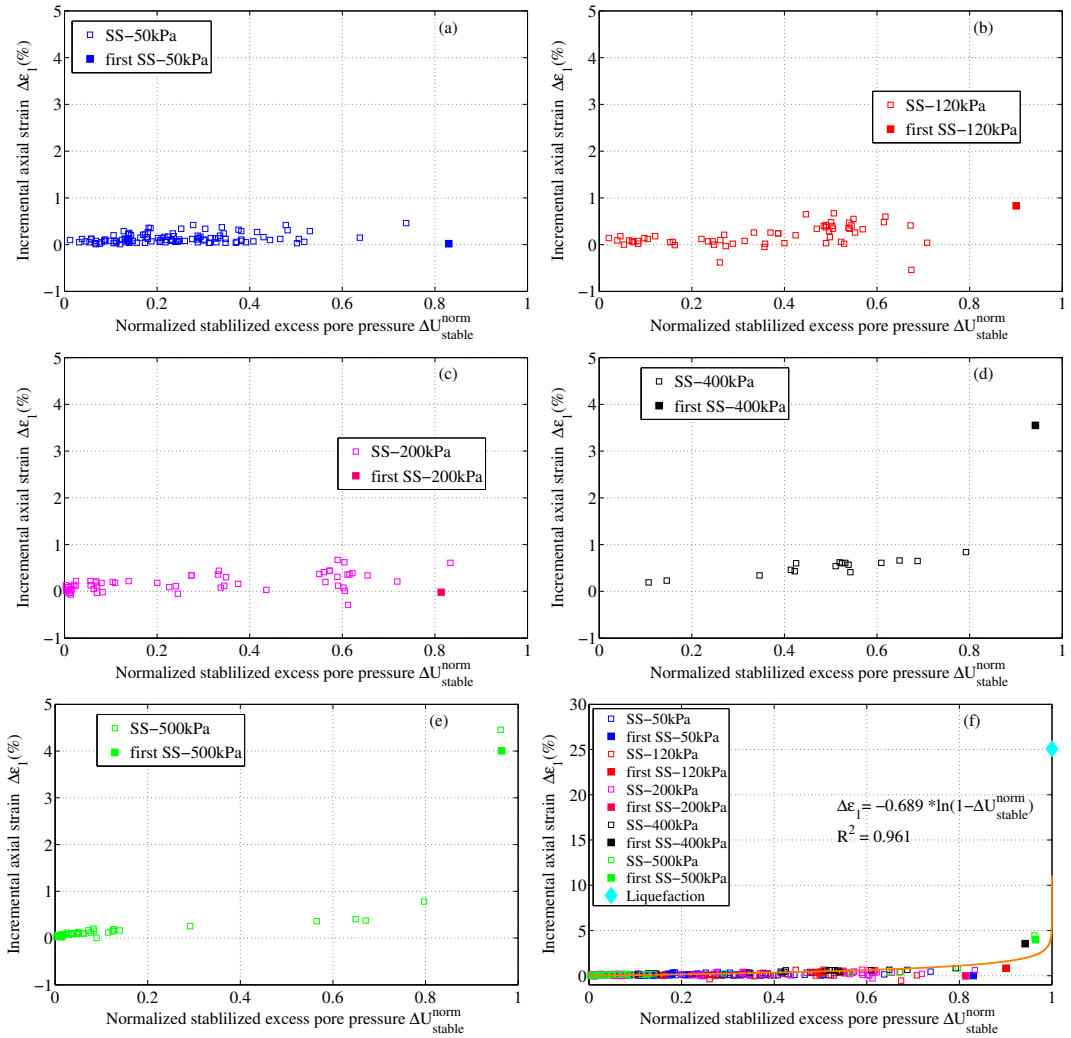

Figure 4.26: Relation of normalised stabilised excess pore pressure ΔU^{norm}_{stable} and incremental axial strain $\Delta\varepsilon_1$.

Furthermore, parameter $m = f(e_c)$ in equation 4.8 varies in the range of (-0,192 ÷ -0.564) compared with parameter m = -0.689 in equation 4.9, hence the fraction

$$\frac{\Delta\varepsilon_{vol}}{\Delta\varepsilon_1} = \frac{m[\ln(1-\Delta U^{norm}_{stable})]}{-0.688[\ln(1-\Delta U^{norm}_{stable})]} = \frac{-0.192 \div -0.564}{-0.689} < 3$$

that is consistent with the average $< i^{stat} >$ of the whole series around 1 in figure 4.30h thus the correctness of the constant = -0.689 of this fitting equation for $\Delta\varepsilon_1$ is verified.

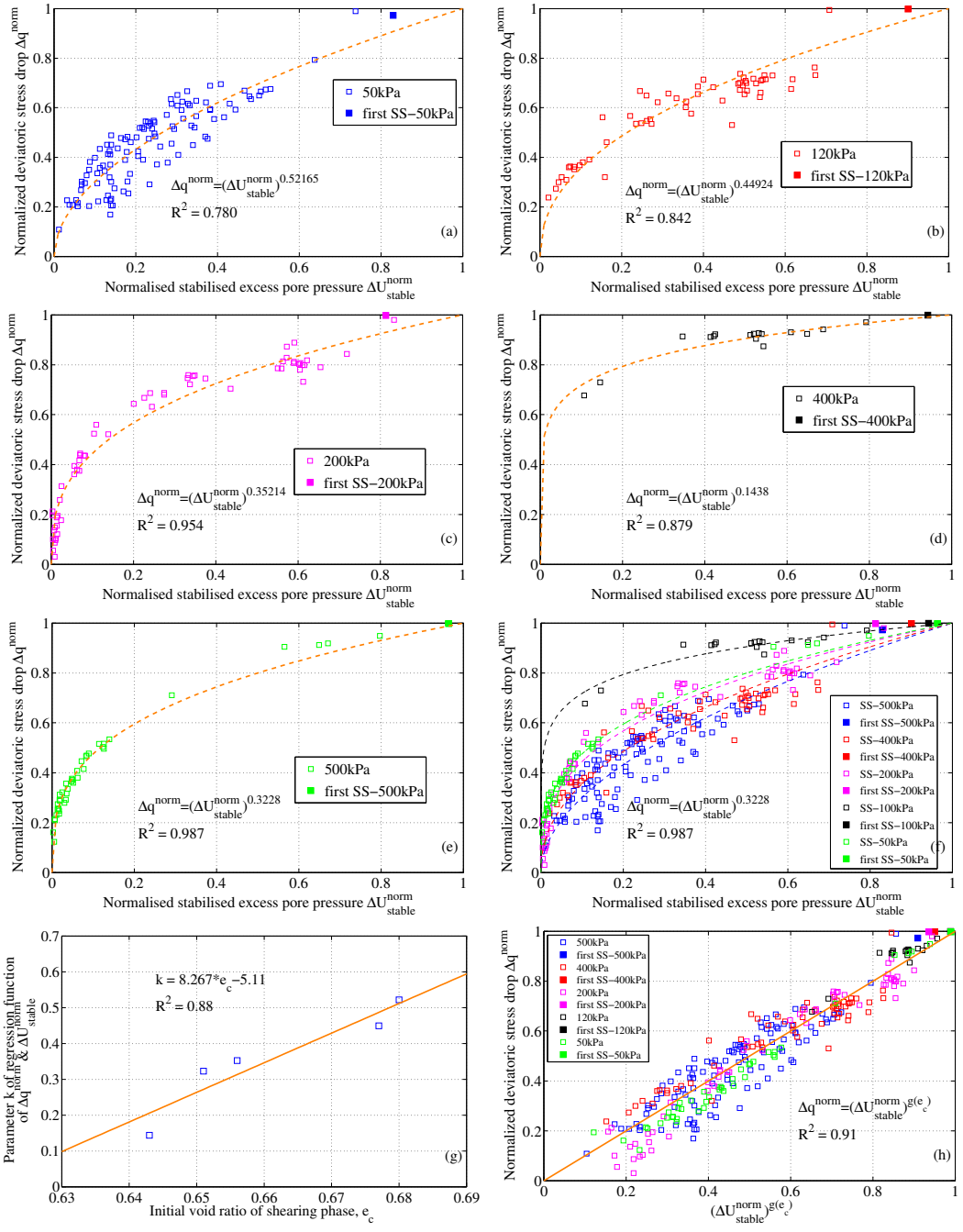

Figure 4.27: Relation of normalised stabilised excess pore pressure ΔU_{stable}^{norm} and normalised deviatoric stress drop Δq^{norm} incorporated with the effect of void ratio e_c.

4.4.4.3 Relation of ΔU_{stable}^{norm} and Δq^{norm}

The relations between normalised amplitude Δq^{norm} and ΔU_{stable}^{norm} are examined separately for each confining pressure p'_0 in figures 4.27a to e. They share the same form of development, starting at the origin (0,0) meaning no stress drop then no excess pore pressure and ending at point (1,1) (named liquefied point) meaning $\Delta U_{stable}^{norm} = 1$ corresponding to liquefaction state when deviatoric stress q drops to zero, $\Delta q^{norm} = 1$. This point (1,1) is the liquefaction under compression shearing state, namely SS liquefaction, which is reported in chapter 5. Thus in figures 4.27a to e all first SSs (solid squares) gathered near the liquefied point of the plot, indicating the possibility of the first SS to liquefy.

The equation suggested here is a power law $y = x^k$ satisfying the liquefied point and starting point with different exponent number k<1, written as: $\Delta q_{norm} = (\Delta U_{stable}^{norm})^k$. In figure 4.27f, 5 tests exhibit a large scatter between different confining pressures. Similar procedure is performed to investigate the relation of power parameter k and e_c. Then a linear relation is found (figure 4.27g)

$$k = g(e_c) \;=\; 8.267\; e_c - 5.11 \tag{4.10}$$

Subsequently the general relation of Δq_{norm} and ΔU_{stable}^{norm} become

$$\Delta q_{norm} \;=\; (\Delta U_{stable}^{norm})^{g(e_c)} \tag{4.11}$$

Although test N120 and test N50 individually have low correlation coefficient R^2 (0.77 and 0.483), all tests in the series exhibit a high correlation coefficient $R^2 = 0.91$ (figure 4.27h). The noise of data at low confining pressure can be responsible in larger errors for tests N50 and N120.

In short, the uncoupled effects of void ratio e_c and confining pressure p'_0 have been suggested in the unified relations between ΔU_{stable}^{norm}, Δq_{norm} and $\Delta\varepsilon_{vol}$, confirming the conclusions of their impacts on macroscopic stress-strain behaviour which were presented in section 4.10. In this section a combined effect of e_c and p'_0 has not been found due to the strong interruptions of uncontrollable isotropic collapses before shearing. So far, the void ratio e_c not only controls the global behaviour but also the detailed behaviour inside individual SS event. Note that the relation between $\Delta\varepsilon_1$ and ΔU_{stable}^{norm} presents a strong correlation without any normalisation by void ratio.

Nevertheless, the macroscopic void ratio parameter e_c is not sufficient to explain the appearance feature of SS events, for example the statistical distribution of the size of SSs. It should be suggested that microscopic measurement as surface roughness of glass beads can be worth studying.

4.4.5 Anisotropy

Anisotropy of granular materials is understandable under anisotropy loading like compression shearing due to the forming of strong force chain along the direction of principal stress. Weak force chains are thus mainly perpendicular to the strong one (53). The model materials used in our works behave surprisingly anisotropically even under isotropic loading (30, 34). This anisotropy has been proposed as one of the two necessarily requirements for the appearance of the instability. In this study, the anisotropy characteristics in dynamic regime are examined during stick-slip events under triaxial compression loading in comparison with isotropic loading.

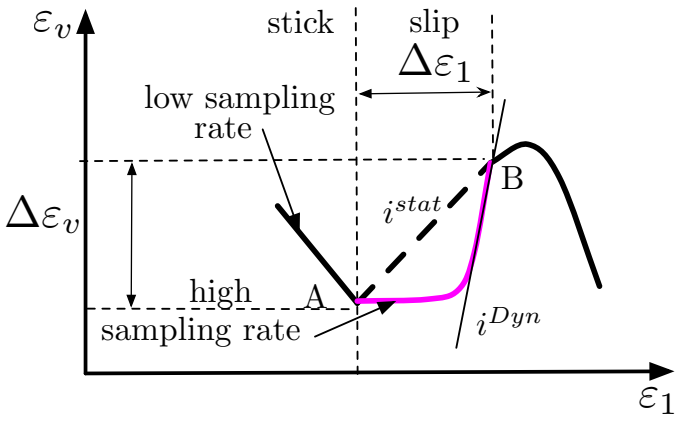

Figure 4.28: Static and dynamic anisotropy coefficients for instability.

A simplified scheme 4.28 illustrates a typical SS event in the axes of volumetric strain ε_{vol} and axial strain ε_1. The static anisotropy coefficient i^{stat} is estimated by $\frac{\Delta\varepsilon_{vol}}{\Delta\varepsilon_1}$. It is also the slope of the SS in low sampling rate behaviour. The magenta curve corresponds to high time-resolved data and represents the dynamic behaviour of stick-slip. Then dynamic anisotropy coefficient i^{Dyn} is the largest slope of this behaviour.

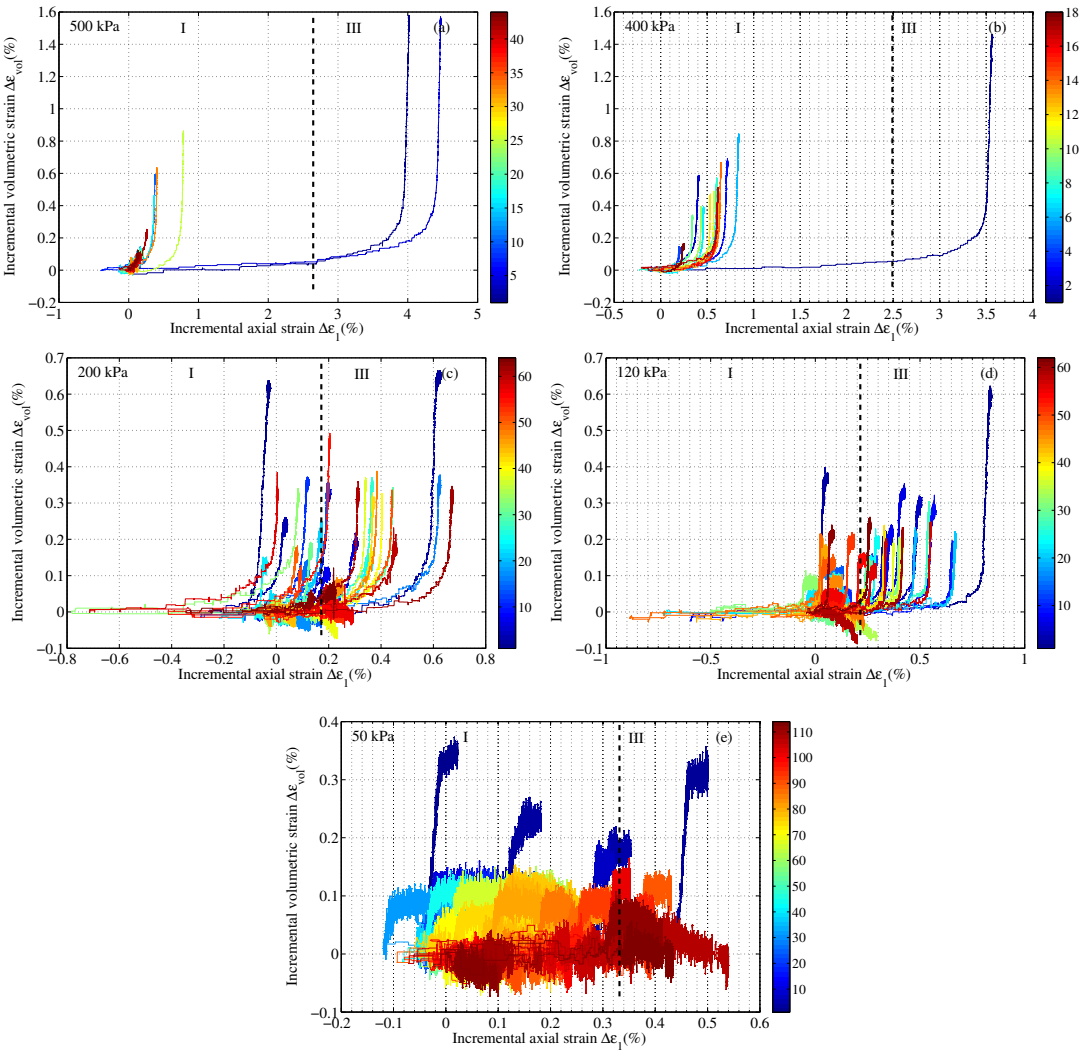

Figure 4.29: Evolution of incremental volumetric strain $\Delta\varepsilon_{vol}$ in accordance with incremental axial strain $\Delta\varepsilon_1$ at different confining pressures.

The detailed evolution of incremental volumetric strain $\Delta\varepsilon_{vol}$ and incremental axial strain $\Delta\varepsilon_1$ with high temporal resolution is presented in figure 4.29 for the whole CIDNC series. There is a time delay in the developments of $\Delta\varepsilon_{vol}$ and $\Delta\varepsilon_1$ thus the evolution is nearly bilinear. The first segment is almost horizontal when only $\Delta\varepsilon_1$ increases and the second with larger slope, namely i^{Dyn}, when $\Delta\varepsilon_{vol}$ climbs up at nearly constant $\Delta\varepsilon_1$. It depends on the dynamic behaviour of the strains. In figure 4.29, both dark blue curves representing very first SSs of all tests show noticeably large magnitudes

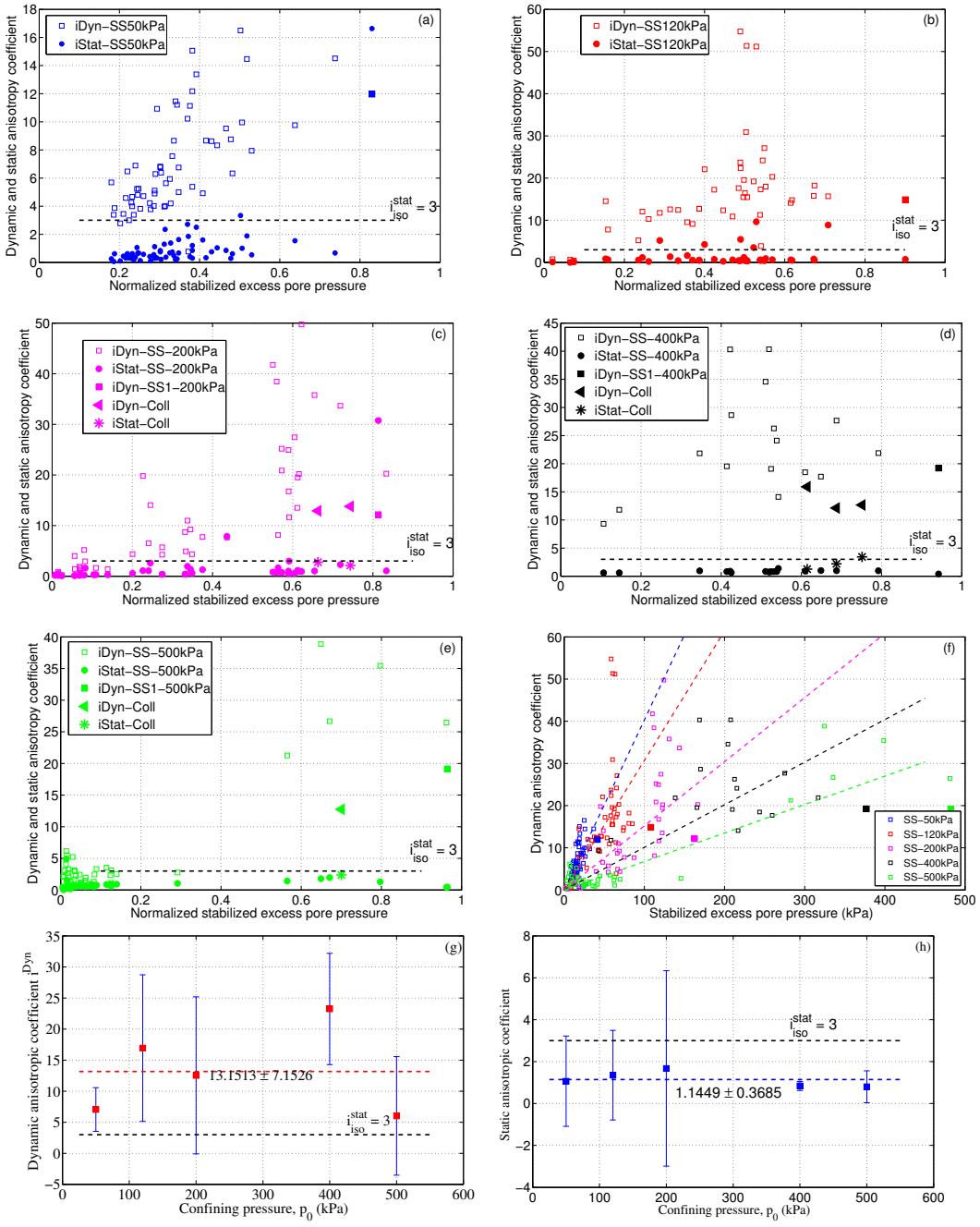

Figure 4.30: Static and dynamic anisotropy coefficients at different confining pressures.

and steepnesses.

In figures 4.30a to e, i^{stat} is often lower than i^{Dyn} except for some abnormal first SSs

with higher i^{stat}. Albeit during dynamic development i^{Dyn} is too high, when the strains reach the stable state i^{stat} is lower than 3 which is the anisotropy coefficient for isotropic materials. The mean $< i^{Dyn} >$ and $< i^{stat} >$ as well as their standard deviations are presented in figures 4.30g,h. However no direct relation between $< i^{Dyn} >$ and confining pressure p'_0 is identified, then they are represented by their mean at 13.15 $\pm$ 7.15. $< i^{stat} >$ is a constant around 1.14 $\pm$ 0.37. The standard deviations of i^{stat} are much less than those of $< i^{Dyn} >$ due to the unknown complexity of the dynamic evolution of the strains before jumping to the stable state of the stick phase. The same situation happens to isotropic collapses in test N200, N400, N500 with large $< i^{Dyn} >$ and $< i^{stat} >$ $\approx$ 3 due to strong effect of isotropic loading. Tests N50 and N120 have no isotropic collapse event.

Further explorations are necessary to examine the variation of i^{Dyn}. Figure 4.30f unveils that i^{Dyn} seems to linearly related to ΔU_{stable} and the effect of confining pressures p'_0 also exhibits in controlling the slope of this linear relation. The lower the p'_0, the stronger the dynamic anisotropy. But the scatter of data is quite large with $R^2 \simeq 0.27 \div 0.79$. This drawback can be improved by other techniques for instance using fast cameras to acquire high time-resolved data of strains.

4.4.6 Dynamic consolidation behaviour

In the effective stress p'-q plane of soil mechanics (fig. 4.31), where q is deviatoric stress ($q = \sigma_1$ - σ_3) and p' is mean effective stress ($p = (\sigma_1 + 2\sigma_3)/3$, $p' = p$ - U), an arbitrary stress state is represented by a point. Thus continuous loading draws a continuous stress path. Our tests are conducted under drained shearing, the effective stress path is the inclined line GA with the constant slope 1:3. With drainage condition, the effective stress path of CID test coincides with the total stress path GA.

For a typical stick-slip event, the initial state of shearing phase locates on abscissa at a target confining pressure p'_0, point G, corresponding to final stress of isotropic phase, $q = 0$. When the axial loading ram applies an axial force on the top of sample resulting in increasing deviatoric stress q, the mean effective stress p' also increases. The stress state goes up along linear effective stress path from G to point A. At unanticipated triggering stress q_{trig}, point A, stick-slip event happens. In the very early portion of slip phase (only 1-2 ms), while U has no variation, the deviatoric stress q drops instantaneously along the stress path downwards to the lower level of q_{stable}, point M,

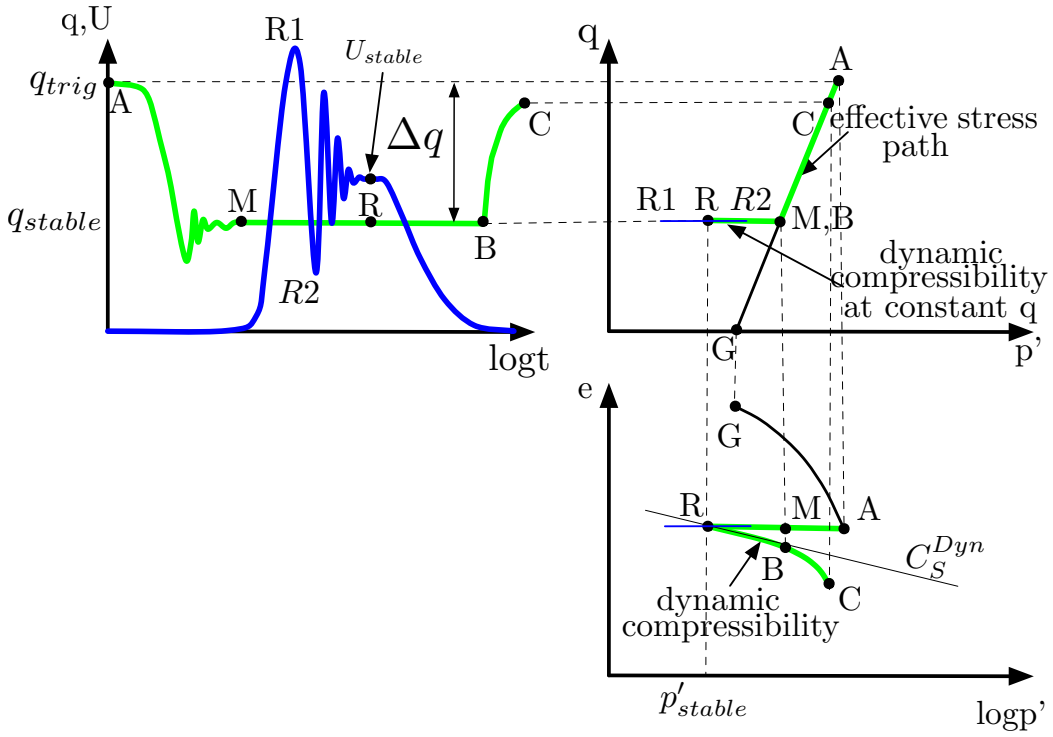

Figure 4.31: Description of stress path and dynamic consolidation of a stick-slip event on $q - p'$ plane.

lower than q_{trig} depending on the magnitude of SS. The larger the SS, the closer point M to p' axis. Following the drop of deviatoric stress q, pore pressure starts to raise up. This excess pore pressure causes a decline in effective pressure, hence p' reduces at constant q. As a result, the stress state moves horizontally apart from conventional stress path (towards the left side of stress path oriented from M to R). In details, p' actually has damped vibration horizontally at constant q_{stable} from R1 to R2 until it stabilises at p'_{stable} represented by point R. At point R (p'_{stable},q_{stable}), as the pore pressure begins the dissipation phase, U_{stable} decreases gradually leading to increasing p'. During this process q still remains at q_{stable}, the effective stress state keeps translating horizontally to the right, gets closer to the usual effective inclined stress path. When finishing the dissipation phase, as U returns to the static state before the event, the effective stress state meets the conventional CID stress path at point B. Subsequently the stick phase takes place with increasing q and the stress state again moves up along the stress path from B to C prior to the next slip. The projection of this behaviour on the (e-p')

plane is the dynamic compressibility of shearing behaviour RB, similar to the isotropic consolidation. In isotropic phase, the compressibility is characterised by C_c in loading and C_s in unloading and reloading. Previous publications identified these coefficients of CVP glass beads within 500 kPa as $C_c \approx C_s = 0.012 \div 0.021$ (33).

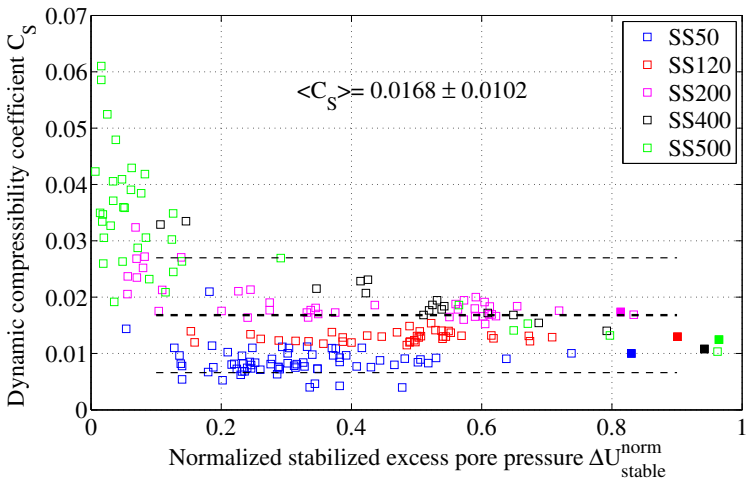

Figure 4.32: Compressibility of individual test in both isotropic and triaxial compression and relation between C_s and ΔU^{norm}_{stable}.

Figure 4.32 gives the relation between C_s and ΔU^{norm}_{stable}. Excepting for test N500 with numerous small SSs and noisy measurements resulting in large scatter of data, the remaining tests show small fluctuations of C_s around a mean $< C_s > = 0.0168 \pm 0.0102$, approximately close to C_s under isotropic state in the range of 0.011 to 0.02. It can be considered that the dynamic compressibility at constant deviatoric stress q_{stable} is similar to the static compressibility at isotropic state. The only difference is the duration of the process.

4.4.7 Effect of confining pressure p'_0 and initial void ratio e_c on boundary surface of stabilised state on $p' - q$ plane

On p'-q plane according to soil mechanics, the critical state line (CSL) is defined by the line $q = M{*}p'$ where $M = q/(p' + q/3)$. The stabilised states of all SSs at different confining pressure p'_0 are presented together in figure 4.33. CSL line is the limit of all stress paths of granular materials under various loading condition meaning every state at any moment during both global quasi static shearing and dynamic SS events, the stress

state of sample cannot exceed the CSL. For each p'_0 the stabilised stress states determine a separate boundary representing the position of effective mean pressure created by ΔU on the effective stress plane. The existence of this boundary surface in which the effective stress path cannot cross implies that liquefaction (p'_{stable}, q_{stable}) = (0,0) can occur only for $q_{stable} = 0$ or $\Delta q_{norm} = 1$ meaning only the first SS can liquefy.

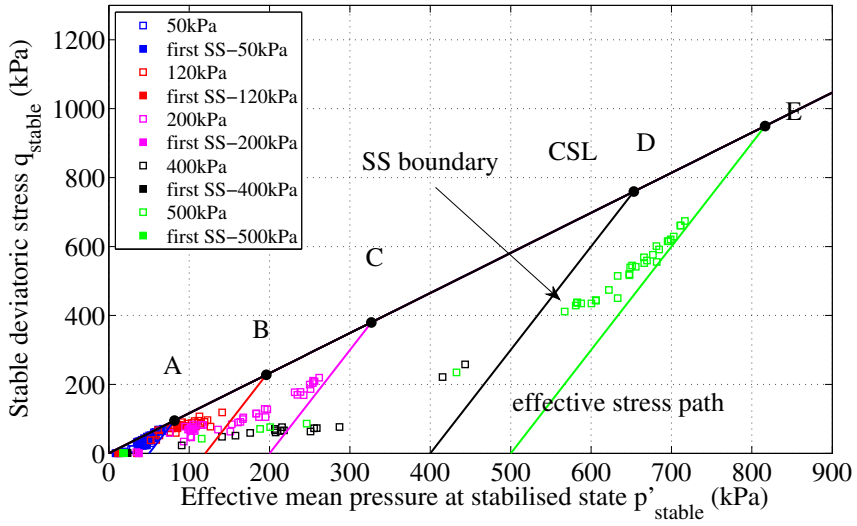

Figure 4.33: Behavior at stabilised stress state in $(p' - q)$ plane.

All curves share the same form with different scaling parameters. To exclude the effect of confining pressures p'_0, a normalisation method is applied again by critical effective stress (p'_{crit},q_{crit}) at the points where the conventional CID stress path reaches the yielding surface which are the coordinates of point A, B ,C, D, E respectively in figure 4.33. p'_{crit} and q_{crit} are written as:

$$p'_{crit} = p_0 \frac{3}{3 - M}; q_{crit} = M * p'_{crit} \tag{4.12}$$

In which M is the frictional constant at critical state identified by global stress strain behaviour.

The equation determining the boundary surface should be a power law $y = x^a$ with power number $a > 1$, written as:

$$\frac{q_{stable}}{q_{crit}} = (\frac{p'_{stable}}{p'_{crit}})^a \tag{4.13}$$

Five curves are established separately in figures 4.34a to e and show the scatter when plotting together in figure 4.34f. The normalisation by e_c is performed again to

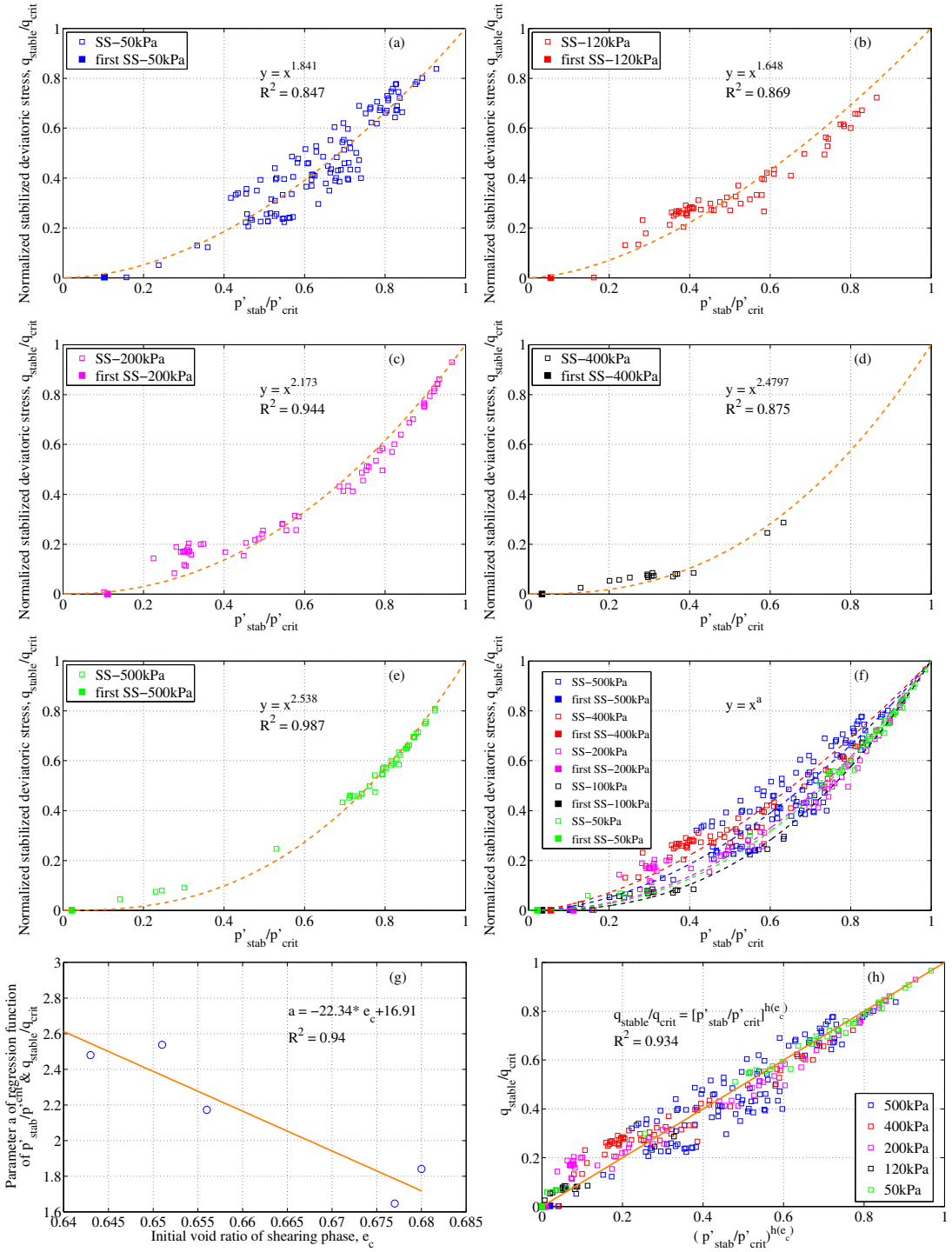

Figure 4.34: Boundary surface at different confining pressures p'_0 incorporated with the effect of void ratio e_c.

unify five presumably pressure-dependent behaviours in a unique master relation as a power law with very high $R^2 = 0.934$. So the unique boundary is identified by this equation with the uncoupling effect of void ratio e_c and p'_0 again:

$$\frac{q_{stable}}{q_{crit}} = \left(\frac{p'_{stable}}{p'_{crit}}\right)^{h(e_c)} \tag{4.14}$$

$$h(e_c) = -22.34\, e_c + 16.91 \tag{4.15}$$

4.4.8 Discussions

Commonly the global behaviors of stick-slip are characterised by the amplitude, the recurrence time of stick-slip events, and the distribution of amplitudes. Some possible factors affecting the global behavior of stick-slip have been assessed in this chapter including the confining pressure p'_0 and the initial void ratio e_c. The effects of p'_0, strain rate, size of particles and other factors have been widely studied. However, the dynamics of the slip phase is poorly understood. Consequently sensitive factor like e_c does not dominate clearly and is easily neglected. When the stick-slip is amplified as in loose and saturated media, combined with high resolution data, the effect of void ratio is facilitated to expose significantly. Furthermore the **unexpected collapses** in isotropic compression phase result in the **uncontrolled initial void ratio** at the beginning of shearing phase e_c. At first this can be seen as one of the disadvantages of the work, but with high quality data, the variation of input parameter e_c unveils the strongest effects on global and detailed behaviors.

In loose materials the impact of p'_0 is less overwhelming, however the combined and uncoupled effects of p'_0 and e_c are examined in this study. This uncoupled effects of p'_0 and e_c are quite popular in soil mechanics such as the study of elastic modulus at very small deformation (11, 49). The underestimated role of e_c now appears as the pronounced factor controlling mostly the functional behaviours with highly accurate relations presenting quantitative predictions. It shows the throughout dominant impacts in all quantitative relations. Anyway the factor controlling the distribution of amplitude of stick-slip is still missing. Still in loose material the existence of very large first stick-slips is an abnormally behavior compared to stick-slip in dry media. Its extremely large amplitude keeps the important role to reveal the transition from local to total failure. Its characteristics need to be inspected and compared to some

rare liquefactions occurring during the first stick-slip events to discover the possible controlled factors in chapter 5. The comprehensive conditions of the appearance of instabilities will be presented in chapter 5 after exploiting the complementary isotropic instabilities.

Regarding the dynamic aspect, the estimated inertial number $I \approx 10^{-3}$, three orders of magnitude smaller than the value of I for the quasi-static regime ($\approx 10^{-6}$) in stick phase, indicates a real dynamic character of slip phase. The dynamic behavior of pore pressure is an important link between local instabilities and liquefaction since it mostly connects to the whole measurements. The expected aim is to characterise the behaviour of pore pressure in which the first transient phase is characterised by the amplitude of ΔU_{max}, ΔU_{stable}, the frequency, its characteristic duration t_{trans} and Δt_{05} of the stabilised phase II. The dissipation phase III is represented by the consolidated coefficient C_v. The effort has been spent but not completed, the characteristic time is going to be connected to other kinds of instability in chapter 5 and the nature of the vibration frequency of U is still mysterious.

The striking point in anisotropic property of material has been analysed both in dynamic and static regime. It supported quantitative relations of $\Delta\varepsilon_1$ and $\Delta\varepsilon_{vol}$. The scatter of dynamical anisotropy coefficient i^{Dyn} and the presence of axial strain $\Delta\varepsilon_1$ in extension lead to questions on the resolution of our measuring devices which should be improved to get new insights and explanations. In fact, a preliminary study by fast camera has been conducted and has given some results. This reveals the real dynamic evolution of axial strain during very brief slip phase simultaneously with deviatoric stress drop, depicting a full stress-strain dynamics of slip phase. A global failure of the whole granular body is recognised and a non-homogeneous stress, strain field is observed.

Concerning the effective stress path, our new results indicated a common inside space where the effective stress state cannot exceed, namely the stick-slip boundary in p'-q plane, with a unified equation for all p'_0 and e_c.

Beside mechanical measurements, the existence of audible sound coupled with stick-slip events and the acoustic measurements presented in one typical SS also give a promising direction to find the still missing triggering mechanisms.

4.5 Conclusions

A high time-resolved study was performed to provide detailed behaviour inside stick-slip event, based on a set of drained isotropic and triaxial compression of normally consolidated model granular materials, complemented by a new set of static and dynamic pore pressure sensors to eliminate as much as possible the artefacts concerning the unexpected pore fluid pressure outburst.

The often overlooked drained isotropic compression is crucial to the precise determination of the void ratio e_c at the beginning of compressive triaxial compression. The **uncontrollability of** e_c due to the presence of numerous isotropic collapses during this mandatory drained isotropic compression stage simply wipes out the repeatability of stick-slip phenomenon in the subsequent drained triaxial compression.

This new set of experiments confirms the existence of very large and regular stick-slip in drained triaxial compression, with deviatoric stress drop down to the isotropic stress level; as well as the presence of unexpected pore fluid pressure surge at the beginning of every stick-slip event. As in isotropic collapse and liquefaction, this excess pore pressure is not the main causative mechanism for the stick-slip phenomenon since it always happens after the completion of deviatoric stress drop in the slip phase. It merely amplifies the development of axial and volumetric strains by reducing the effective stress. Furthermore, the similarity of pore pressure development in isotropic and triaxial instabilities points to the same triggering mechanisms; and its development in two-phase to the interpretation of the **slip phase as dynamic consolidation at constant deviatoric stress**.

Careful measurements and analyses reveal the **uncoupling effects of confining pressure** p'_0 **and void ratio** e_c on the mechanical behaviour on the level of individual stick-slip events, leading to consistent unified empirical relations with very strong correlations. Specifically, if deviatoric stress drop Δq and triggering stress q_{trig} are known then

(i) the normalised stabilised excess pore pressure ΔU^{norm}_{stable} can be roughly estimated from normalised deviatoric stress drop $\Delta q_{norm} = \frac{\Delta q}{q_{trig}}$ by equation 4.11,

(ii) the incremental axial strain $\Delta\varepsilon_1$ can be deduced by equation 4.9, based on ΔU^{norm}_{stable},

(iii) and the incremental volumetric strain $\Delta\varepsilon_{vol}$ is estimated equally from ΔU^{norm}_{stable} in equation 4.8.

(iv) the study revealed also a unique stress boundary in the effective stress plane by equation 4.14.

The time characteristics of dynamic pore pressure are established in quasi-static regime by one value scalar ΔU_{stable} as follows:

(i) the duration of the transient phase I, t_{trans}, is estimated from normalised stabilised mean pressure $\frac{p'_{stable}}{p'_{crit}}$ by equation 4.5, in which $\frac{p'_{stable}}{p'_{crit}}$ is function of stabilised excess pore pressure ΔU_{stable} and deviatoric stress drop Δq,

(ii) the duration of the negligible intermediate phase II, Δt_{05}, is estimated from $\frac{p'_{stable}}{p'_{crit}}$, by equation 4.6,

(iii) the duration of the dissipation phase III is characterised by C_v, evolving non-linearly with confining pressure p'_0. All the time characteristics and all coupling effects of pore pressure with stress, strain measurements showed the smooth and continuous evolution to final liquefaction failure.

Furthermore, the duration of deviatoric stress drop t^q_{drop} is revealed as a very brief and constant time around 2.254 ms regardless of confining pressure p'_0 from 50 to 500 kPa.

Unfortunately, the physics of the pore pressure buildup, its transient oscillation and triggering mechanisms are still missing. The current LVDT technique is also insufficient to resolve the dynamic evolution of axial and volumetric strain. Other techniques, i.e. fast stereoscopic cameras or laser displacement transducer can be used. Preliminary acoustic measurements point out some controlling parameters of the slip phase, potentially useful for the prediction of deviatoric stress drop Δq and triggering stress q_{trig} (chapter 6).

4. TIME-RESOLVED STUDY OF DRAINED COMPRESSION STICK-SLIP ON NORMALLY CONSOLIDATED STATE

5

Liquefaction of model granular material

5.1 Introduction

Beyond the well-known static and cyclic liquefaction under undrained conditions in granular mechanics, the serendipitous discovery of isotropic liquefaction under **drained isotropic compression** in our previous works (30, 34) on loose and fully saturated model materials raises many unanswered questions, experimentally, numerically and theoretically. Can we find new members of this family of liquefactions? With new and complementary results, do we have some evolutionary rules capable of transforming local instabilities (isotropic collapses and compression stick-slips) into global liquefaction failure? Can the pore fluid outburst, while definitively not a causative mechanism, specifically the short-lived stabilised excess pore pressure, be a key component controlling the mechanical parameters of the newly observed instabilities, using empirical correlations? And can we uncover the physical significance behind the three phases of the surprising pore pressure development?

Consequently, based on a new set of well-designed drained isotropic and triaxial compression testings, supplemented by a new set of pore pressure and passive acoustic sensors, this chapter aims (i) to replicate the previously reported liquefactions below 500 kPa of effective confining pressure with new and better results, (ii) to extend the unexpected isotropic liquefaction to quasi-saturated sample and (iii) to explore the uncharted domain. In particular, we will try to understand the underlying physical

mechanisms and the appearance conditions of these instabilities.

5.2 Notation

To follow subsequent contents, all parameters used in this chapter are described on figure 5.1. In this diagram the blue curve is the evolution of pore pressure during collapse

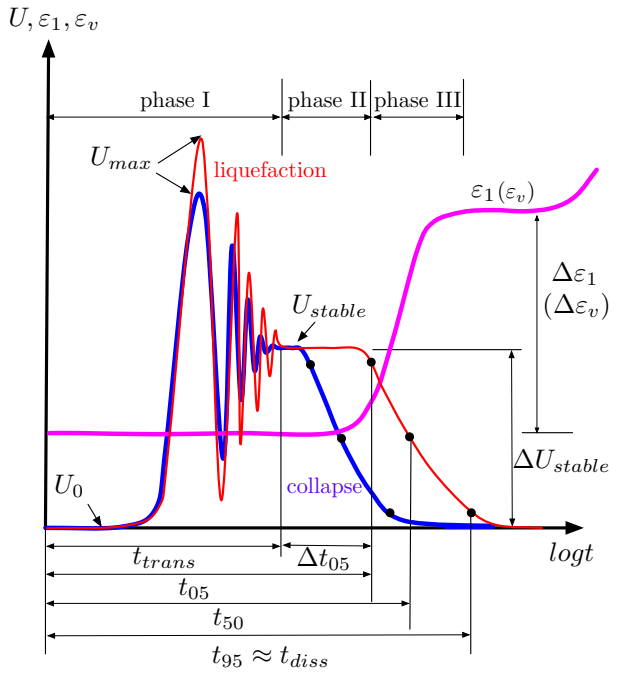

Figure 5.1: Schematic diagram of measurements within the study.

event and the red one during liquefaction. They are two independent instabilities but to have an intuitive comparison on the stabilised state it is simply assumed that the collapse and liquefaction have the same transient phase I and the same magnitude of stabilised excess pore pressure. The main difference between them depends on phase II. The magenta curve represents the development of axial strain ε_1 as well as volumetric strain ε_{vol}. The parameters used in this study are defined as follows:

U_0 : back pressure (kPa)

U_{max} : pore pressure at the peak of vibration phase (kPa)

U_{stable} : stabilised pore pressure (kPa)

$\Delta U_{stable} = U_{stable}$ - U_0 : stabilised excess pore pressure (kPa)

$\Delta U_{max} = U_{max}$ - U_0 : maximum excess pore pressure (kPa)

$\Delta U^{norm} = \frac{\Delta U}{\Delta U_{stable}}$: normalised excess pore pressure by ΔU_{stable}

$\sigma_{trig} = p$: triggering total stress, the total confining stress p at the occurrence of the instability (kPa)

$\sigma'_{trig} = \sigma_{trig}$ - U : effective triggering stress (kPa)

$\Delta U^{norm}_{stable} = \frac{\Delta U_{stable}}{\sigma_{trig}}$: normalised stabilised excess pore pressure by triggering stress σ_{trig}

$\Delta U^{norm}_{max} = \frac{\Delta U_{max}}{\sigma_{trig}}$: normalised maximum excess pore pressure by triggering stress σ_{trig}

$\Delta\varepsilon_1$: incremental axial strain (%)

$\Delta\varepsilon_v$: incremental volumetric strain (%)

t_{trans} : duration of the transient vibration phase of pore pressure counted from the origin of pore pressure development (s)

t_{05}, t_{50}, t_{95} : duration from the origin of pore pressure surge to the moment when excess pore pressure dissipates the amount of 5%, 50%, 95% of ΔU_{stable} (s). The amount of 5%, 95% are recommended due to their acceptable errors of 5% while those at 1%, 99% are difficult to identify.

$\Delta t_{05} = t_{05}$ - t_{trans} : duration of stabilised phase II (s)

$t_{100} = t_{diss}$: duration of excess pore pressure to totally dissipate (s), in soil mechanics $t_{diss} \approx t_{95}$

k_{diss} : slope of pore pressure dissipation phase (kPa/s)

k^{norm}_{diss} : slope of normalized pore pressure dissipation phase (1/s).

5.3 Experimental information

This first series, called Liquefaction series, essentially consists of liquefaction events mostly in saturated condition but under different loadings (isotropic and triaxial compression) and different drainage conditions (drained and undrained). In most cases, virgin CVP 0.7 mm beads were used excepting few rare cases with used beads or virgin CVP 0.4 mm beads (test IL3) to provide extended assessments in various conditions. Essential information are given in table 5.2. During very long testing procedure of a single test, different failures are generated in various situations. The essential basic steps at which the sample is likely to experience failures are in table 5.1. After the

fabrication, CO_2 is injected into the sample with gradient pressure of 0.2 kPa under 10 kPa of confining pressure, there has been no failure acquired. In subsequent **water imbibition** to gradually raise the water level inside the specimen, it is likely to liquefy once the sample is totally filled with desired water, namely WL for water imbibition liquefaction. During the night of very slow **flushing of water** through the specimen, the failure is called FL for flushing liquefaction. Another situation that can leads to liquefaction is the application of **back pressure** U_0, it is named BL for back pressure liquefaction. During the measurement of Skempton coefficient B, no global failure has been detected within our study. Under isotropic consolidation, the usual **isotropic liquefaction** is abbreviated by IL. In the last stage of shearing, if drainage is allowed, failure can occur at the first SS event called **SS liquefaction** SL. In case of **undrained condition, liquefaction** is called UL for undrained static liquefaction. Consequently liquefaction do happen in nearly all steps of the fabrication process.

Table 5.1: Nomenclatures of liquefaction corresponding to different stages of test.

CO_2	Water imbibition	Flushing overnight	Back pressure	Drained isotropic compression	Drained triaxial compression	Undrained triaxial compression
-	WL	FL	BL	IL	SL	UL

Note that not most tests are fully saturated, verified by Skempton's coefficient B $\geqslant$ 0.95. In table 5.2, the lowest B within this series is 0.88. N is the number of re-use of glass beads, N = 1 means virgin material, 'a' means the beads used to experience one global failure at very low confining stress (less than 20 kPa) at some preparation steps before main stage of loading, such as imbibition process, application of back pressure, etc. N = 2 means material liquefied once in main loading phase before. σ'_{trig} is triggering stress ranging from 30 kPa to 400 kPa.

Within this series, test IL_{03} is a rare recorded liquefaction occurring with small beads of 400 μm. Its presence strengthened the validity of the phenomenon. The unique stick-slip liquefactions SL_{01} is another special case which happened at the first compression stick-slip (SS) with the material already liquefied once under drained isotropic loading (IL_{09}). The first liquefaction happened isotropically in test IL_{09} at 134.5 kPa then the material liquefied again under triaxial drained compression shear at confining

pressure of 200 kPa of test SL_{01}. This very rare case of double liquefaction means that liquefaction can occur on already liquefied soils. While the remaining liquefaction cases in the series are the events occurring only with virgin material. The behaviours of excess pore pressure during collapse and liquefaction are primarily distinguished by the duration of the stabilised phase II. Therefore the basic measurements of the phase II are introduced including t_{05}, t_{50}, t_{diss} (s) which are respectively the duration from the origin of pore pressure to the moment when excess pore pressure dissipates the amount of 5%, 50%, 95% of stabilised excess pore pressure ΔU_{stable}. The characteristics of phase III is the slope of the pore pressure in time, k_{diss} is in the last column. Due to some technical problems in the development of the acquisition system, few liquefactions have no full data, as tests IL_{07} and IL_{13}.

Additionally, the second series, namely Collapse series, including 56 isotropic collapse events are added to explore the link between the local instability of the Collapse series and the global liquefaction of the Liquefaction series. The data of stick-slip (SS) events from CIDNC series (chapter 4) can be sometimes used to compare and prove the link between stick-slip as local instability and stick-slip liquefaction as the global one under shear loads. The parameters of the Collapse series are presented in table 5.3. The last column indicates necessary information to recognize the origin of the studied collapse. For instance, CIDNC is normally consolidated drained shearing test, N500 is the test of the CIDNC series with confining pressure p'_0 of 500 kPa which is analysed in chapter 4. CIDOC represents the overconsolidated drained shearing tests in which the sample experiences the fixed maximum pressure of 500 kPa then unloaded to targeted effective confining pressure p'_0. For example CIDOC400 means overconsolidated drained shearing test with $p'_0 = 400$ kPa. CIUNC500 means undrained shearing test for normally consolidated (NC) sample at 500 kPa. CIUOC400 undrained shearing test for overconsolidated (OC) sample at 400 kPa. IL_{01} means that this current collapse is from the test isotropic liquefaction IL_{01} of the Liquefaction series. It can be seen all collapses belonging to the core series of this thesis and additional collapses of other tests are explored together. This improves the validity of the results. Though these collapses belong to different tests under different conditions but substantially all collapse events are under the same type of drained isotropic loading, excepting $Coll_{49}$ highlighted by red which is an extremely large collapse under unloading condition. It is very helpful

Table 5.2: Summarized characteristics of liquefaction tests in the Liquefaction series.

Drained isotropic compression											
	Test	B	N	σ'_{trig} (kPa)	e_{trig}	e_{20}	t_{trans} (s)	t_{05} (s)	t_{50} (s)	t_{diss} (s)	k_{diss} (kPa/s)
1	IL_{01}	0.98	1	212	0.680	0.707	0.246	2.922	4.054	6.302	1151.79
2	IL_{02}	0.99	1	152	0.696	0.708	0.259	7.348	8.869	12.87	1261.96
3	**IL_{03}***	**0.88**	1	**418.2**	0.728	0.745	0.428	2.53	3.333	5.617	2111.33
4	IL_{04}	0.99	1	330.8	0.666	0.693	0.266	1.805	3.061	5.034	1447.93
5	IL_{05}	0.94	1	252	0.672	0.686	0.148	1.308	2.778	5.725	912.35
6	IL_{06}	0.99	1	315.7	0.678	0.699	0.170	2.424	3.823	6.861	1529.48
7	IL_{07}	0.9	1	98.26	0.695	0.702	0.532				
8	IL_{08}	0.99	1	203.4	0.675	0.696	0.243	2.278	4.033	8.849	1091.75
9	IL_{09}	**0.88**	1	134.5	0.680	0.700	0.493	2.306	3.83	8.922	579.18
10	IL_{10}	0.98	1a	154.1	0.672	0.683	0.224	2.985	4.67	8.991	818.77
11	IL_{11}	0.98	1a	69.67	0.677	0.682	0.142	9.221	12.21	21.68	444.50
12	IL_{12}	1.00	1	47.54	0.685	0.688	0.202	38.94	50.665	81.19	312.30
13	IL_{13}	0.92	1	52.7	0.691	0.695	0.617	29.99			
14	IL_{14}	0.94	1a	71.73			0.609	7.391	10.27	24.37	382.32
15	IL_{15}	0.97	1	**29.88**	0.698	0.697	0.115	36.34	43.14	56.67	263.25
16	IL_{16}	0.99	1	35.78	0.686	0.687	0.132	18.61	24.42	42.63	230.16
17	IL_{17}	0.99	1a	383.9	0.666	0.695	0.202	1.502	2.742	8.918	1302.98
Drained triaxial compression shearing (CID)											
	Test	B	N	p_0	e_{trig}	e_{20}	t_{trans}	t_{05}	t_{50}	t_{diss}	k_{diss}
1	SL_{01}	0.89	**2**	200	0.672	0.694	0.489	1.691	2.871	8.698	562.76
2	SL_{02}	**0.97**	1	50	0.708	0.711	0.151	141.2	191.8	359.6	241.87
Undrained triaxial compression shearing (CIU)											
	Test	B	N	p_0	e_{trig}	e_{20}	t_{trans}	t_{05}	t_{50}	t_{diss}	
1	UL_{01}	0.98	1	100	0.674	0.679	0.144				
2	UL_{02}	0.97	1	50	0.673	0.676	0.365				
Application of back pressure											
	Test	B	N	σ'_{trig}	U_{back}	e_{20}	t_{trans}	t_{05}	t_{50}	t_{diss}	
1	BL_{01}		1	32	31	0.717	0.485				
2	BL_{02}		1	42	52	0.677	0.500				
Water imbibition											
	Test	B	N	σ_3	ΔU_{stable}	e_{fabric}	t_{trans}	t_{05}	t_{50}	t_{diss}	
1	WL_{01}		1	20	0.5	0.714	0.198				
Water flushing											
	Test	B	N	σ_3	ΔU_{stable}	e_{fabric}	t_{trans}	t_{05}	t_{50}	t_{diss}	
1	FL_{01}		1	12.3	6.75	0.733	3.100				

Table 5.3: Summarized characteristics of isotropic collapses.

	Test	N	B	e_{20}	e_{trig}	σ'_{trig} (kPa)	ΔU_{stable} (kPa)	Information
1	$Coll_{01}$	1	0.99	0.682	0.673	108.2	35.4	CIDNC. Test T1. no V. M. G
2	$Coll_{02}$	1	0.99	0.682	0.666	187.7	104.5	CIDNC. Test T1. no V. M. G
3	$Coll_{03}$	1	0.99	0.682	0.644	446.8	305.8	CIDNC. Test T1. no V. M. G
4	$Coll_{04}$	2	0.95	0.700	0.691	108.2	70.5	CIDNC. test T2
5	$Coll_{05}$	2	0.95	0.700	0.681	133.7	73.5	CIDNC. test T2
6	$Coll_{06}$	2	0.95	0.700	0.647	475.6	391.5	CIDNC. test T2
7	$Coll_{07}$	3	0.99	0.696	0.689	79.7	33.3	CIDNC. test T3
8	$Coll_{08}$	3	0.99	0.696	0.684	101.8	70.9	CIDNC. test T3
9	$Coll_{09}$	3	0.99	0.696	0.667	140.9	61.2	CIDNC. test T3
10	$Coll_{10}$	1	0.87	0.663	0.660	55.4	25.1	CIDNC. test T5
11	$Coll_{11}$	1	0.87	0.663	0.651	137.2	2.6	CIDNC. test T5
12	$Coll_{12}$	1	0.87	0.663	0.649	195.4	154.0	CIDNC. test T5
13	$Coll_{13}$	1	0.98	0.676	0.669	95.7	67.0	CIDNC. N500
14	$Coll_{14}$	1a	0.86	0.687	0.684	51.3	31.5	CIDNC. N400
15	$Coll_{15}$	1a	0.86	0.687	0.673	160.0	110.0	CIDNC. N400
16	$Coll_{16}$	1a	0.86	0.687	0.655	292.9	220.1	CIDNC. N400
17	$Coll_{17}$	2	0.98	0.687	0.683	52.0	30.7	CIDNC
18	$Coll_{18}$	2	0.98	0.687	0.677	68.6	45.8	CIDNC
19	$Coll_{19}$	2	0.98	0.687	0.663	147.6	97.4	CIDNC
20	$Coll_{20}$	2	0.98	0.687	0.659	146.0	104.0	CIDNC
21	$Coll_{21}$	2	0.98	0.687	0.646	255.3	157.0	CIDNC
22	$Coll_{22}$	1a	0.99	0.685	0.679	77.2	51.2	CIDNC. N200
23	$Coll_{23}$	1a	0.99	0.685	0.664	138.1	102.7	CIDNC. N200
24	$Coll_{24}$	1a	0.98	0.684	0.681	85.4	67.9	CIDOC400
25	$Coll_{25}$	1a	0.98	0.684	0.670	101.9	80.0	CIDOC400
26	$Coll_{26}$	1a	0.98	0.684	0.659	170.4	144.6	CIDOC400
27	$Coll_{27}$	1	0.91	0.725	0.718	88.7	73.8	CIDOC200
28	$Coll_{28}$	1	0.91	0.725	0.705	158.4	117.7	CIDOC200
29	$Coll_{29}$	1	0.99	0.678	0.673	65.8	48.6	CIDOC100
30	$Coll_{30}$	1	0.99	0.678	0.660	186.9	179.1	CIDOC100
31	$Coll_{31}$	1	0.96	0.686	0.683	41.6	24.4	CIDOC50
32	$Coll_{32}$	1	0.96	0.686	0.677	60.7	39.6	CIDOC50
33	$Coll_{33}$	1	0.96	0.686	0.671	82.1	56.6	CIDOC50
34	$Coll_{34}$	1	0.96	0.686	0.658	241.1	200.5	CIDOC50, no V,M,G
35	$Coll_{35}$	1a	0.98	0.686	0.679	90.1	64.7	CIUNC500, no V,M,G
36	$Coll_{36}$	1	0.95	0.677	0.670	88.7	69.5	CIUNC400, no V,M,G
37	$Coll_{37}$	1	0.95	0.677	0.660	141.4	133.1	CIUNC400, no V,M,G
38	$Coll_{38}$	1	0.95	0.677	0.640	344.5	271.5	CIUNC400, no V,M,G
39	$Coll_{39}$	1a	0.98	0.678	0.670	124.1	110.4	CIUOC200
40	$Coll_{40}$	1a	0.98	0.678	0.651	360.1	321.2	CIUOC200
41	$Coll_{41}$	2	0.99	0.687	0.682	58.5	45.4	CIUOC100
42	$Coll_{42}$	2	0.99	0.687	0.679	52.4	40.9	CIUOC100
43	$Coll_{43}$	2	0.99	0.687	0.673	56.3	36.3	CIUOC100
44	$Coll_{44}$	2	0.99	0.687	0.664	92.6	70.2	CIUOC100
45	$Coll_{45}$	2	0.99	0.687	0.654	129.5	75.1	CIUOC100
46	$Coll_{46}$	2	0.99	0.687	0.643	308.8	240.2	CIUOC100
47	$Coll_{47}$	1a	1.00	0.674	0.669	74.2	52.8	CIUOC50
48	$Coll_{48}$	1a	1.00	0.674	0.662	102.4	87.5	CIUOC50
49	**$Coll_{49}$**	1a	1.00	0.674	0.644	440.9	439.5	CIUOC50, extremely large unloading collapse
50	$Coll_{50}$	1	0.98	0.707	0.702	57.1	42.4	IL_{01}
51	$Coll_{51}$	1	0.98	0.707	0.693	92.6	66.8	IL_{01}
52	$Coll_{52}$	1	0.99	0.693	0.682	126.7	102.8	IL4
53	$Coll_{53}$	1	0.99	0.699	0.697	31.6	13.1	IL6
54	$Coll_{54}$	1	0.99	0.696	0.693	42.7	33.4	IL8
55	$Coll_{55}$	1	0.99	0.696	0.688	43.2	26.7	IL8
56	$Coll_{56}$	1	0.88	0.700	0.692	127.8	103.8	IL9

to identify the transition from local instability to a global liquefaction in forthcoming sections.

5.4 Testing results

5.4.1 Global behaviour

5.4.1.1 Isotropic liquefaction (IL)

In isotropic consolidation, the compressibility behaviour is delineated in the conventional compressibility e-log(p) plane as in figure 5.2. One typical test IL_{01} is presented in figure 5.2a, the sample is isotropically compressed from 20 kPa following the blue arrow up to particular targeted confining pressure p'_0. Generally on the way to reach p'_0, instead of a continuous evolution of void ratio e in decreasing with stress like the realistic geo-materials, the behaviour is interrupted by numerous collapses and occasionally a final liquefaction can occur at unpredictable triggering stress σ'_{trig}. The existence of isotropic liquefaction is unanticipated for a slowly compressed experiment of about 1 kPa/s under full drainage condition. For over hundreds of test, only 17 isotropic liquefactions have been collected. Each collapse such as $Coll_{50}$ or $Coll_{51}$ in test IL_{01} is characterised by a sudden surge of pore pressure resulting in the release of effective stress accompanied by a drop of void ratio Δe. The dashed blue curve is the behaviour acquired by slow data acquisition system. The superimposed red curve is the one acquired by fast acquisition system which is globally coherent with the slow data. Furthermore, adequate acquisition system also reveals the complex behaviour of effective stress σ' during collapse events including the oscillation of σ' at constant void ratio. Subsequently the effective stress σ' gradually recovers to reach the level prior to the collapse event.

Separately, the different features of the liquefaction event IL_{01} are depicted by an extremely large drop of void ratio Δe, a negative peak of effective stress and a vanishing effective stress, illustrated by zero mean effective pressure in the linear scale (appendix C2).

Other collapse and liquefaction events in 17 tests of the series are presented individually in figures 5.2b to q. Only slow data is introduced since the purpose here is to have a global view on the random appearance of liquefaction and collapse. The initial void ratio e_{20}, the triggering stress σ'_{trig} and the number of collapses preceding liquefaction

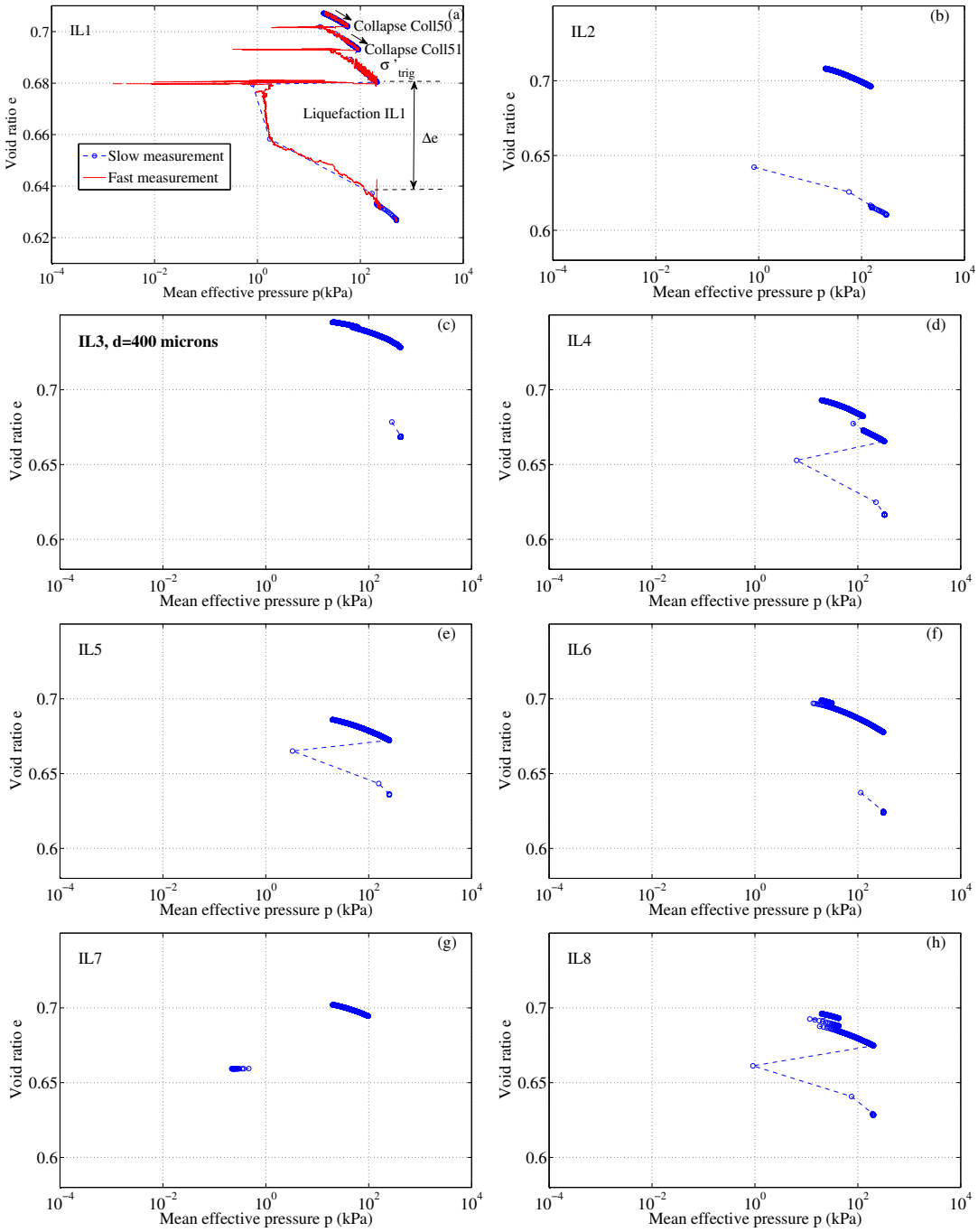

Figure 5.2: Compressibility behaviour in isotropic liquefaction from Test IL_{01} to IL_{08}.

are all uncontrolled. Specifically, the triggering stress σ'_{trig} distributes in a wide rage of magnitude within the investigated range of confining pressure up to 500 kPa. The

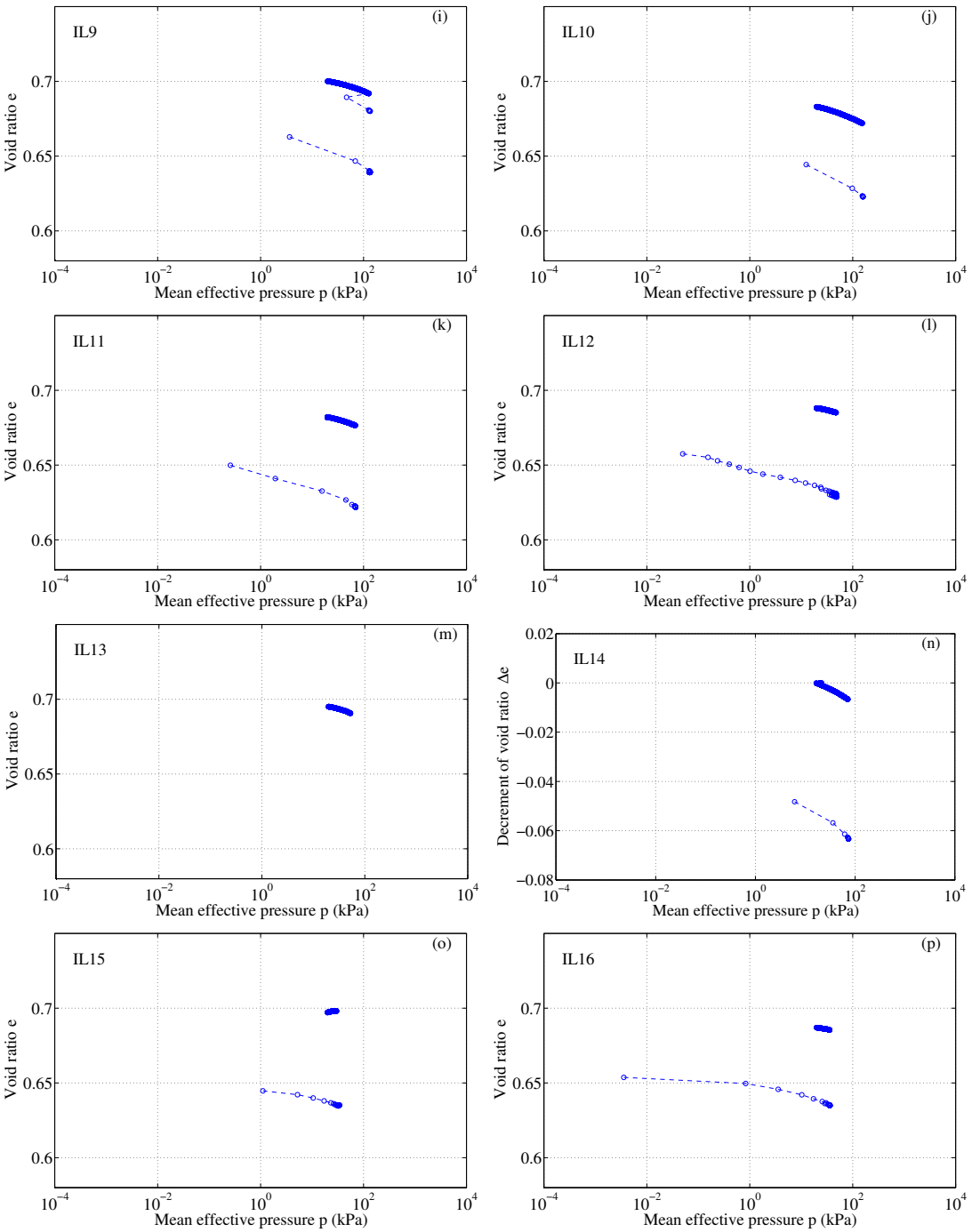

Figure 5.2: Compressibility behaviour in isotropic liquefaction (cont, from test IL_{09} to IL_{16}).

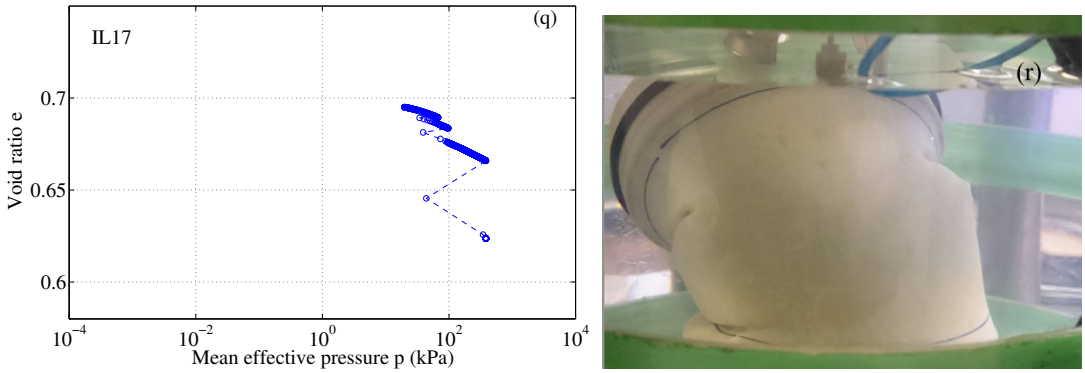

Figure 5.2: Compressibility behaviour in isotropic liquefaction (cont, test IL_{17}).

minimum σ'_{trig} is 30 kPa and the maximum σ'_{trig} is 418 kPa. The distribution of σ'_{trig} is far away from normal gaussian distribution (see appendix C1). This is due to the insufficient number of liquefaction events to get significant statistics. One observation on the number of collapse events within a single test is that there are no more than five isotropic collapses happening before liquefaction. This leads to a notice on the triggering void ratio e_{trig} of liquefaction which will be explored in section 5.5.1.

Among 17 isotropic liquefactions, one rare event, IL3, happens with glass beads of 0.4 mm of diameter in figure 5.2c. One typical picture of the sample experienced liquefaction failure is presented in figure 5.2r. During collapses, smaller drop of void ratio Δe results in the maintaining of the cylindrical shape of the sample. While during liquefaction, the distinct large Δe is equivalent to the global failure of the sample as in figure 5.2r with the destruction of the sample shape.

5.4.1.2 Drained stick-slip liquefaction (SL)

After isotropic consolidation phase, if no liquefaction happens the sample undergoes drained triaxial shearing phase and in some rare cases, instead of experiencing numerous successive SS events, the sample liquefies right at the first stick-slip, named stick-slip liquefaction SL.

Figure 5.3a shows the traditional stress strain behaviour under drained compression shear in which SS_{01} occurs at triggering deviatoric stress of 127 kPa with total drop of stress to zero and creates a very large jump of axial strain up to $\varepsilon_1 = 17.4\%$. Coupling with the stress drop is a single jump of volumetric strain ε_{vol} (figure 5.3b) up to 2.2%

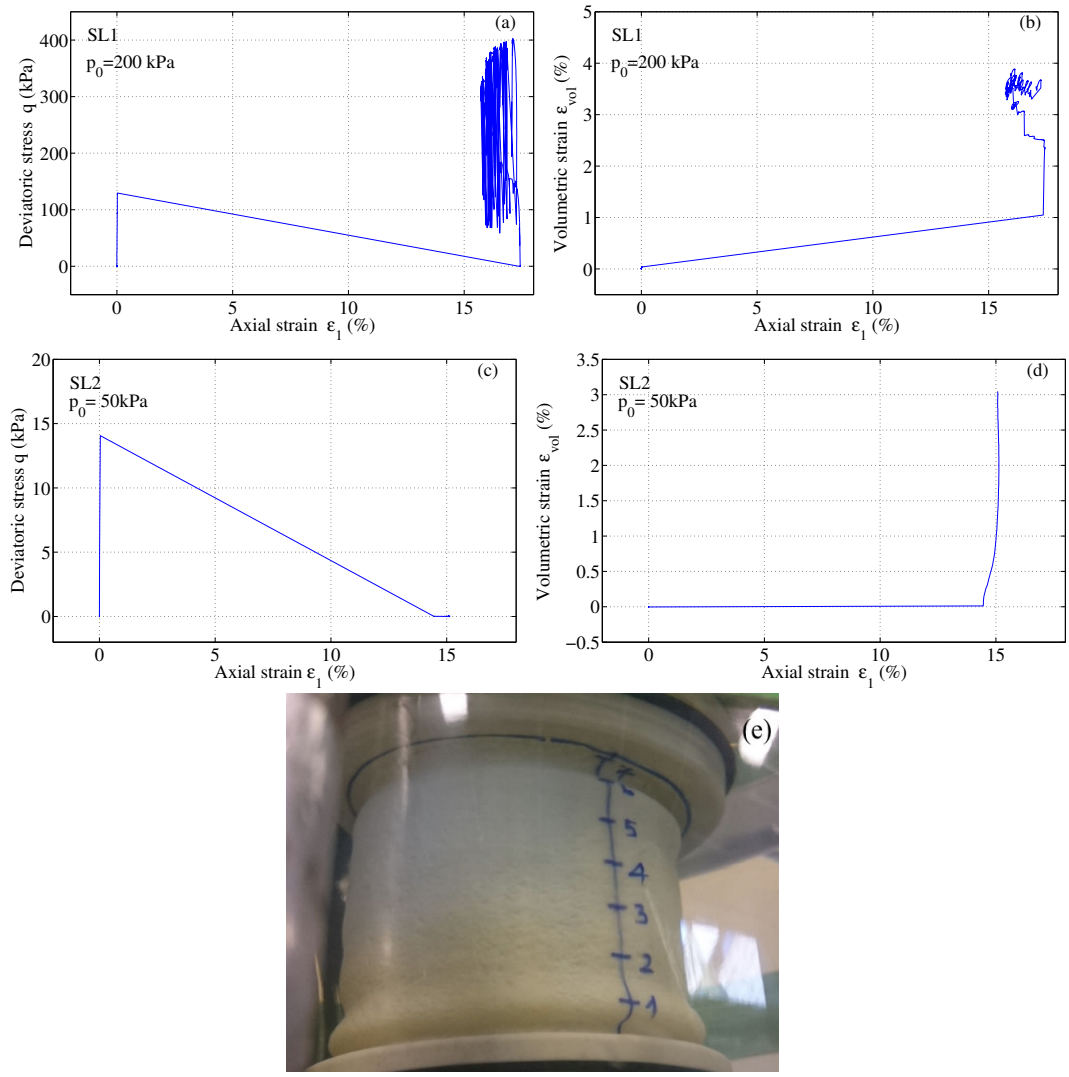

Figure 5.3: Global behaviour in stick-slip liquefaction: Stress-strain behaviour and volumetric strain behaviour of test SL_{01} at confining pressure $p_0 = 200$ kPa (a,b), test SL_{02} at $p_0 = 50$ kPa (c,d), illustration of the failure deformation after stick-slip liquefaction SL_{01} (e).

corresponding to the liquefaction state. In test SL_{01} at 200 kPa of confining pressure, after stick-slip liquefaction event, instead of the normal response, the sample totally falls down as in isotropic liquefaction (figure 5.2r). The sample still maintains the upright configuration but generates many pockets full of water or bellies around the circumference (figure 5.3e). The top cap is titled, the lower position of the top cap is touched by the LVDT, the higher one is opposite. Then the loading ram keeps moving

downward and gradually distributes the deformation of the top cap to balance it again. Therefore, the lower part of top cap rises up creating the extension axial strain in some subsequent SS events.

In test SL_{02} at confining pressure of 50 kPa (figure 5.3c,d), when stick-slip liquefaction occurs at the first stick-slip with triggering deviatoric stress of 14.0 kPa, the sample does not keep its cylindrical geometry. The test has been stopped at the axial strain $\varepsilon_1 = 14.4\%$. Only two stick-slip liquefaction events SL_{01} and SL_{02} are examined, other SSs after SL_{01} are ignored. In both tests SL_{01} and SL_{02}, the deviatoric stress totally drops to zero similar to many first large SSs within CIDNC series. The forthcoming detailed behaviours will reveal the differences.

5.4.1.3 Undrained static liquefaction (UL)

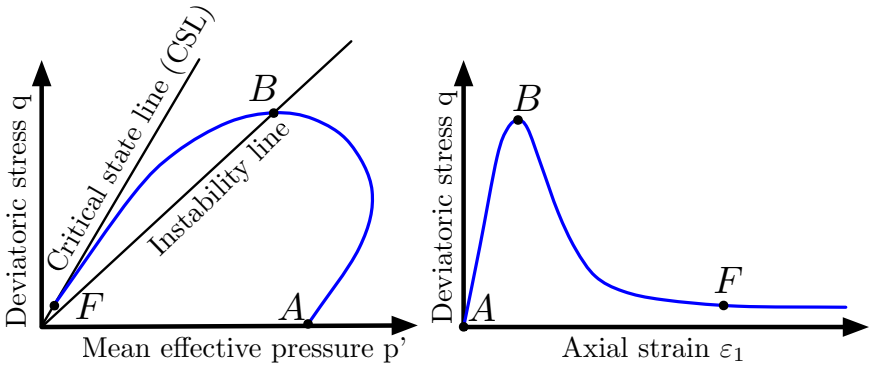

Figure 5.4: Static liquefaction of soil in the literature.

In undrained shearing the effective stress path for soil is illustrated in figure 5.4. Point A in q-p' plane represents the ending state of previous isotropic consolidation phase at a specific effective confining pressure $p'_0 = p'_A$ and $q = 0$. This ending point A is also the starting one for undrained compression shearing phase. In case of very loose material, the material contracts leading to positive excess pore pressure equivalent to the decrease of p' to the deviatoric peak B with small axial strain ε_1. At point B the sample reaches the unstable state located on the instability line, the shearing strength of sample declines sharply, p' moves from B toward the origin of q-p' plane. At point F the sample reaches the steady state of deformation and, in some rare cases, ε_1 quickly develops from around 1% to more than 20% as the pore pressure approaches the initial

effective confining pressure p'_0. Point F exhibits the static liquefaction in the literature.

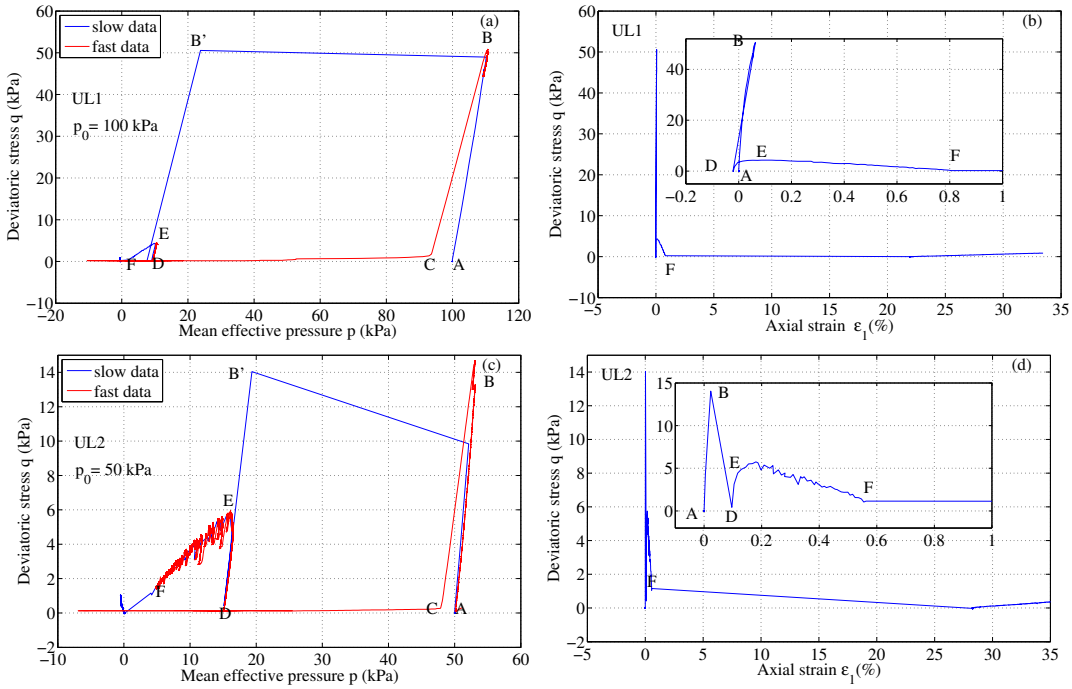

Figure 5.5: Global behaviour in static liquefaction of test UL_{01} (a,b) and UL_{02} (c,d).

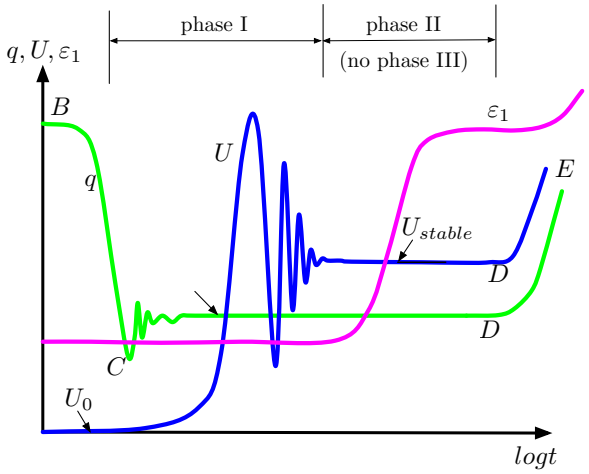

Figure 5.6: Scheme of the time evolution of deviatoric stress q, pore pressure U and axial ε_1 during undrained stick-slip.

For model granular material, the smooth undrained behaviour is also interrupted by

SS events. Specifically in figures 5.5a,c the well-known effective stress path still globally moves backward from p'_0 at point A, to the origin of the q-p' plane but both two tests UL_{01} and UL_{02} experienced the first large SS creating a drop of q from the peak B to point C representing the slip phase of SS1, followed by the stick phase from point D to E. After these two large SSs, the sample keeps undergoing shear load from E to F with plenty of subsequent smaller SS events on the traditional effective stress path moving close to the origin. At point F of the steady state of deformation (figures 5.5b,d), axial strain ε_1 fastly jumps up to 25%. The behaviour at point F represents the traditional static liquefaction and will be analysed while ignoring other undrained SS events within the portion EF. The distinction of static liquefaction UL and SS liquefaction SL as well as isotropic liquefaction IL is the low magnitude of triggering stress σ'_{trig} in case of static liquefaction UL. Particularly, σ'_{trig} in test UL_{01} and UL_{02} is only 2.12 and 3.85 kPa respectively. Similar to the drained condition in which liquefaction can happen in the first slip due to $\sigma' = 0$ and its long duration of phase III, liquefaction can also happen in the first slip at point C in undrained condition. At this point, it provides the equalisation of confining pressure by stabilised excess pore pressure ΔU_{stable} at the end of the transient phase I (figure 5.6). The undrained condition inhibits the dissipation of pore pressure in phase III. However, for our very limited undrained series, the dynamic undrained liquefaction at the first slip has never been observed since the stabilised excess pore pressure ΔU_{stable} never approached the confining pressure p'_0 resulting in a positive mean effective pressure p' at point D and undrained stick-slip behaviour afterwards at point E.

Note the wrong effective stress path ABB'D from the usual slow data acquisition system of 0.5 Hz in figures 5.5a,c, since the ephemeral point B' gives an inconsistently large frictional angle ϕ' as in the case of drained loading. The correct effective stress path ABCD is obtained by the adequate sampling rate above 1 kHz. The slow data missed the dynamic behaviour of pore pressure resulting in differences in the effective mean pressure. The insets in the stress-strain behaviour are provided in figures 5.5b,d to show the detailed stress-strain relation from the beginning A to the static liquefaction state F in which test UL_{01} exhibits the extension axial strain in the first SS event. Similar to other drained SSs in chapter 4, the extension axial strain during undrained SS can be explained by the inhomogeneous strain state within the assembly leading to the unbalance of the sample top cap after the event. These insets also show the

traditional smooth stress-strain response BF of soil (figure 5.4) is interrupted by large first SS and numerous subsequent small SSs.

5.4.2 Anatomy of typical liquefaction and collapse behaviour

After this global view on the occurrence of various kinds of liquefaction, the detailed remaining measurements are presented for each kind of liquefaction, showing the differences and similarities between them.

5.4.2.1 Isotropic liquefaction (IL)

Figure 5.7 shows, for an individual drained isotropic liquefaction event, IL5, the temporal evolution of normalised stabilised excess pore pressure ΔU^{norm}, incremental volumetric strain $\Delta\varepsilon_v$, incremental axial strain $\Delta\varepsilon_1$, vertical top cap acceleration G and lateral sound pressure M as well as lateral vibration V.

As stated in previous works, ΔU^{norm} has a 3-phase behaviour with special long phase II that distinguishes liquefaction from other local instabilities (stick-slip and collapses). The inferred liquefaction point (red solid circle) indicates the amplitude of stabilised excess pore pressure ΔU_{stable} reaching an effective confining pressure p'_0 at 252 kPa. Consequently at this liquefaction point and for the whole stabilised phase II, ΔU^{norm} equals 1 and $\sigma' \approx 0$. The incremental volumetric and axial strain $\Delta\varepsilon_v$, $\Delta\varepsilon_1$ develop rapidly after ΔU^{norm} as usual with extremely large amplitudes. The occurrence of vertical acceleration G at 2 ms prior to ΔU^{norm} suggests some perturbations of grain skeleton as a plausible cause of the liquefaction. The negative G is consistent with contractive $\Delta\varepsilon_1$, as well as three subsequent signals of G coincide the three aftershocks of ΔU^{norm} taking place around 1 to 3 seconds. To complement the measurement of G, the signals of microphone (M) and laser vibrometer (V) occur before the evolution of pore pressure in approximately 1 ms. The time delay of the measurement of G, M, V, U permits to identify the time sequence of measurements. Other characteristics as magnitude and frequency of passive acoustic measurements will be exploited in next chapter. The small variation of acceleration G from 0.02 to 0.04 seconds correlates with the vibration of pore pressure but is not captured by V and M. They are not coherent to other signals from pore pressure, microphone and vibrometer.

All liquefaction events of the series are investigated in figure 5.8 with the colour bar representing the ascending index of test in the series. Irrespective of triggering stress,

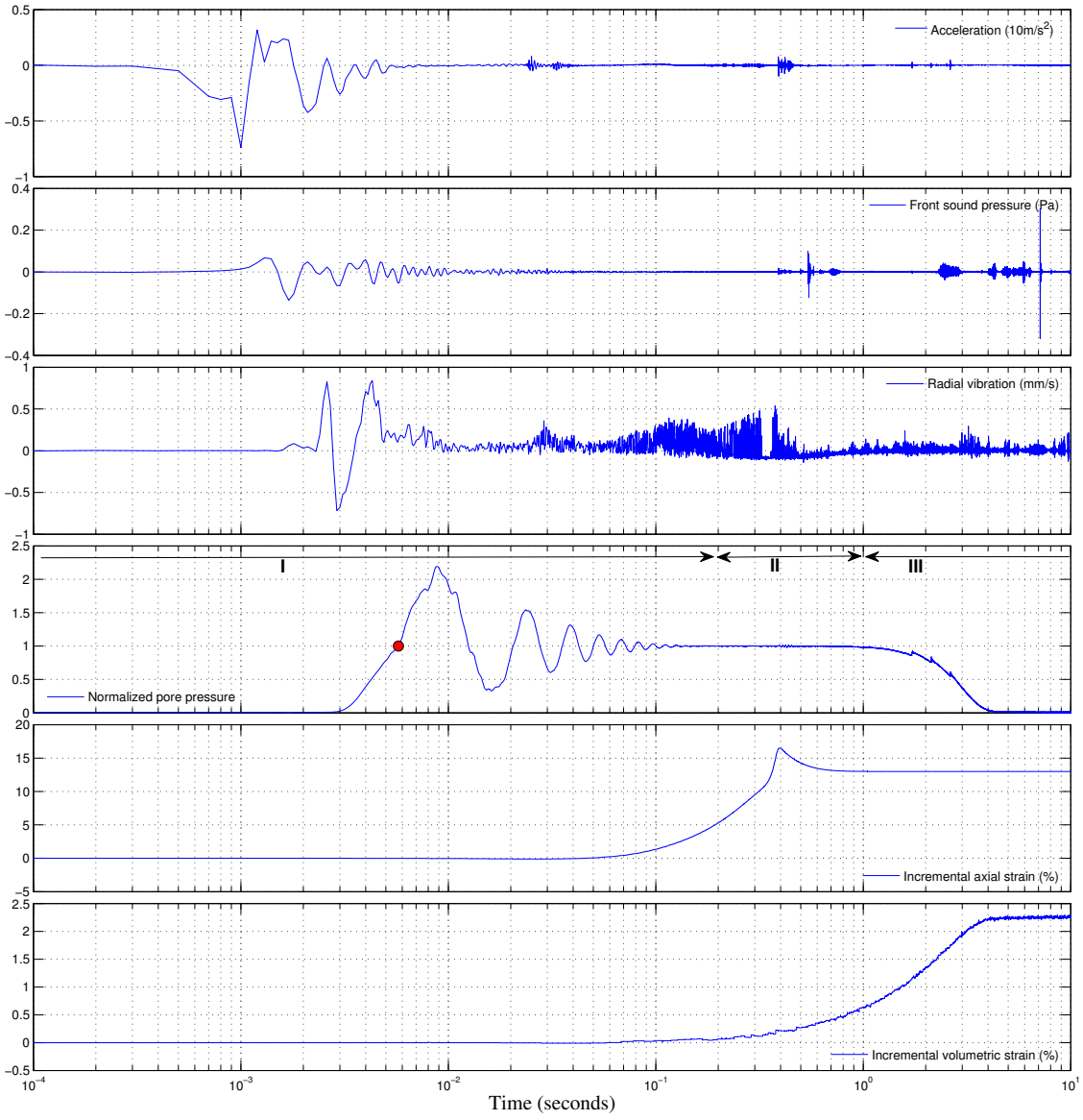

Figure 5.7: Detailed behaviour in typical isotropic liquefaction event IL_{05} at 252 kPa.

they show the same features including 3 phase-response of ΔU^{norm} but the duration of phase II is significantly different. The first transient phase also exhibits remarkable varying frequencies in figure 5.8a. The duration of the stabilised phase II varies significantly between isotropic liquefaction events, from 0.2 to more than 100 seconds for the longest. The axial extension after the peak at large compression state (figure 5.8b) is a measurement error, since the steel core of the internal LVDT moves outside the recom-

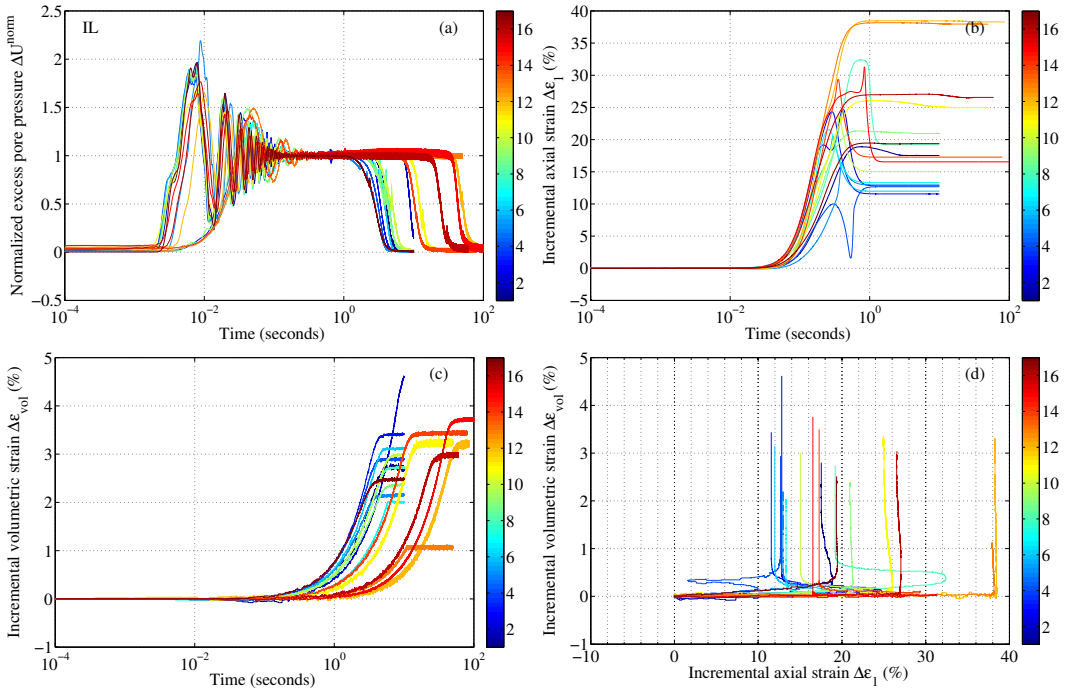

Figure 5.8: Detailed behaviour in isotropic liquefaction series.

mended measurement of linear range. The large deformation of the specimen creates the out-of-range displacement of the moving core on LVDT. Thus, the actual $\Delta\varepsilon_1$ in some liquefactions cannot be estimated, here they are assumed to be the peak values. The temporal evolution of incremental axial strain $\Delta\varepsilon_1$ happens simultaneously despite different magnitudes; they almost raise up together at around 0.02 s similar to that of SS events in chapter 4. The starting time of the incremental volumetric strain $\Delta\varepsilon_v$ is significantly dependent on the duration of phase II of pore pressure in figure 5.8a. For example in figure 5.8c blue curves ($\Delta\varepsilon_v$) rise first corresponding to the shortest durations of phase II of pore pressure while the red or orange curves develop later corresponding to longer duration of phase II. This observation indicates that volumetric strain develops as the consequence of the dissipation process. The relations of incremental volumetric strain $\Delta\varepsilon_v$ and incremental axial strain $\Delta\varepsilon_1$ exhibit the strongest anisotropy compared to collapses and SS events.

In some cases, isotropic liquefaction events, IL_{07} and IL_{13}, without dissipation phase or with unfinished very long stabilised phase due to the inappropriate manipulation which will be rejected in some specific analyses.

5.4.2.2 Drained stick-slip liquefaction (SL)

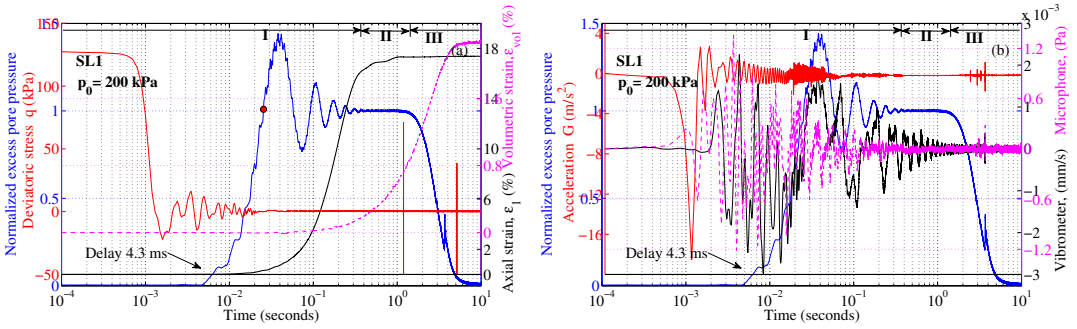

Figure 5.9: Detailed behaviour in drained stick-slip liquefaction event SL_{01} at confining pressure of 200 kPa.

The detailed temporal evolution of essential measurements of one typical stick-slip liquefaction SL is presented in a more compact form on figure 5.9. This rare SL event is characterised by a total drop of deviatoric stress q, transferring the deviatoric shearing state before stick-slip to isotropic stress state during the variation of pore pressure and axial strains.

After the drop of deviatoric stress, the responses occur in the same temporal sequence as in isotropic liquefaction. ΔU^{norm} vibrates at low frequency (14.21 Hz) and stabilises for more than 1 second before dissipating. The measurement G (red curve in figure 5.9b) reaches very large amplitude up to 1.8 g, 2 times larger than the largest of G in isotropic liquefaction (IL) event. The variation of G almost is simultaneous with the drop of deviatoric stress q and both are sooner than ΔU^{norm}. All measurements of G, M, V obtain higher amplitudes than isotropic liquefaction IL due to the presence of deviatoric stress q. Similar to isotropic liquefactions IL, the measurements of microphone M and vibrometer V also are coherent to the signal of acceleration G, especially at the aftershock of pore pressure at 3.3 seconds. They also support the appearance of G before the surge of pore pressure.

The series of drained SL includes two rare tests, SL_{01} (blue) at 200 kPa and SL_{02} (red) at 50 kPa, in figure 5.10. Some features are revealed including the total drop of deviatoric stress q, the uncontrolled frequency of pore pressure and the significant distinction in the duration of phase II. Mostly simultaneous development of $\Delta\varepsilon_1$ (figure 5.10c) but clearly delay evolution of $\Delta\varepsilon_v$ between two SL events (figure 5.10d)

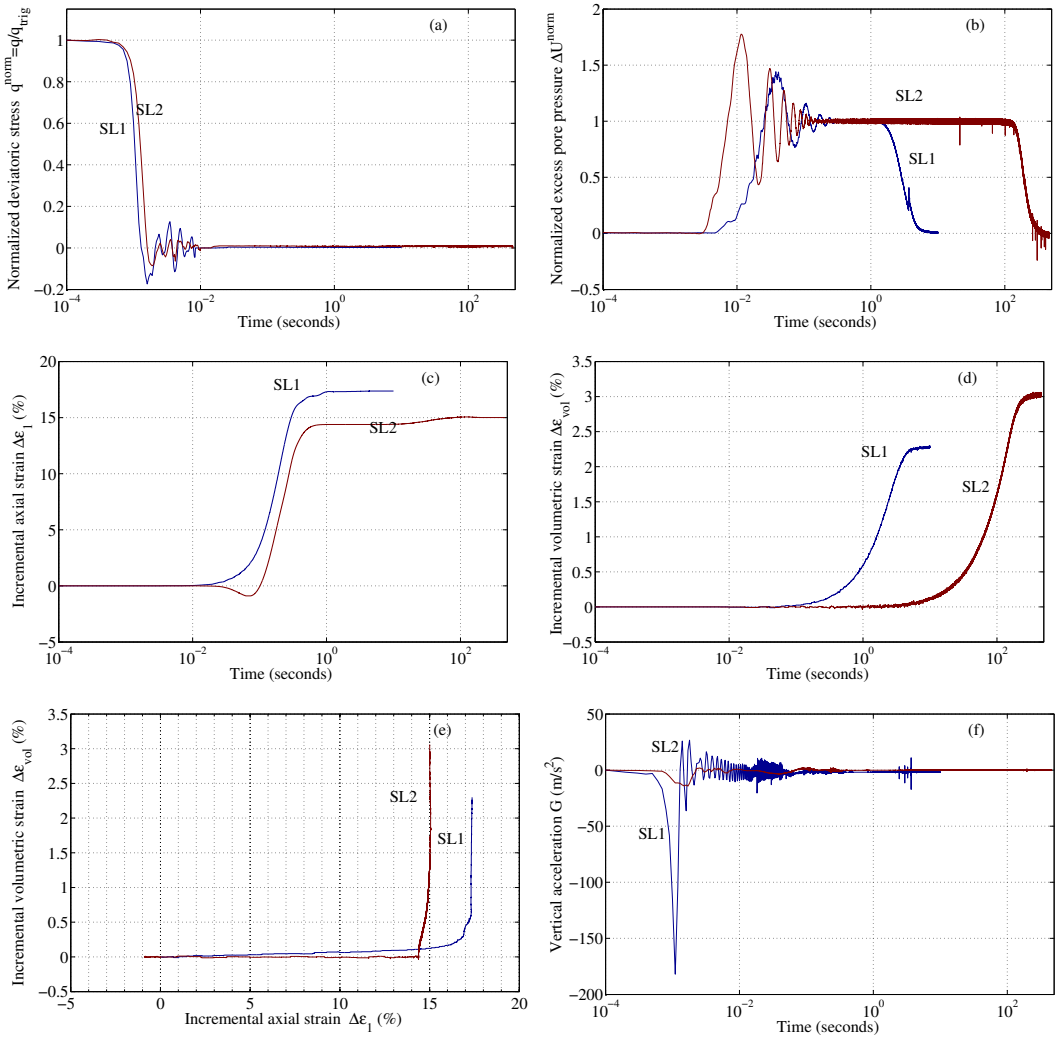

Figure 5.10: Detailed behaviour in drained stick-slip liquefaction events: (a) temporal evolution of normalised deviatoric stress q^{norm}, (b) normalised excess pore pressure ΔU^{norm}, (c) incremental axial strain $\Delta\varepsilon_1$, (d) incremental volumetric strain $\Delta\varepsilon_{vol}$ and (e) evolution of $\Delta\varepsilon_{vol}$ in accordance with $\Delta\varepsilon_1$ (e), (f) time history of vertical top cap acceleration.

strongly suggest that volumetric strain $\Delta\varepsilon_v$ is coherent to the duration of phase II while axial strain $\Delta\varepsilon_1$ is independent of phase II. The remarkable distinction in amplitude of acceleration G in figure 5.10f noticed further exploration in absolute magnitude of deviatoric stress drop q and stabilised excess pore pressure U_{stable} instead of normalised quantities.

5.4.2.3 Static liquefaction (UL)

As described above in section 5.4.1.3, only the behaviour of static liquefaction at point F close to the steady state of deformation in effective stress path is analysed. The temporal evolution of deviatoric stress q, pore pressure U, acceleration G, axial strain ε_1 during the failure at point F with small mean effective pressure, $p' = 2.12$ kPa, of test IL_{01} is presented in figure 5.11a.

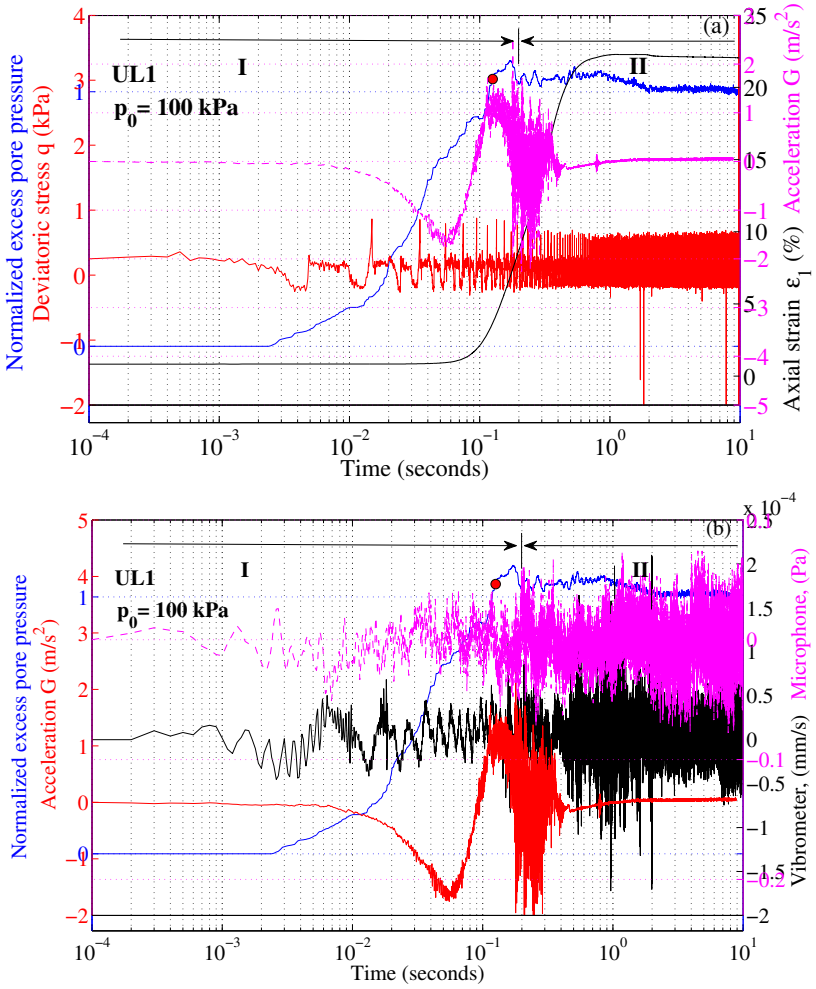

Figure 5.11: Detailed behaviour in static liquefaction event UL_{01} at initial confining pressure of 100 kPa.

The pore pressure exhibits completely different behaviour. It gradually rises from a stable state to reach the confining pressure without the first transient vibration and

dissipation phase due to undrained condition. The whole variation occurs in around the same duration (200-300 ms) as phase I of dynamic liquefaction. The development of incremental axial strain $\Delta\varepsilon_1$ is still the latest. The variation of acceleration G is significantly small in figure 5.11a, only 0.2 g, with very low frequency representing the static regime of phenomenon. The evolution of pore pressure U and acceleration G implies a different mechanism. In static liquefaction UL, at point F in effective stress path, since the pore pressure is nearly equal to confining pressure, and the effective stress state is adjacent to the origin of the effective space, very small pertubation is sufficient to release the contact network of grains, separate the particles. The sample totally collapses in less than 1 second which is attributed to the slow and small acceleration G, 1.7 m/s^2, compared to the noise level of G signal during undrained shearing before liquefaction, 0.06 m/s^2. The modifications of microphone signal M, vibrometer V are not clear to identify, hence the gentle destruction of grain skeleton.

The second typical static liquefaction IL_{02} at confining pressure of 50 kPa in figure 5.12 even exhibits no variation of acceleration G although the drop of deviatoric stress q is more obvious. Similarly, the variations of V, M are negligible. The whole series of static liquefaction UL are plotted together in figure 5.13 showing the same features of static liquefaction. The drop of deviatoric stress q takes place in longer duration of 4 ms compared to only 1 ms of dynamic liquefaction, the pore pressure does not fluctuate and does not dissipate. There is only phase I without vibration. Note the infinite duration of phase II. The acceleration G is lower than 2 m/s^2.

5.4.2.4 Isotropic liquefaction during application of back pressure (BL)

To highlight and verify some relations afterwards, some global failures in different loading conditions are considered to add new aspects. During the stage of applying back pressure, some liquefaction events have been acquired. After the flushing stage using de-aired water throughout one complete night under constant $\sigma_3^{'}$, (σ_3,U_0) = (20,0), and under constant stress gradient of 5 kPa between the top and bottom platens, a constant and stable effective stress state was created (σ_3,U_0) = (40,20). This initial back pressure U_0 of 20 kPa was imposed as the minimum value by the back pressure regulator. Then the back pressure U_0 and the total cell pressure σ_3 were simultaneously and manually increased slowly to keep $\sigma^{'}$ as constant as possible at 20 kPa. The final level will be (220,200) with σ_3 = 220 kPa, U_0 = 200 kPa.

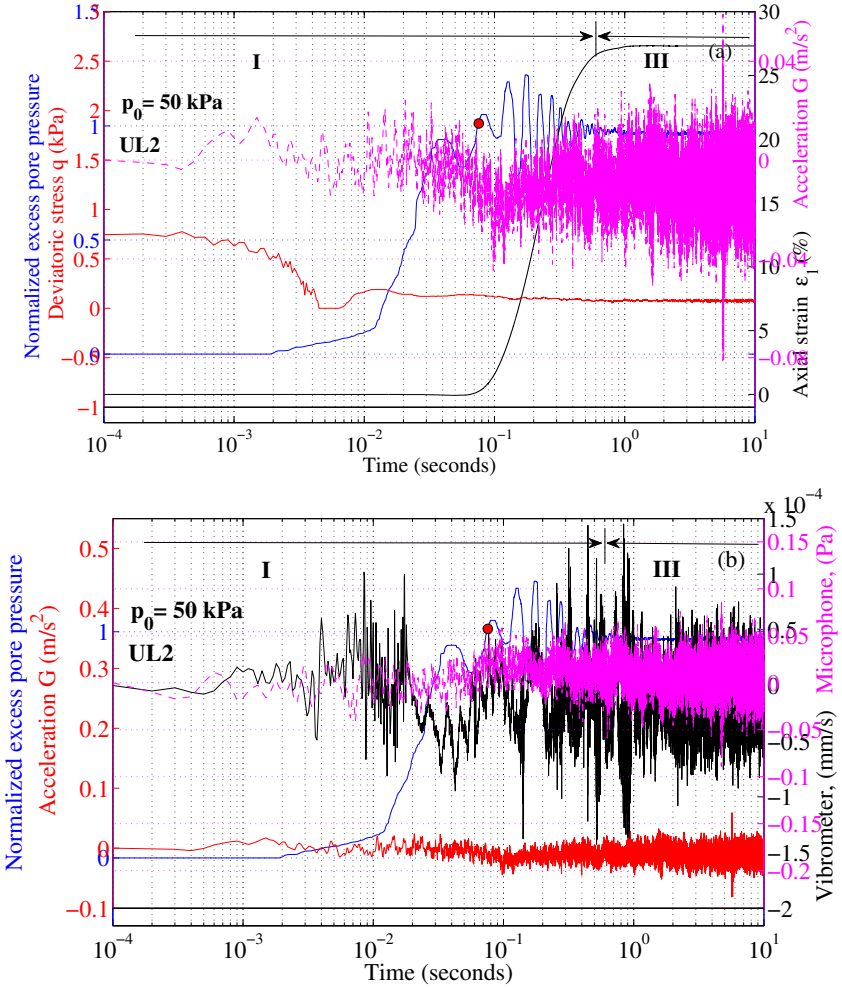

Figure 5.12: Detailed behaviour in static liquefaction event UL_{02} at initial confining pressure of 50 kPa.

Two back pressure liquefaction events BLs happened at the lowest effective triggering stress σ'_{trig}, 31 and 42 kPa, are examined. These triggering stress states corresponding to back pressure of the sample is gradually increased at level of 32 kPa and 52 kPa, total cell pressure are 63 kPa and 94 kPa respectively. Although the procedure of back pressure application designs to keep the constant effective confining pressure of 20 kPa, meaning at back pressure of 32 kPa and 52 kPa, the total cell pressure should be 52 and 72 kPa. But this process was manually conducted in this study thus the simultaneous increase of pore pressure and cell pressure was not well employed resulting in unexpected large effective confining pressure up to about 40 kPa. The detailed

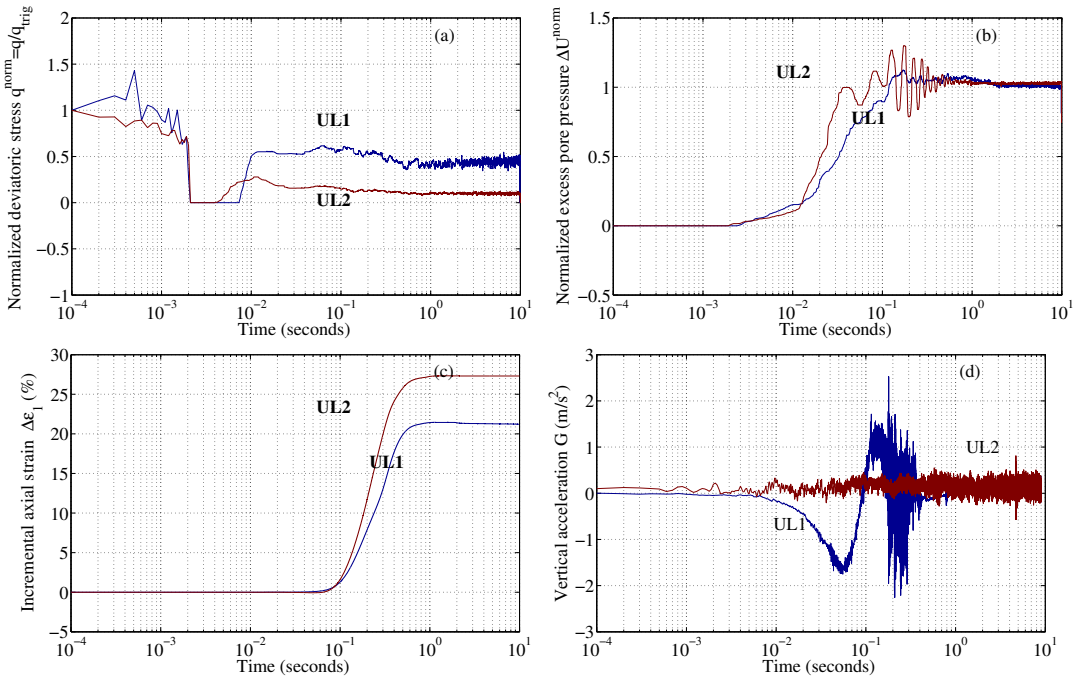

Figure 5.13: Detailed behaviour in static liquefaction events.

behaviour is in figures 5.14 and 5.15.

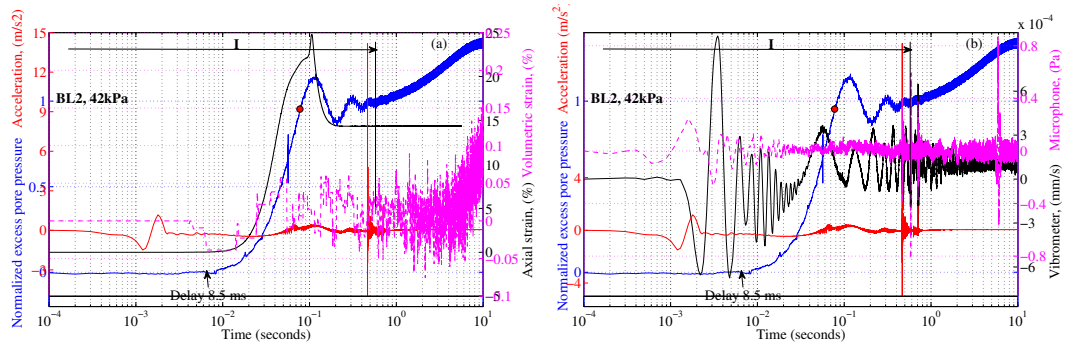

Figure 5.14: Detailed behaviour in liquefaction event BL_{02} at effective confining pressure of 42 kPa during application of back pressure.

Pore pressure shows a gradual rising and a lack of phase III. The first transient phase I still remains at low frequency. The phase II is not exactly the constant stabilized state due to the manual manipulation but it should be constant. In this case the duration of phase II also is unidentified since the manual action cannot control strictly the constant effective confining stress. The acceleration G drops much sooner than pore pressure

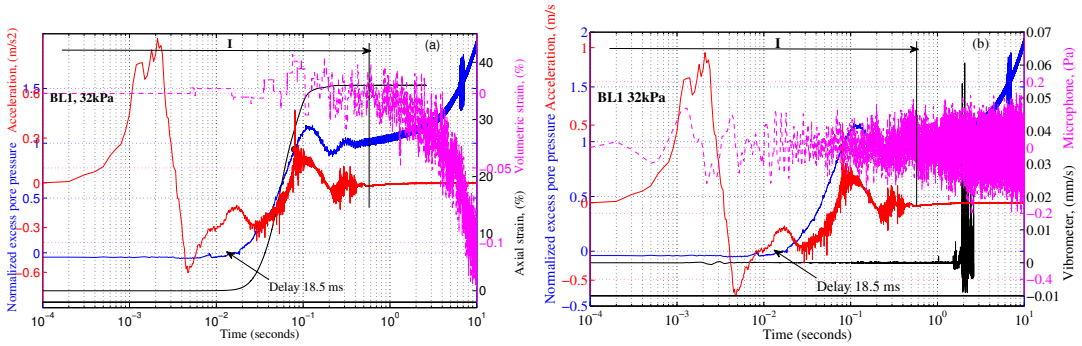

Figure 5.15: Detailed behaviour in liquefaction event BL_{01} at effective confining pressure of 32 kPa during application of back pressure.

with amplitude of 0.1 g, the same order as isotropic liquefaction. But other abnormal large peak of acceleration G of 14.17 m/s^2 is detected at 0.5 s, long after the end of the development of axial strain. The fast development of incremental axial strain $\Delta\varepsilon_1$ is mostly concurrent with the generation of pore pressure while incremental volumetric strain $\Delta\varepsilon_{vol}$ as usual varies very little of about only 0.1% after the first transient phase of pore pressure. If the effective confining pressure is strictly kept constant at 20 kPa, no $\Delta\varepsilon_{vol}$ is obtained. But as previously described, the manual operation leads to the rising of effective confining pressure then the volumetric strain slightly changes. Moreover, the complicated physics with the presence of remaining gas CO_2 might attribute to the small negative volumetric strain of about 0.1% in figure 5.15a. Note that the saturation in these two tests has not been estimated at this step, thus the unknown Skempton's coefficient B. Figure 5.14b confirms the variations of M, V after G but much sooner than pore pressure. The large peak of G is consistent with the sound pressure peak of M of 0.2 Pa at around 0.5 s and the peak of lateral vibration V of 0.8 $*10^{-4}$ mm/s. This might be due to the manner that the sample falls down. In reality, the way and the form of the sample after liquefaction is different. Sometimes the sample falls down totally (as in figure 5.2)r so that the moving core of LVDT drops out of the device, sometimes the specimen shape after failure is nearly a cylinder but experienced very large strain with the bellies around the surface (figure 5.3e). This response leads to complicated signals after the end of the axial strain.

To check this interpretation, test BL_{02} is presented in figure 5.15. The modification of acceleration is even sooner, 18.5 ms, than the surge of pore pressure. The develop-

ment of axial strain still takes place no later than pore pressure. It can be suggested that this is one of the signature of BL compared to SL and IL. In this liquefaction case, it seems that axial strain is not the consequence of the pore pressure build up. In this case, no additional large peak of G, M or V are detected after the axial strain jump. Therefore that large abnormal peak of G in test BL_{01} can be ignored. This spike is expected to be an artificial interference.

5.4.2.5 Flowing liquefaction during imbibition (WL)

Another liquefaction during imbibition process is introduced to add some observations under unsaturated inhomogeneous medium with the existence of the pressure of flowing fluid. In this process, since water is injected slowly by the bottom valve under constant pressure of 3.5 kPa, the water level rises gradually inside the sample and sometimes the specimen totally collapses which is named WL for liquefaction during imbibition. The material is partially dry at the top and immersed in water at the bottom. The signal of static pore pressure sensor at the top of sample (dry part of sample) is only 0.5 kPa although the total confining pressure is 20 kPa. Because the sample top connects to the atmosphere, the excess air pressure detected at the top pore pressure sensor is very small, mostly negligible. Accordingly, the pore pressure gradient between the top and bottom of sample is estimated as 0.5 kPa/cm. The detailed behaviour is exhibited in figure 5.16.

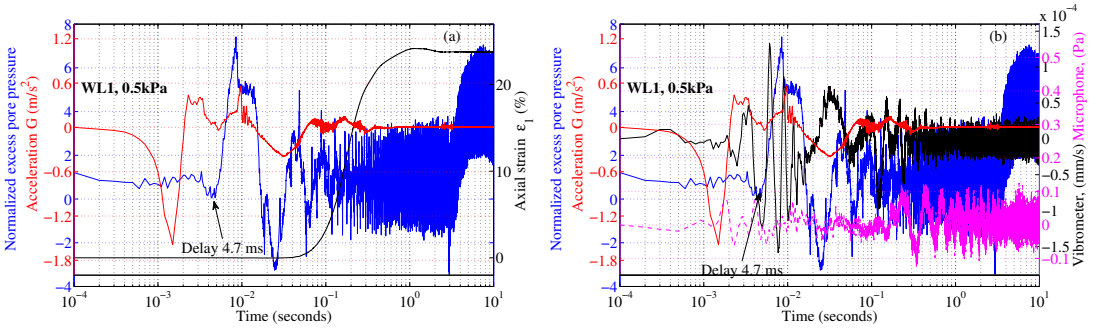

Figure 5.16: Detailed behaviour in liquefaction event during imbibition at effective triggering stress of 0.5 kPa.

In this case, the pore pressure also does not show the full 3-phase behavior (figure 5.16a). It has only a first vibration phase then a long stable state. The duration of

phase II can be considered as infinite. The acceleration G, sound pressure M, lateral vibration V are all modified prior to the generation of excess pore pressure (figure 5.16b). The magnitude of G is the same order of that of isotropic liquefaction IL and back pressure liquefaction BL.

5.4.2.6 Isotropic collapse (Coll)

The series of 56 isotropic collapses in figure 5.17 differs from other dynamic liquefactions by the lack of phase II. Additionally, among 56 studied collapses, some of them are double or triple events thus they exhibit the subsequent surge of pore pressure mostly in the phase III as in figure 5.17a. Some appreciably long stable states of ΔU^{norm}

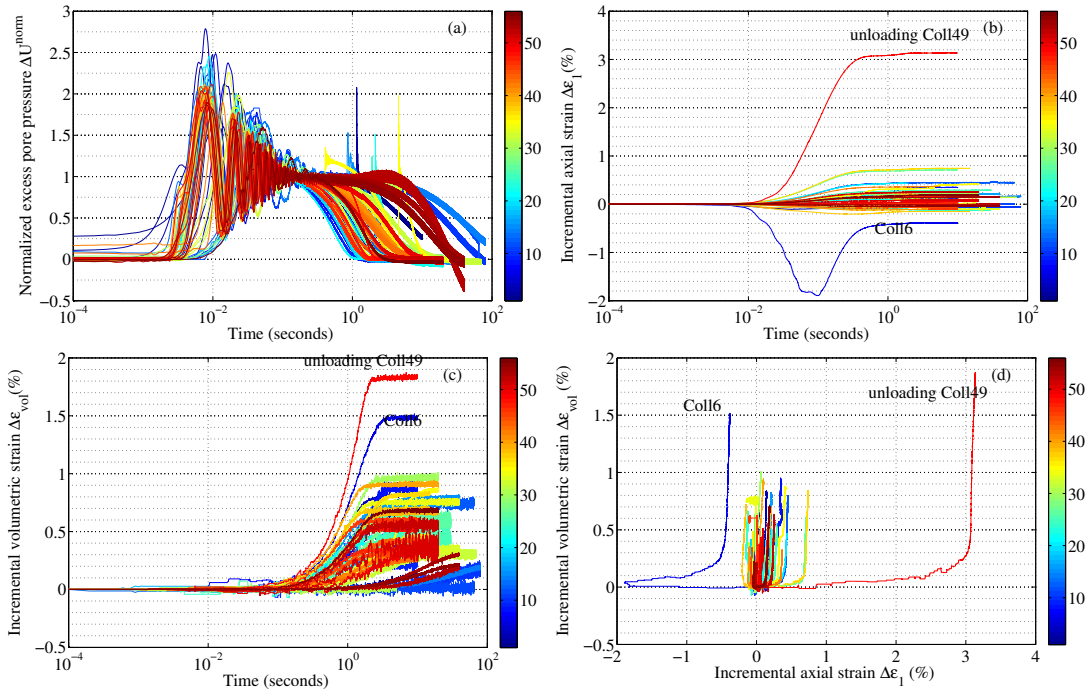

Figure 5.17: Detailed behaviour in isotropic collapse events.

are also acknowledged. The frequency of pore pressure seems not to be a constant. Although, the pore pressure shares the same feature of 2-phase behaviour, the axial strain $\Delta\varepsilon_1$ shows some distinct responses. One significant large extension axial strain of test Coll_{06} as other cases of SS was attributed to the unbalance of the sample top cap. The extremely large axial strain $\Delta\varepsilon_1$ of test Coll_{49} is a special case which is an extremely large collapse under unloading condition from 500 kPa at one of the largest

triggering stress, σ'_{trig} = 440.5 kPa, within the whole series. In this test $Coll_{49}$, the stabilised excess pore pressure ΔU_{stable} nearly reaches the confining pressure p'_0 to liquefy thus both $\Delta\varepsilon_1$ and $\Delta\varepsilon_{vol}$ are notably larger than other collapses of the series (figures 5.17b,c). Specifically $\Delta\varepsilon_{vol}$ of $Coll_{49}$ reaches the range of magnitude of isotropic liquefaction around 1% to 4%.

5.5 Analysis and discussion

5.5.1 Threshold of void ratio e^{thres}

As in our previous works, the void ratio e was explored to see how it controls the occurrence of instabilities. Figure 5.18 draws a picture of the distribution of the initial void ratio e_{20} (e_{30} in case the confining pressure of the fabrication process is 30 kPa) in relation to the induced incremental axial strain $\Delta\varepsilon_1$. Essentially, liquefaction series including 6 kinds of liquefaction (isotropic liquefaction IL, stick-slip liquefaction SL, static liquefaction UL, imbibition liquefaction WL, flushing liquefaction FL, back pressure liquefaction BL) located in the region of high void ratio e_{20} and large $\Delta\varepsilon_1$. The threshold of initial void ratio $e_{20}^{thres,Liq}$ is identified. Below this threshold no liquefaction is observed. The published data (30, 34) of isotropic liquefactions (magenta solid circles) are added to show the old threshold e_{30}^{thres} = 0.690 (D_r = -3.6%). New threshold e_{20}^{thres} = 0.682 (D_r = 3.57%) is established as the improvement of current study with 35 liquefactions of all kinds. The presence of new types of liquefaction located on the same region with isotropic liquefaction IL well improved the result. Moreover, one rare isotropic liquefaction with 0.4 mm glass beads (red solid circles) also strengthens the validity of this new threshold.

Isotropic collapses are distinguished by significant small range of axial strain $\Delta\varepsilon_1$. The old series of collapse (magenta circle) helped pointing out the lower threshold of void ratio around 0.608 (D_r = 69.64%) for saturated sample.

In figure 5.19, the triggering void ratio e_{trig} instead of initial void ratio e_{20} is investigated in accordance with $\Delta\varepsilon_1$. Imbibition liquefaction WL, flushing liquefaction FL, back pressure liquefaction BL are excluded in this figure since e_{trig} cannot be estimated for these liquefactions. Because e_{trig} is always lower than the initial void ratio e_{20} in isotropic compression then it creates lower threshold $e_{trig}^{thres,Liq}$ = 0.665 (D_r = 3.57%). It means that if the current void ratio of the medium is lower than

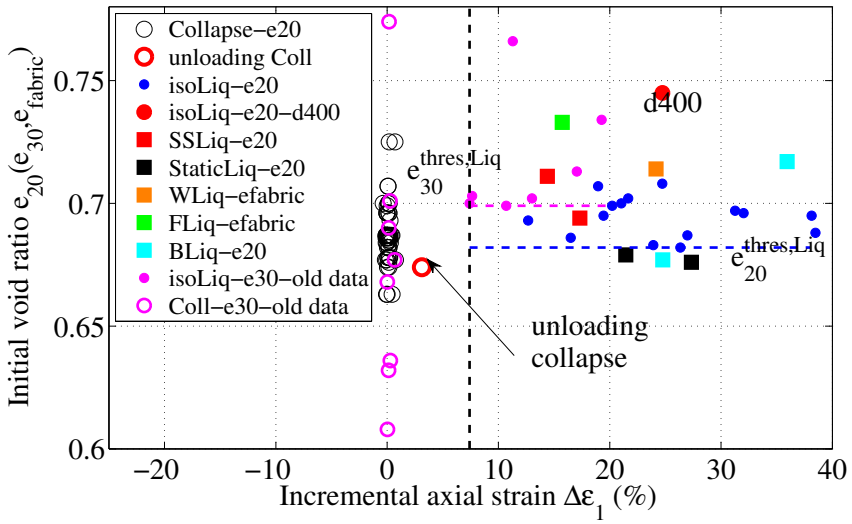

Figure 5.18: Location of initial void ratio e_{20}, e_{30} of studied liquefaction, collapse and large first stick-slip events in relation to incremental axial strain $\Delta\varepsilon_1$.

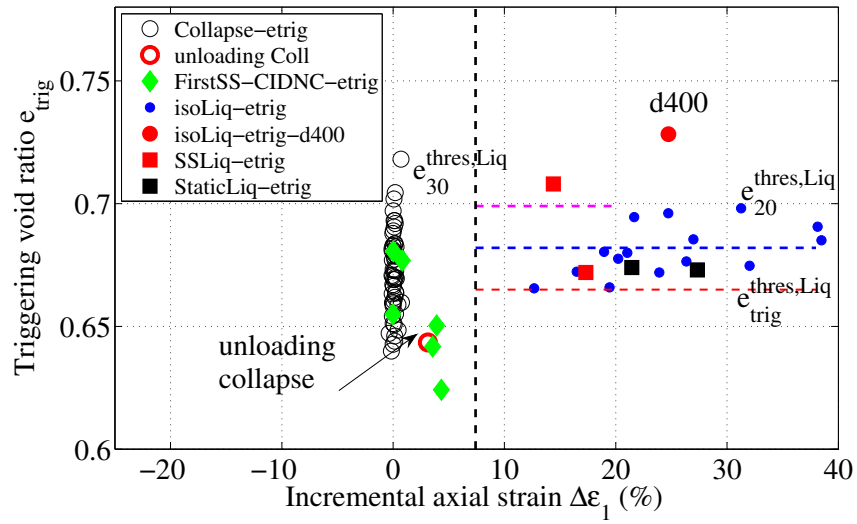

Figure 5.19: Location of triggering void ratio e_{trig} of studied liquefaction, collapse and large first stick-slip events in relation to incremental axial strain $\Delta\varepsilon_1$.

this threshold liquefaction is impossible. A group of first large SSs of CIDNC series is also added (orange solid square). Note that those first SSs are most likely to liquefy. There is a special SS event with the triggering void ratio $e_{trig} = 0.624$ lower than the threshold even though with very large $\Delta\varepsilon_1 = 4.34\%$ this event is still a local failure, not

total failure. Its presence confirms the reliability of $e_{trig}^{thres,Liq}$. However the presence of other large SSs (green diamonds) and unloading collapse which is mostly liquefied but they still do not move to the zone of liquefaction means the void ratio is not the unique parameter governing the occurrence of liquefaction.

5.5.2 Effect of saturation and pressure on the frequency of pore pressure

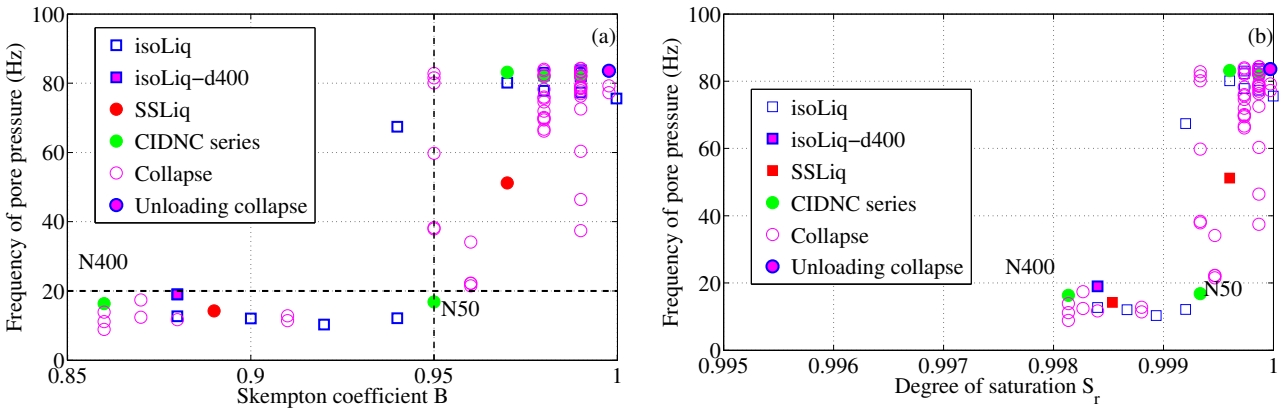

Figure 5.20: Impact of saturation of granular medium on the vibration frequency of pore pressure for all collapses and liquefaction events.

Due to the existence of two separated groups of pore pressure frequency in the set of isotropic liquefactions (fig 5.8), an investigation is performed to find the impact of saturation on low frequency group in figure 5.20.

Similar to CIDNC series, the threshold B = 0.95 emerges as the sensitive limit where the frequency of pore pressure f_U sharply increases. Low saturation, B < 0.95, results in low frequency of pore pressure, around 20 Hz. Flushing liquefaction FL and back pressure liquefaction BL are not included since B cannot be estimated at those cases. The diversification of dynamic instabilities under various loadings strengthens the conclusion. As aforementioned in section 5.20, pressure can be a parameter influencing the frequency of pore pressure f_U. Additionally, the presence of both liquefactions and collapse with the frequency in the range between 20 and 80 Hz confirms the assessment that confining pressure has some effects on the frequency of pore pressure. Hence, an investigation of the effects of triggering stress σ'_{trig} on the frequency f_U is conducted in figure 5.21.

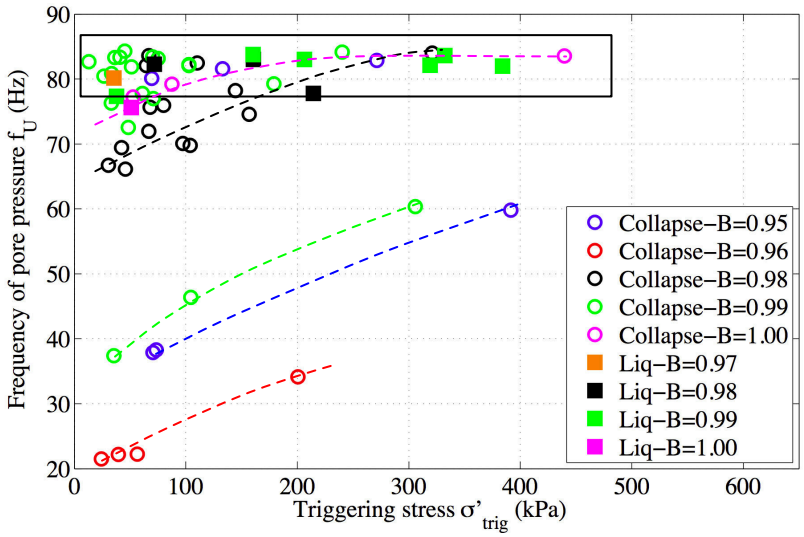

Figure 5.21: Impact of triggering stress σ'_{trig} of granular medium on the vibration frequency of pore pressure for all collapses and isotropic liquefaction events.

In this figure, isotropic instabilities are separated in 5 groups of B from 0.95 to 1.00, marked by different colours. At a specific saturation, the increasing tendency of frequency is observed depending on the increase of triggering stress σ'_{trig}. That tendency is exhibited qualitatively by dashed curves in the figure. Within the rectangle with high B $\geq$ 0.99, the frequency of pore pressure f_U seems to saturate at a constant frequency around 80 Hz. This result points out the combined effect of saturation and pressure.

The saturation S_r is inferred from the measured Skempton's coefficient B according to the following relation of B and S_r suggested by Black and Lee (7, 67) for the case of stiff sands with void ratio around 0.6.

$$B = \frac{\Delta U}{\Delta \sigma_3} = \frac{C_d}{C_d + n.S_r.C_w + (1-n).C_g + n.\dfrac{1-S_r}{u_2}} \tag{5.1}$$

with n the porosity related to void ratio e by $n = e\ /\ (1+e)$. C_d the compressibility of the soil skeleton ($1.45{*}10^{-5}$(m^2/kN) for glass beads). C_w the compressibility of water, approximately $4.8{*}10^{-5}$(m^2/kN). C_g the compressibility of gas, in case of adiabatic process, at atmospheric pressure, C_g the inverse of bulk modulus $E_g = 1.01325{*}10^5$(N/m^2). u_2 the sum of the absolute pressure in the pore fluid before the pressure increment and

the increment in cell pressure during the procedure of measuring B coefficient of the test. In our test, $u_2 = 200 + 100 = 300$ kPa. All performed tests are quasi-saturated with S_r larger than 0.998 and figure 5.20b shows the effects of S_r on f_U with the translated threshold $S_r = 0.999$.

The computed variation of velocity c of vibration of pore fluid with the increasing of Skempton's coefficient B is shown in figure 5.22 for a set of isotropic liquefactions and collapse series using the development of D. MacWilliam (79) and Kieffer (60) for bubbly fluid.

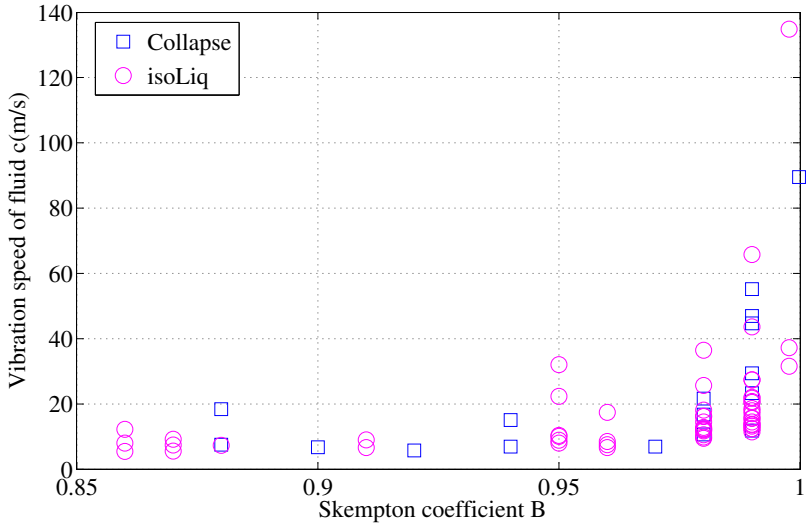

Figure 5.22: Variation of velocity of vibration of pore fluid in the relation to Skempton's coefficient B.

Note that velocity c of the vibration of gas-water mixture is proportional to the vibration frequency by the wavelength λ which is not measured in this study. However it is the proportional parameter, thus frequency of pore pressure $f_U = c \ / \ \lambda$. A referenced value $\lambda = 1$ m for the range of low frequencies $\approx$ 10-100 Hz is suggested by R. Delannay (26) using passive acoustic probing. Figure 5.22 exhibits the decrease of velocity c from 120 m/s at B = 1 to around 15 m/s at lower B, approximately 8 times of the decrement. Theoretically it corresponds to the same drop of frequency. Compared to the decrement of frequency in experiment data of figure 5.20 with the decrease of 5 times, it shows an appropriate estimation of the theory. The theory can well predict the frequency at low B < 0.95. In the range of high B up to 1, there is a discrepancy.

However, the theory also shows the variation of frequency depending on pressure which explains the range of experimental data between 20 and 80 Hz. The discrepancy of experiment and theory in the range of high B > 0.95 is due to the resolution of the measured B. In this study, the error of the measured stress is ± 3 kPa for low range which impacts the resolution of measured B. The relation (5.1) is very sensitive in the range of 0.95 up to 1 since when B approaches 1 the function S_r = f(B) is asymptotic to 1 (67). In other words, the error of measured B is quite significant in the range above 0.95. Because in the step of measuring B during testing procedure, the initial purpose is just to ensure B above 0.95. The sensitiveness of B was underestimated.

5.5.3 Effect of the slenderness of sample on the frequency of pore pressure

On the purpose to find the mechanisms at the origin of vibration of pore pressure in phase I, one verification test is introduced in this section. This test is conducted with slender sample (H/D = 14/7). When doubling the sample height, unfortunately, the inside space is not sufficient to install the internal LVDT. Consequently, the void ratio at different stages is unknown, excepting the initial void ratio at fabrication stage of 0.809 (extremely loose, Dr = -110%). As usual, CVP virgin glass beads 0.7 mm are used with the same fabrication method. Skempton's coefficient B is 0.98. The traditional CID testing procedure is applied comprising isotropic consolidation stage up to confining pressure p'_0 = 500 kPa, followed by drained triaxial shearing. The sampling rate is increased up to 20 kHz on two 4472B acquisition boards instead of 10 kHz as usual. The most important measurement is pore pressure, still detected at the top and bottom of sample by static and dynamic pore pressure sensors. Furthermore, vertical accelerometer G, lateral vibrometer and microphones are still maintained.

First, the isotropic compressibility of figure 5.23 shows three isotropic collapses A, B, C at 36, 61 and 121 kPa respectively. In the next stage of drained shearing, figure 5.24 bottom shows the traditional drained compression stick-slips at 500 kPa of confining pressure with external axial strain, up to only 15%. The stress-strain behaviour of the first stick-slip is incorrect due to the use of external LVDT. This test gives globally a marked softening behaviour in stress-strain curve with large deviatoric stress drops, a clear localised shear band at the end of test and a loose character

in volumetric behaviour. Note the first two unusual stick-slips with relatively large incremental external axial strain, of about 0.5%.

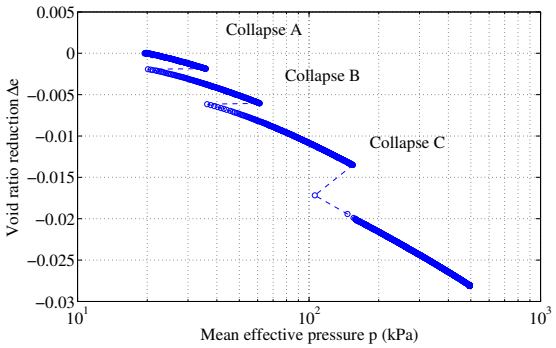

Figure 5.23: Compressibility behaviour during isotropic consolidation of slender sample H/D = 2.

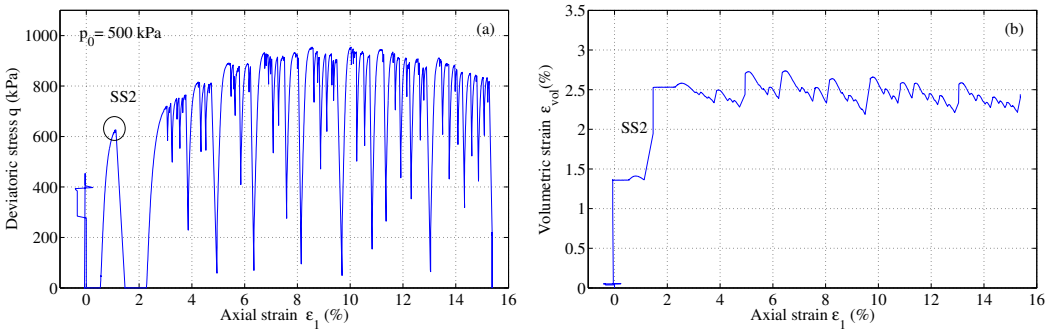

Figure 5.24: Global behaviour of stick-slip during triaxial compression of slender sample H/D = 2.

The core content is the exploration of the behaviour of pore pressure within a single dynamic instability. Figure 5.25 gives the typical isotropic collapse C, with f_U of 75.8 Hz, nearly in the range of 80-100 Hz in the case of short sample (L = 7 cm); and typical drained compression stick-slip SS_{02} of 83.8 Hz. The remaining collapses and stick-slips are also analysed to identify f_U which are in the range of 70 to 76 Hz for collapse and 77 to 84 Hz for stick-slip. This indicated that doubling the sample slenderness has no effects on the frequency of pore pressure f_U. If the vibration in the first transient phase I is due to the structural vibration of granular assembly, doubling the height will reduce the dominant frequency by half.

The stacking plot of SS_{02} confirms previous findings on short sample (H/D = 1.0):

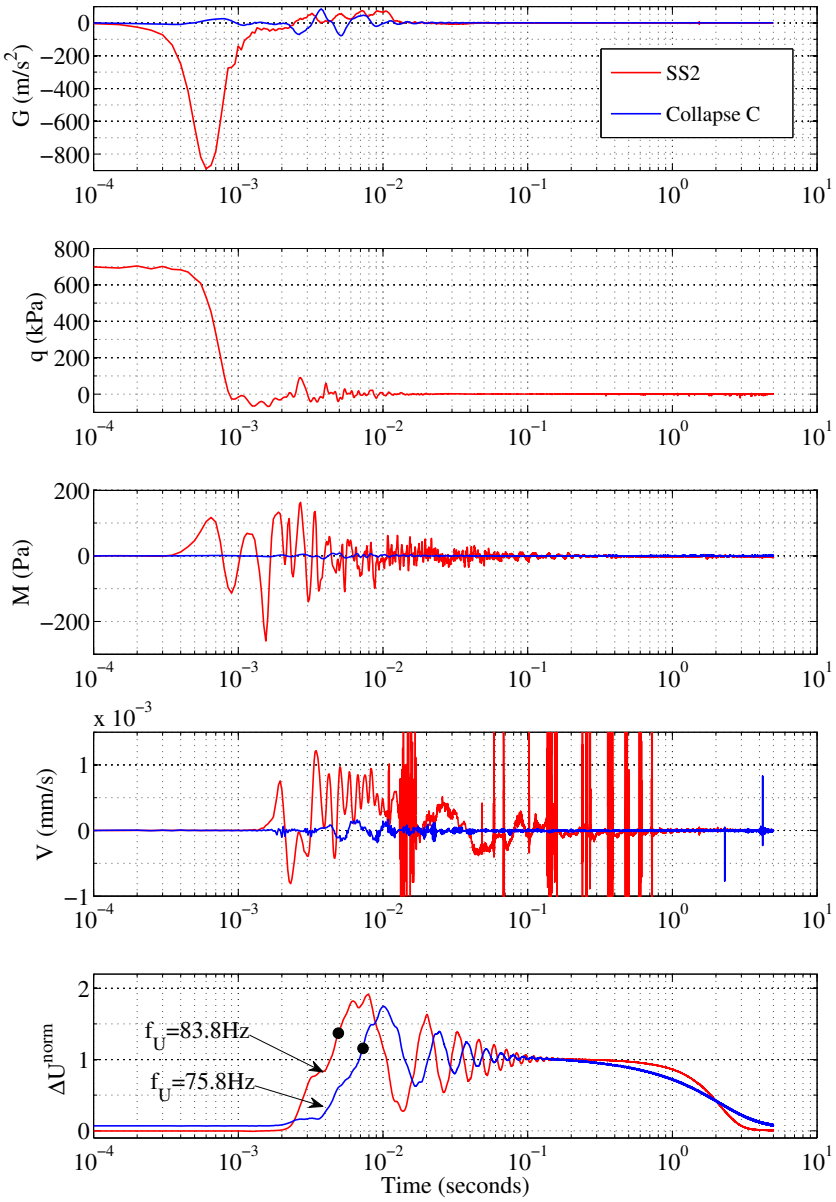

Figure 5.25: Detailed temporal evolution of measurements vertical acceleration, deviatoric stress, lateral sound pressure, lateral vibration, normalised excess pore pressure ΔU^{norm} during stick-slip SS_{02} and collapse C.

the presence of isotropic collapse and drained compression stick-slip with volumetric coupling, the outburst of pore pressure in two phases, the stress drop duration of about 1 ms, the sequence of dynamic event (modification of granular structure with vertical top cap acceleration and deviatoric stress drop, lateral sound pressure and

radial vibration, pore pressure, axial strain and finally volumetric strain), the differences between isotropic collapse and drained compression stick-slip.

Briefly, this verification test consistently validates the dynamic instabilities and paves the way for the physical feasibility of isotropic liquefaction on slender sample. It contributed a complementary evidence to the prevail effect of saturation and pressure to the frequency of pore pressure. It also means the fluctuation of pore pressure seems not to be related to the vibration of the grain skeleton.

5.5.4 Effect of grain size on the frequency of pore pressure

Further verification tests are added in an attempt to discover the controlling parameters of the vibration of pore pressure. One short series D including three tests is introduced to investigate the effect of the grain size and the fabrication process on the frequency of pore pressure. Table 5.4 presents three tests in which glass beads composed by the same material but different fabrication processes. To compare to the usual series with glass beads of 700 μm of diameter, other diameter are explored including test D1000 with Sili beads of 1000 μm and two mixtures constituted from half of 400 μm beads and half of 700 μm beads. The confining pressure $p'_0 = 500$ kPa and drainage condition are the same for the whole series. The measured Skempton's coefficient B is significant low, B = 0.82, only for test Dmix_{02}.

Table 5.4: Summarized characteristics of series D on the effects of grain size on the frequency of pore pressure.

Series D	Test	N	Material	d (mm)	p'_0 (kPa)	Loading	B	f_U (Hz)
1	D1000	1	Sili	1000	500	CID	0.98	81.68
2	Dmix_{01}	1	CVP	50%d400+50%d700	500	CID	0.95	72.28
3	Dmix_{02}	1	CVP	50%d400+50%d700	500	CID	0.82	14.6

The aim of this investigation is to identify the frequency of pore pressure in figure 5.26. Consider two tests D1000 (red curve) and Dmix_{01} (blue curve) at the same saturation with high B, the effect of saturation is excluded. Their frequencies of pore pressure are indicated directly in the figure that both the granular material of large size (1000 μm) or the mixture vibrates at the range of 80 Hz similar to the referenced

material throughout the thesis (CVP 700 μm). In the preliminary tests, the composition of the material, Sili or CVP, and the grain size (1000, 700, 400 μm) does not affect the frequency of pore pressure. Test Dmix_{02} is very meaningful to compare with test Dmix_{01} due to the low B. Its low frequency of pore pressure f_U = 14.6Hz confirmed previous conclusion that saturation is the strongest factor influencing f_U.

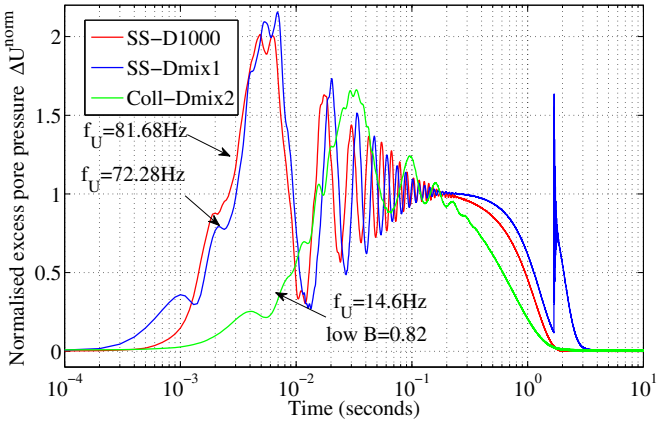

Figure 5.26: Temporal behaviour of pore pressure during instabilities within different assembly of various grain size.

So far, the dominant frequency of pore pressure f_U of 80 Hz is unaffected by the variation of the sample slenderness and the grain size, during various kinds of instability, under different loadings and drainage conditions. This results in the mechanisms of the vibration of pore pressure being still unknown. Only two parameters, saturation degree and pressure, impact on the frequency of pore pressure.

5.5.5 Time-resolved analysis

In this section, some time characteristics of pore pressure are measured and the links between collapse and liquefaction explored.

5.5.5.1 Time characterisation of pore pressure during liquefactions

Since the frequency of dynamic instabilities evolves according to saturation basically gathering in two groups, lower than 20 Hz and around 80 Hz, the first characteristics on the first transient phase of pore pressure, t_{trans} (defined in figure 5.1), is explored in accordance with frequencies of events in figure 5.27a. It is understandable that the

time of the transient vibration t_{trans} evolves according to the frequency since the speed of vibration is explained as the function of saturation and pressure. For Liquefaction series, the data of t_{trans} separates into 2 groups of high and low frequency in figure 5.27b independent of stabilised excess pore pressure ΔU_{stable}. This is similar to two separate curves of t_{trans} in CIDNC series in figure 4.22.

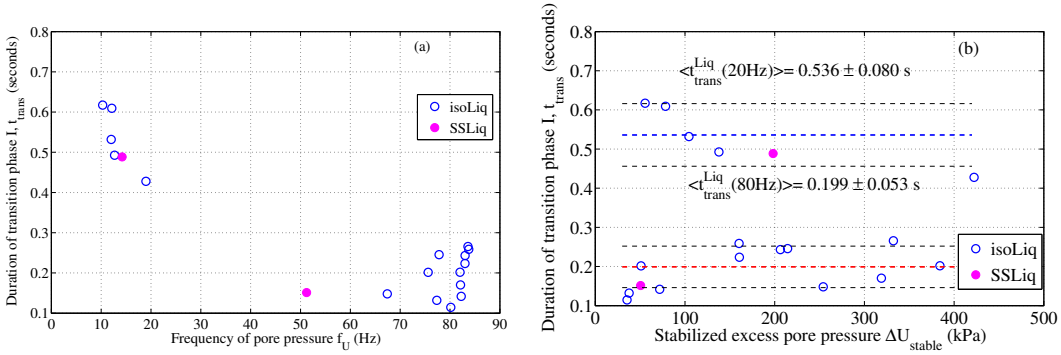

Figure 5.27: Evolution of duration of transient phase according to ΔU_{stable} during isotropic liquefaction events.

Since the objective of this study is on fully saturated medium, in figure 5.27b within this referenced group including 13 tests of high frequency, t_{trans} is reasonably constant, characterised by the mean value $< t_{trans} >$ $= 0.199 \pm 0.0534$ s. The other group of only 6 tests of low frequency yields at a large value of 0.536 ± 0.080 s

Next, the duration of stabilised phase II represented by $\Delta t_{05} = t_{05}$ - t_{trans} is explored. Figure 5.28 reveals that the duration of phase II extends with the decline of the magnitude of stabilised excess pore pressure ΔU_{stable}. Among 17 isotropic liquefactions, test Il7 and $IL_{01}3$ do not have the full data. Stick-slip liquefactions SL_{01} (magenta) and SL_{02} (black) are also added to the comparison. Then the results are presented in figure 5.29 with the decreasing trend when ΔU_{stable} increases meaning the larger the triggering stress (the media is denser), the shorter the phase II. But it still requires the minimum value of one second (inset figure) to liquefy as in previous works.

In summary, in looser media or with lower excess pore pressure, the required time to propagate the global failure is longer. This trend is verified by back pressure liquefaction BL and flushing liquefaction FL which are introduced previously with their t_{05} being considered as infinite listed on table 5.2. These cases of BL and FL at low confining pressure less than 30 kPa, exhibited the behaviour without phases II and III. In other

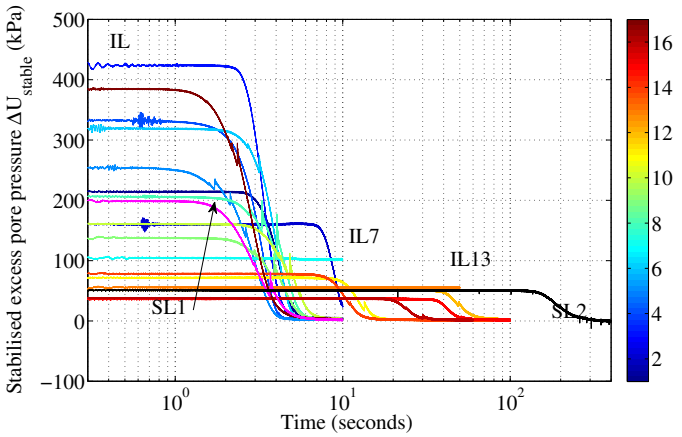

Figure 5.28: Dissipation phase of isotropic liquefaction events.

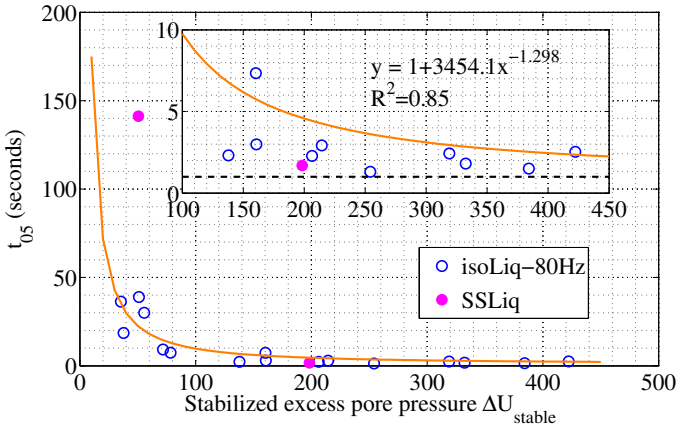

Figure 5.29: Evolution of the stabilised phase according to ΔU_{stable} during isotropic liquefaction events.

words t_{05} is infinite. These infinite points cannot be denoted in the plot. The addition of two stick-slip liquefactions SL (magenta circle) helps to enhance the evolution of t_{05} depending on ΔU_{stable}. But these two SL events are not taken into account in the fitting equation due to their low frequencies ($f_U^{SL_{01}} = 14.2$ Hz, $f_U^{SL_{02}} = 51.2$ Hz). It can be suggested here a regression equation with vertical and horizontal asymptote to approach the ordinate axis and the horizontal line at $t_{05} = 1$s. The following fitting equation is found with good correlation coefficient $R^2 = 0.85$.

$$t_{05} \;=\; 1 + 3454.1(\Delta U_{stable})^{-1.298} \tag{5.2}$$

With constant t_{trans}, the duration of phase II can be estimated from equation 5.2 qualitatively. The experimental dependence of t_{05} on ΔU_{stable} gives the first strong indication toward a better understanding of this still mysterious stabilised phase II. The remaining question is what are the real causes generating this stabilised excess pore pressure ΔU_{stable}?

Lastly the dissipation phase III is clearly seen in figure 5.28. Qualitatively, it seems that the slope of the dissipation process relates to the amplitude of stabilised excess pore pressure ΔU_{stable} which is also the effective triggering stress σ'_{trig} in case of liquefaction. A quantitative exploration is conducted to measure the slope of this phase, k_{diss}. In figure 5.30, the pore pressure dissipation rate is linearly related to the effective triggering stress σ'_{trig}:

$$k_{diss} \;=\; 4.59\ \sigma'_{trig} \tag{5.3}$$

This fitting equation included two stick-slip liquefactions regardless of different frequencies f_U. The duration of dissipation phase III is much longer compared to that of the first transient phase I. The frequency of pore pressure f_U, radically dependent of the sensitive influence of saturation, only impacts the time characteristics of dynamic regime within the transient and stabilised phase.

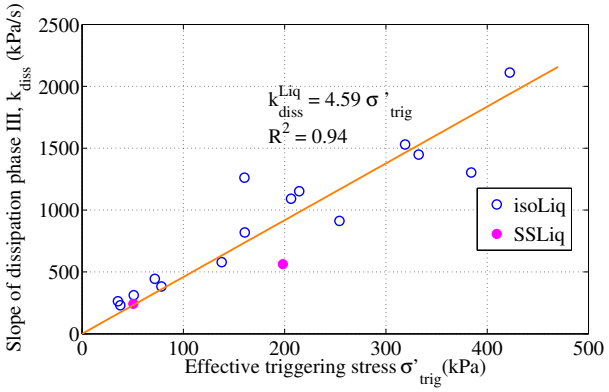

Figure 5.30: Slope of the dissipation phase III, k_{diss} as function of triggering stress σ'_{trig}.

5.5.5.2 Time characterisation of pore pressure during collapses

The time-resolved characteristics of liquefaction need to be improved by a set of collapse events to explore the transition of local failure to global one. The analysis is carried out respectively in phase I, II, III of pore pressure U. Firstly the whole Collapse series

is explored to get the variation of the first transient phase t_{trans} in relevance with the frequency of pore pressure f_U in figure 5.31a. It can be seen that similar to liquefaction series, the time characteristics are strongly affected by the vibration frequency of pore pressure. To keep the same reference to liquefaction series, only collapse at high frequency (larger than 80 Hz) are extracted and analysed in figure 5.31b. The analysis in section 5.5.2 already pointed out the very sensitiveness of the frequency depending on the very narrow variation of saturation. It means all time characteristics relevant to this vibration response of pore pressure is so sensitive with frequency. Therefore, only high frequency collapse are collected. The first transient phase t_{trans} exhibits the independence of stabilised excess pore pressure ΔU_{stable}. The vibration time of pore pressure in collapse or liquefaction share the same mechanism thus t_{trans} is represented by the mean value $< t^{Coll}_{trans} > = 0.1512 \pm 0.0243$ seconds, totally similar to Liquefaction series, $< t^{Liq}_{trans} > \ = 0.199 \pm 0.0534$ seconds (figure 5.27b).

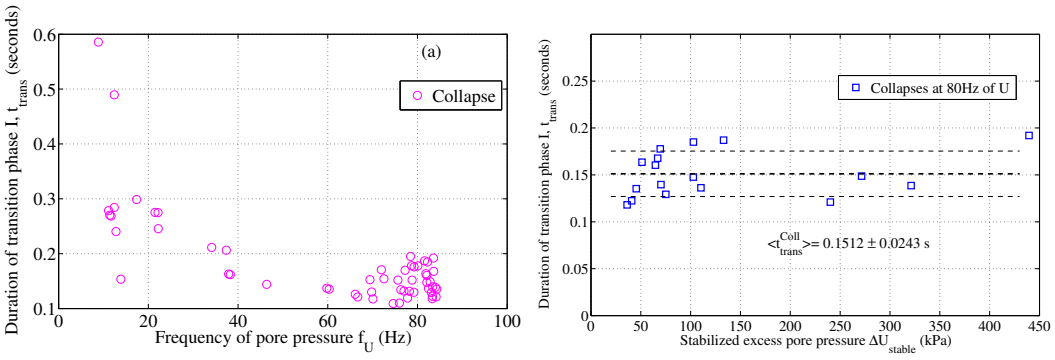

Figure 5.31: Time characteristics of phase I during collapse events.

Next, in the quasi-static stabilised phase II, similar analysis of t_{05} and ΔU^{norm}_{stable} is introduced with collapse events in figure 5.32. The quantity ΔU^{norm}_{stable} is of importance since it denotes the transformation from local instabilities to global failure when ΔU^{norm}_{stable} goes from 0 to 1. t_{05} evolves from the state of smallest collapse $\Delta U^{norm}_{stable} \approx 0$ where $t_{05} \approx < t^{Coll}_{trans} >$ represented by green diamond, to the largest state as isotropic liquefaction symboled by cyan diamond, at which $\Delta U^{norm}_{stable} = 1$ and t_{05} should extend to the threshold of 1 second. The equation satisfied these conditions is written as

$$t_{05} \ = < t^{Coll}_{trans} > -0.0773 \ln(1 - \Delta U^{norm}_{stable}) \tag{5.4}$$

Subsequently, figure 5.33 gives the preliminarily observations on the slope of dissipa-

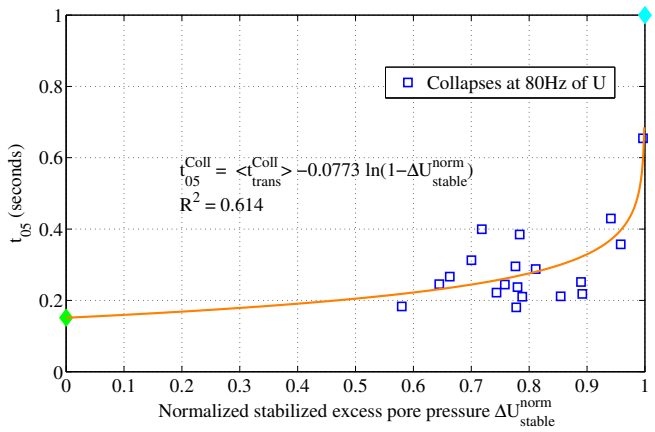

Figure 5.32: Time characteristics of phase II during collapse events.

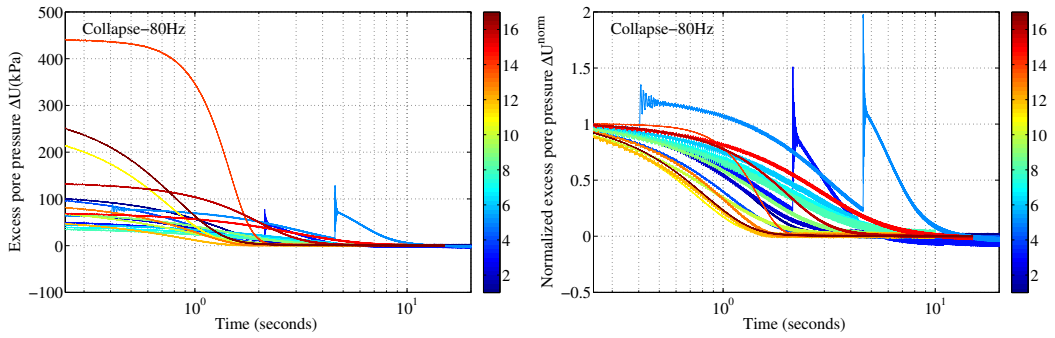

Figure 5.33: Evolution of excess pore pressure ΔU in time within dissipation phase III.

tion phase. The investigation was conducted and no correlation was obtained between the slope and stabilised excess pore pressure ΔU_{stable} in figure 5.33a. After normalisation by ΔU_{stable}, the dissipation process of normalised excess pore pressure ΔU^{norm} is characterised by the normalized slope of phase III, k_{diss}^{norm}. It is clear to see the slope still varies independently of ΔU_{stable}. Figure 5.34 shows the evolution from low k_{diss}^{norm} of small collapse to large k_{diss}^{norm} which nearly liquefies and approaches liquefaction events (cyan diamond). With the existence of very large unloading collapse Coll_{49}, $\Delta U_{stable}^{norm} = 0.997$, this relation as a logarithmic function is established with high correlation coefficient $R^2 = 0.841$.

$$k_{diss}^{norm} = -0.72126 \ln(1 - \Delta U_{stable}^{norm}) \tag{5.5}$$

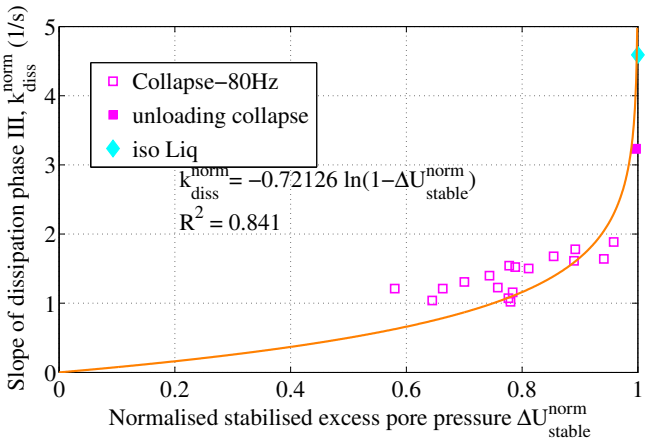

Figure 5.34: Slope of dissipation phase II during collapse events.

5.5.6 Pore pressure in relation to strains

5.5.6.1 Stabilised excess pore pressure ΔU_{stable} and incremental axial strain $\Delta\varepsilon_1$

The incremental axial strain $\Delta\varepsilon_1$ of all liquefaction events is presented in figure 5.35a. It appears to be independent of the magnitude of generated excess pore pressure ΔU_{stable}. Among the own collection of liquefaction events, liquefaction at high frequency and low one have $\Delta\varepsilon_1$ fluctuating around the same mean value. The frequency of pore pressure seems not to notably affect the amplitude of strain during this kind of eventually global failure. The stick-slip liquefaction SL and and static liquefaction UL also locate on the

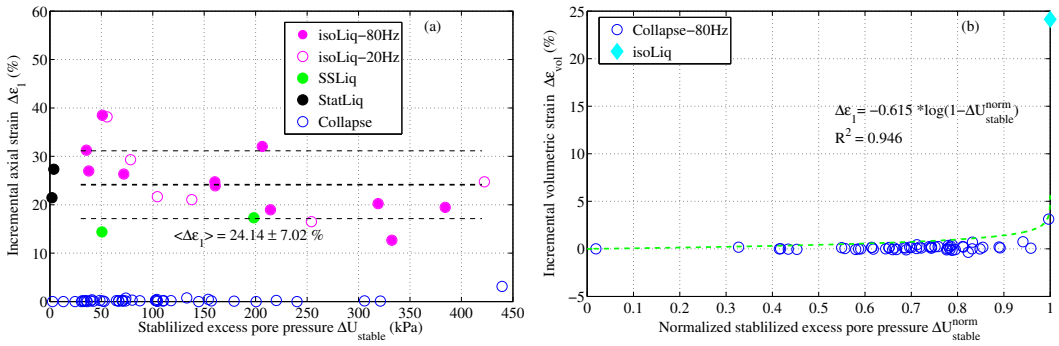

Figure 5.35: Incremental axial strain and stabilised excess pore pressure of liquefaction and collapse.

average range of $\Delta\varepsilon_1$ regardless of drainage and loading condition. All liquefaction

events show very large $\Delta\varepsilon_1$, the mean is estimated as $< \Delta\varepsilon_1^{Liq} > = 24.14 \pm 7.02$ %. Similarly to SS instabilities under shear, all collapses irrespective of frequency of U are investigated. Parameter $\Delta U_{stable}^{norm} = \frac{\Delta U_{stable}}{\sigma_{trig}}$ is introduced to show the evolution of local isotropic collapse ($0 < \Delta U_{stable}^{norm} < 1$) to the global failure ($\Delta U_{stable}^{norm} = 1$). The established relation is the logarithmic function as below.

$$\Delta\varepsilon_1 \;=\; -0.61364 \ln(1 - \Delta U_{stable}^{norm}) \tag{5.6}$$

The discrepancy in frequency did not impact the relation with high correlation coefficient $R^2 = 0.946$ in figure 5.35b. Missing data occurs in the range 5-10% of $\Delta\varepsilon_1$ to fill the gap of fitting curve. In reality, these large events indeed occurred but being lost due to some organisational problems and computer glitches.

5.5.6.2 Stabilised excess pore pressure ΔU_{stable} and incremental volumetric strain $\Delta\varepsilon_{vol}$

The volumetric strain $\Delta\varepsilon_{vol}$ is explored in the same way as $\Delta\varepsilon_1$ in figure 5.36a. The evenly spread and concentration around a constant of $\Delta\varepsilon_{vol}$ of liquefaction events is disclosed. If liquefactions at low frequency are rejected; the mean is not much affected with $< \Delta\varepsilon_{vol}^{Liq} > = 2.864 \pm 0.753$ %. Static liquefaction UL is not included due to constant volume under undrained shearing, $\Delta\varepsilon_{vol} = 0$. For Collapse series, $\Delta\varepsilon_{vol}$ also evolves as logarithmic function to develop into a total failure in figure 5.36b. The exclusion of low frequency collapses improved the correlation coefficient R^2 to 0.882 while with all collapses $R^2 = 0.673$.

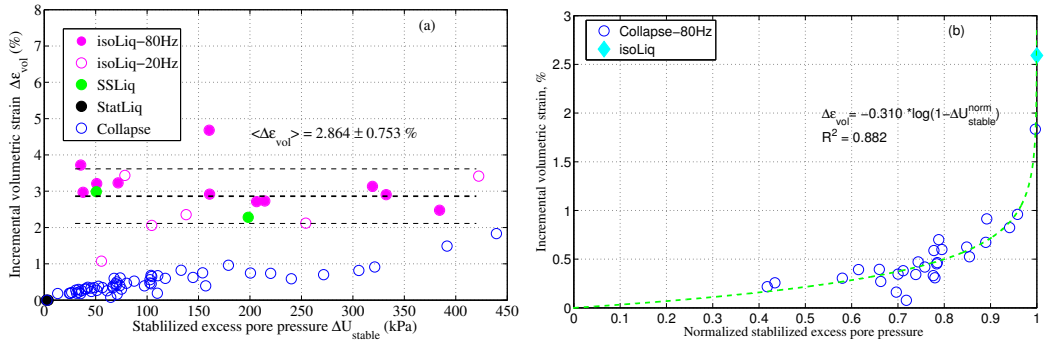

Figure 5.36: Incremental volumetric strain and stabilised excess pore pressure of liquefaction and collapse.

Finally, the evolution of $\Delta\varepsilon_{vol}$ of collapse to liquefaction is fitted by following equation

$$\Delta\varepsilon_{vol} \;=\; -0.31036\,\ln(1-\Delta U^{norm}_{stable}) \tag{5.7}$$

5.5.6.3 Stabilised excess pore pressure ΔU_{stable} and maximum excess pore pressure ΔU_{max}

Quasi-static parameter ΔU_{stable} showed its controlling role in relation to macroscopic strains $\Delta\varepsilon_{vol}$ and $\Delta\varepsilon_1$ and it also is the intermediate state of the dynamic response in phase I and static one in phase III. The link between dynamic maximum excess pore pressure ΔU_{max} and quasi-static ΔU_{stable} is exploited in figure 5.37.

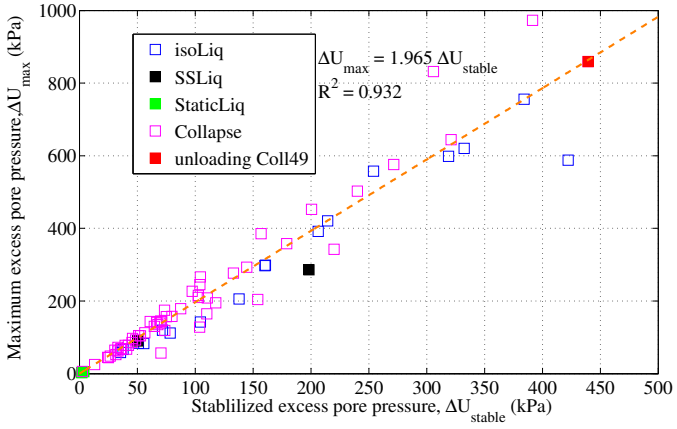

Figure 5.37: Maximum and stabilised excess pore pressure during liquefactions and collapses.

A unique linear relation 5.8 with very high correlation, $R^2 = 0.932$, has been established among isotropic liquefactions IL and all collapse events. The addition of static liquefaction UL and stick-slip liquefaction SL enhances this relation irrespective of the loading and drainage condition.

$$\Delta U_{max} \;=\; 1.965\;\Delta U_{stable} \tag{5.8}$$

In spite of the differences in frequency of pore pressure U, all liquefactions and collapses are surveyed in figure 5.37. In another way, the frequency appears to affect significantly on time characteristics but does not impose the influences on stress and strain measurements for both CIDNC, Liquefaction and Collapse series. The consistency between

collapse and liquefaction series emphasises again that the same mechanisms governs the first transient phase I of collapse and liquefaction phenomenon.

5.5.7 Anisotropy

As indicated in previous works, anisotropy is one of the requirements for the appearance of dynamic instabilities. This characteristic is upgraded in this study with a large number of liquefaction events, a diversified new subtypes of liquefaction, and with high resolution data. The same method of determination (figure 4.28 of section 4.4.5) of dynamic anisotropy coefficient i_{Dyn} and static one i_{stat} is applied. The results are presented in figure 5.38. Firstly for liquefactions in figure 5.38a, the dynamic anisotropy coefficient i_{Dyn}^{Liq} distributes sparsely in relevance with ΔU_{stable}, some isotropic liquefaction events show extremely high i_{Dyn}^{Liq} which can be considered as infinite since the evolution of $\Delta\varepsilon_{vol}$ and $\Delta\varepsilon_1$ is mostly vertically (figure 5.8d). While the static anisotropy coefficient i_{stat}^{Liq} in figure 5.38b is remarkably smaller than 3 since $\Delta\varepsilon_1$ in global failure is too large up to 30%, an order of magnitude larger than $\Delta\varepsilon_{vol}$ around 3%.

For collapse series in figure 5.38c,d, the situation is totally different, i_{Dyn}^{Coll} is larger than i_{Stat}^{Coll} but both of them are larger than 3 and their amplitudes are not too much dissimilar. In both series of collapse and liquefaction and in both dynamic or static regime, and irrespective of the isotropic loading, the material exhibits strong anisotropy characteristics.

The statistics of i_{stat} and i_{Dyn} are estimated by the whole data regardless of the frequency of pore pressure U since the group of low frequency events (blue circle and square) does not considerably affect the scatter of data. No quantitative relation is established for i_{stat} and i_{Dyn} with the key measurement ΔU_{stable} due to the complexity of detailed evolution of $\Delta\varepsilon_1$ and $\Delta\varepsilon_{vol}$. However, i_{stat} and i_{Dyn} confirm the strong anisotropy of material like other previous works in shear under both drained and undrained condition, as well as in isotropic loading.

5.5.8 Disscussion

In this study, high resolution data in various loadings and drainage conditions as well as the saturation, the size of glass beads, the range of stresses, highlighted the occurrence of local and global instabilities. Within the studied range of 20-500 kPa, it appears

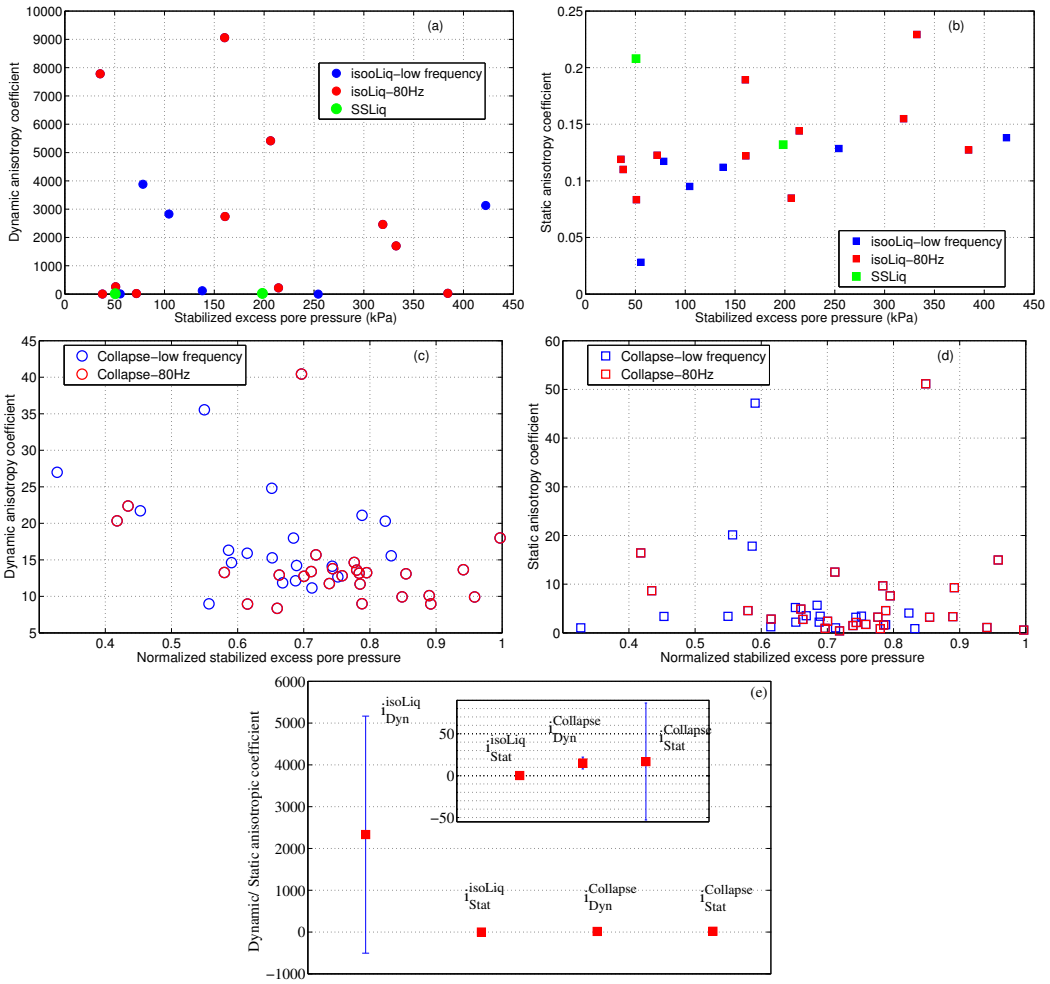

Figure 5.38: Dynamic and static anisotropy coefficients during liquefactions and collapses.

that larger triggering stress σ'_{trig} leads to larger generated ΔU_{stable} (figure 5.39a). A specific very large collapse Coll_{49} ($\Delta U_{stable} = 439.5$ kPa $\approx \sigma'_{trig} = 440.9$ kPa), mostly lying on liquefaction line (solid magenta squares) has not liquefied due to the lack of time condition of t_{trans} less than 1s. Combined with the evolution of triggering void ratio e_{trig} and ΔU_{stable} (figure 5.39b) for isotropic collapse, one can see that denser material at higher pressure creates larger ΔU_{stable}. This is coherent to CIDNC series that higher confining pressure results in larger stick-slip with higher generated stabilised excess pore pressure ΔU_{stable}, excepting the precursor events which are out of scope of this work.

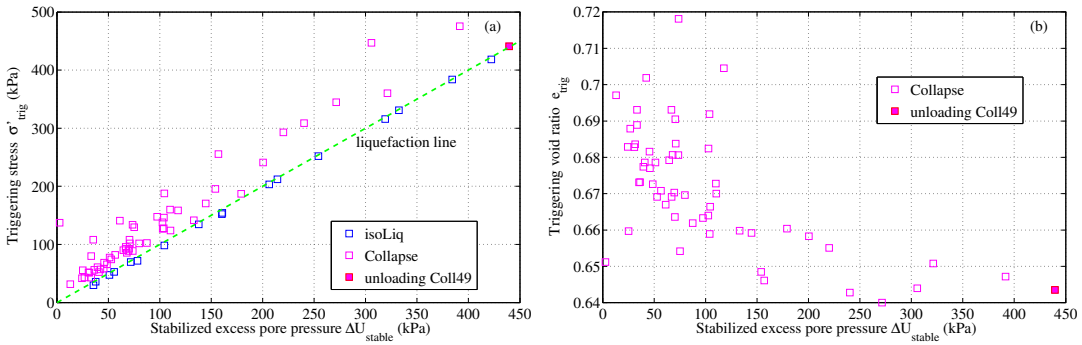

Figure 5.39: Triggering state in relevance with generated ΔU_{stable}.

One of the most important parameters controlling the frequency of pore pressure is the saturation of sample. The second parameter is the pressure which well explained the variation of frequency between 20 and 80 Hz. This analysis filled the missing point in CIDNC series which only has the frequency at either 20 or 80 Hz. Through all analyses on time, stress and strain, it can be stated that the frequency of pore pressure U, more radically the degree of saturation, only notably impacts on time characteristics of phase I and II for example t_{trans}, t_{05}. It interprets the independence of frequency on the relations, $(\Delta U^{norm}_{stable} \sim \Delta\varepsilon_1)$, $(\Delta U^{norm}_{stable} \sim \Delta\varepsilon_{vol})$, $(\Delta U^{norm}_{stable} \sim \Delta q^{norm})$, of macroscopic amplitudes of other stress or strain measurements.

The link between local instabilities and global ones is very strong from stick-slip to collapse and finally liquefaction in stress, strain and time characteristics. Remind the boundary surface of stick-slip in stress path plane (figure 4.33), in which normalised parameter, $\frac{p'_{stable}}{p'_{crit}}$, is of importance to control the behaviour of stick-slip. This parameter presents in all equations of time characteristics of stick-slips. Consider a very large stick-slip SS_{01} but not liquefied, where $q_{stable} = 0$, p'_{crit} turns to p_0 (M goes to 0), the shearing state translates to isotropic state, $\frac{p'_{stable}}{p'_{crit}}$ is rewritten as:

$$\frac{p'_{stable}}{p'_{crit}} = \frac{p_0 + \frac{q_{stable}}{3} - \Delta U_{stable}}{p_0 \frac{3}{3-M}} = \frac{p_0 - \Delta U_{stable}}{p_0} = (1 - \Delta U^{norm}_{stable}) \tag{5.9}$$

Thus the controlling parameter of stick-slip transforms to ΔU^{norm}_{stable} which is the controlling parameter in most equations of collapse series. Subsequently collapse event connects to liquefaction when ΔU^{norm}_{stable} evolves to the limit of 1 of the liquefied state. Lastly within the variation of liquefaction events, the controlling parameter is $\Delta U_{stable} (= \sigma'_{trig})$.

It can be stated that pore pressure plays the key role in saturated granular medium. Additionally, even in case of deviatoric stress q totally dropping to zero, it does not mean $\Delta U^{norm}_{stable} = 1$ to create a stick-slip liquefaction SL, thus ΔU_{stable} is still uncontrolled in the zone of transition from solid to fluid state.

Back to equation 4.6

$$\Delta t_{05} \;=\; -0.06186 \ln(\frac{p'_{stable}}{p'_{crit}})$$

in which the smooth evolution of duration of phase II, Δt_{05}, from a stick-slip event with nonzero deviatoric stress q to the largest stick-slip event transforming to isotropic state is described at the intercept where $\frac{p'_{stable}}{p'_{crit}} = 0$. At that state the behaviour of pore pressure U must approach a very large collapse and nearly liquefaction as test Coll_{49}:

$$\frac{p'_{stable}}{p'_{crit}} \;=\; (1 - \Delta U^{norm}_{stable}) \;=\; 1 - 0.9968 \;=\; 0.0032$$

The prediction for this Coll_{49} by equation 4.6 is Δt_{05} = -0.06186 ln(0.0032) = 0.3554 seconds, which is in well agreement to the measured Δt_{05} = 0.424 seconds of Coll_{49}.

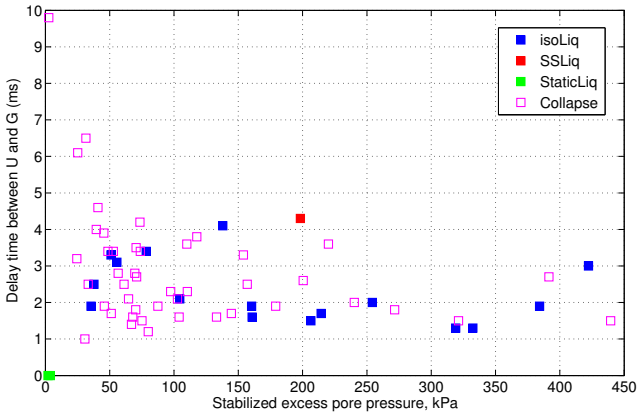

Figure 5.40: Time delay between acceleration G and excess pore pressure U of all kinds of liquefaction and collapse.

The presence of different liquefactions like back pressure liquefaction BL, flushing liquefaction FL, static liquefaction UL at very low confining pressure elucidates the tendency of t_{05} that under low pressure it takes longer to propagate the $\Delta U_{stable} = p'_0$ throughout the sample to liquefy. Especially the distinction in amplitude, frequency and time development of vertical acceleration G, lateral sound pressure M, lateral vibration V, pore pressure U measurements of static liquefaction UL implies different

mechanisms of dynamic liquefaction and static one. To be more specific, in undrained shearing the pore pressure globally rises in a static regime as the response to the contractive behaviour of grains. Only high time-resolved data exposed the detail at the unstable state namely static liquefaction, in which pore pressure climbs up gradually and statically without any significant modification of lateral vibration V and lateral sound pressure M. When pore pressure U reaches the confining pressure p'_0, the effective stress supported by grain contact vanished, consequently the soil fails with large deformation. The sample cannot sustain itself without any contact-network and falls down with very small amplitude of acceleration G and low frequency of pore pressure U as the consequence of static regime. This indicates probably a gentle destruction of the granular structure with weak contacts. On the contrary, in dynamic stick-slip liquefaction SL, the drop of deviatoric stress q happens simultaneously with large amplitude of acceleration G, indicating a rapid and brutal destruction of granular structure with strong contacts. This abrupt drop is confirmed by microphone signal M, vibrometer V a little later, then pore pressure suddenly surges up and vibrates. The systematic positive time delay detected between acceleration G and pore pressure U is presented in figure 5.40 as the evidence that pore pressure is not the cause of liquefaction. It merely accelerates and facilitates the liquefaction process. Specifically for stick-slip liquefaction, it requires three conditions to liquefy: (i) The deviatoric stress q must drop to zero ($q = 0$), the shearing state returns to isotropic stress state. However there are many first stick-slips having zero deviatoric stress and no liquefaction. (ii) The pore pressure U must cancel the confining pressure p'_0, hence the vanishing case of the effective stress between grains $\sigma' = 0$. And (iii) the duration of the stabilised phase t_{05} must exceed 1 second.

The detailed behaviour highlighted the fact that liquefaction phenomenon always happens in isotropic stress state. With the presence of shear stress, it still moves to isotropic state to liquefy.

One hypothesis suggested here to explain the liquefaction is a sudden rearrangement of the grain skeleton resulting in the drop of acceleration signal within only 1-2 ms. The grain structure actually deforms creating volumetric strain of the grain frame, but the whole volume of two phases, grains and fluid, is still constant. It means the volume of the pore inside the grain structure decreases leading to the increase of pore pressure. The dominant vibration of pore pressure in the first phase I is left aside

without any explanation, but the excess pore pressure indeed surges up to reach the stabilised value ΔU_{stable}. This amplitude of ΔU_{stable} is controlled by the amplitude of G (chapter 6). Within the duration from the drop of acceleration G until the stabilised state of pore pressure, around 200 ms, the assembly responses as an undrained system. Then the pore pressure maintains at the stabilised state. Note that the value of ΔU_{stable} reaching confining pressure p'_0 is detected at the top of sample and it is a dead end. The pore pressure at the bottom is always lower since it is the unique drainage way of the sample. The maintaining state of $\Delta U_{stable} = p'_0$ at the top needs to propagate to a certain sufficient region inside the sample to create the total failure, not necessarily $\Delta U_{stable} = p'_0$ at every point in the sample. The duration of this phase II is impacted by the triggering moment of the dissipation phase. The dissipation is delayed compared to the extremely fast response of the skeleton and it also occurs at the bottom first (the top is a dead end). The water goes out of the sample with the beginning of pore pressure dissipation and the volumetric strain is detected. The dissipation takes place stronger at the bottom and propagates upwards to release the excess pore pressure and save the sample. The other process is the maintaining of $\Delta U_{stable} = p'_0$ at the top and propagate downwards. The competition between these two processes governs the level of failure. The larger generated $\Delta U_{stable} = p'_0$ at the top corresponds to a larger gradient of pore pressure between top and bottom. Thus a stronger dissipation process with Darcy's law. This can explain the relation of the duration of phase II, t_{05}, as a function of ΔU_{stable} (equation 5.4) in which at low ΔU_{stable} t_{05} is longer prior to the decreasing of pore pressure at the top. The competition between these two processes also explains some collapse events with very large $\Delta U_{stable} = p'_0$ (e.g. Coll_{49}) with no liquefaction. Because large magnitude of ΔU_{stable} means large gradient, the dissipation phase at the bottom is sufficiently strong to release the excess pore pressure faster in a larger region compared to the zone keeping $\Delta U_{stable} = p'_0$ at the top. As a result, the sample only locally collapses.

5.6 Conclusions

This study provides a comprehensive analysis of all new kinds of liquefaction with the support of collapse series to identify the connections between local and global failures, triaxial compression shearing and isotropic loading. Associated with the CIDNC series

in chapter 4, it draws a global and detailed picture of instabilities. New never seen before **subtypes of liquefaction** are investigated including isotropic liquefaction IL, stick-slip liquefaction SL, static liquefaction UL, back pressure BL, flushing liquefaction FL, imbibition liquefaction WL. Basic distinctions of various kinds of liquefaction are listed in following table 5.5 with essential parameters.

Table 5.5: Recapitulation on fundamental characteristics of liquefactions.

	IL	SL	UL	BL	FL	WL
Dynamic/Static behavior	D	D	S	D	S	S
Pore pressure frequency (Hz)	80	80	0	-	0	0
Vertical top cap acceleration (g)	10	10	0	0.01	0.1	0.01

The presence of vertical top cap acceleration detected in all dynamic liquefactions prior to the surge of pore pressure strongly suggests that pore pressure is not the cause of the phenomenon. The most striking distinguished points are the magnitude of acceleration G and the vibration regime of the pore pressure. Isotropic liquefaction IL and stick-slip liquefaction SL, despite the presence of deviatoric stress q in the first stick-slip, have the largest acceleration G at the range of 10 g, three orders of magnitude larger than back pressure liquefaction BL, flushing liquefaction FL and imbibition liquefaction WL. Specially, the strong distinction between dynamic liquefaction and static liquefaction is that in static regime no acceleration is acquired and there is no vibration of pore pressure.

Additionally, this study also provided the proof of liquefactions even in not fully saturated media (Skempton's coefficient B = 0.85-0.95). On the objective of fully saturated medium, at the dominant frequency of 80 Hz consistent with the CIDNC series, all time characteristics of collapses are estimated from the key parameter ΔU^{norm}_{stable}. The first transient phase I is characterised by a constant $< t^{Coll}_{trans} >$. The stabilised state t_{05} is estimated from ΔU^{norm}_{stable} by equation 5.4. The duration of the dissipation phase is identified by k^{norm}_{diss} in equation 5.5. The magnitude of excess pore pressure ΔU^{norm}_{stable} relates to other strain measurements which are respectively incremental axial strain $\Delta\varepsilon_1$, incremental volumetric strain $\Delta\varepsilon_{vol}$ by equations 5.6 and 5.7. It means that the key parameter ΔU^{norm}_{stable} helped to recover the remaining measurements.

Similarly for isotropic liquefactions, substantial relations are constructed by the key parameter ΔU_{stable}. The duration of the first transient phase I t_{trans}^{Liq} is represented by a constant mean value. The intermediate transient phase II t_{05} is estimated from ΔU_{stable} by equation 5.2. The dissipation phase III is characterised by the slope k_{diss} linearly proportional to effective triggering stress σ'_{trig} by equation 5.3. At the end of liquefaction events, the magnitude of incremental axial stress $\Delta\varepsilon_1$, incremental volumetric strain $\Delta\varepsilon_{vol}$ are considered as constants. The same relation between quasi-static pore pressure ΔU_{stable} and dynamic one ΔU_{max} in equation 5.8 is a quantitative proof of the same mechanisms controlling the vibration of pore pressure in the first transient phase.

However like stick-slip instabilities, the unknown determination of the drop of deviatoric stress Δq and of the triggering deviatoric stress q_{trig} prevents a full understanding of stick-slip behaviour. In isotropic instabilities the generated excess pore pressure ΔU_{stable} and triggering stress σ'_{trig} are still unpredictable.

The triggering mechanisms leading to the drop of acceleration G are still uncovered, but the void ratio can be considered as the initial parameter showing the potential of liquefaction with the new threshold established in this study. The long maintaining of stabilised phase II is found as a function of stabilised excess pore pressure ΔU_{stable} but the mechanism is still mysterious. The cause of the vibration of pore pressure U in phase I is still unknown but an advanced step is revealed that the transient fluctuation of pore pressure is not the acoustic resonance of pore fluid with the grains, since it is independent of the slenderness of sample and of the grain size. The degree of saturation and pressure are two main parameters governing the frequency of pore pressure in that phase I.

6

Acoustic signature of the instabilities on saturated granular material

6.1 Introduction

Distinct audible crackling noises were systematically emitted and heard for every granular instability, regardless of loading (isotropic or triaxial compression), of drainage (drained or undrained), of saturation (dry, wet or saturated), of shearing conditions (triaxial or annular apparatus) and even particle size distribution (mono or poly-dispersed particles). Equipped with a new set of passive acoustic sensors (vertical piezoelectric accelerometer, lateral prepolarized microphones) complemented with a lateral laser vibrometer, this chapter deals with passive measurements of acoustic emission (AE) in low frequency range, below 5 kHz, of isotropic collapse, compression stick-slip and even different kinds of liquefaction failure (static and dynamic, especially the isotropic liquefaction) in triaxial environment.

The primary objective of this chapter is to relate quantitatively some macroscopic stress and strain parameters of the instability event (stress drop, effective triggering stress), excess pore pressure, incremental axial and volumetric strain) to passive acoustic measurements (event magnitude and acoustic energy). This chapter also explores the low-frequency vibrational mode of the granular structure with the help of Fast Fourier Transformation (FFT), Continuous Cauchy Wavelet Transform (CCWT) and

numerical analyses of computational model using Comsol. Some elastic parameters of a homogeneous structure can be identified using dominant frequencies.

6.2 Experimental information

In this study, previous series are exploited including CIDNC, Liquefaction and Collapse series in which $Coll_{01}$ to $Coll_{03}$, $Coll_{34}$ to $Coll_{37}$ lacking of lateral sound measurements are excluded in some analyses. One additional test with mixed material is added to give some insights into the factors influencing the frequency content. The material comprises 50 % of 0.7 mm and 50 % of 0.4 mm of glass beads. The testing procedure is similar to the standard CID test. Essential information of previous series are already introduced, excepting the test for mixed beads as table 6.1.

Table 6.1: Summarized characteristics of a full CID test for binary mixture of 0.7 and 0.4 mm beads at 500 kPa.

Test	$\sigma_3^{'}$ (kPa)	Number of isotropic collapse	Number of SS	e_{20}	e_c	ϕ ($\circ$)	Brief description
$Dmix_{01}$	500	4	33	0.643	0.609	31.04±3.1	wide ranged amplitude SS, B = 0.95

Figure 6.1 presents the global behaviour of collapse during isotropic compression and SS during drained triaxial compression shearing. The compressibility of test $Dmix_{01}$ has five collapse events before reaching the targeted confining pressure of 500 kPa with C_c in the range of 0.0098 to 0.0170, not too different from mono disperse beads of 0.7 mm (C_c = 0.018). The internal frictional angle is 31.04 ± 3.1 degrees, consistent to the case of 0.7 mm beads.

Under triaxial compression the stress-strain behaviour still have stick-slips with deviatoric stress drop down to zero. Globally, though the initial void ratio of shearing stage, e_c = 0.605, is lower than other studied tests in CIDNC series, the global behaviour during shearing is similar to that of 0.7 mm beads.

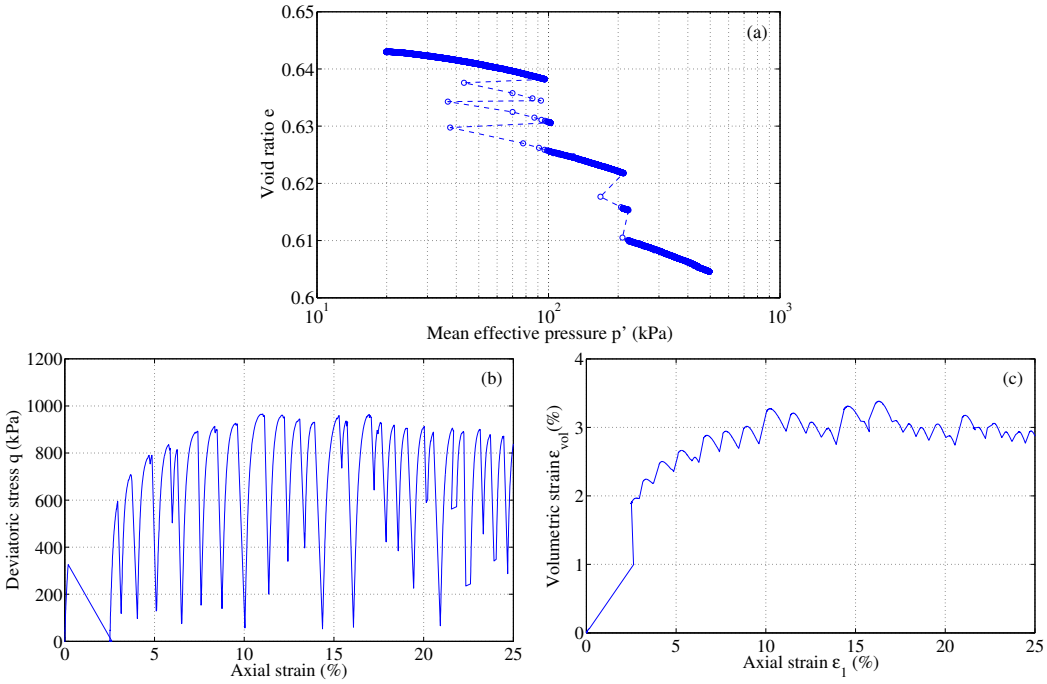

Figure 6.1: Global behaviour in (a) isotropic compression and drained shearing (b,c) of a binary mixture.

A brief notation on the parameter of AE signal is introduced in figure 6.2 in which the representative fluctuation of vertical top cap acceleration G begins at the stable state prior to the instability. Then G signal varies with the first peak of which the amplitude is named G_{01} (similarly M_{01}, V_{01} for lateral sound pressure and lateral vibration). The positive extremum is G_{max} (M_{max}, V_{max}) and the negative minimum is G_{min} (M_{min}, V_{min}).

6.3 Testing results

6.3.1 Global time series of stress associated with G, M, V

One concern of the application of acoustic measurement is the correlation of acoustic signal and other mechanical measurements. Accordingly, figure 6.3 shows the synchronised time series of deviatoric stress q, pore pressure U, vertical top cap acceleration G, lateral sound pressure M and lateral vibration V during a series of stick-slip events in test N120 (CIDNC series). At any time, q, U, G, M, V are synchronously recorded

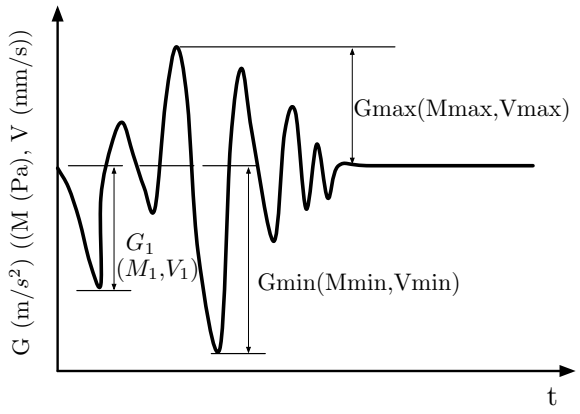

Figure 6.2: Notations of acoustic measurements.

together. There are some bursts of AE signal before the large SS event, considered as precursors. The resolution of acquired data is inspected by progressively reducing the time scale of a typical large SS event (in black rectangle in figure 6.3).

The detailed temporal evolutions of AE measurements in a representative collapse ($Coll_{21}$), isotropic liquefaction (IL_{17}) and large SS (SS_{01}-N50) are separately presented in figure 6.4 to show the potential links between mechanical and acoustic measurements. All of them are systematically consistent, significant, coherent to each other. This representation provides valuable information but the primary significance is represented by 3 characteristics : the amplitude, the frequency content and the duration of the motion. Basically in liquefaction, collapse and stick-slip event, the top cap acceleration G drops first then the lateral sound pressure M and lateral vibration V signals vary subsequently after the same range of time delay. The maximum amplitude of G, M, V in collapse event is smallest, larger in isotropic liquefaction and largest in SS event with the presence of deviatoric stress. The time origin of the variation of G is determined manually by eyes with the resolution of 0.1 ms. The strong vibration of G briefly takes place within 10 ms. This very large SS exhibits the pulse-like feature of G while in collapse and liquefaction G response like damping vibration. Subsequent analysis on frequency content is helpful to give further information.

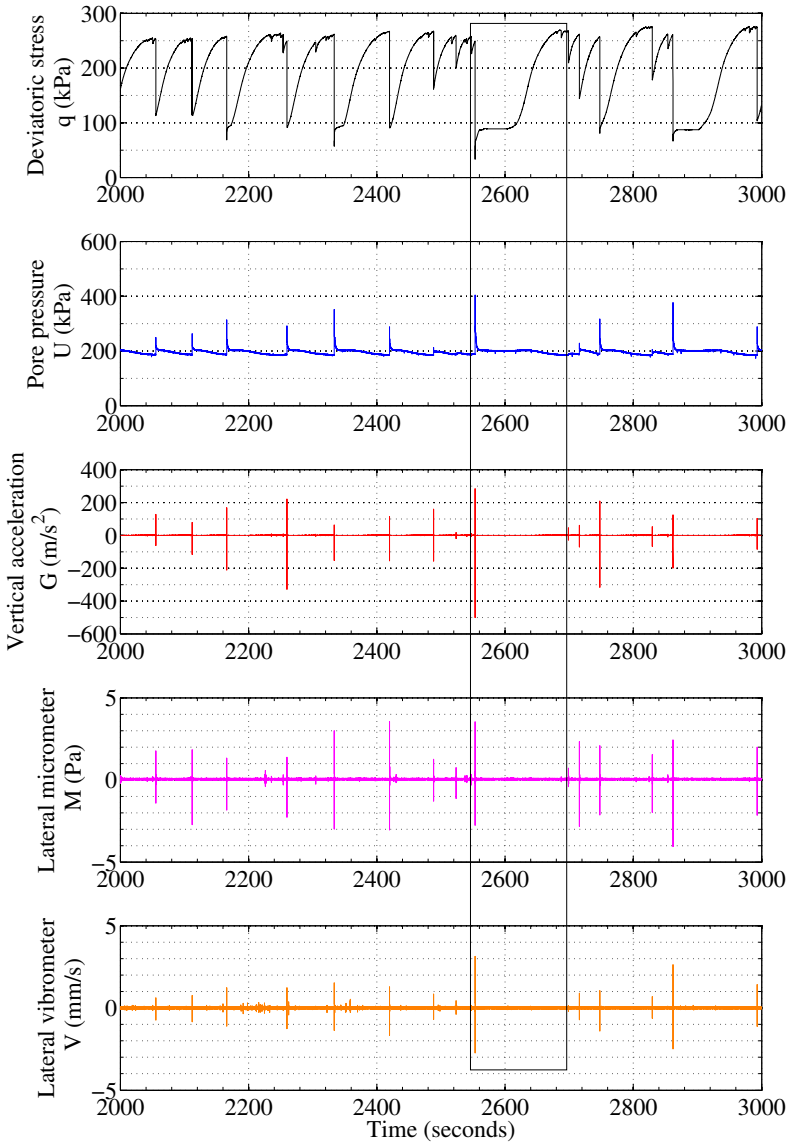

Figure 6.3: Mechanical and acoustical measurements within 1000 seconds of test N120-CIDNC series.

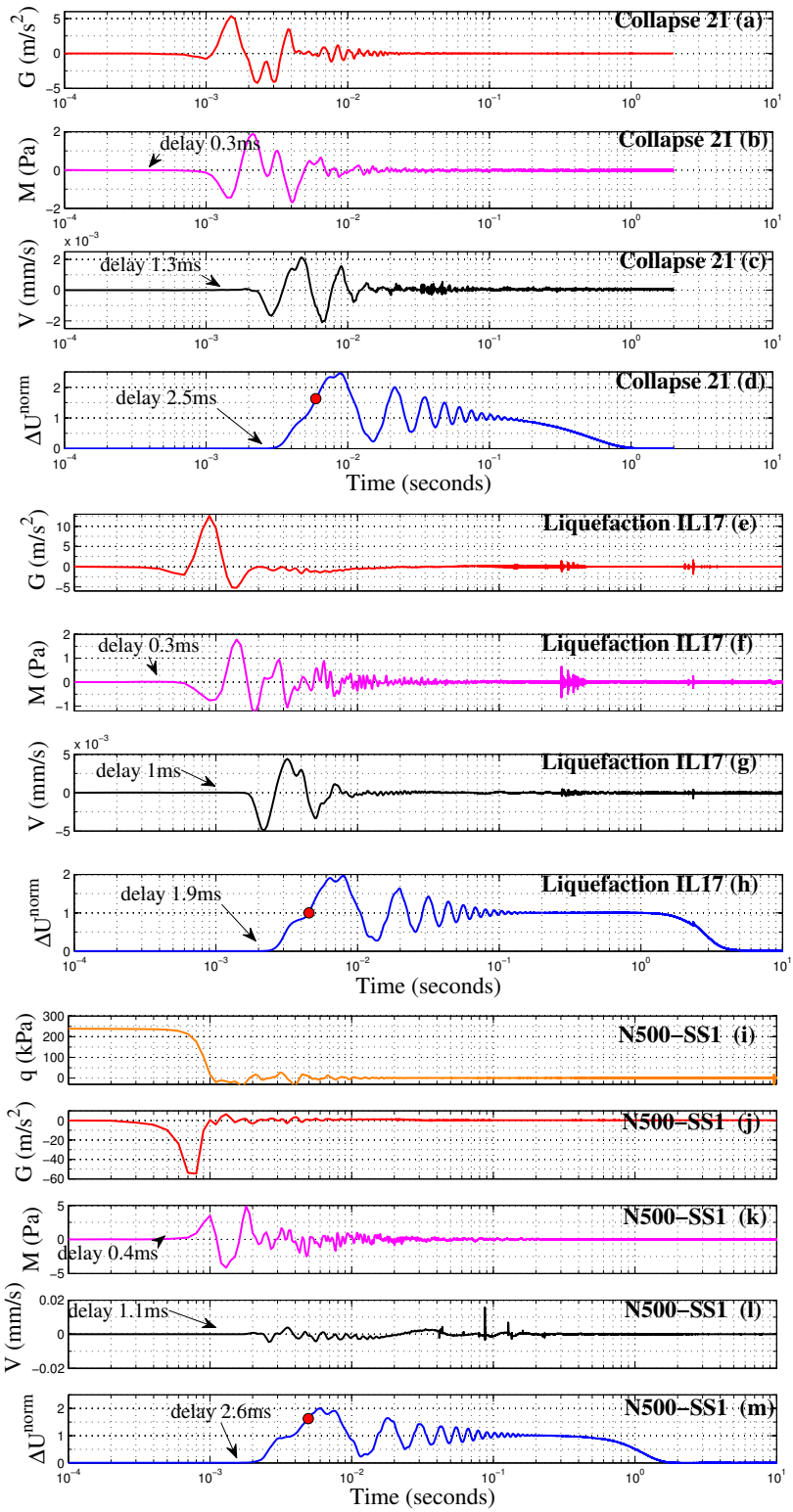

Figure 6.4: Detailed temporal evolution of vertical acceleration (G), lateral sound pressure (M), lateral vibration (V) and normalised excess pore pressure (ΔU^{norm}) during an isotropic collapse Coll_{21} at triggering stress of 255.3 kPa (a to d), isotropic liquefaction IL_{17} at 383.9 kPa (e to h) and one large SS_{01} of test N500 at confining pressure of 500 kPa (i to m).

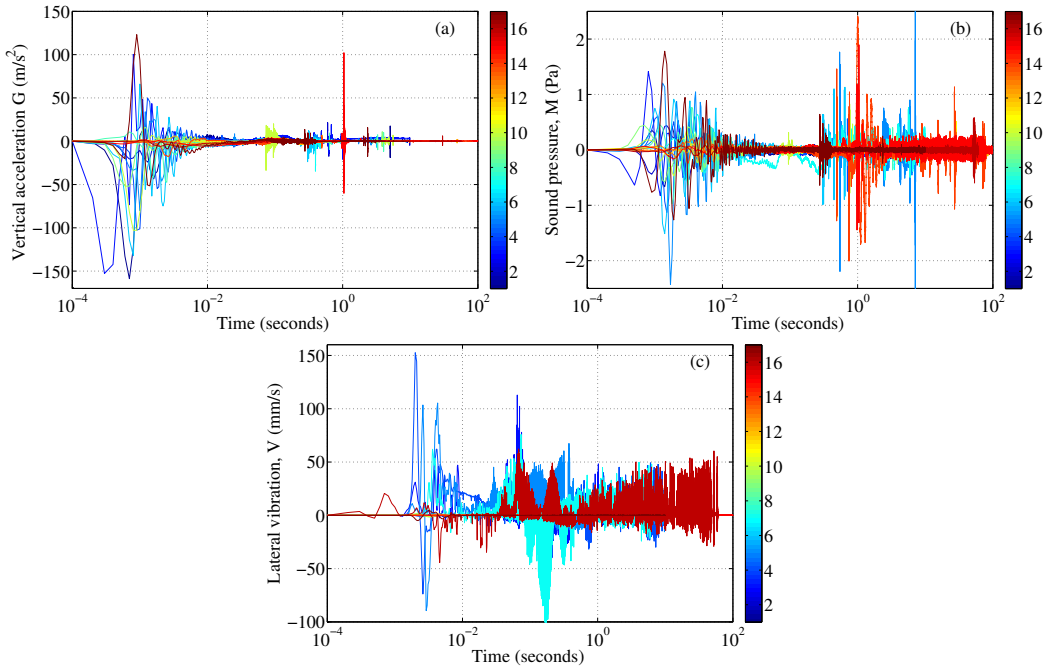

Figure 6.5: Detailed temporal evolution of G, M, V measurements of isotropic liquefaction series.

6.3.2 Times series of G, M, V in drained compression, liquefaction and collapse series

In all cases, the top cap vertical acceleration shows a peak of one single cycle being remarkably large compared to other quickly damping cycles. Within this study the feature of single-cycle peak is dominant, then the maximum peak amplitude is sufficient to characterise the dynamic motion.

For isotropic instabilities in figures 6.5 and 6.6, the maximum amplitude of G is 15 g for liquefaction. The isotropic collapse reaches lower G excepting the extreme large unloading collapse at triggering stress of 441 kPa reaching acceleration G up to 27 g. The average duration of acceleration signal is within 20 ms followed by some aftershocks; this should be noticed to localise the length of signal in calculation of frequency and to assess and recognise the dominant frequency. The larger peak amplitude of G is on negative direction corresponding to downward motion and it is not always but frequently the first drop of G. The measurement of lateral sound pressure M is quite symmetric and the duration of signal is longer than G. The lateral vibration V shows

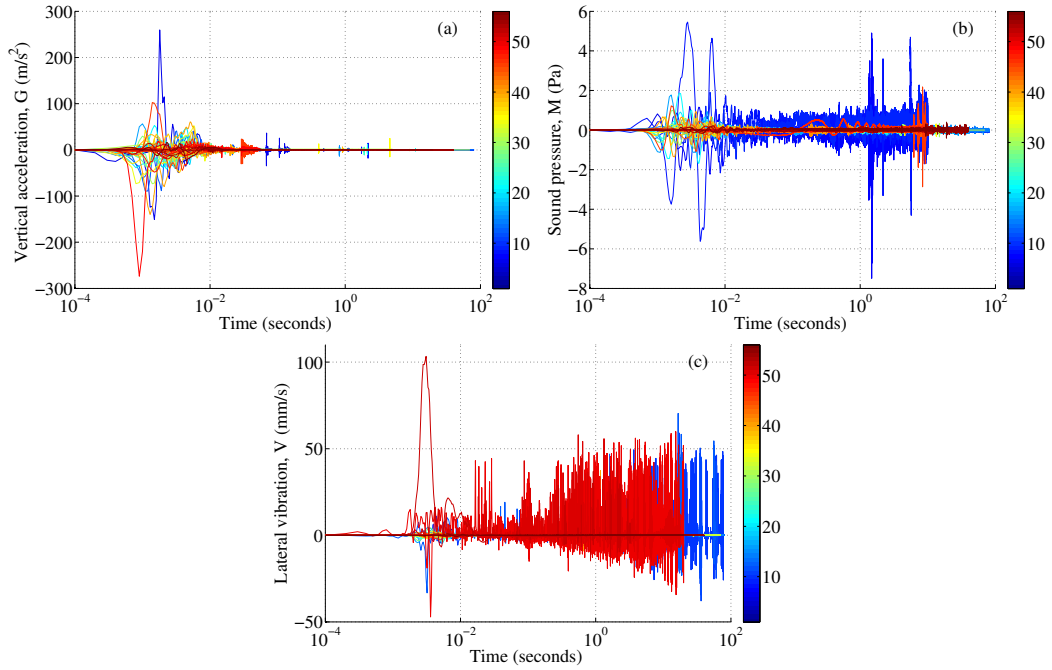

Figure 6.6: Detailed temporal evolution of G, M, V measurements of Collapse series.

significant larger amplitude in positive direction meaning the sample mostly bulges out. One difficulty when using vibrometer is that the incident ray must be orthogonal to the surface to capture correctly the reflecting ray and deliver the clearest signal. But during long time testing the lateral displacement of sample is quite large and not homogeneous along the height of the cylindrical sample, the generator of cylinder surface is not exactly vertical. Therefore the incident ray of vibrometer is no longer orthogonal to the surface, creating a disturbance of V signal during testing procedure. Sometimes, careful manually adjustment is needed during the testing procedure.

For stick-slip events, the maximum of G is one order of magnitude larger than that of isotropic instabilities. The presence of axial stress amplified all responses in magnitude and duration of all signals of V, M, G. The representative behaviour of G looks like an underdamped system with the first largest peak then the decaying vibration towards the equilibrium state. Distinct from acceleration G, measurement M shows the response with the gradually initial growth in amplitude, reaching the peak then a decreasing stage. Since the microphone was installed outside the triaxial chamber, the growing stage of M signal is due to the wave propagation process. Some rare abnormal features

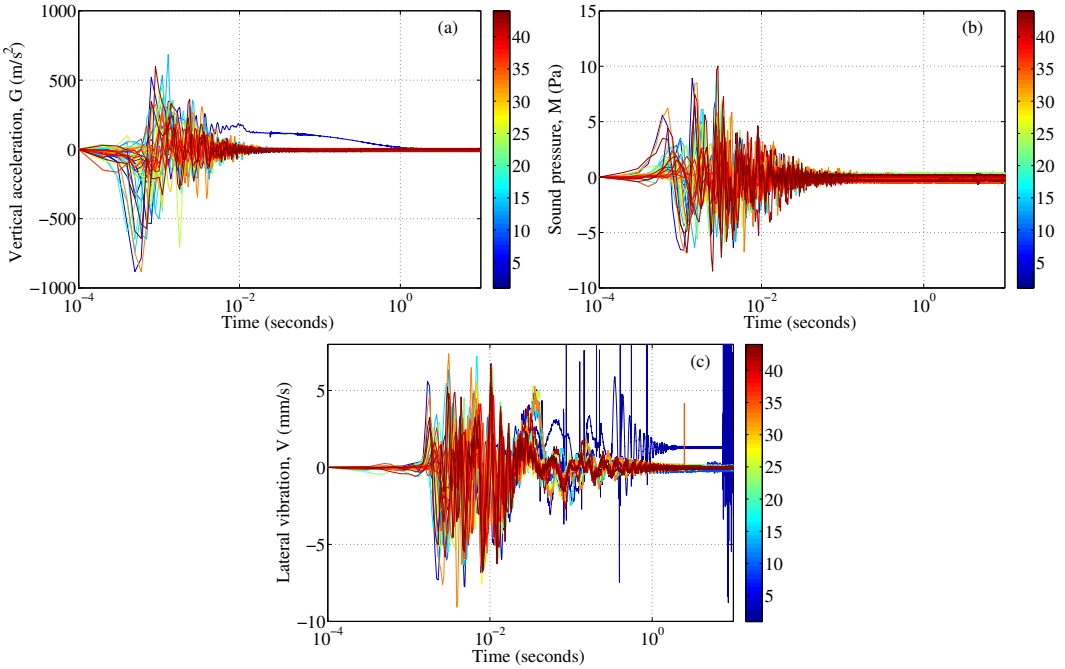

Figure 6.7: Detailed temporal evolution of G, M, V measurements of stick-slips at confining pressure of 500 kPa.

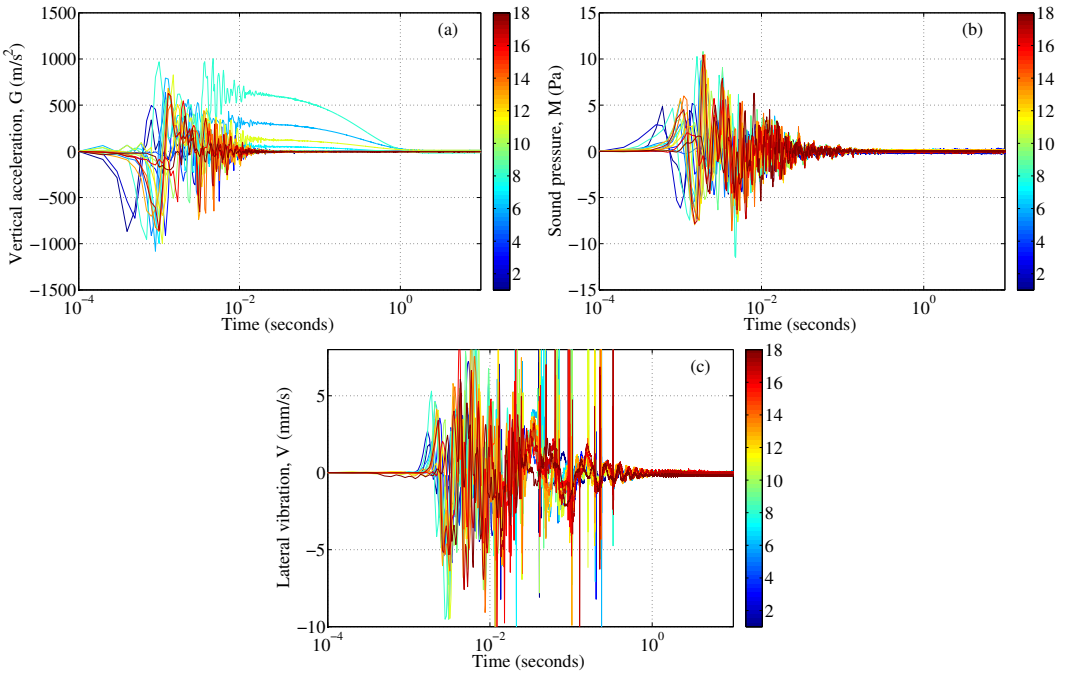

Figure 6.8: Detailed temporal evolution of G, M, V measurements of stick-slips at confining pressure of 400 kPa.

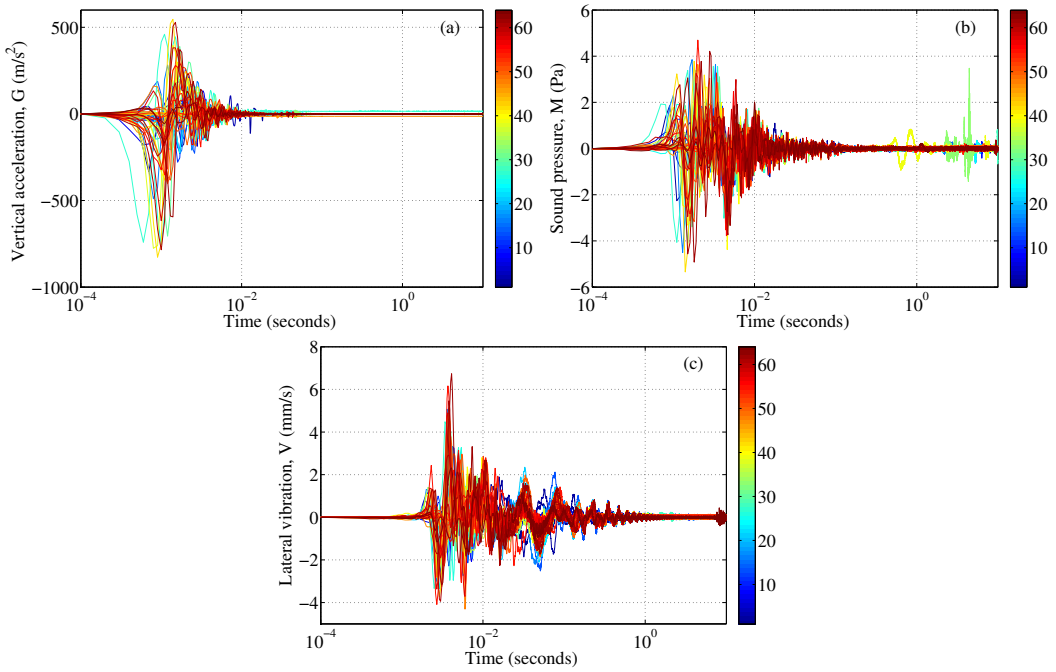

Figure 6.9: Detailed temporal evolution of G, M, V measurements of stick-slips at confining pressure of 200 kPa.

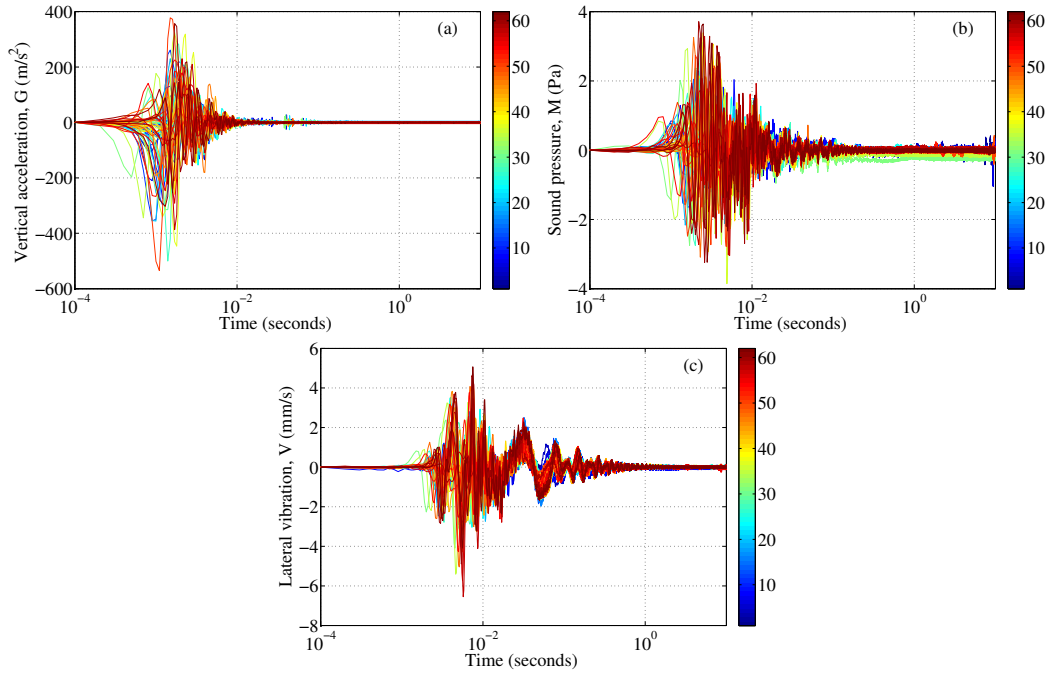

Figure 6.10: Detailed temporal evolution of G, M, V measurements of stick-slips at confining pressure of 120 kPa.

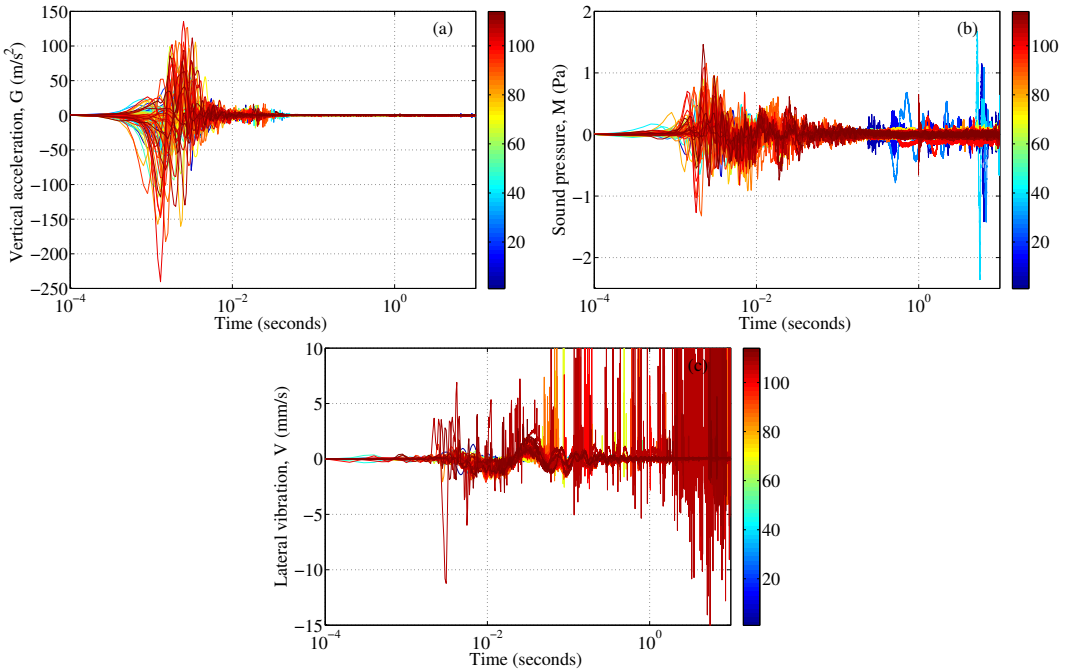

Figure 6.11: Detailed temporal evolution of G, M, V measurements of stick-slips at confining pressure of 50 kPa.

of G are observed (figures 6.7a and 6.8a): after the abrupt variation within 10 ms, G stabilises at non zero value then gradually turning back to the equilibrium state after one second.

6.4 Method of analysis

One of the main assignments is to extract the dynamic parameters from the mechanical and acoustical measurements and show how they relate to each other in different conditions. The essential parameter of a multi degrees-of-freedom system is its frequency. First, a common Fast Fourier Transformation (FFT) method is employed; then a complementary Continuous Wavelet Transformation (CWT) is applied to recognise the most energetic frequencies and to localise them within the initial transient duration of signals.

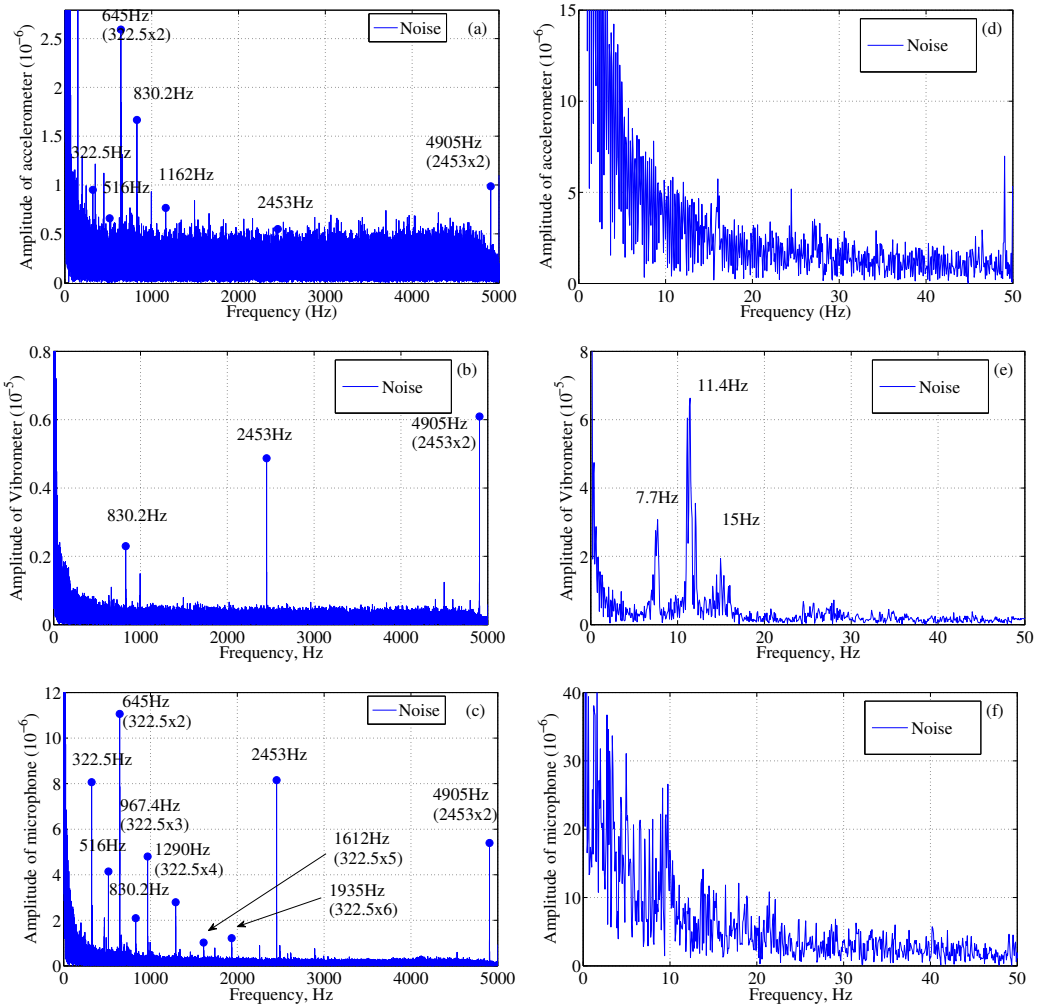

Figure 6.12: Frequency analysis by FFT of acceleration G (a,d), lateral vibration V (b,e), lateral sound pressure M (c,f) of the noise of 10 s prior to isotropic liquefaction event IL_{01}.

6.4.1 Fast Fourier Transformation (FFT)

A typical liquefaction IL_{01} of about 10 seconds is analysed together with the noise (Noise1) of 10 seconds prior to liquefaction IL_{01}. The 50 Hz of power-line noise is removed from the lateral vibration signal (figure 6.12b) using Butterworth notch filter, prior to analysis. Figure 6.12 shows the frequency content up to 5 kHz since the measurements were acquired at 10 kHz. Figures 6.12a,b,c in the left column show the possible frequencies above 300 Hz while the right column are the ones at low frequency below 50 Hz. The shape of Fourier amplitude spectrum may be narrow like a pulse

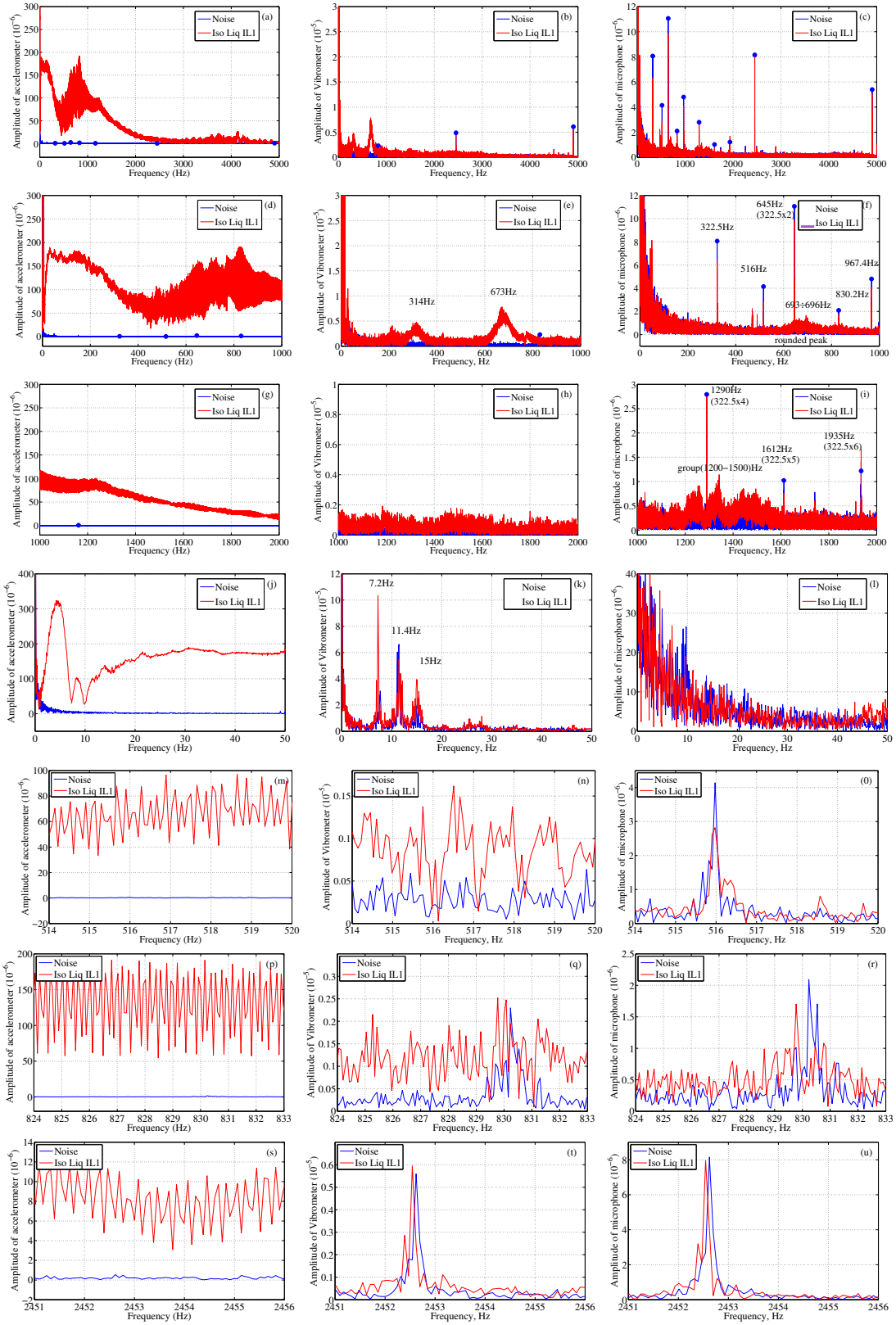

Figure 6.13: Frequency analysis by FFT of acceleration G (left), lateral vibration V (middle), lateral sound pressure M (right) of isotropic liquefaction event IL_{01}.

or broad. A pulse-like shape indicates the predominant frequency, inversely the broad shape implies the vibration containing multiple frequencies. In figure 6.12c, the lateral sound pressure has its first significant frequency at 322.5 Hz then an array of the multiple of this frequency as 645, 967.4, 1290, 1612, 1935 Hz. Other dominant frequencies are 516, 830.2 and 2453 Hz (as well as the multiple, 4905 Hz). For the lateral vibration, two frequencies are recognised, 830.2 and 2435 Hz (4905 Hz = 2435 Hz $*$ 2). The most reliable measurements, the top cap acceleration G, in figure 6.12a contains significant frequencies at 322.5, 516, 830.2, 2453 Hz and multiples of these main frequencies. In low frequency range, three dominated frequencies around 8, 11 and 15 Hz are detected by vibrometer V and less significantly by microphone M. These results implied the three independent techniques captured consistent dominant frequencies.

Furthermore, to verify these spikes of frequency, a different section of noise is analysed. This noise is the signal of 10 s before the collapse event Coll_{50} presented in figure 5.2a. Detailed results are presented in appendix D. The similarity of dominant spikes between these two noises confirmed the consistence and reliability of the data.

Figure 6.13 superimposes the results of liquefaction (red) on those of noise (blue) at different ranges of frequency. The first row, figures 6.13a,b,c, are the whole FFT plots for acceleration G, lateral vibration V, and lateral sound pressure M respectively with different and complicated shapes. G owns the wide distribution but the peak amplitude of G locates at low frequency range less than 2000 Hz. The significant peak is around 820 Hz. Noticeable distinguished response is observed for vibrometer and microphone measurements. They exhibit a narrower shape with many sharp spikes distributed throughout the examined range of frequency up to 5 kHz. Blue dots represent the extracted dominant frequencies of noise identified in figure 6.12. Globally, acceleration G has the greatest variability with exceedingly large amplitude of FFT and varied peaks of frequency. However, lateral sound pressure and lateral vibration basically keep the essential feature of FFT results similar to the noise, since the blue dots still coincide with the peak of the phenomenon signal. During liquefaction, these coincident frequencies are still included in the signals but their sustainable existence in the noise (figure 6.12) without the liquefaction proved that they are absolutely not the natural frequency of the phenomenon.

A closer inspection (figure 6.13e) reveals two rounded groups of frequency at 314 and 673 Hz in the FFT spectrum of lateral vibration. In figure 6.13f, beyond the

dominant frequencies coinciding with the noise, a rounded peak of frequency at around 696 Hz is also shown. Those implies the difference of the noise and the liquefaction phenomenon.

Continuing the next range from 1000 to 2000 Hz, figures 6.13g,h,i reveal another broaden group of frequency around 1200-1500 Hz, another difference between the liquefaction and the noise. The lowest range below 50 Hz is exhibited in figure 6.13k with three low frequencies of 7, 11, 14 Hz. They are pronounced with vibrometer. Although the microphone misses this group of frequency (figure 6.13l) but the accelerometer still depicts two small peaks at 4 and 8 Hz despite intensively changes during liquefaction phenomenon (figure 6.13j).

The remaining dominant frequencies are explored such as 516, 830.2 and 2453 Hz. They are still maintained during liquefaction but only vibrometer and microphone can captured them (figures 6.13 o,q,r,t,u). It is due to the implication of these peaks in the largely broad peak of G during liquefaction.

Briefly, the vertical vibration is the direct measurement revealing several dominant frequencies and being completed by additional lateral measurements. They complement as well as confirm each other to produce a full picture on the frequency content of phenomenon. Their permanent presence of dominant peaks in both noise and liquefaction implies that they are likely the eigenfrequencies of the assembly. The differences between liquefaction and the noise are the rounded peaks which are significant in acceleration signal and being confirmed by lateral vibrometer as well as microphone, pointing out they are the natural frequencies of the phenomenon.

In summary, the possible detected common frequencies are harmonic frequencies belong to the audible range. They are divided in 3 groups in table 6.2: the first group is the low frequency less than 50 Hz, the second is the sharp spikes ranging from 322 to 4900 Hz, the third group is the rounded peaks only present in liquefaction event. In which various colors represents different arrays of harmonic frequency with the first excited mode is the lowest frequency among them. Then the second group includes four colors representing four dominant frequencies at 322.5, 516, 830 and 2453 Hz.

The dominant frequency at 322.5 Hz is very close to note E_4 above middle C_4, in the audible range. This is the characteristic sound of granular instability.

Table 6.2: Detected frequencies during iso liquefaction IL_{01} at 212 kPa from vertical acceleration, lateral vibration and lateral sound pressure.

Isotropic liquefaction IL_{01} at 212 kPa, 0.7 mm beads, analysed by FFT									
f, Hz	Group 1 (below 50 Hz)								
Noise1	7.3	12.1	15.9	–	–	–	–	–	–
Noise2	7.7	11.4	14.9	–	–	–	–	–	–
Liq	7.2	11.4	15	–	–	–	–	–	–
f, Hz	Group 2 (300-5000 Hz)								
Noise1	322.6	516.2	645.3	833.9	967.9	1291.0	1936.0	2452.5	4905.0
Noise2	322.5	516.0	645.0	830.2	967.4	1290.0	1935.0	2452.7	4905.2
Liq	322.5	516.0	644.9	829.8	967.5	1290.0	1935.2	2452.6	4905.1
f, Hz	Group 3 (rounded peaks)								
Noise1	–	–	–	–	–	–	–	–	–
Noise2	–	–	–	–	–	–	–	–	–
Liq	314	673	1200÷1500	–	–	–	–	–	–

6.4.2 Wavelet analysis

By application of FFT, the AE measurements can be decomposed into frequency and amplitude of Fourier coefficient which are independent of time. In another way, that frequency composition is considered to be stationary with time while in this situation the measurements are indeed transient signals. Continuous Cauchy wavelet transform (CCWT) can supplement the previous FFT method in analysing the temporal evolution of the frequency content of a non-stationary time series. Consequently, the duration of dominant frequencies can be identified more precisely in CCWT spectrogram, which is an advantage of CWT method over the traditional FFT.

The efficiency of CCWT is going to be assessed with signals from V, M, G respectively. Firstly, the global continuous wavelet analysis for V in a segment of noise before liquefaction event is presented in figure 6.14a. It shows the scaleogram (time-frequency contour plot) of the wavelet power spectrum of lateral vibration. The colorbar on the right gives the absolute value of the wavelet coefficients. No clear and sustained frequency above 2000 Hz is observed. It is not available to identify all natural frequencies

as by FFT listed in table 6.2, the dominant frequency of membrane is 11 Hz and maintains nearly continuously throughout the duration of signal. The point here is that in noise signal the maximum CCWT amplitude is $3*10^{-5}$ at 11 Hz, all of the remaining eigenfrequencies (in group 1 and group 2) have much lower CCWT amplitudes. The amplitude of CCWT is independent of type of wavelet or the number of steps of calculation. CCWT amplitude is the convolution of mother Cauchy wavelet and the Fourier transformation of signal. Intuitively its geometrical meaning can be described as the intersection area when sliding the wavelet along the signal at a specific scale. Therefore with the same Cauchy mother wavelet function and the same range of investigated scales, among the spikes of eigenfrequencies, due to the same form of sharp spike with mostly equal widths, the CCWT amplitude relates to the area of the spikes. It explains the highest CCWT amplitude of the spike at 11 Hz of the noise signal because of its largest FFT amplitude. This result of CCWT for noise is consistent to the FFT method.

The spectrogram of lateral vibration V during liquefaction event is shown in figure 6.14b. Only some sparse vertical marks are exhibited; one at around the 5th second is equivalent to the aftershock of V (M, G, U also). It should be highlighted that the dynamic behaviour only lasts within the first 30 ms thus a close examination is provided in figure 6.14d. In case of liquefaction signal, the first peak of 691 Hz occurs at 5.2 ms, prior to the second one of 313.6 Hz at 6.8 ms. The peak at 313.6 Hz in figure 6.14d has CCWT amplitude of $1.98*10^{-4}$, 7 times larger than the maximum amplitude of $3*10^{-5}$ at 11 Hz of noise signal. Remind that, for the noise, the amplitude of $3*10^{-5}$ with the darkest red is certainly remarkably larger than any other remaining eigenfrequencies (group 2). Although group 1 and group 2 are still included in the signal of liquefaction (table 6.2), only the peaks at 313.6, 691 Hz are captured in CCWT plot of liquefaction. It is understandable since group 1 and group 2 have too far low CCWT amplitudes to denote in the range of $0.5*10^{-5}$ to $5*10^{-5}$. The analogy indicated the existing peaks of liquefaction signal (in the right column) representing the frequencies which only occur in liquefaction but absent in the noise signal, that should be group 3 in table 6.2. CCWT also helps to find the rounded peaks around 1200 Hz (figure 6.13h) which is not too pronounced in FFT of vibrometer so it was underestimated.

The exploration is repeated with lateral sound pressure in figure 6.15. In the global CCWT spectrogram for noise signal, several frequencies as 322, 645, 967 and 1290

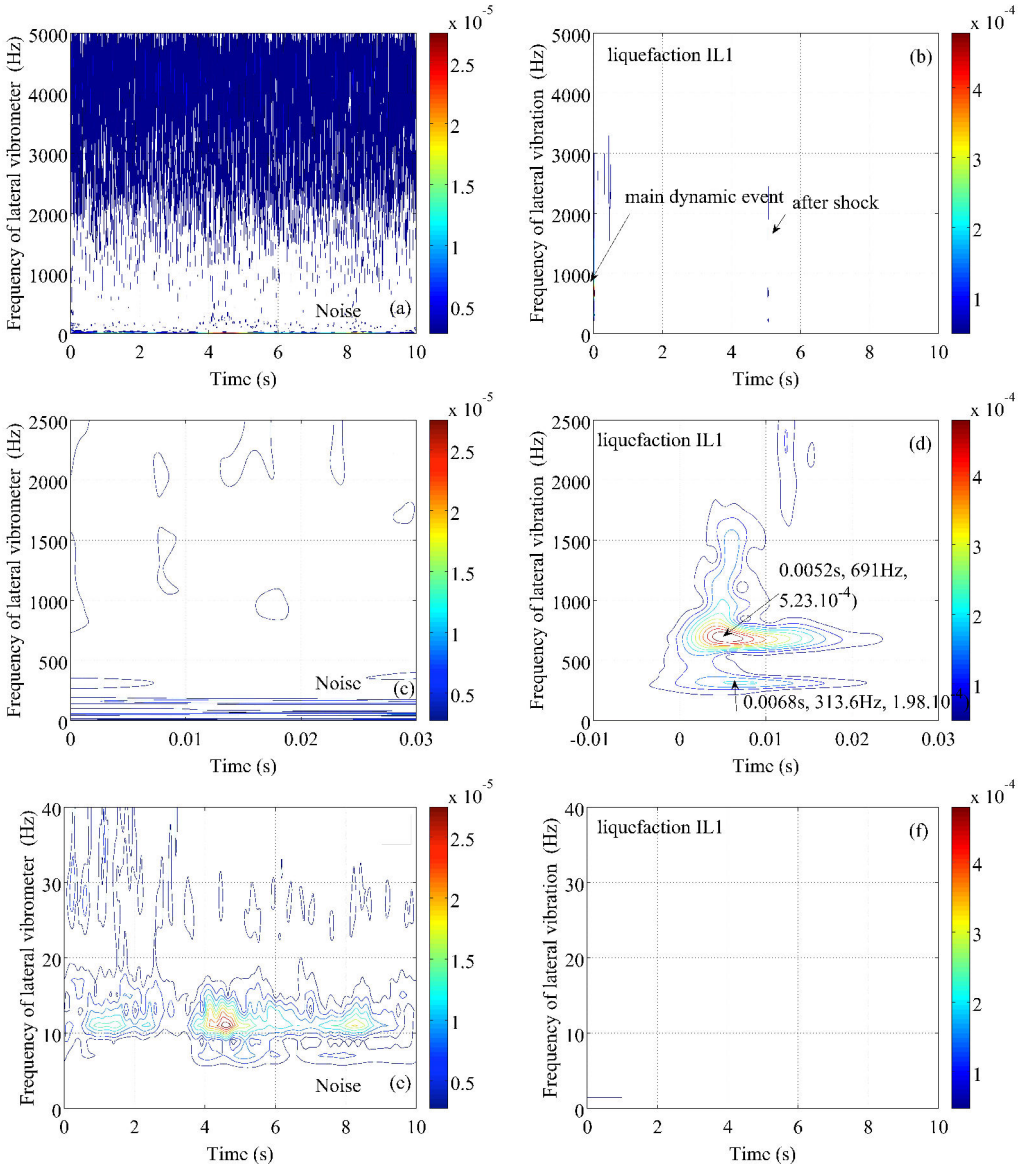

Figure 6.14: CCWT spectrum of lateral vibration V for noise signal (left) and isotropic liquefaction IL_{01} (right).

Hz do not truly continuously persist throughout the signal duration. They fade in and out but nearly form discontinuously horizontal bands within 10 s. The maximum CCWT amplitude for noise signal is $1.8{*}10^{-5}$ at 9 Hz (figure 6.15e). Considering the CCWT of liquefaction event in figure 6.15b, the mark at very low frequency happening around the 4th second corresponds to the frequency of 7 Hz in noise signal with the

identical CCWT amplitude. Similarly to lateral vibration, other frequencies of group 1 and group 2 are not included in this plot due to substantially low amplitudes. Closer exploration within 300 ms in figure 6.15d depicts the dominant frequencies of dynamic response with several peaks as 696 Hz, and a group of rounded peaks from 1200 to 1500 Hz (in details they are 1376 and 1416 Hz). Compared to the FFT, these frequencies probably relate to the broad peaks in figures 6.13f,i.

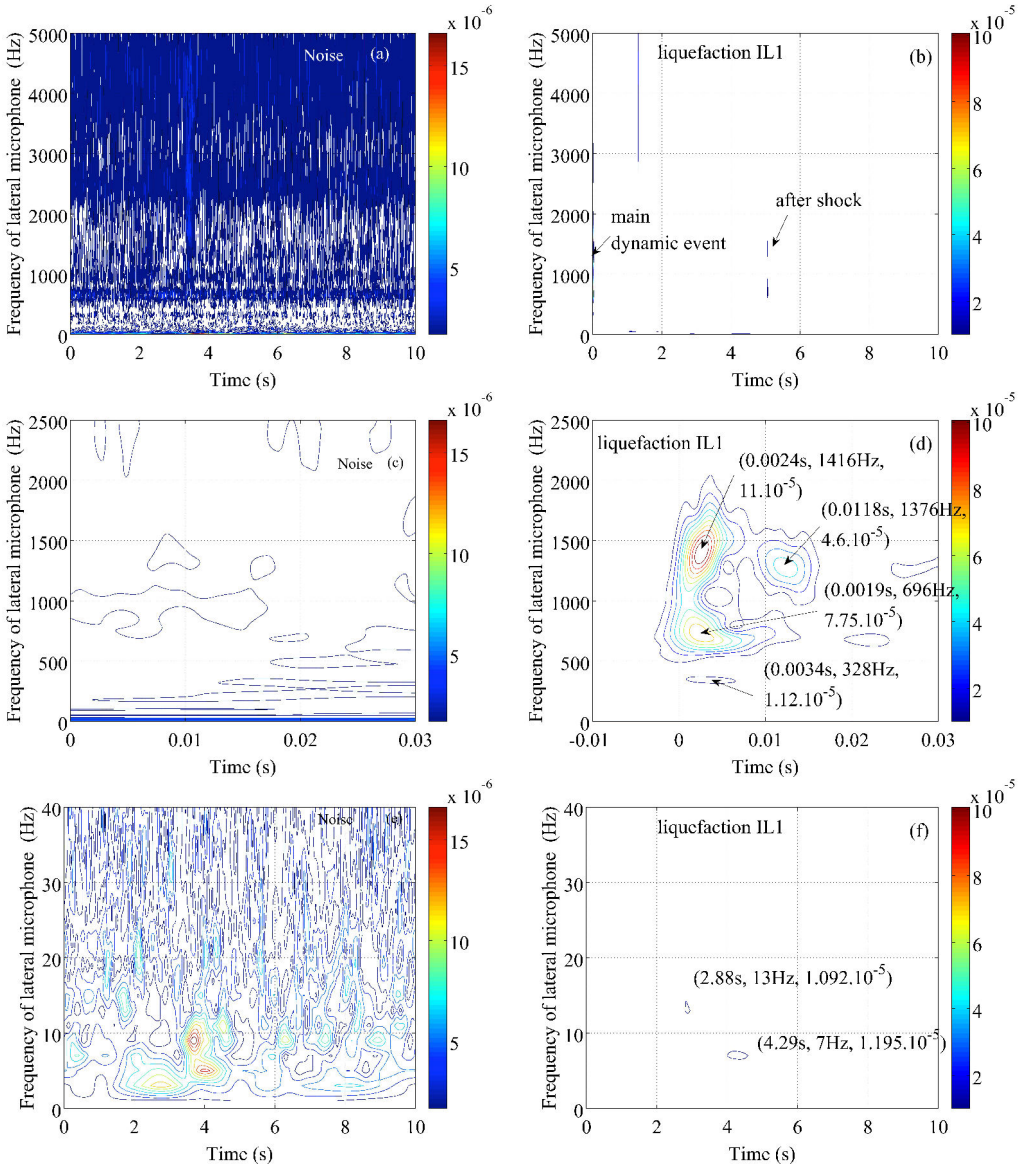

Figure 6.15: CCWT spectrum of lateral sound pressure M for noise signal (left) and isotropic liquefaction IL_{01} (right).

Here the quantitative estimation of CCWT amplitude is suggested to recognise the peaks on CCWT spectrogram and assign them to the peaks on FFT. Since in FFT of microphone M (figure 6.13f), the sharp spike at 645 Hz (group 2) of liquefaction is quite close to the frequency of rounded peak at 696 Hz which can cause the mistaken recognition. The elimination is useless since both the spike and broad peak are acquired by microphone. The additional figure 6.16 is illustrated for the approximate CCWT amplitude as the area under FFT plot within the spike and rounded peak. This figure is the FFT spectrum of studied liquefaction IL_{01} as the inset of figure 6.13f from 500 to 800 Hz. The CCWT amplitude of the spike of 645 Hz is approximately equal the area A1 = $3.7{*}10^{-6}$. That of the broad peak of 696 Hz is A2 = $7.86{*}10^{-5}$ which is well equivalent to CCWT amplitude ($7.75{*}10^{-5}$) of the peak in yellow at 696 Hz in the scaleogram denoted in figure 6.15d. Similarly, the upper peaks at 1200 to 1500 Hz are recognised as the group of rounded peaks in figure 6.13i.

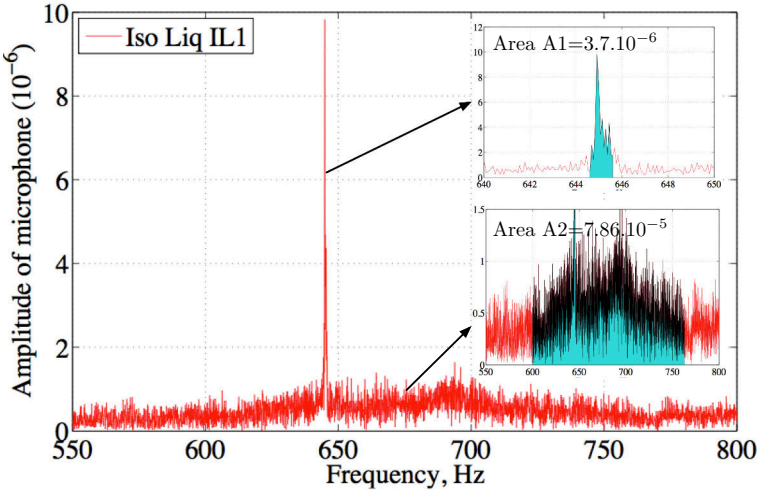

Figure 6.16: Approximate estimation of CCWT spectrum of microphone M for spike frequency and round frequency during isotropic liquefaction IL_{01}.

Shortly, CCWT is effective to recognise the frequency having the large energetic power spectrum which corresponds to broad peaks rather than very sharp spike. In this study those large power spectra are in the third group. This CCWT tool provides the method to identify the distinct frequencies only occurring during the liquefaction.

The most challenging measurement to identify dominant frequency by FFT concerns the vertical acceleration due to the wide distribution of frequency. For such case, CCWT

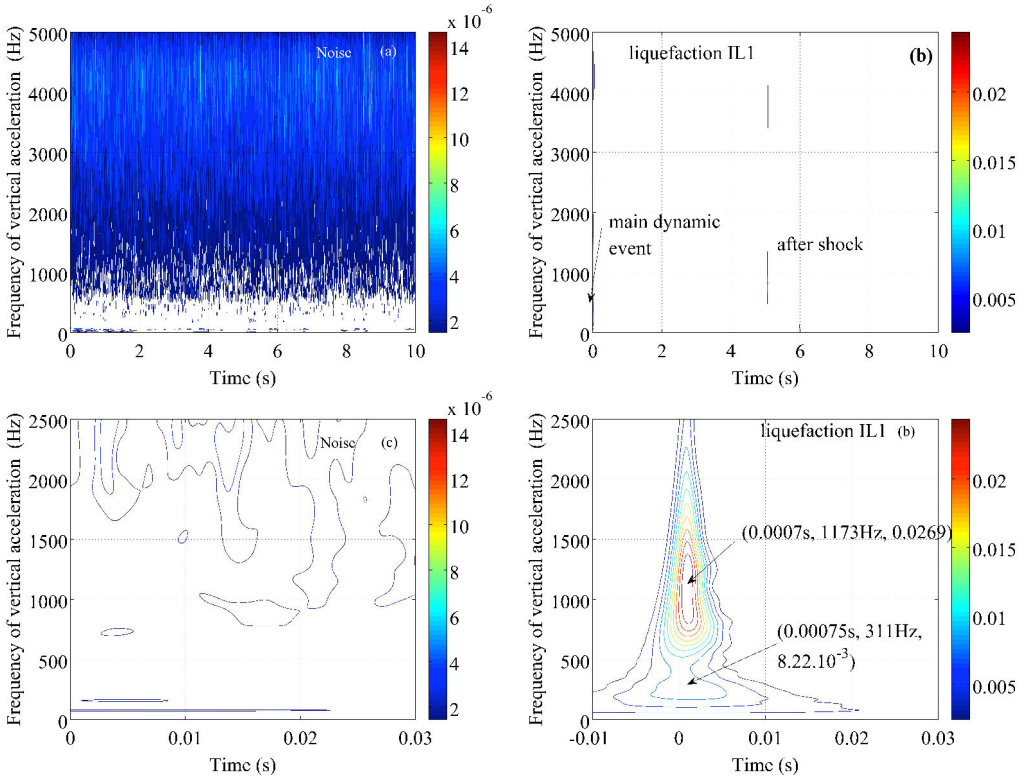

Figure 6.17: CCWT spectrum of vertical top cap acceleration G for noise signal (left) and isotropic liquefaction (right).

shows the advantage in localisation of frequency in time. The CCWT of noise signal still exhibits the basic frequency of 322 Hz fading in and out during 10 seconds. The CCWT modulus of the other frequencies in group 2 are not significant to identify. By FFT (figure 6.13a), the Fourier amplitudes of liquefaction event are completely distinguished from those of noise, thus the CCWT spectrogram of liquefaction excludes any natural frequency of noise signal excepting the very early stage and a spot around 5 s corresponding to a small aftershock illustrated in figure 6.17b. Similarly the close-up figure 6.17d at the early stage within the first 30 ms of the event helps identify the most dominant frequency of top cap acceleration G during the isotropic liquefaction IL_{01} at 1173.5 Hz (figure 6.17d).

The supplementary result in figure 6.18a concerns the normalised excess pore pressure ΔU^{norm}. The frequency is 77.74 Hz with largest CCWT amplitude of 0.06 at 0.021 s and the lasting time of the peak is around 150 ms, exactly coherent to the

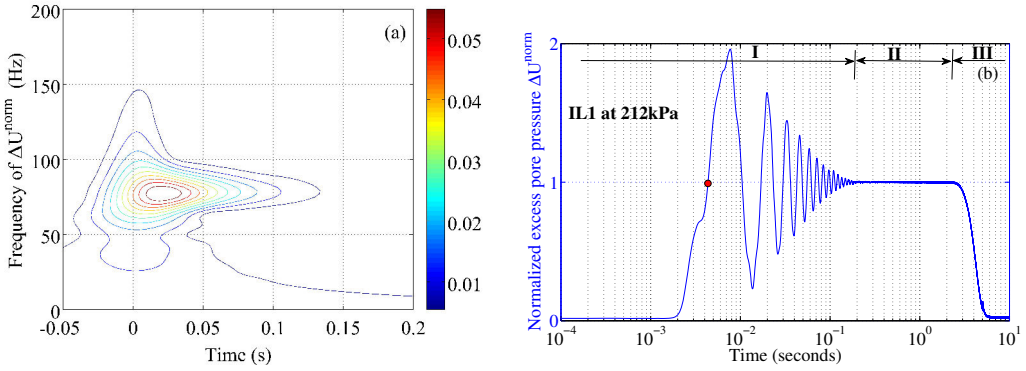

Figure 6.18: CCWT spectrum of normalised excess pore pressure ΔU^{norm} during isotropic liquefaction IL_{01}.

transient vibration phase I of U recalled in figure 6.18b. Moreover the asymmetric vibration of pore pressure is also reflected in the shape of peak of CCWT plot. The spontaneous response of acoustic measurements are well highlighted by CCWT spectrogram in figures 6.14d, 6.15d, 6.17d by the sudden appearance of contours at dominant frequencies, the sharp rising time before reaching the peak, longer fading time and the whole short-lived of the spectrum.

As above evaluations, CCWT exhibits efficient ability to capture the brief transient vibration of the phenomenon, excludes other frequencies due to the distinction in CCWT amplitude in our case. Furthermore its advanced capability on identifying the duration of the dominant frequency provides a strong tool to better understanding the phenomenon, for instance capturing the vibration mode in the time sequence.

The analyses by FFT and CCWT are also applied for a representative stick-slip and a collapse event. A very large stick-slip mostly liquefied, SS_{04} of test N500 in CIDNC series, is explored, and an average isotropic collapse at 108.2 kPa, $Coll_{04}$ of Collapse series is added on the purpose to compare with the isotropic liquefaction IL_{01}. The detail results for SS_{04} event is illustrated in appendix D.2 and those of $Coll_{04}$ in appendix D.3.

6.5 Analysis

6.5.1 Amplitude of AE measurements

One of the most popular parameters characterising the amplitude of ground motion is the peak acceleration which is the largest value of acceleration in accelerogram. In engineering applications the horizontal acceleration is primarily considered due to the natural relation to the more critical horizontal inertial force generated in civil structures. In this study the vertical acceleration is of most importance since it is on the direction of deviatoric stress drop during SS events. Consequently, a direct relation between vertical acceleration and deviatoric stress drop is very useful to figure out the factors controlling the stress drop and can be the indispensable link between mechanical and AE measurements. This relation is established firstly for SS events in CIDNC series as in figure 6.19. The downward and upward maximum amplitude of acceleration, G_{max} and G_{min}, both show the same tendency that stronger motion of the system links to larger stress drop, creating linear relations to deviatoric stress drop regardless of effective confining pressure p'_0 and initial void ratio e_c at the beginning of shear stage. The single parameter of linear fitting function for G_{min} is higher, 1.0983, instead of 0.8044 for G_{max} and since mostly the larger acceleration is downward due to the effect of gravity. This linear relation also means no measurable G (or very small fluctuation) in absence of SS event. So far there are two evidences on the correlation between the stress drop and acoustic measurement. The first is the systematic accompanying acoustic measurements detected simultaneously with the stress drop. The second is the linear relation on the amplitude which supported the correlation between mechanical and acoustical processes. However the correlation between G_{min} and Δq coefficient, $R^2 = 0.717$, is not so high but still acceptable.

Similarly, the lateral sound pressure is also linearly proportional to Δq with higher correlation coefficient $R^2 = 0.836$. The supplementary measurements of lateral vibration are the confirmation of strong consistency of data in both vertical and lateral direction. Both sound pressure M and lateral vibration V show larger amplitudes on the positive side, equivalent to radial direction since the signals emitted from the source to the acquiring devices. V_{max} and V_{min} exhibit nearly symmetrical response with lowest correlation coefficient R^2 among three measurements. One plausible interpretation

is suggested that due to the strong anisotropy of the material and V is the speed of vibration at one fixed spot on the cylinder thus it depends on the complicated generation of vibration modes which will be analysed in coming section.

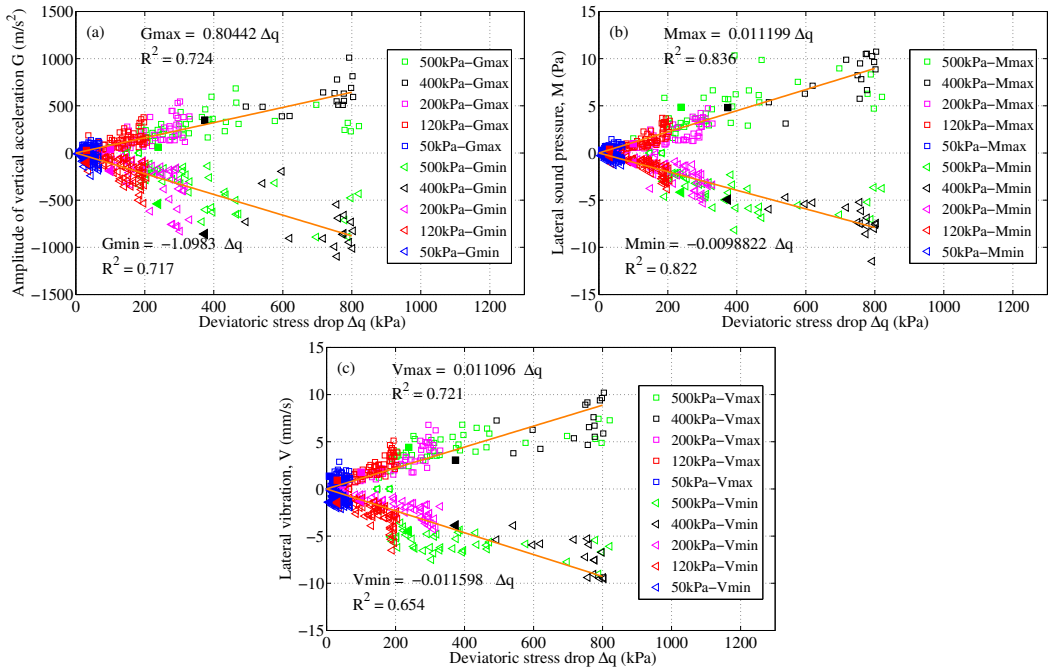

Figure 6.19: Relation of amplitude of vertical acceleration G, lateral sound pressure M, lateral vibration V and deviatoric stress drop Δq during stick-slip events.

Next, the explorations for Liquefaction and Collapse series are conducted. In case of liquefaction, a linear relation is attained between G_{max} and effective triggering stress σ'_{trig} in figure 6.20a. For liquefaction event, the effective triggering stress equals the stabilised excess pore pressure, $\Delta U_{stable} = \sigma'_{trig}$. The distribution of events with high pore pressure frequency, 80 Hz (solid circles), and low frequency, 20 Hz (open circles), obviously does not influence the relation implying the independence of amplitude of stabilised excess pore pressure on its frequency. Static liquefaction (black) is so far coherent to other liquefactions despite the undrained condition but it can be a bias due to its low amplitude of G, nearly zero. Stick-slip liquefactions (green) are not included in fitting function since the amplitude of vertical acceleration under shearing with the addition of axial force is much larger than isotropic loading.

Liquefaction still repeats the linear relation between microphone amplitude and triggering stress σ'_{trig} $(= \Delta U_{stable})$ with quite low $R^2 = 0.362$ for M_{min} (figure 6.20b),

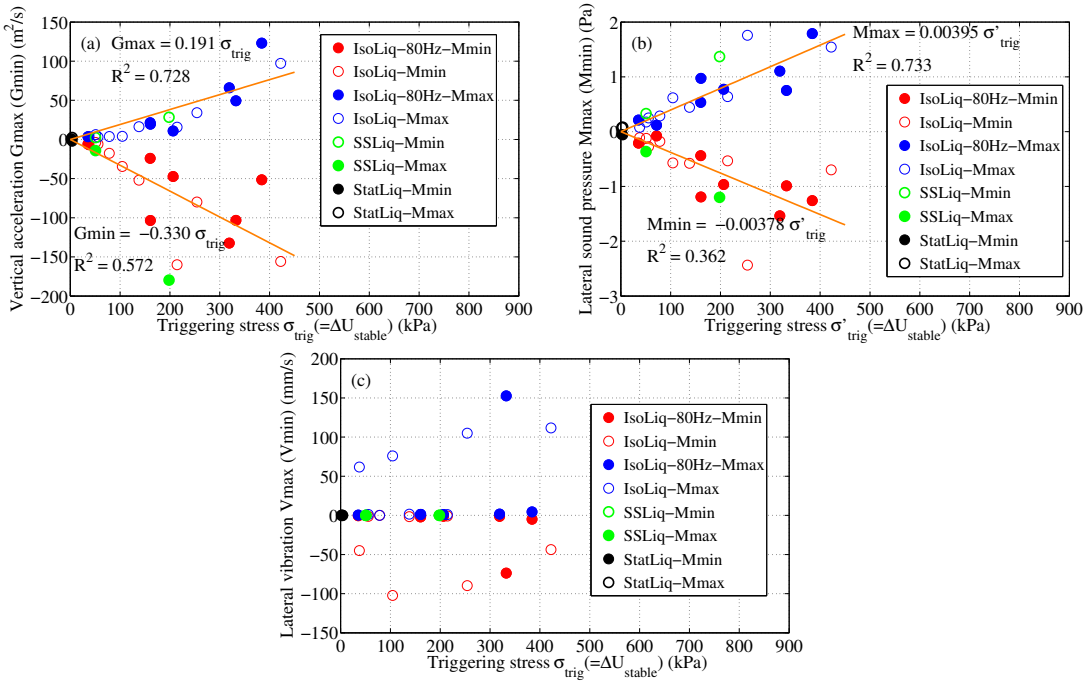

Figure 6.20: Relation of amplitude of vertical acceleration G, lateral sound pressure M, lateral vibration V and effective triggering stress σ'_{trig} ($= \Delta U_{stable}$) during liquefaction events.

nevertheless M_{max} representing the first variation in most cases still shows strong correlation to triggering stress. As shown in chapter 5, liquefaction is the phenomenon having the strongest dynamic anisotropic behaviour with an extremely wide range of dynamic anisotropy coefficient from less than 1 up to thousands and no link has been discovered to other measurements, hence there is no clear relation for lateral vibration V and triggering stress here (figure 6.20c). Remind that the difficulty in the employment of vibrometer during this global failure is the condition of orthogonal incident and reflexing ray to the surface of sample so that the vibrometer can capture correctly. During liquefaction the magnitude of all strains is extremely large leading to large deviation of reflexing ray then the measurements are noisy. Some tests with very high magnitudes of V up to 150 mm/s and some are around 10 mm/s since the different mean of failure as aforementioned. Some liquefactions fall down totally and others still maintain the cylindrical shape with large deformations and lateral bellies.

In case of collapse event, the amplitude of all measurements is lower than the global

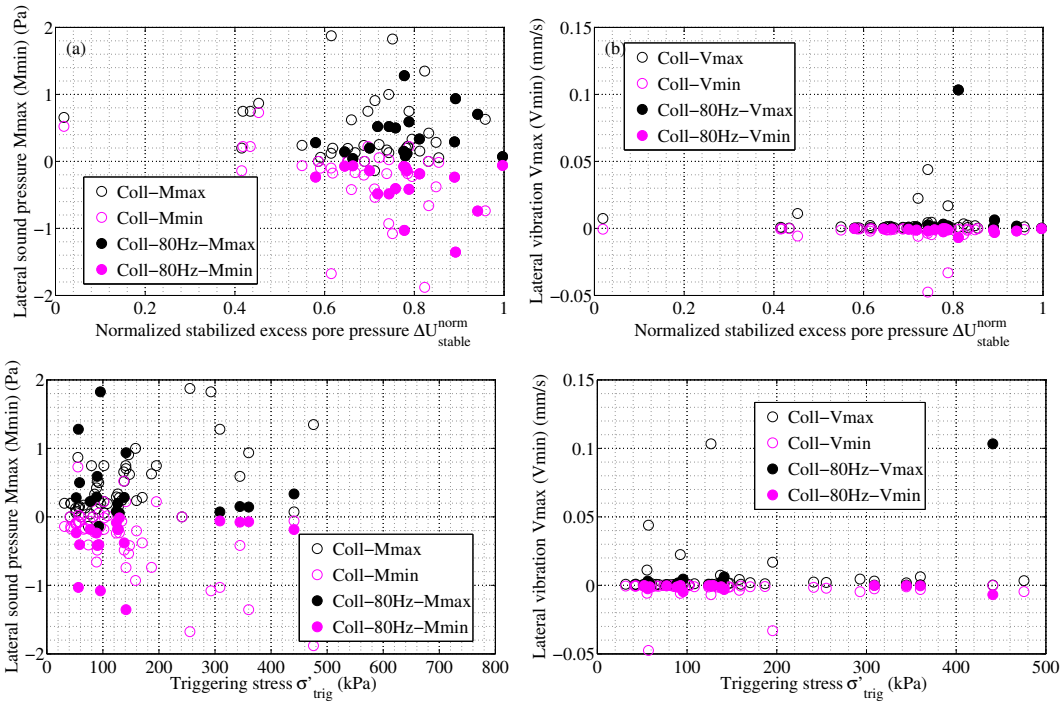

Figure 6.21: Relation of amplitude between lateral sound pressure M, lateral vibration V and normalised stabilised excess pore pressure ΔU^{norm}_{stable} during collapse events (respectively in accordance with triggering stress σ_{trig}).

liquefaction failure. M and V measurements are noticeably small in amplitude and scatter as figure 6.21 thus only vertical acceleration G is of significance in relevance with normalised stabilised excess pore pressure ΔU^{norm}_{stable} and triggering stress σ'_{trig}. G_{max} and G_{min} are actually not symmetric in case of collapse. Only G_{min}, which is larger in amplitude than G_{max}, renders a possible correlation with ΔU^{norm}_{stable} and σ'_{trig} in figure 6.22. Very small collapse and extremely large unloading collapse contribute to portray the evolution by a nonlinear two-variable function as following.

$$G^{Coll}_{min} = 0.330 * \sigma'_{trig}[0.03775 * \log(1 - \Delta U^{norm}_{stable}) \quad (6.1)$$

$$= G^{Liq}_{min} * [0.03775 * \log(1 - \Delta U^{norm}_{stable})] \quad (6.2)$$

This fitting surface delivered a remarkable correlation coefficient $R^2 = 0.859$. It also depicts that at constant triggering effective stress σ'_{trig}, it is possible to occur arbitrary collapse with $0 < \Delta U^{norm}_{stable} < 1$. The amplitude of G_{min} evolves as an increasing logarithmic function of ΔU^{norm}_{stable}. As collapse at any triggering stress approaches liq-

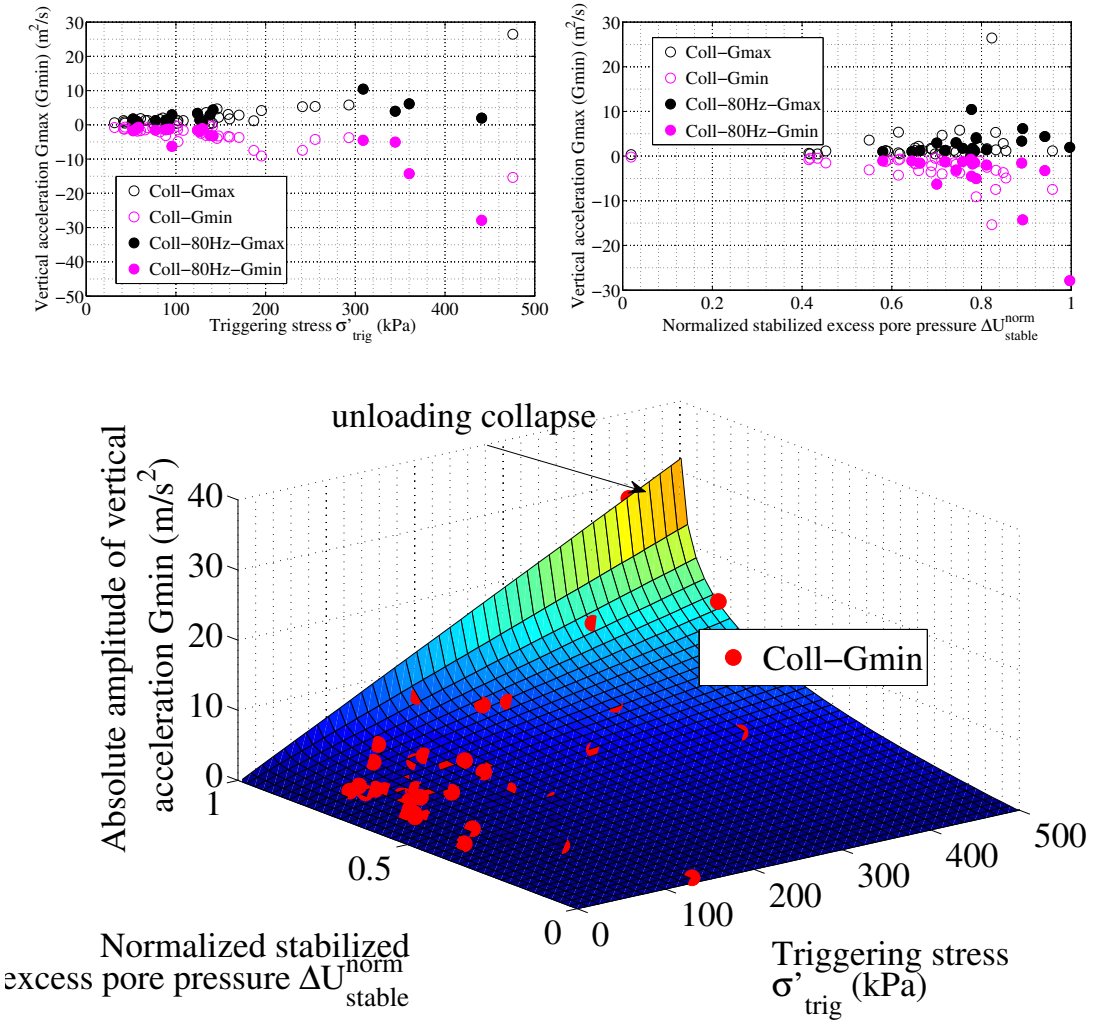

Figure 6.22: Relation of amplitude of G as a function of triggering stress σ_{trig} and normalised stabilised excess pore pressure ΔU^{norm}_{stable} during collapse events.

uefaction condition, $\Delta U^{norm}_{stable} \rightarrow 1$, (1-$\Delta U^{norm}$) $\rightarrow 0$ and 0.03775*log(1-ΔU^{norm}_{stable}) $\backsimeq 1$, equation (6.2) becomes $G^{Coll}_{min} = 0.330{*}\sigma'_{trig} = G^{Liq}_{min}$. The presence of parameter 0.03775 is only to compensate the accuracy of measured ΔU^{norm}_{stable} which is very sensitive in the asymptotic function. The contribution of all collapses, regardless of different frequencies of pore pressure in phase I, proved that the effects of the stabilised state of excess pore pressure ΔU_{stable} and σ'_{trig} are uncoupled in estimating the amplitude of G in phase I.

Finally, a global estimation on the absolute amplitude of G, M, V is provided to have

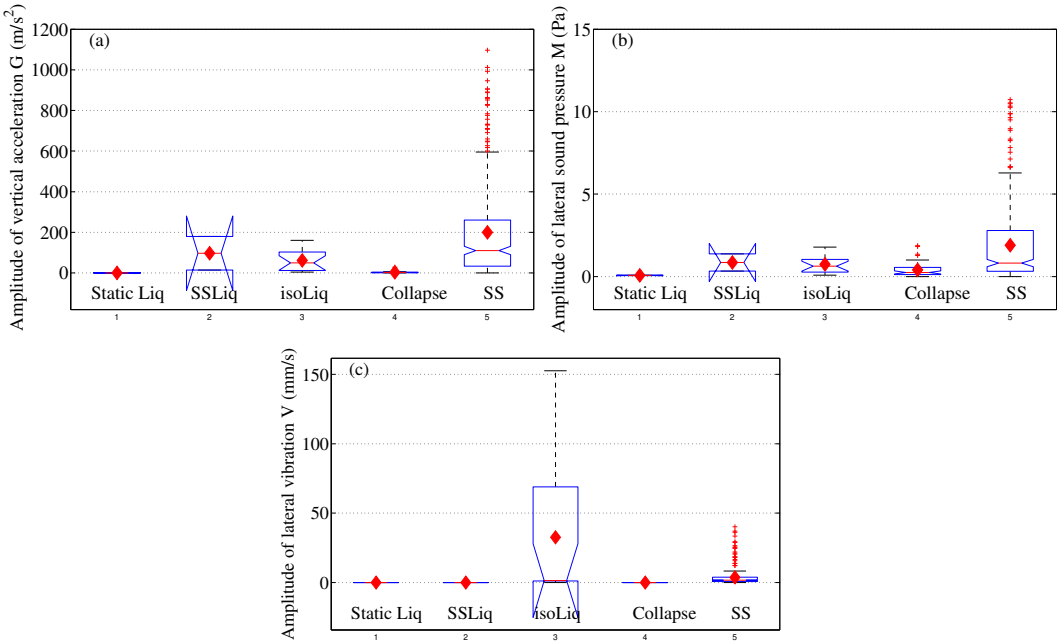

Figure 6.23: Amplitude of G, M, V in various kinds of instability events.

Table 6.3: Amplitude of various kinds of instability.

	Liquefaction			Non liquefaction	
	Static	Stick-slip	Isotropic	Collapse	Stick-slip
Vertical acceleration (m/s^2)	1.4 ± 1.2	96.95 ± 117.02	61.5297 ± 54.41	3.25 ± 4.52	199.60 ± 236.90
Lateral sound pressure (Pa)	0.067 ± 0.013	0.85 ± 0.74	0.75 ± 0.55	0.40 ± 0.43	1.90 ± 2.38
Lateral vibration (mm/s)	0.0001 ±0.0001	0.0014 ±0.0013	32.58 ± 51.27	0.0060 ± 0.017	3.73 ± 6.21
Number of data	2	2	17	56	302

a comprehensive view between different kinds of instabilities. Figures 6.23a,b point out the resemblance of G and M that under compression shearing the amplitude of G(M) is largest, consequently both stick-slip liquefaction SL and stick-slip events have larger G(M) than isotropic liquefaction and collapse. Within shearing instabilities, the mean of G(M) of SS is greatly higher than that of SS liquefaction. At first this seems to be

inappropriate that local instabilities are stronger than global failure under shearing but actually it is rational since the SS liquefaction happens only for first SS events at the initial stage of shearing, equivalent to very low Δq compared to much larger stress drop Δq within the plateau of stress-strain curve. The linear relation of vertical acceleration G and stress drop Δq (figure 6.19a) also allows to infer V of stick-slip liquefaction SL lower than that of large SS events in the plateau. Within isotropic instabilities, collapses as local failures are ten times smaller than global isotropic liquefactions in magnitude of G(M). The small mean amplitude of G(M) in static liquefaction (G = 1.4 m/s^2, M = 0.067 Pa) implies different mechanisms for this failure. Only lateral vibration introduces a distinct large amplitude of 32.58 mm/s in isotropic liquefaction, ten times larger than lateral vibration in stick-slip of 3.725 mm/s. Stick-slip liquefaction obtains lower lateral vibration than collapse, since there were only two stick-slip liquefaction events and both of them still kept the geometry configuration when failing, not similar to the totally destruction of the cylinder shape under isotropic liquefaction.

Summarily, the first measurement captured in an instability is the top cap acceleration G and its amplitude have a strong role in controlling the amplitude of the event and the generated excess pore pressure afterward. Furthermore, in previous chapter the link between collapse and liquefaction is depicted by the evolution of mechanical measurements. In this section, the transformation from a local collapse to liquefaction is strengthened in the evolution of acoustic measurement G in equation 6.2. The amplitude characteristics of G, V, M appear to be the first indicators controlling all subsequent amplitudes of mechanical measurements (stress and strain). Their frequency characteristics is going to be analysed in next sections.

6.5.2 Numerical simulation

The extraction of frequency content is estimated by FFT and CCWT. Now to identify the physics of these frequencies, a numerical simulation of the eigenfrequency of the sample is conducted. This analysis employs Comsol Multiphysics software in the attempt to simulate the vibrational modes of a short full cylinder of circular cross-section of diameter D and length H = D = 7 cm. A homogeneous and simple isotropic elastic solid material is described by only 3 material parameters : Young's modulus E (in this case the isotropic bulk modulus K), Poisson's modulus ν and density ρ. For simplicity,

the two end conditions are clamped (top and bottom caps have no allowed displacement), and free lateral surfaces are allowed. The finite element mesh of this cylinder has 14 000 tetrahedral elements.

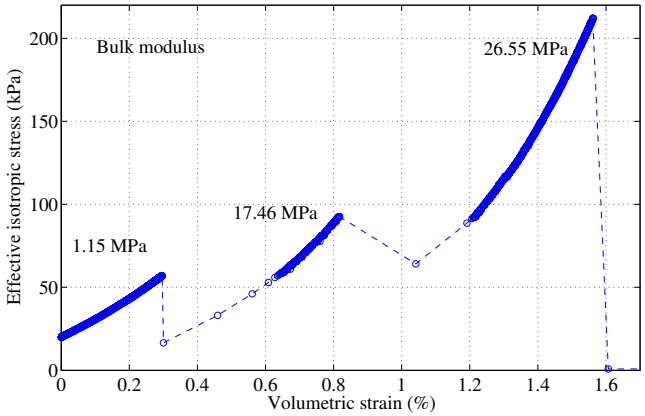

Figure 6.24: Bulk modulus of material during isotropic consolidation phase.

Table 6.4: Isotropic elastic material parameters.

Materials	Beads	Membrane
Bulk density ρ, 1000 kg/m^3	1.428	1.00
Bulk modulus K, MPa	7.28	0.92
Poisson's ratio ν,	0.25	0.49

The numerical values adopted for the isotropic elastic material in this simple problem are in table 6.24. With fixed ρ and ν, a simple trial and error procedure on the bulk modulus K is used to fit the first known measured modal frequency of 322 Hz with K = 7.28 MPa. This value is lower than K = 26.55 MPa between 100 to 200 kPa of confining pressure in figure 6.24 but it is still in the range from 1 to 17 MPa at 20 to 100 kPa of confining pressure. Simulation results in table 6.5 gives all natural vibration modes from 322 Hz illustrated in figure 6.25, without the frequency of 4905 Hz. The frequency of 322 Hz detected by microphone (absent in lateral vibration signals) is suggested to be the first axial vibration mode of the granular media. Then the progression of this axial vibration at 646 Hz (n=2), 969 Hz (n=3), 1292 Hz (n=4), 1938 Hz (n=6). The remaining modes of 517 and 833 Hz are associated to two different radial vibration

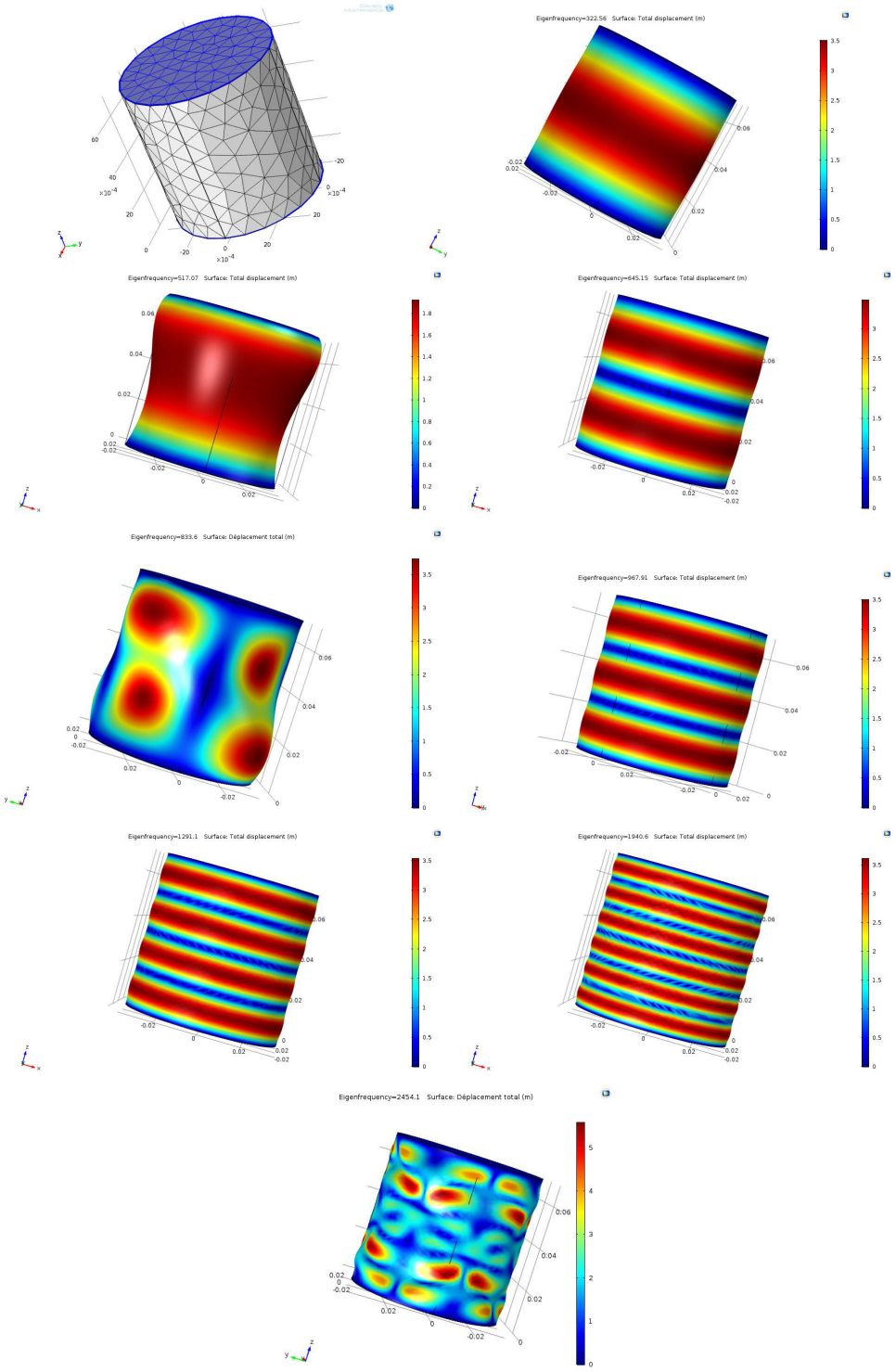

Figure 6.25: Model of cylinder saturated granular sample and possible vibration modes at 322, 517, 654, 833, 968, 1291, 1940, 2454 Hz.

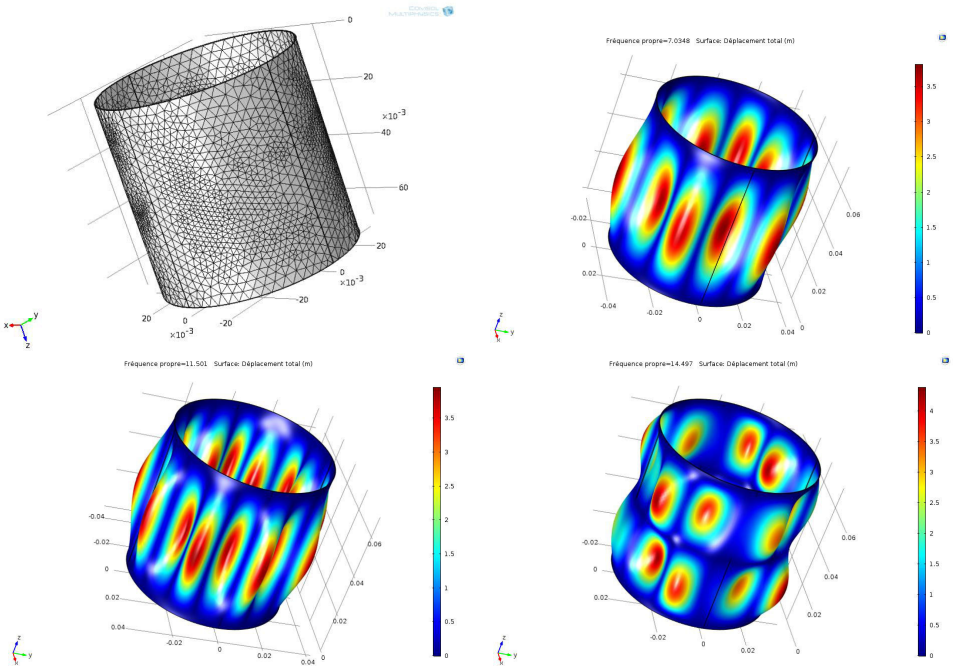

Figure 6.26: Model of hollow thin cylinder membrane and possible vibration modes at 7, 11, 14 Hz.

modes of 833 Hz and its multiple at 2454 Hz (n=3), directly captured by vibrometer in figures 6.13q, r. The frequency of 517 Hz is not clear in figure 6.13n but still present clearly in microphone signal, figure 6.13o.

The indispensable membrane of the granular sample is simulated by a hollow cylinder of circular cross-section of small thickness (0.3 mm) with equally homogeneous and isotropic elastic material. The finite element mesh of this membrane use 15 000 tetrahedral elements. All natural vibration modes below 50 Hz are found in figure 6.26 and listed in table 6.5.

However the group of modes of rounded peaks at around 300, 600 and 1200-1400 Hz is absent from the simulation. It can be the frequency signature of the liquefaction phenomenon. Further simulation with a layer thick cylinder representing a thin latex membrane enveloping a granular cylinder does not reveal the lower modes below 20 Hz. It seems that the granular cylinder and the thin membrane are decoupled in numerical experiments.

Table 6.5: Identification of eigenfrequency by numerical simulation.

Comsol Multiphysics								
	Membrane							
f (Hz)	7.0	11.5	14.5	–	–	–	–	–
	Granular							
f (Hz)	322	517.1	645.2	833.6	967.9	1291.1	1940.6	2454.1

6.5.3 FFT characteristic feature of instability

The FFT spectra of liquefaction IL_{01}, very large stick-slip SS_{04} and collapse $Coll_{04}$ were described in section 6.4.1, appendix D.2, appendix D.3 respectively. Now they are gathered in figure 6.27 and compared to find their characteristic features in FFT spectrum. Only the global qualitative features are focused and compared in this section. Since the quantitative characteristics such as dominant frequency, amplitude are more effectively identified by CCWT spectrum and will be presented in section 6.5.4. The most reliable acoustic measurement, vertical acceleration G, is presented in figure 6.27a. The noise included in the figure is the signal at 10 s before the collapse $Coll_{04}$, denoted by green curve with the lowest FFT amplitude and a set of sharp spikes marked by green dots. The increasing of amplitude from collapse to liquefaction and SS event is understandable since collapse is a local failure compared to total failure, liquefaction, and the presence of deviatoric stress is attributed to the largest amplitude of SS4. Furthermore, SS_{04} is one of the largest SS at confining pressure of 500 kPa and mostly liquefied. Frequencies below 1000 Hz are mostly the largest amplitudes. The evolution from a collapse to a liquefaction is characterised by widening the range of excited frequencies. Particularly, the dominant frequencies of collapse is within 1000 Hz, then when developing to a liquefaction the range of excited frequencies is extended to 2000 Hz, and in SS event almost every frequencies are excited. This is considered as the characteristic feature of FFT spectrum of instability.

The similarity of lateral vibration measurements is depicted in figure 6.27b, the similar two rounded peaks of around 300 and 600 Hz are detected in all instabilities. The signal of SS event still is the largest one and still has the broader range of excited frequencies. Eigenfrequencies marked by green dots are consistent between collapse,

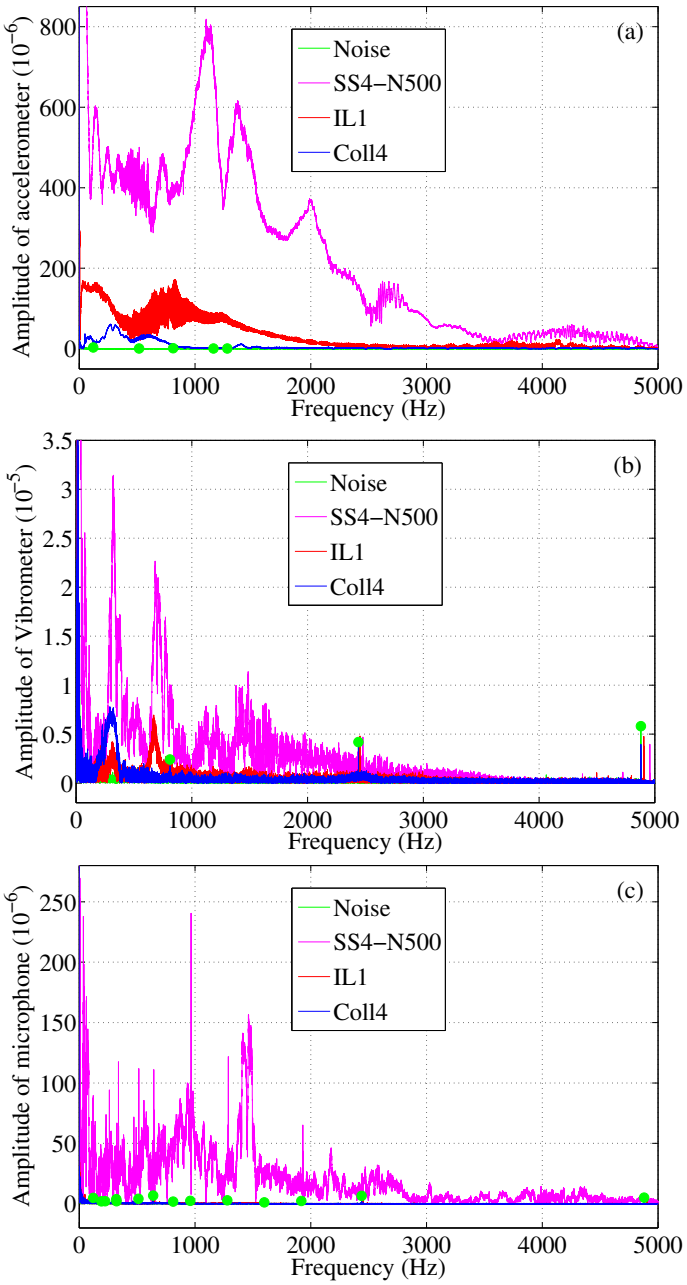

Figure 6.27: FFT spectra of collapse Coll_{04}, liquefaction IL_{01}, stick-slip SS_{04}-test N500.

liquefaction and stick-slip. The response of FFT spectrum for lateral sound pressure M of collapse and liquefaction is not significantly distinct in the amplitude, only stick-slip shows the distinguished amplitude.

6.5.4 Frequency of granular structure from AE measurements

As analysed for a typical liquefaction in section 6.4.2, V well detects low frequencies, M is effective at higher frequencies and G is the most reliable measurement since it is attached directly on the sample top. V and M supplement effectively G to fully obtain the signature frequencies of the dynamic instabilities. CCWT is applied for all CIDNC, liquefaction and collapse series to search for the links between them.

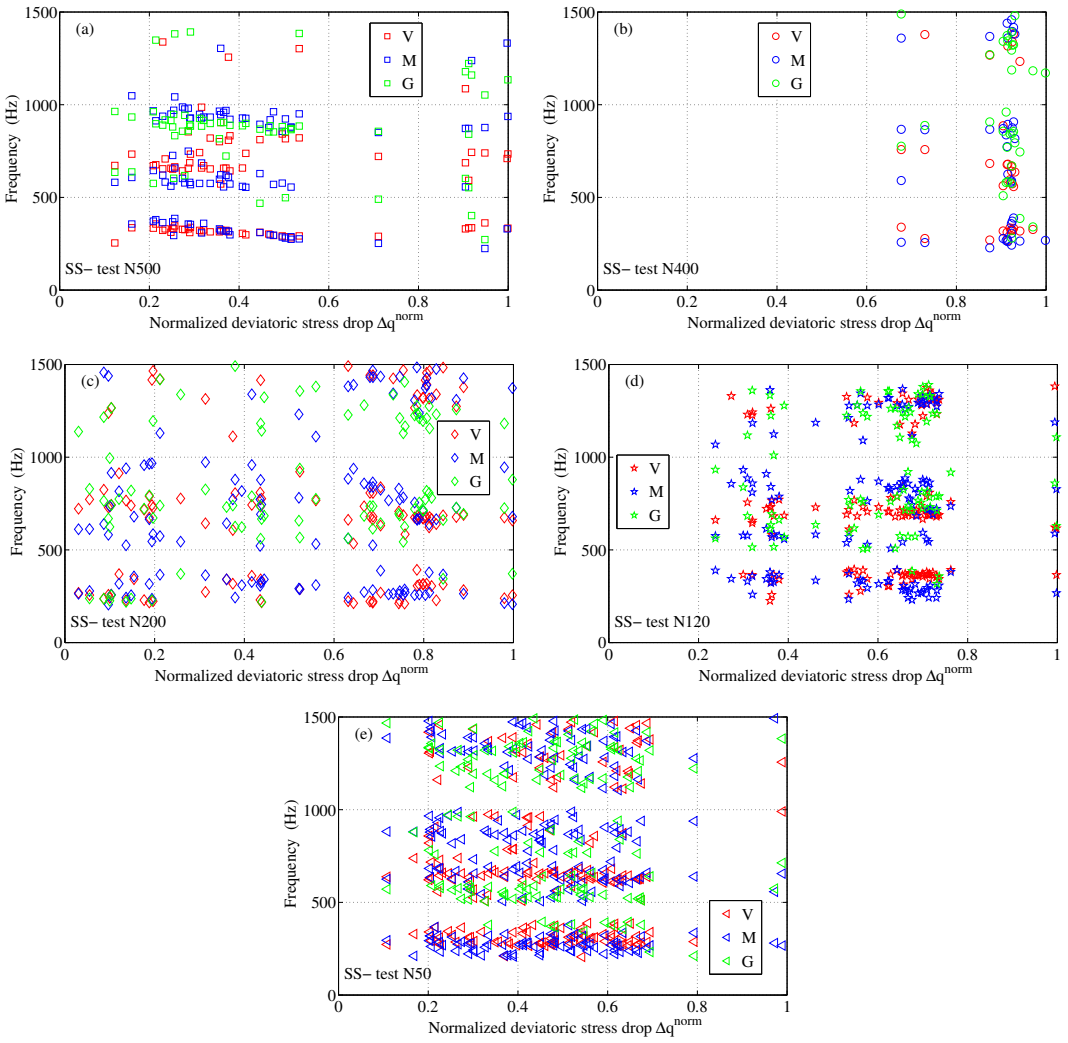

Figure 6.28: Characteristic frequencies of stick-slip event at different confining pressures identified by CCWT.

CIDNC series is analysed firstly. Figure 6.28 presents all possible significant fre-

quencies detected by V, M, G using CCWT. It contains only the detected frequencies during the instabilities compared to those of noise. The largest confining pressure of 500 kPa exhibits the three emergent groups of frequency around 325, 638, 899 and 1242 Hz in figure 6.28a.

Other tests respectively at 400, 200, 120 and 50 kPa are subsequently presented in figures 6.28b to e. As in figure 4.10, low confining pressure p'_0 leads to low Δq and the increasing scatter of data due to the insignificance of signal compared to the noise. This disturbance creates the larger standard deviation of frequency at low p'_0. However the mean values are still consistent to those of 500 kPa in table 6.6. Regardless of normalised amplitude Δq^{norm} of stick-slip, 4 groups of signature frequency are pointed out at 335.6, 571.4, 841.7 and 1252.8 Hz. Furthermore, within CIDNC series with low Skempton's coefficient B, the consistency of dominant frequencies means that the vibration modes is independent of the saturation of the assembly.

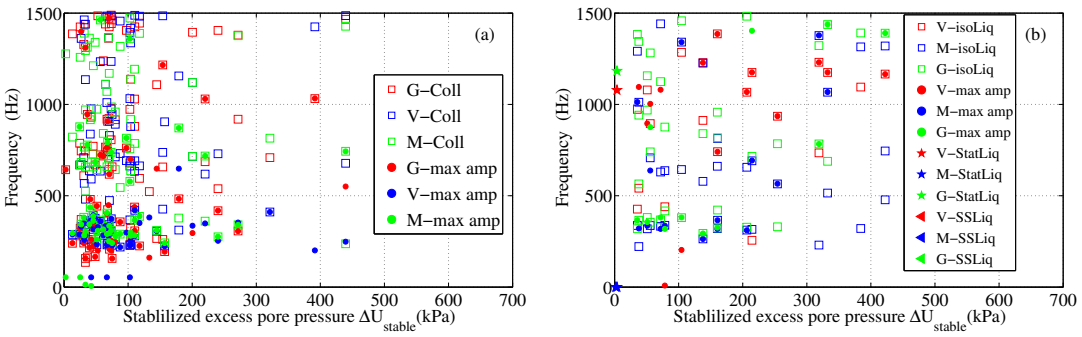

Figure 6.29: Characteristic frequencies of collapse and liquefaction identified by CCWT.

Another kind of local instability, collapse, are analysed showing the similar four groups of frequency irrespective of ΔU_{stable} (figure 6.29a). The first excited frequency is still 311.4 Hz followed by 667.7, 877 and 1322 Hz. Finally Liquefaction series is completed (figure 6.29b) and delivers 4 groups of 341.4, 653.2, 884.5 and 1268.4 Hz.

In table 6.6, the strong consistency on the signature frequencies for 3 kinds of instability implies the same nature of the vibration of the grains regardless of the loading conditions. However as indicated in chapter 4 and 5 the dominant frequency of pore pressure is only 80 Hz at full saturated condition and drops dramatically to 20 Hz for nearly saturated sample. This distinction in frequency of the grains and pore pressure thickened the question of the physical interaction of the grains and the

Table 6.6: Identification of natural frequencies of instability by CCWT.

	Characteristic frequency of instability event (Hz)			
Compression stick-slip	335.6 ± 81.61	636.9 ± 65.13	863.6 ± 64.68	1252.8 ± 101.07
Isotropic collapse	311.4 ± 74.39	667.7 ± 56.60	877.0± 74.23	1322.2 ± 144.61
Isotropic liquefaction	341.4 ± 59.58	653.2 ± 74.19	884.5 ± 69.78	1268.4 ± 132.23

surrounding fluid. Unfortunately, the mechanisms of fluctuation and the pore pressure buildup are still unknown.

6.5.5 High-resolved time sequence of AE measurements

The time series of both acoustic and mechanical measurements have been revealed individually in some typical events in previous chapter to exclude the suspect that pore pressure is the cause of the instability, especially in case of liquefaction. The inclusion of time domain of CCWT analysis exhibited the robust usefulness to localise the dominant frequency within very brief duration of slip phase. The essential questions on the links between of acoustic signals and mechanical measurements have been resolved. The remaining question is whether acoustic signals is the resultant of mechanical failures (stress drop). Figure 6.30 presents the systematic estimated time of the peak of CCWT amplitude from sensor of acceleration G, microphone M and vibrometer V. Note that each colour (e.g. green) represents data from one sensor including the peaks at all possible localised natural frequencies can be detected within the duration of the signal around 200 ms. Firstly, the peak of G at five studied confining pressures always emerges prior to M and V later, confirming previous assessments on the time delay between measurements counted at the begining of G. The main point here is the time sequence of G and deviatoric stress drop. Thus a comparison is shown in table 6.7.

It can be seen that the time to reach the peak of CCWT amplitude of acceleration signal is mostly equal and even prior to the duration for deviatoric stress q drop during slip phase (t^q_{drop}). Low frequencies of acoustic signal are generated simultaneously with the mechanical stress during stick-slip instability. The precursors, defined as small stick-slip with magnitude of deviatoric stress drop Δq below 5 kPa, are not included in this study.

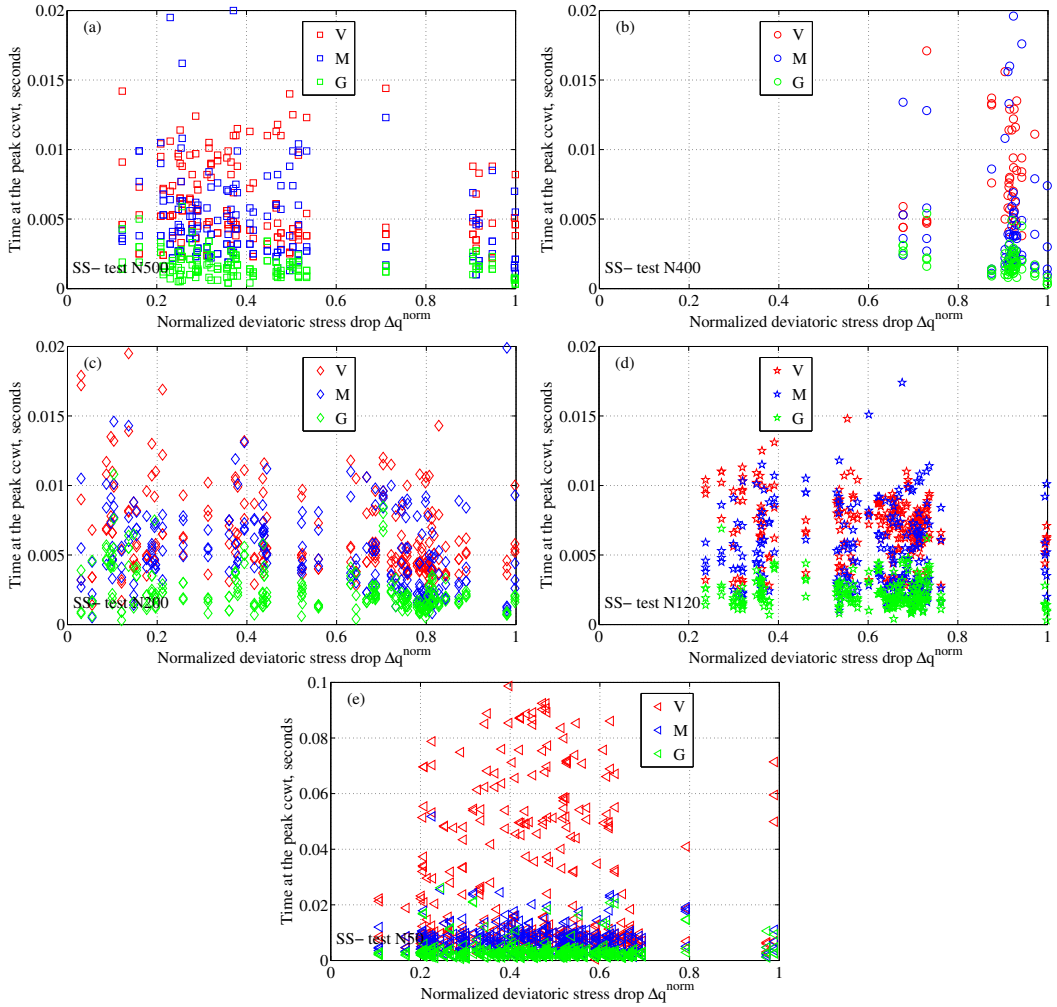

Figure 6.30: Time at the peak of CCWT amplitude of stick-slip events at different confining pressures(CIDNC series).

Table 6.7: Identification of time at the peak of CCWT amplitude of G, M, V signal during stick-slip events in CIDNC series.

Test	N500	N400	N200	N120	N50
Time of CCWT peak of G (ms)	1.5 ± 0.85	1.5 ± 0.69	2.5 ± 2	2.2 ± 1.3	2.6 ± 2.7
t^q_{drop} (ms)	1.37 ± 0.6	1.39 ± 0.43	2.5 ± 0.0013	2.1 ± 0.58	2.7 ± 0.77

The time sequence of the most energetic frequencies which possibly excited during collapses and liquefactions is provided in figure 6.31. For isotropic liquefaction IL, likewise stick-slip events, the CCWT amplitude of acceleration G reaches the peak first, then the lateral sound pressure and lastly the lateral vibration. Two stick-slip liquefactions SL (triangles) are added and verify the same sequence. Different situation is observed for collapses, it seems all G, M and V signals reach the CCWT peak simultaneously. Note that the time sequence of CCWT peaks is not the time sequence of the appearances of the acoustic measurement.

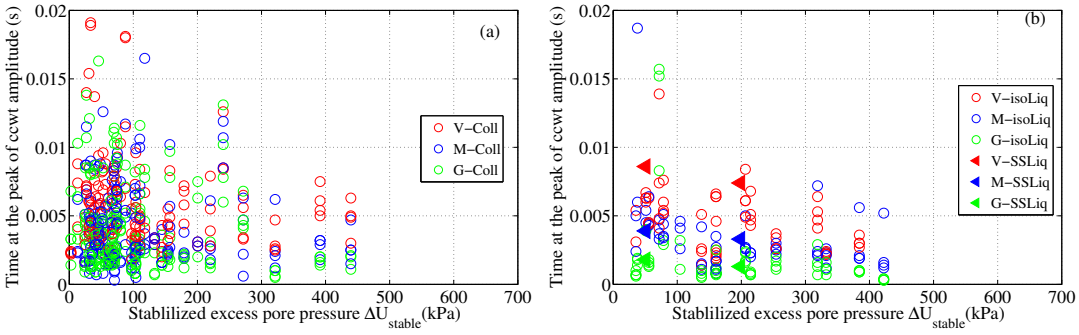

Figure 6.31: Time at the peak of CCWT amplitude of collapse (a) and liquefaction (b).

6.5.6 Energy release

The strain energy of an event is defined as proportional to the squared amplitude of AE signals during that event. This energy release is introduced in this analysis due to its importance. It reflects the comprehensive meaning of the acoustic measurements, not individual amplitude, frequency, duration, rising time, decaying time etc. This energy can be the signature of the acoustic measurements. Figure 6.32 presents the individual energy of each instability during the process of triaxial shearing phase up to ε_1= 25%.

Since figure 6.19 pointed out the linear relation of amplitude of AE measurements and the amplitude of stress drop, one can see the individual energy of the event is not even, exactly like the generated unpredictable SS event. Test N500 have one event at axial strain ε_1 of 5% with distinct high energy. This is coherent to the temporal development of acceleration G (figure 6.7a) in which G (dark blue) stabilised at a non zero level than gradually declined back to the previous static state. This behaviour

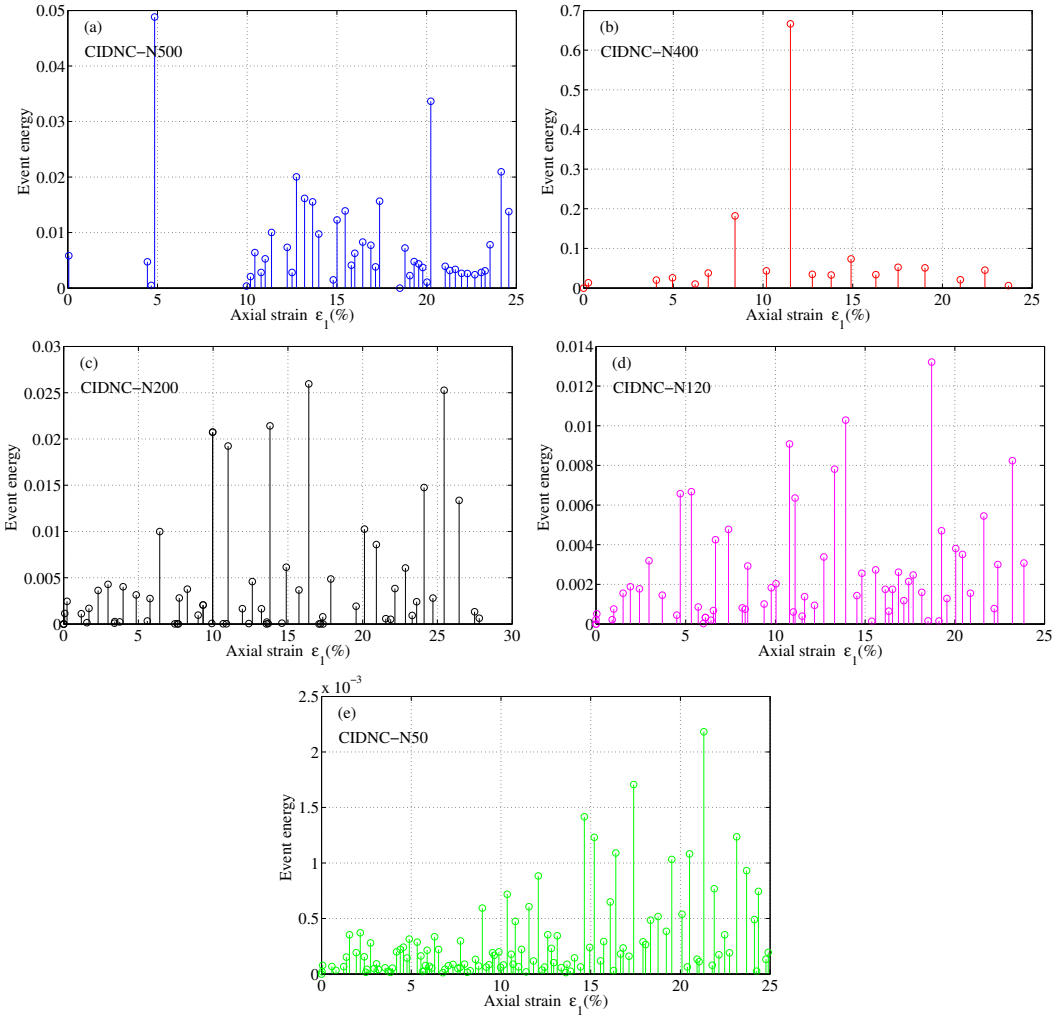

Figure 6.32: Energy release in each stick-slip event estimated for CIDNC series.

results in larger amplitude than other common SSs. Similarly, in test N400 (figure 6.32b, two noticeable peaks correspond to two SS events (cyan and pale green) having similar response in figure 6.8a. Unfortunately no explanation has been figured out. In the series of 5 CID tests with decreasing confining pressure p_0 the magnitude of energy release seems to decline.

Subsequently, the energy release rate is estimated as the sum of energy release of all events occurring within a specific interval of axial strain. The studied interval is identified as 4 % to contain at least 1 SS event to diminish the strong fluctuation of the energy rate. Five stress-strain curves in figure 6.33a recall the global behaviour of SS at

different confining pressure. All of them gradually approach the plateau (critical state), approximately at $\varepsilon_1 = 12\%$. The average evolution of AE characteristics during the progressive deformation up to 25% is presented in figure 6.33b. Correspondingly, the energy rate curves of test N50 and N120 also reach a certain stabilised level. Other tests with strong fluctuation of energy rate can be represented by the mean value within 12 % to 25 % of axial strain. These mean values are governed by both of confining pressure p_0 and initial void ratio e_c. This stabilised level of energy rate is of importance since it partially explains the compensation of the occurrence frequency of stick-slip and the amplitude of the generated event. Thus, the same energy rate means the same amount of energy release within an interval of axial strain, the large number of stick-slip corresponds to the small amplitude of stick-slip events and inversely. Nevertheless, the factor governing the repetition of global stick-slip events in stress-strain relation even at the same initial parameter as void ratio, confining pressure, is still missing.

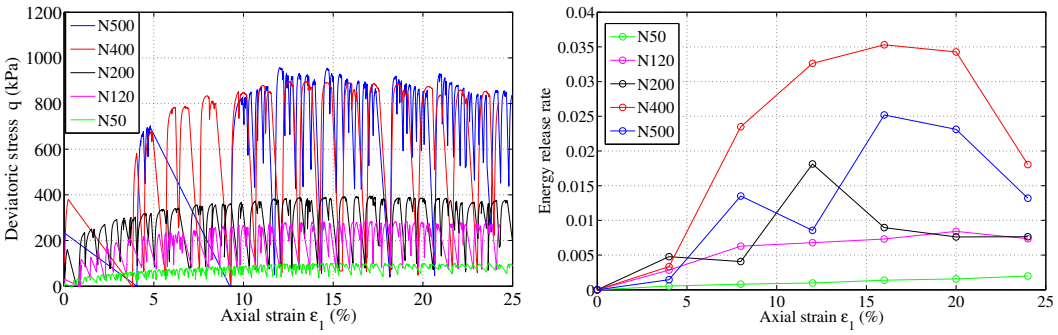

Figure 6.33: Energy release rate during shearing stage at different confining pressure (CIDNC series).

The stabilised level of energy release rate should be verified by the relation to the mechanical strain energy during very brief slip phase of the stress drop. However, within this study this target is impossible to obtain since the real dynamic regime of stress-strain behaviour (q-ε_1) during slip phase is missed. The infinite modulus of the material during slip phase was pointed out in figure 4.18b due to the inability of LVDT to capture the transient dynamic strain behaviour. This disadvantage could be improved by another technique like fast camera or laser displacement sensor. An additional investigation on the link between magnitude of SS and AE measurements is performed by qualitative comparison between probability density function (pdf) of

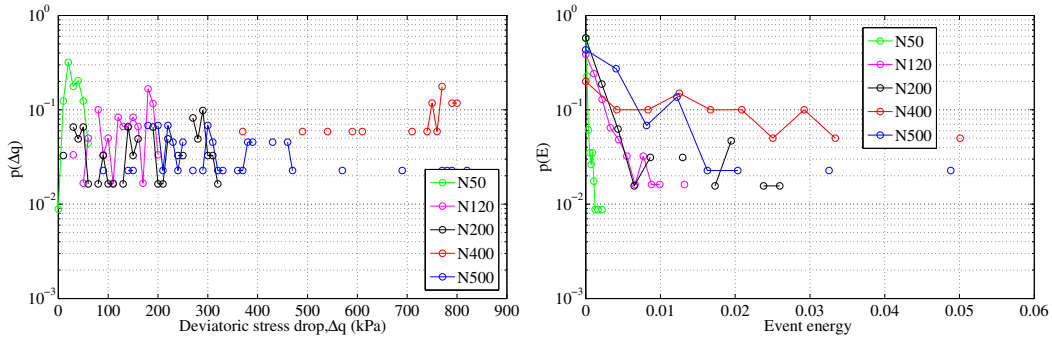

Figure 6.34: Possibility of (a) normalised deviatoric stress drop Δq^{norm}, (b) Energy release during single stick-slip event.

stress drop and AE characteristics. The probability of stress drop seems to be uniform that is quite far from either common power law for weak force chains or exponential rule for strong force chains in dry condition (71, 98, 120). Excepting for the initial segments with obvious slopes, figure 6.34b shows the resemblance of amplitude distributions for low frequency AE signal with the features of stress drop. By visual inspection, the similarity between them means the source attributing to the generated AE energy is merely the release of contact forces (the stress drop) without other accompanying processes. The quantitative correlation between the probability of stress drop and AE energy is not necessary to estimated here since the fitting parameter for the two possibility plots are not properly identified when lacking the AE from the precursors. The portion of possibility plot containing major slip roughly share the same law. The attempt to apply the statistics distribution on the amplitude of stick-slip and of energy release needs the direct link between stress drop Δq and G (figure 6.19a). Finally the direct deterministic correlation between amplitude of low frequency AE and stress drops established by a strong linear relation in figure 6.19a contributed the important link to enhance the possibility to predict SS event in saturated media from low frequency acoustic measurements.

6.5.7 Effect of diameter of grains

Among 17 liquefactions within Liquefaction series, one liquefaction IL3 at 418 kPa for grains with diameter of 0.4 mm is highlighted to compare with other liquefactions of 0.7 mm. Furthermore one special test Dmix_{01} of series D at 500 kPa (presented in

chapter 5) using the mixture of 50 % in weight of 0.7 mm and 50 % of 0.4 mm beads is exploited here. The primary matters need to be analysed are the frequency of the grains and the CCWT amplitude relating to the energy generated during dynamic events. CCWT analysis is applied to identify dominant frequency from V, M, G illustrated in figure 6.35, detail for SS events is shown in subfigure a and collapse in subfigure b. Similarly to test N500 of CIDNC series at 500 kPa, the frequency of grains locates in 5 groups with mean and standard deviation listed on table 6.8, which are respectively 325, 667, 874, 1153 and 1402 Hz. Compared to table 6.6, it can be seen that the grain size does not affect the dominant frequencies of SS events. Collapse events are collected in separate figure 6.35b. Test Dmix_{01} has 4 collapses, combined with two liquefactions which are IL_{01} for 0.7 mm beads and IL_{03} for 0.4 mm beads. The dominant frequency in isotropic collapses seems to vary lightly compared to liquefaction however globally the responses of both IL_{03} (0.4 mm) and Dmix_{01} are still consistent with the whole series liquefaction and collapse for the beads of 0.7 mm of diameter.

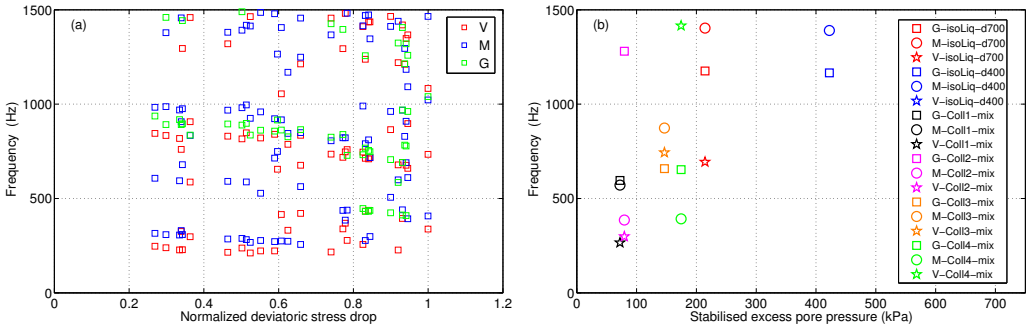

Figure 6.35: Characteristic frequency of stick-slip event for a binary mixture of 0.7mm and 0.4 mm at $p_0 = 500$ kPa.

Table 6.8: Identification of natural frequencies of instability by CCWT of the mixture.

	Characteristic frequency of instability event of mixture materials (Hz)			
SS	325.8 ± 46.44	638.1 ± 59.40	899.2 ± 47.57	group(1153.1÷1402.9)
Collapse	311.4 ± 74.39	667.7 ± 56.60	877.0 ± 74.23	group(1200÷1400)

The influence of grain size is further evaluated by CCWT amplitude in figure 6.36. In test N500 (blue squares), there is almost a linear relation between the amplitude of G

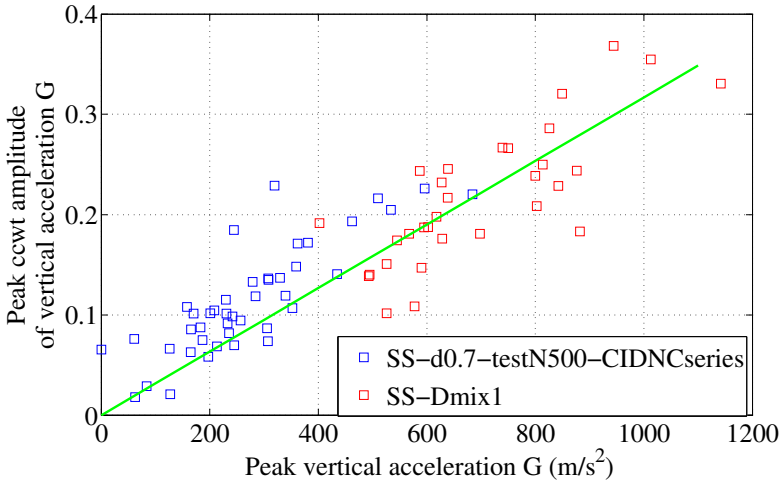

Figure 6.36: CCWT amplitude of vertical top cap acceleration between monodisperse material and binary mixture.

signal and its CCWT amplitude, meaning the consistence on the frequency and duration of all SSs within this test. The addition of red squares of test Dmix_{01} exhibits no significant difference on the slope from test N500 but larger amplitude of G. In contrast to previous study (57) in ring shear test for dry material with the range of frequency from 1 to 30 kHz, in which they indicated the decrease of power spectral density with the decrease of grain size, as well as the modification of dominant frequencies, our result reveals that mixture and nearly mono size material exhibit identical response in G and CCWT amplitude. It improves the independence of dominant frequencies on the grain size, meaning grain size has no strong effect.

6.6 Conclusions

This chapter produced a comprehensive analysis on the dynamic characteristics of AE measurements as a complement to conventional mechanical measurements in previous chapters. Three series of tests including various kinds of instability associated with additional tests on binary mixture were exploited. High time-resolved data of top cap acceleration, lateral sound pressure, lateral vibration revealed the abrupt motion of the grain skeleton (vertical acceleration and stress drop) systematically occurring before the generation of excess pore pressure.

Frequency analysis was applied with FFT to extract the frequency content below 5 kHz. The combined use of 3 techniques (vertical accelerometer, lateral sound microphone and lateral vibrometer) is helpful to verify and support each other to obtain the full frequency content of the dynamic instability. The **FFT signature spectra** of instability can be recognised by the broad band of frequency range with almost every frequencies being excited in liquefaction and stick-slip.

Furthermore, numerical simulation was employed to figure out the eigenfrequencies of the idealised solid homogeneous granular structure. The simulation results reasonably matched the measuring data and help to explain the dominant frequencies of the instability event. An advanced step was conducted by CCWT to recognise the duration and confirm the **dominant frequency** of the failure phenomenon. It gives precise details on the temporal evolution of the dominant frequencies. All these careful measurements and analyses delivered the essential identical frequencies of dynamic instabilities around 320, 640, 870, 1260 Hz in the audible range. This same group of natural frequency identified in liquefaction, stick-slip and collapse implied that all three kinds of instability are probably originated from the same physical triggering mechanisms. These constant frequencies are the signature of a vibrating system. From these main vibration modes, the **elastic characteristics (bulk modulus K, poisson ratio ν)** can be deduced by back-calculation. Acoustic emission results can be use to characterise different kinds of instability. They offer for the first time the distinction between dynamic and static liquefaction and estimate quantitatively many important macroscopic parameters.

Direct relations between the amplitude of acceleration G (lateral sound pressure M, lateral vibration V) and other mechanical measurements were established to predict the missing parameters left in previous chapters:

(i) the triggering deviatoric stress q_{trig} and the amplitude of stress drop Δq for stick-slip event;

(ii) the triggering effective stress σ'_{trig} and the generated stabilised excess pore pressure ΔU^{norm}_{stable} for isotropic collapse and liquefaction events.

So far, in this chapter three parameters Δq, σ'_{trig}, ΔU_{stable} are introduced in three empirical relations with the top cap acceleration G. The relations of G$\backsim\Delta q$ (figure 6.19), G$\backsim\sigma'_{trig}$ (figure 6.20), G$\backsim\Delta U^{norm}_{stable}$ (figure 6.22) help to predict Δq, σ'_{trig} and ΔU^{norm}_{stable}

only from the maximum peak amplitude of acceleration G. This striking result highlighted the overall role of passive acoustic signal especially the accelerometric measurement on sample top in controlling all remaining mechanical stress-strain measurements during the instabilities, including the special case of complete destruction of the granular skeleton during liquefaction failure. These relations between acoustic and mechanical measurements reveal the **quasi-deterministic nature** of granular instabilities.

Furthermore, one rare liquefaction with 0.4 mm beads and one with binary mixture of 0.4 and 0.7 mm are added to preliminary probe the effects of grain size on the dynamic vibration of granular structure. No modification in the dominant frequency was found. However, many unsolved problems remain. Though the macroscopic amplitude of pore fluid showed the strong role in the relations to all mechanic and acoustic measurements, the uncorrelated vibration regime between grain structure and pore fluid has not been explained despite many attempts carried out to exclude the artefacts. Even leaving aside the frequency of the pore fluid pressure in the transient phase I, the mechanism of pore pressure buildup to reach the stabilised state is still missing in drained condition.

7

Conclusion

The stick-slip phenomenon, isotropic collapse, isotropic liquefaction and a new family of liquefaction of model granular materials were studied using triaxial machine within this dissertation. These granular instabilities spontaneously occur at unpredictable triggering effective stress and uncontrollable void ratio with unexpected buildup of excess pore pressure irrespective of fully drained condition, contrasting the instability-free behaviour of natural granular materials.

A special experimental setup was carefully designed with a new set of static and dynamic sensors for pore pressure, passive acoustic transducers (vertical piezoelectric accelerometer, lateral prepolarized microphone) and lateral laser vibrometer. A large number of tests were carefully performed with a high sampling frequency in various loading (isotropic and triaxial compression), drainage (drained and undrained) and saturation (dry, wet and saturated) conditions. At the level of individual instability, high time-resolved data revealed the precise time sequence of events and the dynamics of granular instabilities.

The link between the three kinds of instability was qualitatively established by the similarity of excess pore pressure. Then this link was highlighted by empirical equations describing the evolution from local (collapse and stick-slip with resuming behaviour) to total failure (liquefaction with total destruction of the granular structure). These relations suggested the plausible common triggering mechanisms of these granular instabilities. The high time-resolved response of pore pressure indicated an important role of the short-lived stabilised excess pore pressure ΔU_{stable}, relating to all remaining mechanical and acoustic measurements by strong empirical relations with the uncou-

pled effects of initial void ratio e_c at the beginning of triaxial compression and effective confining pressure p'_0.

Acoustic emission (AE) measurements established the quasi-deterministic nature of dynamic instabilities by the empirical correlations between the peak amplitudes of AE measurements and the mechanical stress drop Δq, the effective triggering stress σ'_{trig} and the excess stabilised pore pressure ΔU_{stable}. AE analysis also identified the dominant frequencies for all kinds of instability. From these dominant frequencies, back analysis by finite element method could estimate the elastic characteristics of the granular assembly.

The improvements on understanding are extracted below, grouped in three separate topics including (i) the mechanical behavior of drained compression stick-slip, (ii) the mechanical behaviour of isotropic collapse and liquefaction, (iii) the AE characteristics of all instabilities of interest and finally (iv) the overall connections between various instabilities.

7.1 Stick-slip

The previously reported quasi-periodic and large stick-slips up to 500 kPa of effective confining pressure were well replicated with new results and better resolution, including the missing pore fluid outburst in the slip phase.

High time-resolved mechanical measurements of all major stick-slip events at different confining pressures p'_0 help identify the precise time sequence of mechanical measurements as follows: first deviatoric stress drop Δq occurs simultaneously with changes of vertical top cap acceleration, then lateral sound pressure, lateral vibration, surge of excess pore pressure, and finally the axial and volumetric strains start to develop. This systematic time sequence of events implied the **non causative mechanism of excess pore pressure** in the stick-slip phenomenon and suggested a rearrangement of the grain structure as a plausible mechanism of the instability.

Time resolved data also contributed to better understand the dynamics of slip phase. The duration of deviatoric stress drop Δq is a constant of 2.27 ms independent of amplitude of deviatoric stress drop Δq with almost no variation of axial and volumetric strain. This raised an unknown issue in the infinite modulus of stress-strain relation. After the very brief slip duration, the system enters in a stabilised state of deviatoric

stress, lasting until the pore pressure completely dissipates. Then deviatoric stress q increases again in the next stick phase.

Concerning the global behaviour of stick-slip during triaxial compression, the effect of effective confining pressure p'_0 is confirmed in this study as in the literature. Our works added the crucial role of void ratio, highlighted in the case of loose and saturated material. The uncontrolled initial void ratio e_c at the beginning of shearing stage influences the amplitude of stick-slip event and the recurrence of the stick-slip as well. Specifically, denser material delivers fewer and larger stick-slips. The combination effect of both confining pressure p_0 and void ratio e_c are not achieved since e_c shows dominant impacts in loose assembly.

The complex dynamic response of pore pressure is decomposed into two phases. The first phase is a vibration partially characterised by its frequency. The drop of frequency is qualitatively explained by the presence of air in the nearly saturated state. The dissipation phase of pore pressure represented by the consolidation coefficient C_v is affected by the confining pressure. The time characteristics of pore pressure are estimated by two empirical equations 4.5 and 4.6. They describes the transient duration t_{trans} and the intermediate duration Δt_{05} depending on the effective stress at the stabilised state of pore pressure.

The role of stabilised excess pore pressure is emphasised by the quantitative strong relations between normalised excess pore pressure ΔU^{norm}_{stable} and other stress and strain measurements including normalised deviatoric stress drop Δq_{norm}, incremental axial strain $\Delta\varepsilon_1$ and incremental volumetric strain $\Delta\varepsilon_{vol}$. In these relations, table 7.1, the **decoupled impacts of void ratio e_c and effective confining pressure p'_0** are introduced in a consistent manner throughout all investigations. With high resolution data, the slip phase can be interpreted as a **dynamic consolidation at constant deviatoric stress**.

A common stick-slip boundary in $(q - p')$ plane is found, lower than Mohr-Coulomb plastic criterion, which limits the space of the quasi-static effective stress state in the slip phase. The effective stress state cannot exceed this boundary unless it reaches the liquefaction.

The stress-induced anisotropy of the material during stick-slip is measured by static anisotropy coefficient $< i^{stat} > = 1.14 \pm 0.37$, lower than 3 for isotropic material. The dynamic anisotropy coefficient i^{Dyn} has large value $< i^{Dyn} > = 13.15 \pm 7.15$. This result

confirmed that the anisotropy of material is an imperative condition for the apparition of stick-slip phenomenon.

7.2 Isotropic instabilities (collapse and liquefaction)

Besides the serendipitiously discovery of drained isotropic liquefaction IL in our published works (30, 34), this thesis presented **new subtypes of dynamic liquefaction**: stick-slip SL, back pressure BL, water flushing FL and water imbibition liquefaction WL. The well known static liquefaction UL is added but high time-resolved data helps to compare and improve the understanding of this new family of liquefaction.

The initial void ratio e_{20} is still the most important parameter in the identification of the appearance threshold of liquefaction. A new threshold was established, $e_{20}^{thres} = 0.682$ ($D_r = 3.57\%$) which slightly improved our previous works.

The time characteristics of pore pressure were investigated including (i) a constant duration of transient phase I, $< t_{trans}^{Liq} > = 0.19 \pm 0.05$ seconds, (ii) the duration of stabilised phase II as an exponent function of triggering stress σ'_{trig}, (iii) the dissipation phase III represented by k_{diss} linearly relating to σ'_{trig}. The relations are listed in detail in table 7.1.

For collapse, the time characteristics of pore pressure were also characterised including (i) a constant duration of transient phase I, $< t_{trans}^{Coll} > = 0.14 \pm 0.02$ seconds in the same range of liquefaction, (ii) the duration of stabilised phase II as a logarithmic function of normalised excess pore pressure ΔU_{stable}^{norm}, (iii) the dissipation phase III represented by k_{diss}^{norm} as logarithmic function of ΔU_{stable}^{norm}.

The evolution from collapse to liquefaction is denoted in the smooth relation of normalised excess pore pressure ΔU_{stable}^{norm} and incremental axial strain $\Delta\varepsilon_1$ and incremental volumetric strain $\Delta\varepsilon_{vol}$.

The precise time sequence of each kind of liquefaction and collapse is very similar to that of stick-slip event. The early strong variation of vertical top cap acceleration implied again that excess pore pressure is not the causative mechanism, even in the case of isotropic instability with the absence of deviatoric stress.

The dynamic anisotropy coefficient does not show a clear relation with confining pressure, and the static anisotropy coefficient of collapse significantly larger than that of

liquefaction. Although under isotropic loading the material still behaves anisotropically, implying a strong inherent anisotropy.

7.3 Passive acoustic signature

The frequency content of the instabilities was extracted by a Fast Fourier Transformation, supplemented in the time domain by Cauchy Continuous Wavelet Transformation. This provided a comprehensive picture on the whole possible frequencies of AE measurements. Three types of frequency were collected including (i) spikes below 50 Hz, (ii) spikes from 300 to 2500 Hz, (iii) broad peaks (around 320, 640, 870, 1260 Hz). With the support from FEM simulation, the resonant frequencies of a solid cylindrical structure are identical to those of acoustic measurements and the low frequencies below 50 Hz likely from the surrounding hollow latex membrane. The group of **rounded broad peaks is the frequency signature of the dynamic instabilities**. Systematic analyses were performed for three kinds of instabilities exhibiting the same frequency signature implying the same underlying physical mechanisms.

No correlation has been found for the dominant frequencies of the grain skeleton and that of pore fluid pressure. The grains and the pore fluid during dynamic regime within initial 300 ms of the first phase seem to work independently, although their quasi-static measurements are strongly correlated. The anomalous frequency of pore pressure saturates at the dominant value of 80 Hz. Despite many efforts to verify and exclude the artefacts, the nature of this frequency remains unknown.

The amplitudes and frequencies of AE measurements are indicators to distinguish various types of instability. Direct relations between AE amplitudes and stress measurements were constructed. For stick-slip, the amplitudes of top cap acceleration, lateral sound pressure and lateral vibration speed are linearly proportional to deviatoric stress drop Δq, and for liquefaction, linearly proportional to triggering effective stress σ'_{trig}. Finally for collapse, the amplitude of top cap acceleration is a two variable function of triggering stress σ'_{trig} and normalised excess pore pressure ΔU^{norm}_{stable}. These relations can be used to predict all subsequent stress and strain variations only by the amplitude of the early AE signals.

7.4 The connection of stick-slip, collapse and liquefaction

Table 7.1 summarises all quantitative and empirical relationships established within this study. Each column corresponds to a kind of instability (collapse or liquefaction or stick-slip). The evolution from local (collapse and stick-slip) to total failure (liquefaction) is encapsulated in these empirical equations.

Starting with liquefaction (central column) and moving upwards from the bottom, if the peak amplitude of vertical top cap acceleration G^{Liq} (or M^{Liq}) is known then the effective triggering stress ${\sigma'}_{trig}$ is deduced. Consequently, all characteristics of pore pressure (upper rows) are identified depending only on ${\sigma'}_{trig}$. For collapse (left column), if the peak amplitude of vertical acceleration G^{Coll} is known and the triggering stress ${\sigma'}_{trig}$ predicted, then equation 6.2 helps to infer ΔU^{norm}_{stable}. Subsequently, all stress and strain characteristics are calculated from the only variable ΔU^{norm}_{stable}.

For stick-slip, two initial parameters, the amplitude of acceleration drop G^{Liq} (M^{Liq} or V^{Liq}) and the triggering deviatoric stress q_{trig}, are essential in estimating the amplitude of deviatoric stress drop Δq of stick-slip. From variable $\Delta q_{norm} = \Delta q / q_{trig}$, ΔU^{norm}_{stable} is estimated by equation 4.11. Next, the axial and volumetric strain ($\Delta\varepsilon_1$, $\Delta\varepsilon_{vol}$) are both calculated from ΔU^{norm}_{stable}. The normalised effective mean pressure at stabilised state ${p'}^{norm}_{stable} = \frac{p'_{stable}}{p'_{crit}}$ is estimated from all known parameters in previous steps (Δq, q_{trig}, ΔU^{norm}_{stable}) together with the effective confining pressure p'_0 and the frictional characteristic M at the critical state of global shearing behaviour.

With identified variable ${p'}^{norm}_{stable}$, all time characteristics of pore pressure are calculated by equations 4.5 and 4.6.

In the direction of vertically moving upward, from the parameters at the bottom row, all characteristics are identified in individual kind of instability. These three separate columns are the empirical relations for three types of instability. Most fitting equations have good correlation coefficients. Thus, they establish the **quasi-deterministic nature of granular instabilities**.

The direction of horizontal translation from outside (local failures) to the central column (total failure) shows the connections and evolution from stick-slip to liquefaction as well as from collapse to liquefaction. Most asymptotic functions of collapse and stick-slip (left and right columns), at the ultimate state of the dependent variables, become

Table 7.1: Summarized relations of key parameters

Parameter	Collapse	Liquefaction	Stick-slip
t_{trans} (s)	$< t_{trans}^{Coll} > = 0.1512 \pm 0.0243$ s	$< t_{trans}^{Liq} > = 0.199 \pm 0.0534$ s	eq 4.5 $t_{trans}^{norm} = \frac{t_{trans}^{SS}}{<t_{trans}^{Liq}>} = (1 - \frac{p'_{stable}}{p'_{crit}})^{0.371}$ $\frac{p'_{stable}}{p'_{crit}} \rightarrow 0$, $t_{trans}^{SS} \rightarrow <t_{trans}^{Liq}>$
Δt_{05} (s)	eq 5.4 $\Delta t_{05}^{Coll} = -0.0773 \ln(1\text{-}\Delta U_{stable}^{norm})$ $\Delta U_{stable}^{norm} \rightarrow 1$, $\Delta t_{05}^{Coll} \rightarrow \Delta t_{05}^{Liq}$=1-0.199=0.801s	eq 5.2 $\Delta t_{05}^{Liq} = 0.801 + 3454.1(\sigma'_{trig})^{-1.298}$ $\Delta U_{stable} \rightarrow$ inf, $\Delta t_{05}^{Liq} \rightarrow 0.801$s	eq 4.6 $\Delta t_{05}^{SS} = -0.061855 \ln(\frac{p'_{stable}}{p'_{crit}})$ $\frac{p'_{stable}}{p'_{crit}} \rightarrow 0$, $\Delta t_{05}^{SS} \rightarrow \Delta t_{05}^{Liq}$=1-0.199=0.801s
k_{diss} (kPa/s) k_{diss}^{norm} (1/s)	eq 5.5 $k_{diss}^{norm} = -0.72126 \ln(1\text{-}\Delta U_{stable}^{norm})$	eq 5.30 $k_{diss} = 4.59\sigma'_{trig}$	NA
ΔU_{max} (kPa)	eq 5.8 $\Delta U_{max} = 1.965\ \Delta U_{stable}$	eq 5.8 ΔU_{max}=1.965ΔU_{stable}=1.965σ'_{trig}	eq 4.1 $\Delta U_{max}^{norm} = 2.262\ \Delta U_{stable}^{norm}$
$\Delta\varepsilon_1$ (%)	eq 5.6 $\Delta\varepsilon_1 = -0.61364 \ln(1\text{-}\Delta U_{stable}^{norm})$	eq 5.6 $<\Delta\varepsilon_1^{Liq}> = 24.14 \pm 7.02$ %	eq 4.9 $\Delta\varepsilon_1 = -0.689\ [\ln(1\text{-}\Delta U_{stable}^{norm})]$
$\Delta\varepsilon_{vol}$ (%)	eq 5.7 $\Delta\varepsilon_{vol} = -0.31036 \ln(1\text{-}\Delta U_{stable}^{norm})$	eq 5.7 $< \Delta\varepsilon_{vol}^{Liq} > = 2.864 \pm 0.753$ %	eq 4.8 $\Delta\varepsilon_{vol} = f(e_c) \ln(1\text{-}\Delta U_{stable}^{norm})$
Δq_{norm}	NA	NA	eq 4.11 $\Delta q_{norm} = (\Delta U_{stable}^{norm})^{g(e_c)}$
Acceleration (m/s^2)	eq 6.2 $G^{Coll} = 0.330.\sigma'_{trig}[0.03775.\log(1\text{-}\Delta U_{stable}^{norm})]$	G^{Liq}=0.33σ'_{trig}	G^{SS}=1.083Δq
Sound pressure (Pa)	NA	M^{Liq}=0.0395σ'_{trig}	M^{SS}=0.01199Δq
Lateral vibration (mm/s)	NA	NA	V^{SS}=0.0111Δq
i_{stat}	16.838 ± 0.069	0.124 ± 0.04	1.149 ± 0.368
Key parameters	σ'_{trig} (kPa) $\lvert G^{Coll}\rvert$ (m/s^2)	$\lvert G^{Liq}\rvert$ (m/s^2)	q_{trig} (kPa) $\lvert G^{SS}\rvert$ (m/s^2)

equations of liquefaction (central column). Consistent evolutions of the fitting function suggest again the same mechanisms for all three kinds of instabilities.

7.5 Perspectives

One of the expected goals of the study is to reveal the mechanisms governing stick-slip, collapse and isotropic liquefaction of saturated model granular medium. This challenging target has not been totally obtained, unfortunately. This study cannot provide answers for all possible issues concerning the dynamics of these novel instabilities, but rather contribute to some enhancements with new and better experimental results.

The improvements in the physical understanding of these phenomena are already presented in the conclusion. Besides the missing goal of identifying the full mechanisms, the physics of the anomalous vibration of the excess pore pressure are poorly understood, the surge of pore pressure and its stabilised state still not well explained, the durations of three phases of pore pressure not well estimated and the strain dynamics of the slip phase during stick-slip event not accurately measured by traditional LVDT technique.

Based on these imperfections, some recommendations are suggested in the form of remaining questions requiring further investigation. New results often require better experimental observations on well designed experiments with better equipment.

How to test the structural hypothesis? Advanced technique, the high resolution computer tomography applied before and after the dynamic event, could be a candidate to detect the potential modification of the granular structure with direct experimental evidence.

How to obtain the correct stress-strain relation during slip phase? Fast camera and laser vertical displacement sensor having a great resolution are highly recommended to overcome the inadequate ability of LVDT to capture the dynamic strains in the slip phase.

How to identify the local or global deformation during slip phase? Numerical experiments using Discret Element Method and fast stereoscopic cameras are helpful to study the stress and strain field of the granular assembly.

How about the repeatability by an independent laboratory? Preliminarily works on the same model material were conducted independently by our colleagues at ENISE[1] showing the validity of isotropic collapse and paving the way for the reproducitibility of granular instabilities. Nevertheless, more laboratory works need to be done.

Can these granular instabilities happen in stress-controlled experiments, instead of strain-controlled ones in this work? The complementary stress-controlled technique on the traditional quasi-static CID stress path, and on constant stress ratio path could yield surprising new results.

Finally, full AE measurements at high frequency range are helpful to give information on the processes at grain contacts. It can improve the statistical analyses of mechanical and AE results and can potentially identify the transition from precursor to major instability (stick-slip, collapse, liquefaction).

[1] École nationale d'ingénieurs de Saint-Étienne

References

[1] Adjemian, F., Evesque, P. **Experimental study of stick-slip behaviour**. *Int. J. Num. Ana. Meth. in Geom.*, **28**(6):501–530, 2004. xv, 10, 11, 18, 33

[2] Alshibli, K. A., Roussel, L. E. **Experimental investigation of slip-stick behaviour in granular materials**. *International journal for numerical and analytical methods in geomechanics*, **30**(14):1391–1407, 2006. xv, 11, 12, 18, 67, 69, 84

[3] Ammi, M., Bideau, D., Troadec, J.P. **Geometrical structure of disordered packings of regular polygons; comparison with disc packings structures**. *Journal of Physics D: Applied Physics*, **20**(4):424, 1987. 5

[4] Anthony, J. L., Marone, C. **Influence of particle characteristics on granular friction**. *Journal of Geophysical Research: Solid Earth*, **110**(B8), 2005. 66

[5] Antony, S. J. **Evolution of force distribution in three-dimensional granular media**. *Physical Review E*, **63**(1):011302, 2000. 7

[6] Belheine, N., Plassiard, J. P., Donzé, F. V., Darve, F., Seridi, A. **Numerical simulation of drained triaxial test using 3D discrete element modeling**. *Computers and Geotechnics*, **36**(1-2):320–331, 2009. 18

[7] Black, D.K and Lee, K.L. **Saturating laboratory samples by back pressure**. *Journal of the soil mechanics and foundations division*, **99**(1):75–93, 1973. 133

[8] Brace, W.F., Byerlee, J.D. **Stick-slip as a mechanism for earthquakes**. *Science*, **153**(3739):990–992, 1966. 8

[9] Bradley, B. A. **Strong ground motion characteristics observed in the 13 June 2011 Mw6. 0 Christchurch, New Zealand earthquake**. *Soil Dynamics and Earthquake Engineering*, **91**:23–38, 2016. xv, 16, 69

[10] Budhu, M. *Soil mechanics and foundations. 3rd Ed.* John Wiley & Sons, 2010. 31

[11] Bui, M. T., Clayton, C. R. I., Priest, J. A. **The universal void ratio function for small strain shear modulus**. In *Fifth International Conference on Recent Advances in Geotechnical Earthquake Engineering and Soil Dynamics*. Missouri University of Science and Technology, 2010. 98

[12] Cadman, J. D., Goodman, R. E. **Landslide noise**. *Science*, **158**(3805):1182–1184, 1967. 25

[13] Cain, R. G., Page, N. W., Biggs, S. **Microscopic and macroscopic aspects of stick-slip motion in granular shear**. *Physical Review E*, **64**(1):016413, 2001. 15, 69

[14] Cain R., Page N., Biggs S. **Microscopic and macroscopic effects of surface lubricant films in granular shear**. *Phys. Rev. E*, **62**(6):83698379, 2000. 10

[15] Cambou, B. **From global to local variables in granular materials**. *Powders and grains*, **93**:73–86, 1993. 7

[16] Carstensen, E. L., Foldy, L. L. **Propagation of sound through a liquid containing bubbles**. *The Journal of the Acoustical Society of America*, **19**(3):481–501, 1947. 73

[17] Çabalar, A.F., Clayton, C. R. I. **Some observations of the effects of pore fluids on the triaxial behaviour of a sand**. *Granular matter*, **12**(1):87–95, 2010. xv, 16, 17, 33

[18] Chang, C. S., Hicher, P. Y. **An elasto-plastic model for granular materials with microstructural consideration**. *International journal of solids and structures*, **42**(14):4258–4277, 2005. 6

[19] Chen, Y., Irfan, M., Uchimura, T., Cheng, G., Nie, W. **Elastic wave velocity monitoring as an emerging technique for rainfall-induced landslide prediction**. *Landslides*, **15**(6):1155–1172, 2018. 25

[20] Christoffersen, J., Mehrabadi, M. M., Nemat-Nasser, S. **A micromechanical description of granular material behavior**. *Journal of applied mechanics*, **48**(2):339–344, 1981. 6

[21] Collins, I. F., Hilder, T. **A theoretical framework for constructing elastic/plastic constitutive models of triaxial tests**. *International Journal for Numerical and Analytical Methods in Geomechanics*, **26**(13):1313–1347, 2002. 7

[22] Cui, D., Wu, W., Xiang, W., Doanh, T. and Chen, Q., Wang, S., Liu, Q., Wang, J. **Stick-slip behaviours of dry glass beads in triaxial compression**. *Granular Matter*, **19**(1):1, 2017. 16, 18, 23, 33, 67, 69

[23] Cundall, P. A and Strack, O. D. L. **A discrete numerical model for granular assemblies**. *Géotechnique*, **29**(1):47–65, 1979. 7

[24] Daouadji, A., Darve, F., Al Gali, H., Hicher, P.Y., Laouafa, F., Lignon, S., Nicot, F., Nova, R., Pinheiro, M., Prunier, F., Sibille, L., Wan, R. **Diffuse failure in geomaterials: Experiments, theory and modelling**. *Int. J. Num. Ana. Meth. in Geom.*, **35**(16):1731–1773, 2011. 26

[25] de Richter, S. K., Zaitsev, V. Y., Richard, P., Delannay, R., Le Caër, G., Tournat, V. **Experimental evidence of ageing and slow restoration of the weak-contact configuration in tilted 3D granular packings**. *Journal of Statistical Mechanics: Theory and Experiment*, **2010**(11):P11023, 2010. 25

[26] Delannay, R., Duranteau, M., Tournat, V. **Precursors and triggering mechanisms of granular avalanches**. *Comptes Rendus Physique*, **16**(1):45–50, 2015. 25, 134

REFERENCES

[27] Desrues, J., Chambon, R., Mokni, M., Mazerolle, F. **Void ratio evolution inside shear bands in triaxial sand specimens studied by computed tomography**. *Géotechnique*, **46**(3):529–546, 1996. 10

[28] Dieterich, J. H. **Time-dependent friction and the mechanics of stick-slip**. In *Rock Friction and Earthquake Prediction*, pages 790–806. Springer, 1978. 10

[29] Dieterich, J. H., Conrad, G. **Effect of humidity on time-and velocity-dependent friction in rocks**. *Journal of Geophysical Research: Solid Earth*, **89**(B6):4196–4202, 1984. 15

[30] Doanh, T., Abdelmoula, N., Gribaa, L., Nguyên, T.T.T., Hans, S., Boutin, C., Le Bot, A. **Dynamic instabilities under isotropic drained compression of idealized granular materials**. *Acta Geotechnica*, **12**(3):657–676, 2017. 2, 20, 23, 53, 58, 60, 69, 90, 103, 130, 206

[31] Doanh, T., Abdelmoula, N., Nguyen, T.T.T., Hans, S., Boutin, C., Le Bot, A. **Unexpected liquefaction under isotropic consolidation of idealized granular materials**. *Granular Matter*, **18**(3):67, 2016. xvi, 1, 20, 22, 23

[32] Doanh, T., Hoang, M. T., Roux, J-N and Dequeker, C. **Stick-slip behaviour of model granular materials in drained triaxial compression**. *Granular Matter*, **15**(1):1–23, 2013. xv, 12, 13, 15, 16, 17, 18, 51, 58, 69

[33] Doanh, T., Le Bot, A., Abdelmoula, N., Gribaa, L., Hans, S., Boutin, C. **Unexpected collapses during isotropic consolidation of model granular materials**. *Comptes Rendus Mécanique*, **344**(2):66–77, 2016. 95

[34] Doanh, T., Le Bot, A., Abdelmoula, N., Hans, S., Boutin, C. **Liquefaction of immersed granular media under isotropic compression**. *Europhysics Letters*, **108**(2):24004, 2014. 1, 68, 84, 90, 103, 130, 206

[35] Dorostkar, O., Johnson, P., Guyer, R., Marone, C., Carmeliet, J. **Do Fluids Modify the Stick-Slip Behavior of Sheared Granular Media?** In *Poromechanics VI*, pages 158–163. 2017. 14, 84

[36] Drescher, A., De Jong, G. D. J. **Photoelastic verification of a mechanical model for the flow of a granular material**. *Journal of the Mechanics and Physics of Solids*, **20**(5):337–340, 1972. 5

[37] Duranteau, M., Tournat, V., Zaitsev, V., Delannay, R., Richard, P. **Identification of avalanche precursors by acoustic probing in the bulk of tilted granular layers**. In *AIP Conference Proceedings*, **1542**, pages 650–653. AIP, 2013. 25

[38] El Korchi, F. Z., Jamin, F., El Omari, M., El Youssoufi, M. S. **Collapse phenomena during wetting in granular media**. *European Journal of Environmental and Civil Engineering*, **20**(10):1262–1276, 2016. 24

[39] Ferdowsi, B., Griffa, M., Guyer, R. A. and Johnson, P. A., Marone, C., Carmeliet, J. **Microslips as precursors of large slip events in the stick-slip dynamics of sheared granular layers: A discrete element model analysis**. *Geophysical Research Letters*, **40**(16):4194–4198, 2013. 25

[40] Gao, Z., Zhao, J., Li, X. S., Dafalias, Y. F. **A critical state sand plasticity model accounting for fabric evolution**. *International journal for numerical and analytical methods in geomechanics*, **38**(4):370–390, 2014. 8

[41] Gardel, E., Sitaridou, E., Facto, K., Keene, E., Hattam, K., Easwar, N., Menon, N. **Dynamical fluctuations in dense granular flows**. *Philosophical Transactions of the Royal Society A: Mathematical, Physical and Engineering Sciences*, **367**(1909):5109–5121, 2009. 25

[42] GDR-MiDi (Groupement de Recherche-Milieux Divisés). **On dense granular flows**. *Eur. Phys. J. E)*, **14**(4):341–365, 2004. 8

[43] Géminard, J.C., Losert, W., Gollub, J.P. **Frictional mechanics of wet granular material**. *Phys. Rev. E*, **59**(5):5881–5890, 1999. 9

[44] Gilles, B., Coste, C. **Low-frequency behavior of beads constrained on a lattice**. *Physical Review Letters*, **90**(17):174302, 2003. 6

[45] Goren, L., Aharonov, E., Sparks, D., Toussaint, R. **Pore pressure evolution in deforming granular material: A general formulation and the infinitely stiff approximation**. *J. Geophys. Research*, **115**(B09216), 2010. 19, 27

[46] Goren, L., Aharonov, E., Sparks, D., Toussaint, R. **The mechanical coupling of fluid-filled granular material under shear**. *Pure and Applied Geophysics*, **168**(12):2289–2323, 2011. xv, 19, 27

[47] Gudehus, G., Jiang, Y., Liu, M. **Seismo- and thermodynamics of granular solids**. *Granular Matter*, **13**(4):319–340, 2011. 26

[48] Halász, Z., Kun, F. **Fiber bundle model with stick-slip dynamics**. *Physical Review E*, **80**(2):027102, 2009. 25

[49] Hardin, B. O., Blandford, G. E. **Elasticity of particulate materials**. *Journal of Geotechnical Engineering*, **115**(6):788–805, 1989. 98

[50] Heckel, R.W. . **Density-pressure relationships in powder compaction**. *Trans Metall Soc AIME*, **221**(4):671–675, 1961. 6

[51] Heslot, F., Baumberger, T., Perrin, B., Caroli, B., Caroli, C. . **Creep, stick-slip, and dry-friction dynamics: Experiments and a heuristic model**. *Phys. Rev. E*, **49**(6):4973–4988, 1994. 8

[52] Hidalgo, R. C., Grosse, C. U., Kun, F., Reinhardt, H. W., Herrmann, H. J. **Evolution of percolating force chains in compressed granular media**. *Physical Review Letters*, **89**(20):205501, 2002. 25

[53] Howell, D., Behringer, R. P., Veje, C. **Stress fluctuations in a 2D granular Couette experiment: a continuous transition**. *Physical Review Letters*, **82**(26):5241, 1999. 90

[54] Howell, D. W., Behringer, R. P., Veje, C. T. **Fluctuations in granular media**. *Chaos: An Interdisciplinary Journal of Nonlinear Science*, **9**(3):559–572, 1999. 5

[55] Iverson, R. M., LaHusen, R. G. **Dynamic pore-pressure fluctuations in rapidly shearing granular materials**. *Science*, **246**(4931):796–799, 1989. xv, 16

[56] Jaeger, H. M., Nagel, S. R., Behringer, R. P. **Granular solids, liquids, and gases**. *Reviews of modern physics*, **68**(4):1259, 1996. 5

[57] Jiang, Y., Wang, G., Kamai, T. **Acoustic emission signature of mechanical failure: Insights from ring-shear friction experiments on granular materials**. *Geophysical Research Letters*, **44**(6):2782–2791, 2017. 58, 200

[58] Jiang, Y., Wang, G., Kamai, T., McSaveney, M. J. **Effect of particle size and shear speed on frictional instability in sheared granular materials during large shear displacement**. *Engineering Geology*, **210**:93–102, 2016. 66

[59] Johnson, P. A., Ferdowsi, B., Kaproth, B. M., Scuderi, M., Griffa, M., Carmeliet, J., Guyer, R. A., Le Bas, P. Y., Trugman, D.T., Marone, C. **Acoustic emission and microslip precursors to stick-slip failure in sheared granular material**. *Geophysical Research Letters*, **40**(21):5627–5631, 2013. 25

[60] Kieffer, S. W. **Sound speed in liquid-gas mixtures: Water-air and water-steam**. *Journal of Geophysical research*, **82**(20):2895–2904, 1977. 73, 134

[61] Kozicki, J., Tejchman, J., Mühlhaus, H. B. **Discrete simulations of a triaxial compression test for sand by DEM**. *International Journal for Numerical and Analytical Methods in Geomechanics*, **38**(18):1923–1952, 2014. 18

[62] Kuhn, M. R. **Structured deformation in granular materials**. *Mechanics of materials*, **31**(6):407–429, 1999. 7

[63] Kuhn, M. R., Bagi, K. **Contact rolling and deformation in granular media**. *International journal of solids and structures*, **41**(21):5793–5820, 2004. 7

[64] Kumar, N., Imole, O. I., Magnanimo, V., Luding, S. **Effects of polydispersity on the micro–macro behavior of granular assemblies under different deformation paths**. *Particuology*, **12**:64–79, 2014. 18

[65] Kumar, N., Luding, S. **Memory of jamming - multi-scale flow in soft and granular matter**. *Granular Matter*, **18**(3):58, 2016. 26

[66] Ladd, R.S. **Preparing test specimens using undercompaction**. *Geotechnical Testing Journal*, **1**(1):16–23, 1978. 36

[67] Lade, P. V. *Triaxial testing of soils*. John Wiley & Sons, 2016. 48, 72, 133, 135

[68] Le Bouil, A., Amon, A., McNamara, S., Crassous, J. **Emergence of Cooperativity in Plasticity of Soft Glassy Materials**. *Physical Review Letters*, **112**:246001, 2014. 26

[69] Lee, S. J., Hashash, Y. M. A., Nezami, E. G. **Simulation of triaxial compression tests with polyhedral discrete elements**. *Computers and Geotechnics*, **43**:92–100, 2012. 18

[70] Li, X. S., Dafalias, Y. F. **Anisotropic critical state theory: role of fabric**. *Journal of Engineering Mechanics*, **138**(3):263–275, 2011. 8

[71] Liu, C-h and Nagel, S. R and Schecter, D. A., Coppersmith, S. N., Majumdar, S., Narayan, O., Witten, T. A. **Force fluctuations in bead packs**. *Science*, **269**(5223):513–515, 1995. 5, 7, 198

[72] Macpherson, J. D. **The effect of gas bubbles on sound propagation in water**. *Proceedings of the Physical Society. Section B*, **70**(1):85, 1957. 73

[73] Mair, K., Frye, K. M., Marone, C. **Influence of grain characteristics on the friction of granular shear zones**. *Journal of Geophysical Research: Solid Earth*, **107**(B10):ECV–4, 2002. 66

[74] Majmudar, T. S., Behringer, R. P. **Contact force measurements and stress-induced anisotropy in granular materials**. *Nature*, **435**(7045):1079, 2005. 5, 10

[75] Marone, C. **Laboratory-derived friction laws and their application to seismic faulting**. *Annual Review of Earth and Planetary Sciences*, **26**(1):643–696, 1998. 10

[76] Marone, C., Hobbs, B. E., Ord, A. **Coulomb constitutive laws for friction: Contrasts in frictional behavior for distributed and localized shear**. *Pure and Applied Geophysics*, **139**(2):195–214, 1992. 9

[77] Mašín, D. **Asymptotic behaviour of granular materials**. *Granular Matter*, **14**(6):759–774, 2012. 26

[78] Mcdowell, G. R., De Bono. **On the micro mechanics of one-dimensional normal compression**. *Géotechnique*, **63**(11):895–908, 2013. 26

[79] McWilliam, D., Duggins, R. K. **Speed of sound in bubbly liquids**. In *Proceedings of the Institution of Mechanical Engineers, Conference Proceedings*, **184**, pages 102–107. SAGE Publications Sage UK: London, England, 1969. 73, 134

[80] Michlmayr, G., Cohen, D., Or, D. **Sources and characteristics of acoustic emissions from mechanically stressed geologic granular media - A review**. *Earth Sci. Rev.*, **112**(3):97–114, 2012. 24

[81] Michlmayr, G., Cohen, D., Or, D. **Shear-induced force fluctuations and acoustic emissions in granular material**. *Journal of Geophysical Research: Solid Earth*, **118**(12):6086–6098, 2013. xvi, 25, 26

[82] Michlmayr, G., Or, D. **Mechanisms for acoustic emissions generation during granular shearing**. *Granular Matter*, **16**(5):627–640, 2014. 26

[83] Miller, B., O'Hern, C., Behringer, R. P. **Stress fluctuations for continuously sheared granular materials**. *Physical Review Letters*, **77**(15):3110, 1996. 5

[84] Morvan, M., Vernay, M., Breul, P. **Study of the variation of B with Sr**. In *E3S Web of Conferences*, **9**, page 10003. EDP Sciences, 2016. 72

REFERENCES

[85] Mueth, D. M., Debregeas, G. F., Karczmar, G. S and Eng, P. J., Nagel, S. R., Jaeger, H. M. **Signatures of granular microstructure in dense shear flows**. *Nature*, **406**(6794):385, 2000. 10

[86] Nasuno, S., Kudrolli, A., Bak, A., Gollub, J. P. **Time-resolved studies of stick-slip friction in sheared granular layers**. *Physical Review E*, **58**(2):2161, 1998. 78

[87] Nasuno, S., Kudrolli, A., Gollub, J. P. **Friction in granular layers: Hysteresis and precursors**. *Physical Review Letters*, **79**(5):949, 1997. xv, 8, 9

[88] Nguyên, T.T.T., Doanh, T., Le Bot, A., Dalmas, D. **On the role of pore pressure in dynamic instabilities of saturated model granular materials**. *Submitted*, **0**(0):0–0. 60

[89] Nguyên, T.T.T., Doanh, T., Le Bot, A., Dalmas, D. **Investigating the dynamic instabilities of model granular materials in isotropic consolidation and triaxial drained compression**. In *Poromechanics VI*, pages 1805–1912. 2017. 2

[90] Nicot, F., Daouadji, A., Laouafa, F., Darve, F. **Second-order work, kinetic energy and diffuse failure in granular materials**. *Granular Matter*, **13**(1):19–28, 2011. 26

[91] Nitka, M., Tejchman, J., Kozicki, J., Leśniewska, D. **DEM analysis of micro-structural events within granular shear zones under passive earth pressure conditions**. *Granular Matter*, **17**(3):325–343, 2015. 18

[92] Oda, M., Kazama, H. **Microstructure of shear bands and its relation to the mechanisms of dilatancy and failure of dense granular soils**. *Géotechnique*, **48**(4):465–481, 1998. 10

[93] Ozbay, A., Cabalar, A. F. **Effects of triaxial confining pressure and strain rate on stick-slip behavior of a dry granular material**. *Granular Matter*, **18**(3):60, 2016. 67, 69

[94] Persson, B. N. J. . *Sliding friction: physical principles and applications*. Springer Science & Business Media, 2013. 8

[95] Radjaï , F., Roux, S. **Contact dynamics study of 2D granular media : critical states and relevant internal variables**. In Hinrichsen, H., Wolf, D. E., editor, *The Physics of Granular Media*, pages 165–187, Berlin, 2004. Wiley-VCH. 26

[96] Radjaï, F., Delenne, J. Y., Azéma, E., Roux, S. **Fabric evolution and accessible geometrical states in granular materials**. *Granular Matter*, **14**(2):259–264, 2012. 7

[97] Radjaï, F., Dubois, F. *Discrete-element modeling of granular materials*. Wiley-Iste, 2011. 7

[98] Radjaï, F., Jean, M., Moreau, J. J., Roux, S. **Force distributions in dense two-dimensional granular systems**. *Physical Review Letters*, **77**(2):274, 1996. 5, 7, 198

[99] Radjaï, F., Roux, S. . **Contact dynamics study of 2D granular media: critical states and relevant internal variables**. *The physics of granular media*, pages 165–187, 2004. 7

[100] Radjaï, F., Roux, S. **Turbulentlike fluctuations in quasistatic flow of granular media**. *Physical Review Letters*, **89**(6):064302, 2002. 7

[101] Radjaï, F., Roux, S., Moreau, J. J. **Contact forces in a granular packing**. *Chaos: An Interdisciplinary Journal of Nonlinear Science*, **9**(3):544–550, 1999. 7

[102] Radjaï, F., Wolf, D. E., Jean, M., Moreau, J. J. **Bimodal character of stress transmission in granular packings**. *Physical Review Letters*, **80**(1):61, 1998. 7

[103] Reynolds, O. **LVII. On the dilatancy of media composed of rigid particles in contact. With experimental illustrations**. *The London, Edinburgh, and Dublin Philosophical Magazine and Journal of Science*, **20**(127):469–481, 1885. 6

[104] Rouse, C., Styles, P., Wilson, S. A. **Microseismic emissions from flowslide-type movements in South Wales**. *Engineering Geology*, **31**(1):91–110, 1991. 25

[105] Roux, S., Radjaï, F. **Texture-dependent rigid-plastic behavior**. In *Physics of dry granular media*, pages 229–236. Springer, 1998. 6

[106] Ruina, A. **Slip instability and state variable friction laws**. *Journal of Geophysical Research: Solid Earth*, **88**(B12):10359–10370, 1983. 10

[107] Samarasinghe, A. M., Huang, Y. H., Drnevich, V. P. **Permeability and consolidation of normally consolidated soils**. *Journal of the Geotechnical Engineering Division*, **108**(6):835–850, 1982. 75

[108] Satake, M. **Fabric tensor in granular materials**. In *IUTAM Conference on Deformation and Flow of Granular Materials, 1982*, pages 63–68. AA Balkema, 1982. 7

[109] Schofield, A., Wroth, P. *Critical state soil mechanics*, **310**. McGraw-Hill London, 1968. 6, 21

[110] Scuderi, M. M., Carpenter, B. M., Johnson, P. A., Marone, C. **Poromechanics of stick-slip frictional sliding and strength recovery on tectonic faults**. *Journal of Geophysical Research: Solid Earth*, **120**(10):6895–6912, 2015. xv, 13, 14, 58

[111] Scuderi, M. M., Carpenter, B. M., Marone, C. **Physicochemical processes of frictional healing: Effects of water on stick-slip stress drop and friction of granular fault gouge**. *Journal of Geophysical Research: Solid Earth*, **119**(5):4090–4105, 2014. 15, 84

[112] Sitharam, T.G., Vinod, J. S. **Critical state behaviour of granular materials from isotropic and rebounded paths: DEM simulations**. *Granular Matter*, **11**(1):33–42, 2009. 26

[113] Skempton, A. W., Taylor, R.N. **The pore pressure coefficients A and B**. *Géotechnique*, **4**(4):143–147, 1954. 40

[114] Smith, A., Dixon, N. **Quantification of landslide velocity from active waveguide–generated acoustic emission**. *Canadian Geotechnical Journal*, **52**(4):413–425, 2014. 25

[115] Tatsuoka, F., Haibara, O. **Shear resistance between sand and smooth or lubricated surfaces**. *Soils and Foundations*, **25**(1):89–98, 1985. 35

[116] Terzaghi, K., Peck, R.P., Mesri, G. *Soil Mechanics in Engineering Practice, 3rd Edition*. John Wiley, 1996. 20, 74

[117] Tordesillas, A., Walker, D. M., Lin, Q. **Force cycles and force chains**. *Physical Review E*, **81**(1):011302, 2010. 80

[118] I. Towhata. *Geotechnical earthquake engineering*. Springer Science & Business Media, 2008. 72

[119] Travers, T., Ammi, M., Bideau, D., Gervois, A., Messager, J. C., Troadec, J. P. **Uniaxial compression of 2d packings of cylinders. effects of weak disorder**. *Europhysics Letters*, **4**(3):329, 1987. 5

[120] van Eerd, A. R. T, Ellenbroek, W. G, van Hecke, M., Snoeijer, J.H and Vlugt, T. J. H. **Tail of the contact force distribution in static granular materials**. *Physical Review E*, **75**(6):060302, 2007. 198

[121] Vanel, L., Howell, D., Clark, D., Behringer, R. P., Clément, E. **Memories in sand: Experimental tests of construction history on stress distributions under sandpiles**. *Physical Review E*, **60**(5):R5040, 1999. 6

[122] Verdugo, R., Ishihara, K. **The steady state of sandy soils**. *Soils and Foundations*, **36**(2):81–91, 1996. 44

[123] Welker, P., McNamara, S. **Precursors of failure and weakening in a biaxial test**. *Granular Matter*, **13**(1):93–105, 2011. 26

[124] Wu, K., Abriak, N., Becquart, F., Pizette, P., Remond, S., Liu, S. **Shear mechanical behavior of model materials samples by experimental triaxial tests: case study of 4 mm diameter glass beads**. *Granular Matter*, **19**(4):65, 2017. 12, 18, 33

[125] Wu, K., Pizette, P., Becquart, F., Remond, S., Abriak, N., Xu, W., Liu, S. **Experimental and numerical study of cylindrical triaxial test on mono-sized glass beads under quasi-static loading condition**. *Advanced Powder Technology*, **28**(1):155–166, 2017. 12, 18, 23, 67, 84

[126] Yang, J., Wei, L. **Collapse of loose sand with the addition of fines: the role of particle shape**. *Géotechnique*, 2012. xv, 18

[127] Zaitsev, V. Y., Richard, P., Delannay, R., Tournat, V., Gusev, V. E. **Pre-avalanche structural rearrangements in the bulk of granular medium: Experimental evidence**. *Europhysics Letters*, **83**(6):64003, 2008. 25

[128] Zhang, J., Majmudar, T., Behringer, R. . **Force chains in a two-dimensional granular pure shear experiment**. *Chaos: An Interdisciplinary Journal of Nonlinear Science*, **18**(4):041107, 2008. 5

Appendix A

Collapse in water imbibition

Imbibition process is briefly reminded here as the following step after the CO_2 percolation, de-aired water is injected into the specimen from the bottom by the water pressure of 3-5 kPa. During this process, water level is gradually rising inside the sample, the axial strain ε_1 of the sample is increasing as in figure A.1. Three significant jumps of axial strain ε_1 are marked by collapse W1, W2, W3. These instabilities are named as collapse since they do not destroy the geometry of the sample like liquefaction failure and they occur under the isotropic effective confining pressure p'_0 of 20-30 kPa.

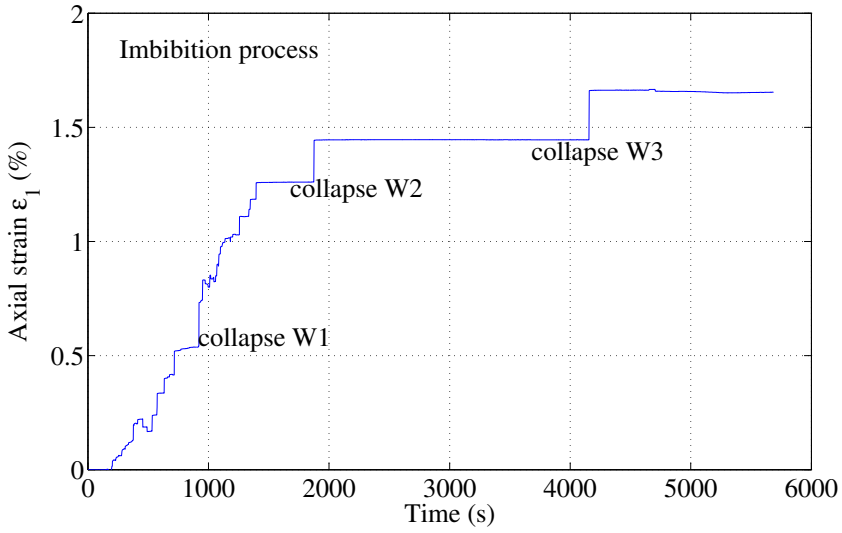

Figure A.1: Temporal evolution of axial strain during imbibition process.

Appendix B

Distribution of major stick-slips

Figures B.1a to e present the distribution of the occurrence of major stick-slip events acquired in CIDNC series; precursors are not included in this investigation. Histograms of the occurrence in cyan columns are far from the normal distribution in red curves, excepting for test N50 at 50 kPa of confining pressure with the sufficient total number of stick-slip within this series. Figures B.1f and g show that both normalised deviatoric stress drop Δq^{norm} and amplitude of stress drop Δq do not correlate to the effective confining pressure p'_0. In figure B.1g, only the maximum stress drop shows the relations to confining pressure p'_0.

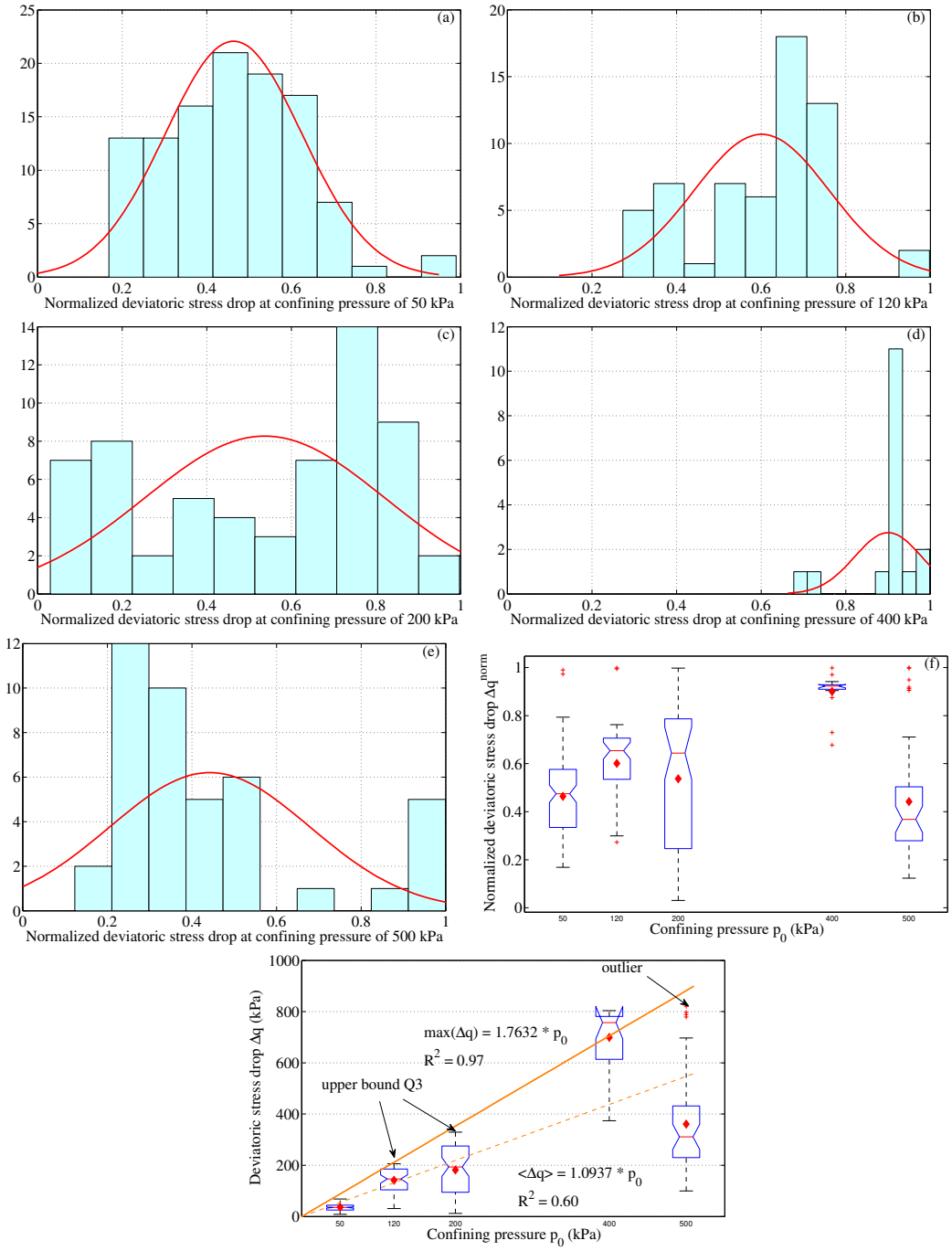

Figure B.1: Statistical estimation of the normalised deviatoric stress drop Δq^{norm} and Δq of major stick-slip events in accordance with effective confining pressure p'_0.

Appendix C

Distribution of liquefaction triggering stress

C.1 Distribution of the triggering stress of liquefaction events

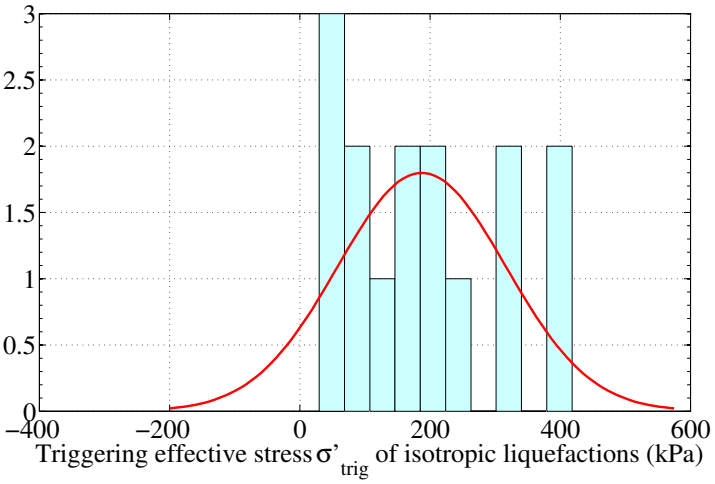

Figure C.1: Distribution of the triggering stress σ'_{trig} of liquefaction events

Figure C.1 presents the distribution of occurrence of isotropic liquefaction event corresponding to various effective triggering stress σ'_{trig}. Obviously the distribution is not a normal distribution. Since only 17 isotropic liquefactions are acquired, we have not obtained a sufficient investigation.

C.2 Vanishing of effective stress at the stable state of pore pressure during liquefaction IL_{01}.

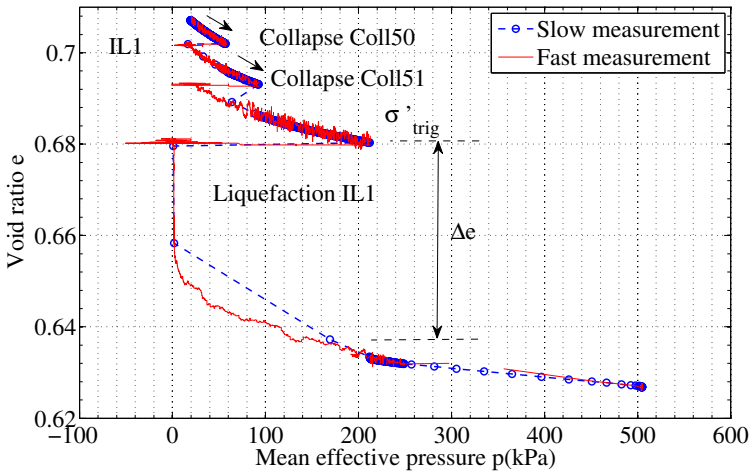

Figure C.2: Compressibility of isotropic liquefaction IL_{01}.

This figure C.2 is added to supplement figure 5.2a since in linear scale, it can clearly emphasise the zero value of mean effective pressure at stabilised state. While in other collapses ($Coll_{50}$, $Coll_{51}$) the effective mean pressures are not vanished, then they cannot liquefy.

Appendix D

FFT analysis of noise and stick-slip

D.1 FFT analysis of two noises during test IL_{01}

Figure D.1 presents the FFT spectrum of two different noises in test IL_{01}. The left column includes the FFT of vertical acceleration G, lateral vibration V and lateral sound pressure M, respectively, within the whole range of frequency up to 5000 Hz. It can be seen the coherence of FFT amplitude and dominant frequencies between two noises in the signals of G and M (figure D.1a and c). The signal of lateral vibration V from $Noise_{02}$ does not show 3 dominant frequencies like $Noise_{01}$ (figure D.1b). Note that the working capability of vibrometer is often affected by large lateral deformation. The smaller scale is additionally explored in the right column with the consistence FFT spectrum of G and M in the range of low frequency below 50 Hz. Although the difference of FFT of lateral vibration, the reliable results of acceleration G and microphone M still sufficiently enhance the reliability of the acoustic measurements.

D.2 Analysis of SS_{04} event

This section is devoted to analyse one representative stick-slip event by the similar procedure as test IL_{01} in section 6.4 to see the characteristics of FFT and CCWT spectrum during a very large stick-slip, mostly liquefied, in test N500 belonging to CIDNC series.

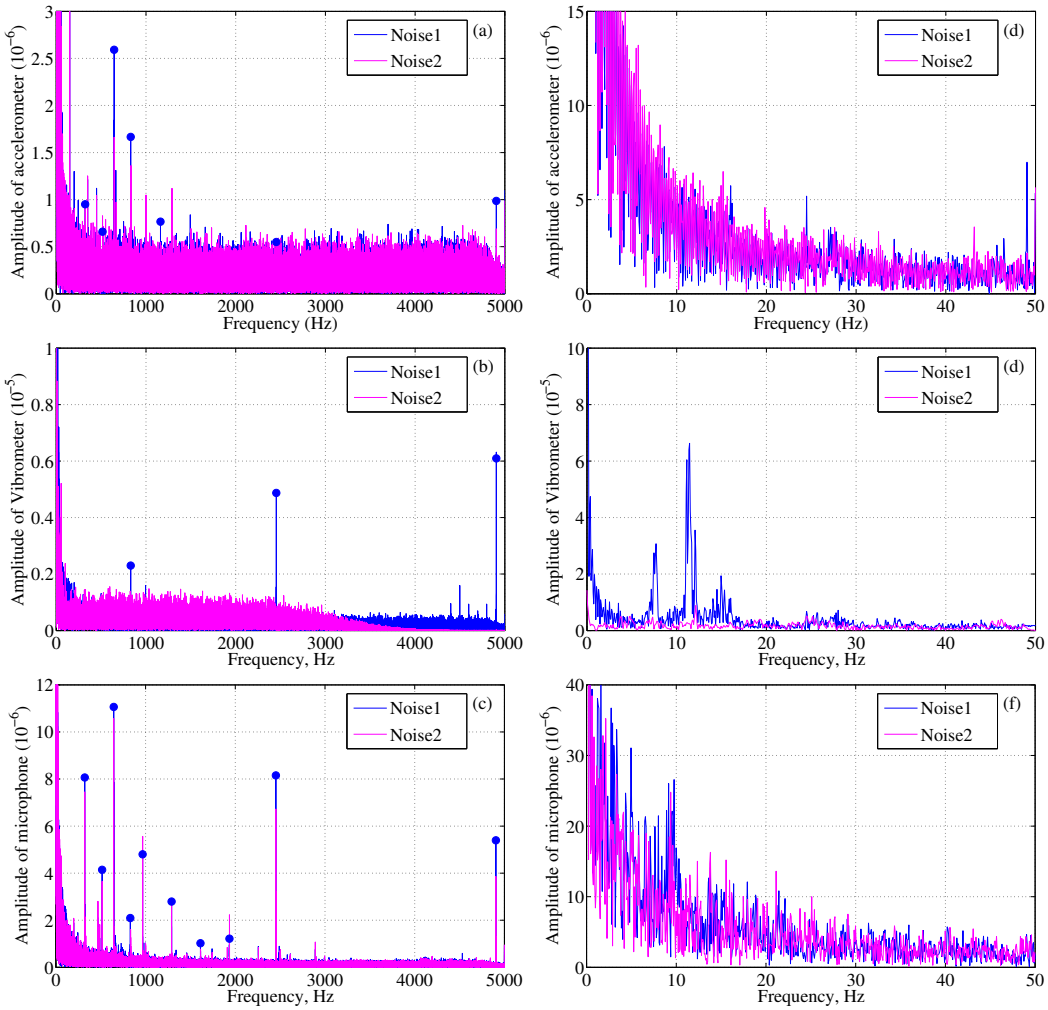

Figure D.1: Frequency analysis by FFT of two portions of noise from vertical top cap acceleration G, lateral vibration V, lateral sound pressure M within test IL_{01}.

FFT spectrum of a segment of noise at 10 seconds before the event and the signals of the dynamic event within 10 s are presented in figure D.2. The first row provides the whole overall frequency content of three acoustic measurements until 5000 Hz, beyond this value no significant FFT amplitude is detected. Solid blue spots are used to mark the dominant spikes acquired from the noise signal. From the global view, vertical acceleration G shows the totally large distinction between the event and the noise with almost all frequencies are excited during the event (figure D.2a). Two supplementary lateral acoustic measurements expose less intense FFT amplitude and different frequency contents also (figures D.2b,c). Compared to the FFT amplitude

of isotropic liquefaction IL_{01} (figures 6.13a,b,c), all FFT amplitudes from G, M, V during SS event are remarkably larger than those of liquefaction due to the presence of deviatoric stress. This is consistent to the systematic experimental observation that the hearing noise during SS is always louder than that of liquefaction and collapse. In the second row, closer looks are introduced to see some details of frequency contents. Acceleration G within 1000 Hz exhibits multiple broad peaks wide spreading throughout the range (figure D.2d). Lateral vibration V exposed two characteristic rounded peaks at 321 and 683 Hz (figure D.2e), very close to isotropic liquefaction IL_{01} (figure 6.13e). Lateral sound pressure M indicates many complicated broad peaks throughout the range of 1000 Hz. In FFT spectrum, the most dominant frequency is quite difficult to identify, it should be done by other tool as CCWT. Mostly the spikes of noise are included in the event signal by the coincidence of red spike and blue spike but with different peak amplitudes. In the adjacent segment from 1000 to 2000 Hz in figures D.2g,h,i, two dominant rounded peaks at around 1100 and 1380 Hz in vertical acceleration are recognised. No clear peaks in lateral vibration signal and a large group around 1400-1500 Hz from lateral sound pressure M are exposed. At low frequency below 50 Hz, G does not captured any peak (figure D.2j) but all frequencies are excited sternly. Vibrometer still works well at the low range of frequency then shows the peak at 8.1 Hz and other rounded peak at 22 Hz (figure D.2k). Both V and M point out that instead of separate spikes in noise (blue dots) (figures D.2k,l), during SS event mostly all low frequencies are excited.

As in section 6.4.2, CCWT is effective in recognition of the rounded peaks. In stick-slip event, since the massive FFT amplitudes of event compared to those of noise, CCWT is more convenient to point out the most dominant rounded peaks of SS event. The temporal evolutions of acoustic measurements G, M, V and normalised excess pore pressure are presented in figure D.3. In which, the response of vertical acceleration G is abnormal. Instead of the strong and brief vibration within the early 10 ms, then reaches the stable state at zero, a rather long decrease of G to return zero level is observed from 10 ms until 1 s. One artificial disturbance is noted at 80 ms with a sharp spike of lateral vibration which is not coherent to lateral microphone signal or pore pressure.

Similar analyses by CCWT are implemented to get CCWT spectra for lateral vibration V, lateral sound pressure M, vertical acceleration G and finally excess pore pressure. Irrespective of dominant frequencies in noise (figure D.4a), the CCWT amplitude of

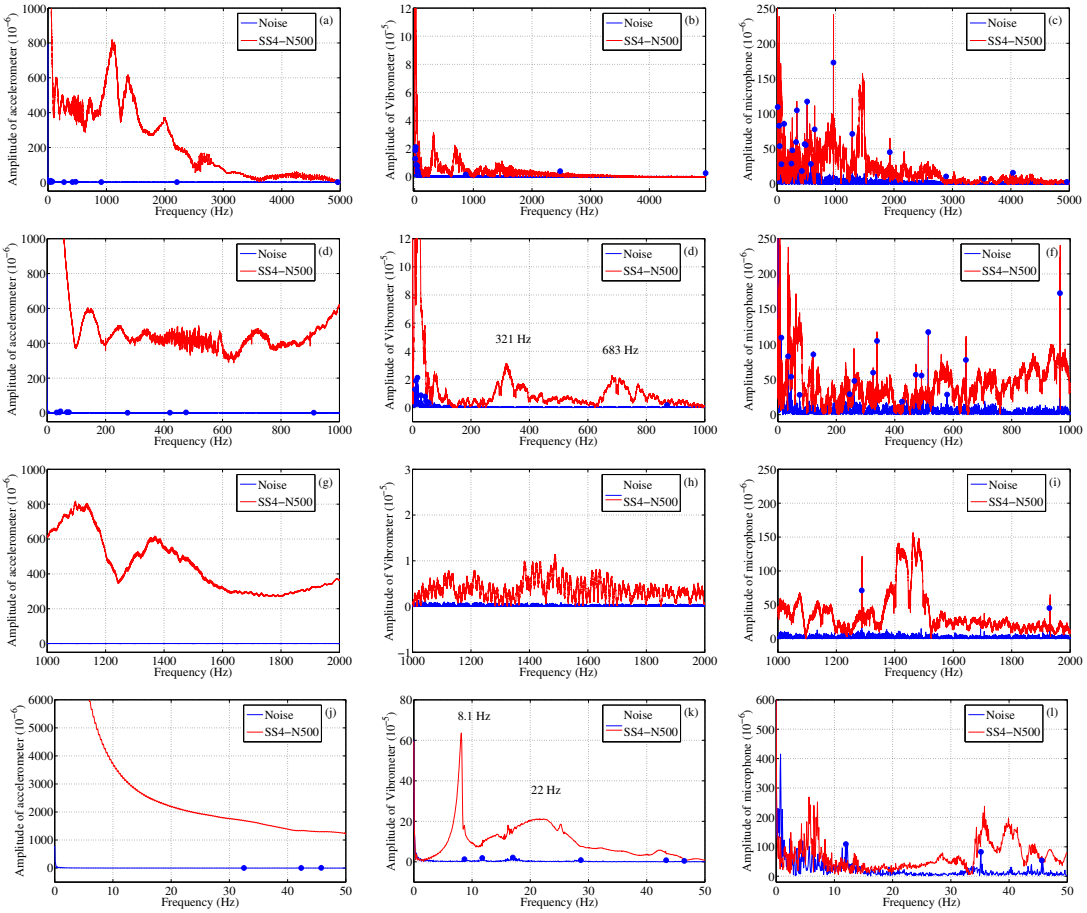

Figure D.2: Frequency analysis by FFT of vertical top cap acceleration G (left), lateral vibration V (middle), lateral sound pressure M (right) of stick-slip event SS_{04} of test N500.

SS_{04} event is two orders of magnitude larger than that of noise (10^{-3} compared to 10^{-5}), hence figure D.4a easily indicate the dominant frequency groups of the dynamic event. By a closer look in the second row, detailed frequencies are identified. Figure D.4c only shows some low frequentcies of noise corresponding to blue dots lower than 100 Hz in figure D.2d. While the dominant frequencies of SS_{04} event are considerably larger in amplitude in figure D.4d, the main dynamic event includes three rounded peaks at 326, 738, 1542 Hz. A representative peak at 1298 Hz is also indicated in figure D.4d and it is not the characteristic frequency of the event since it very low amplitude of $5.2{*}10^{-5}$ which is attributed to the sharp spike with the blue dots prior to the rounded peak of 1542 Hz (figure D.2i) by the approximate estimation of the area

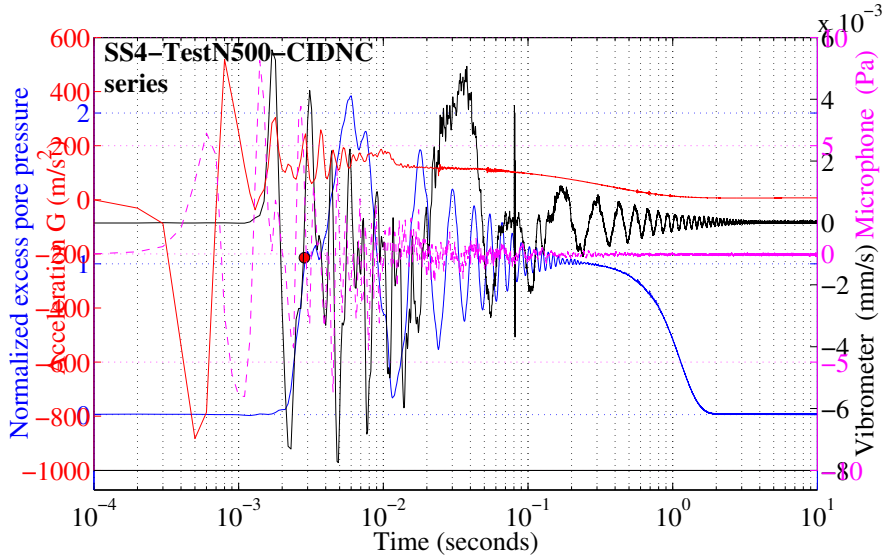

Figure D.3: Temporal evolution of acoustic measurements (G,M,V) and normalised excess pore pressure ΔU^{norm} during SS_{04} of test N500-CIDNC series.

as demonstrated in section 6.4.2. Another separate peak at 0.08 s is equivalent to the disturbance described in figure D.3.

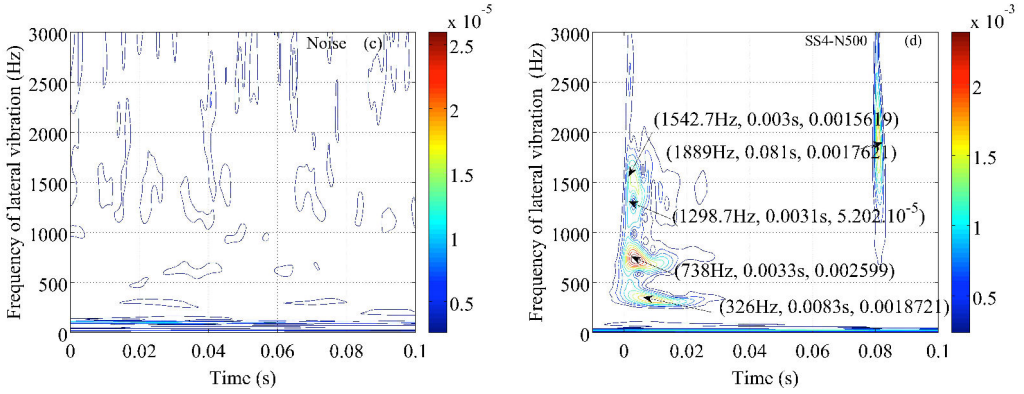

Figure D.4: CCWT spectrum of lateral vibration V for noise signal (left) and stick-slip SS_{04} of test N500 (right).

Similar procedure of analysis is applied to lateral sound pressure M and vertical acceleration G, then the results are introduced in figures D.5 and D.6. Briefly and to avoid the repetition of the same explanation, only main and core results are mentioned here. Three main and most dominant frequencies represented the dynamic SS_{04} event are captured by lateral microphone which are respectively 935, 1471, 2510 Hz (figure

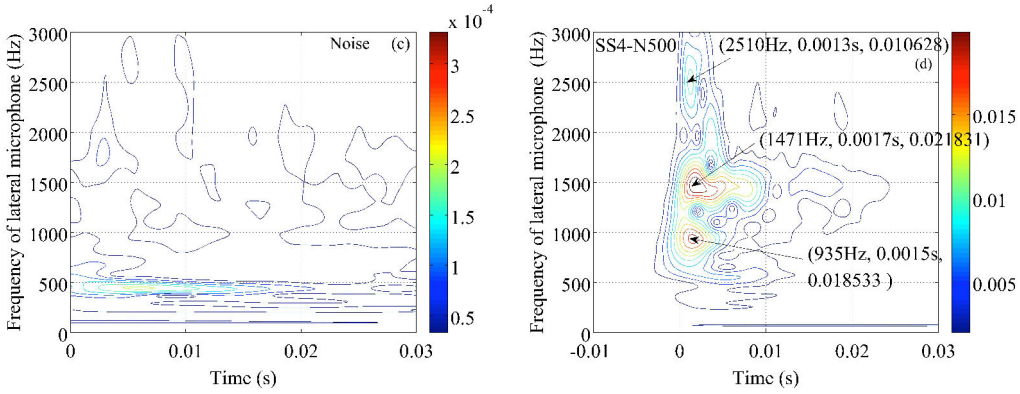

Figure D.5: CCWT spectrum of lateral sound pressure M for noise signal (left) and stick-slip SS_{04} of test N500 (right).

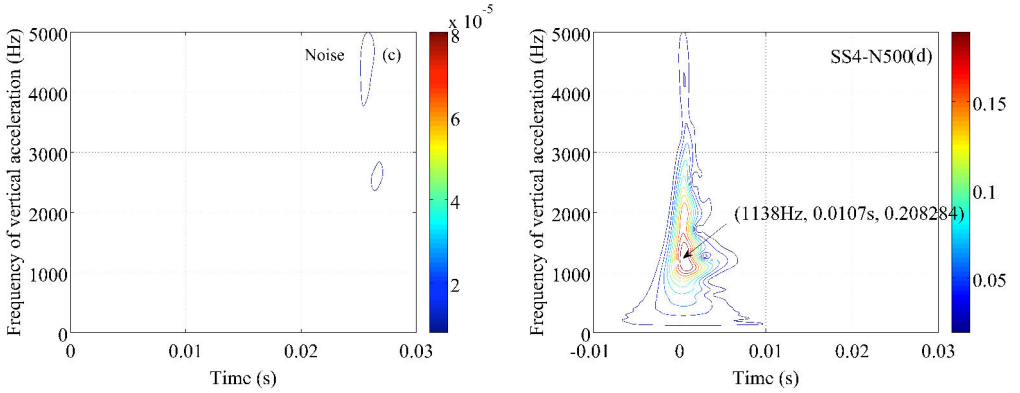

Figure D.6: CCWT spectrum of vertical top cap acceleration G for noise signal (left) and stick-slip SS_{04} of test N500 (right).

D.5d). And by vertical acceleration the most energetic frequency is 1138 Hz (figure D.6d).

The last CCWT spectrum is for normalised excess pore pressure in figure D.7, showing the good coherence to time series of pore pressure signal.

D.3 Analysis of collapse $Coll_{04}$ event

FFT spectrum of a small collapse at 108.2 kPa is constructed by the signal of the collapse event and a segment of noise at 10 s before this collapse. Vertical acceleration G is shown with large and broad peaks within 1000 Hz in figure D.8a. Lateral vibration still exhibits the typical spectrum with the major rounded peak below 1000 Hz like

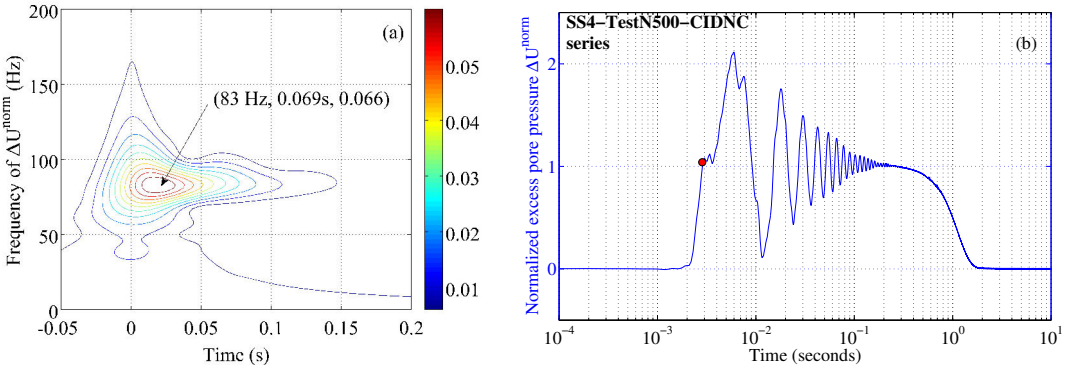

Figure D.7: CCWT spectrum of normalised excess pore pressure ΔU^{norm} of stick-slip SS_{04} of test N500.

IL_{01} and SS_{04} (figure D.8b). Lateral sound pressure M includes all sharp spikes of the noise and the amplitude of event seems not to significantly larger than that of noise (figure D.8c). It could be coherent to the realistic observation that it is rather hard to listen to the sound of collapse than liquefaction and stick-slip. Other smaller scale figures will provide more detail, the most dominant frequency of vertical acceleration G among the widespread peak within 1000 Hz is around 300 Hz, similar to liquefaction. This frequency of approximate 300 Hz is implied also in lateral vibration (figure D.8e). Whereas no significant rounded peak is shown in lateral sound pressure M (figure D.8f). In the range of 1000-2000 Hz, a small peak around 1400 Hz is realised in G spectrum figure D.8g), no large peaks are recognised in the spectrum of V and M (figure D.8h,i). A close look at low frequency below 40 Hz in the last row of figure only shows two frequencies of 8 and 14 Hz by lateral vibration V in both noise and event signals (figure D.8k).

Detail results of CCWT are explored and exclusion are applied to recognise the most energetic frequencies. Only the final extracted results are presented. They are 307 Hz for V (figure D.9), very close to 327 Hz for M (figure D.10), then the other approximate peak of 314 Hz for G (figure D.11). Other broad peaks of vertical acceleration G are revealed at 615 and 1433 Hz.

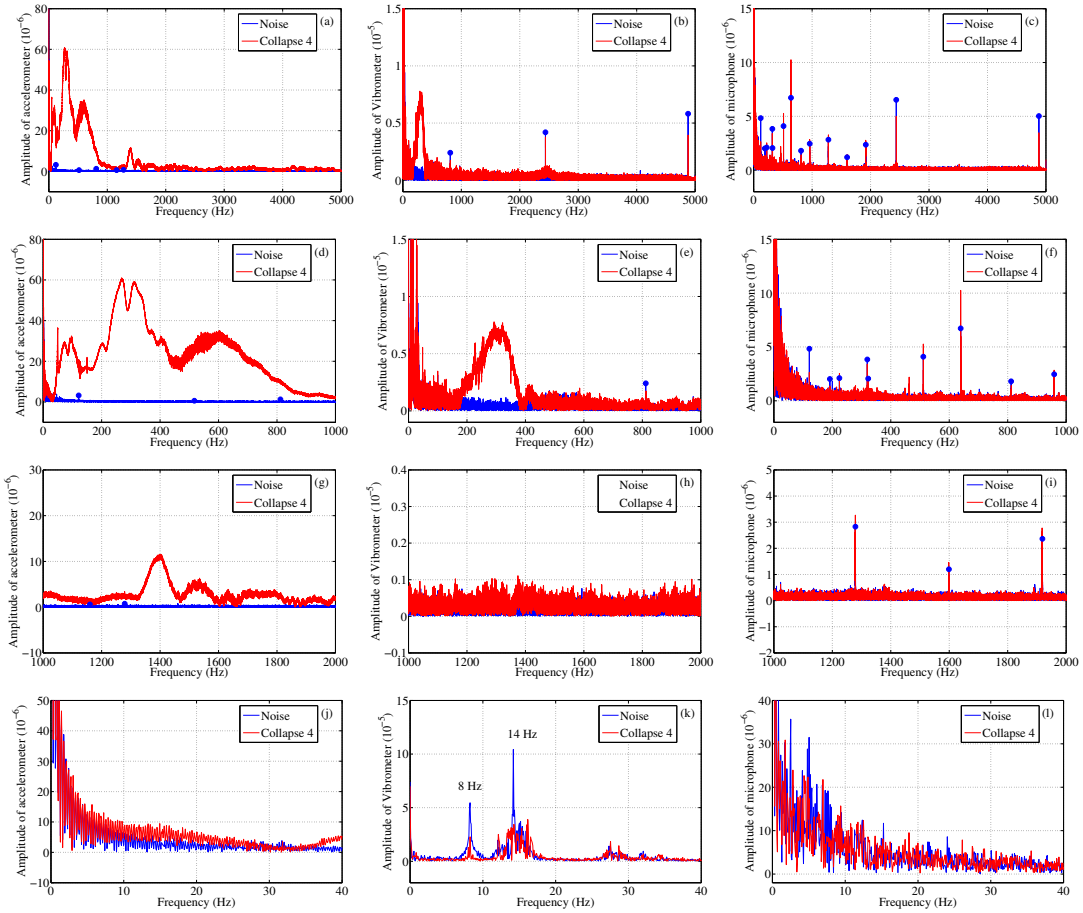

Figure D.8: Frequency analysis by FFT of vertical top cap acceleration G (left), lateral vibration V (middle), lateral sound pressure M (right) of collapse event Coll_{04}.

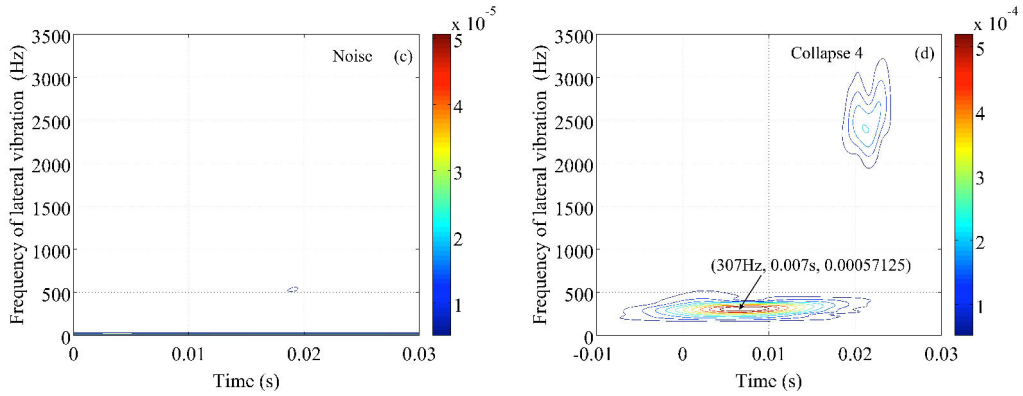

Figure D.9: CCWT spectrum of lateral vibration V for noise signal (left) and Coll_{04} of Collapse series (right).

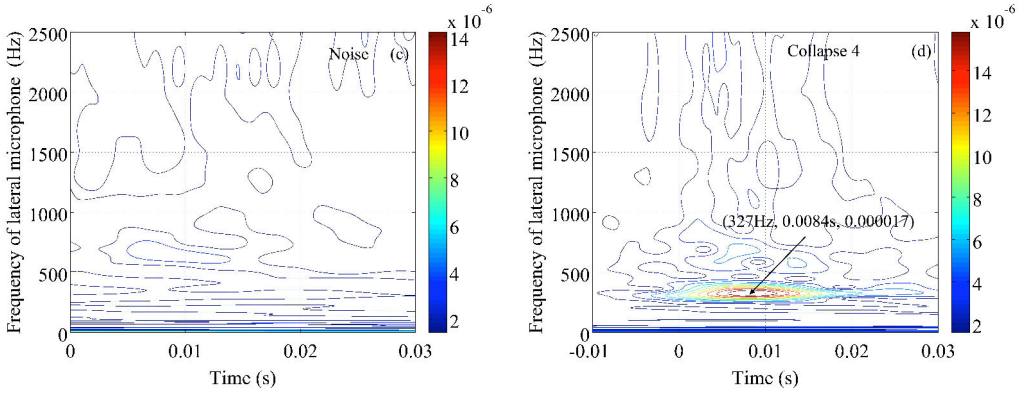

Figure D.10: CCWT spectrum of lateral sound pressure M for noise signal (left) and $Coll_{04}$ of Collapse series (right).

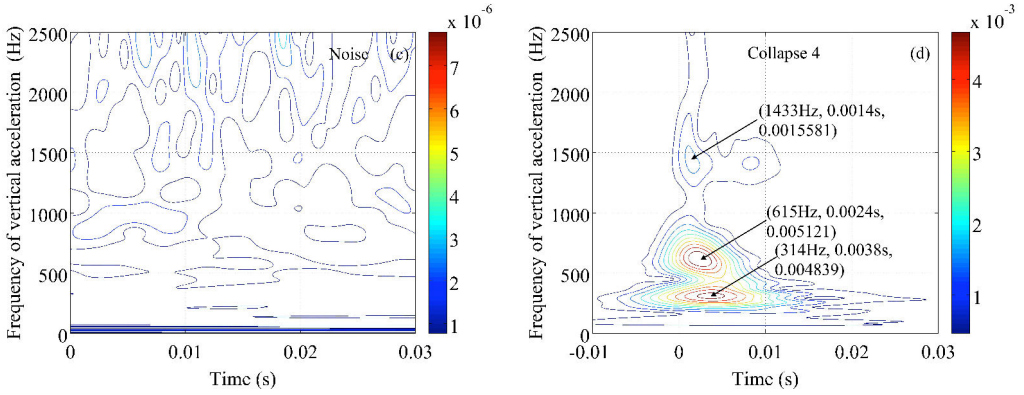

Figure D.11: CCWT spectrum of vertical top cap acceleration G for noise signal (left) and $Coll_{04}$ of Collapse series (right).

Appendix E

Résumé étendu

Cette thèse s'inscrit dans le mouvement, très actif dans les deux dernières décennies, de recherche sur la physique et la mécanique des matériaux granulaires, visant à en comprendre les mécanismes rhéologiques en liaison avec leurs origines microscopiques.

Dans le cadre de la physique, la mécanique des milieux granulaires reste un des rares domaines offrant encore un vaste champ d'études à cause de la complexité des phénomènes mis en jeux et de multiples interactions entre les différents paramètres. De ce fait, la plupart des phénomènes sont imparfaitement compris. En particulier les instabilités et les mécanismes locaux qui pilotent la déformation globale du milieu restent encore mal connus. Ces mécanismes sont associés à la rotation des grains, au frottement intergranulaire, mais également aux plus grandes déformations à des instabilités dynamiques. Il est maintenant connu que les efforts intergranulaires ne se répartissent pas de façon homogène dans le matériau, mais le long de quelques chaînons de contacts qui reprennent l'ensemble des efforts appliqués. Au niveau de ses contacts les efforts peuvent être alors de forte intensité. Au cours de la sollicitation, un chaînon peut alors céder brusquement alors qu'un autre se crée. Un mécanisme de déformation ou de frottement saccadé participe ainsi à la déformation du matériau et éventuellement à la liquéfaction.

La liquéfaction, un aspect particulier des instabilités diffuses, est une composante très importante du comportement des milieux granulaires. Une fois liquéfiés, les sols perdent entièrement leur résistance avec de dramatiques conséquences comme les dévastateurs glissements de terrain ou les catastrophiques effondrements de structures sous séisme. Une des causes de la liquéfaction pourrait être une instabilité structurelle. Une

telle explication est séduisante car encore peu exploitée dans la littérature géotechnique, par rapport à l'instabilité rhéologique.

Les effondrements locaux et les frottements saccadés, deux autres aspects des instabilités diffuses, sont particulièrement bien observables sur des milieux à granulométrie serrée ou monodisperse constitués de grains sphériques au comportement fragile (billes de verre par exemple). Les fortes instabilités observées peuvent alors être rattachées au phénomène de Stick-Slip ou frottement - glissement saccadé. Le phénomène de Stick-Slip a fait l'objet de nombreuses études dans des domaines très variés. Mais l'approche généralement envisagée se place dans un cadre uni ou bidimensionnel. Bien que peu étudié, le cas tridimensionnel, avec pris en compte de la composante volumique du phénomène, reste cependant très intéressant. Les matériaux granulaires ont en effet un comportement volumique très particulier piloté par le phénomène de dilatance associé à une variation de volume sous sollicitation déviatoire.

La simulation numérique à l'échelle des grains, dite "aux éléments discrets" (DEM pour discrete element method) est devenue un outil essentiel dans l'étude du comportement d'assemblages granulaires modèles. Au niveau microscopique, les études par DEM ont permis de bien caractériser l'important désordre qui affecte les propriétés mécaniques des assemblages granulaires. Ce désordre des propriétés mécaniques à petite échelle contraste avec les lois macroscopiques qui, bien que complexes, restent régulières et déterministes, car les fluctuations régressent dans la limite des grands systèmes.

Les phénomènes d'instabilité affectant le comportement à grande échelle comme le frottement saccadé (stick-slip) ou l'effondrement en consolidation isotrope semblent a priori échapper à cet effet de régularisation qui accompagne généralement le passage du microscopique au macroscopique, et leur origine demeure assez mystérieuse. Même si le stick-slip est décrit par les théories du type "rate and state" développées pour les surfaces ou couches de géomatériaux dans les applications géophysiques, le passage de telles lois de frottement dans les contacts intergranulaires au comportement macroscopique en volume reste à élucider. Il faut noter en effet que les comportements macroscopiques diffèrent fortement des comportements des contacts, et que l'effet macroscopique des ingrédients micromécaniques d'un modèle de matériau granulaire échappe aux intuitions naîves, en raison, en particulier, du rôle important de la géométrie des assemblages de grains et de leurs réarrangements.

Cette thèse répond donc au besoin de mieux comprendre les instabilités diffuses et d'identifier les mécanismes fondamentaux de la déformation dans les matériaux granulaires. L'identification des mécanismes fondamentaux permettrait l'explication rationnelle de la liquéfaction, des effondrements et des frottements saccadés, phénomènes typiques de l'instabilité diffuse.

On cherchera, dans ce projet scientifique, à identifier et comprendre les origines physiques des instabilités diffuses des matériaux granulaires modèles par une approche expérimentale. Il s'agira d'identifier le ou les mécanismes de déclenchement de l'instabilité et d'explorer sa dynamique. On privilégiera les expériences modèles, en idéalisant les matériaux granulaires par des billes de verre quasi sphériques qui n'ont pas été beaucoup étudiées par la communauté scientifique dans un contexte tridimensionnel. C'est donc ce type de matériaux modèles, avec des matériaux granulaires réels en complément, qui sera utilisé principalement dans cette étude.

Nous utilisons, dans cette thèse, des échantillons cylindriques de court élancement sur un appareil triaxial de révolution classique de la mécanique des sols, complété avec des capteurs de pression statique et dynamique en tête et au pied de l'échantillon, et par des mesures de l'accélération verticale en tête de l'échantillon G, de la vibration horizontale V à mi-hauteur et de la pression acoustique horizontale M au pied de l'échantillon. Les données expérimentales sont acquises en haute résolution de 10 à 20 kHz.

Frottement saccadé

Le premier objectif de cette thèse est de caractériser expérimentalement et macroscopiquement du phénomène de frottement saccadé sur des billes de verre sodo-calcique mono et polydisperse en compression triaxiale drainée en incluant la compression isotrope précédant celle-ci. Un groupe de cinq paramètres macroscopiques caractériserait ces frottements saccadés en drainé : l'amplitude de la chute de contrainte déviatorique, l'amplitude de la contraction volumique, l'intermittente de déformation axiale entre deux chutes successives, le module quasi-élastique et le coefficient de Poisson au départ de la phase de frottement. Les données expérimentales à haute résolution temporelle ont permis une étude détaillée de la dynamique de la phase de glissement, souvent ignorée dans la littérature des milieux granulaires.

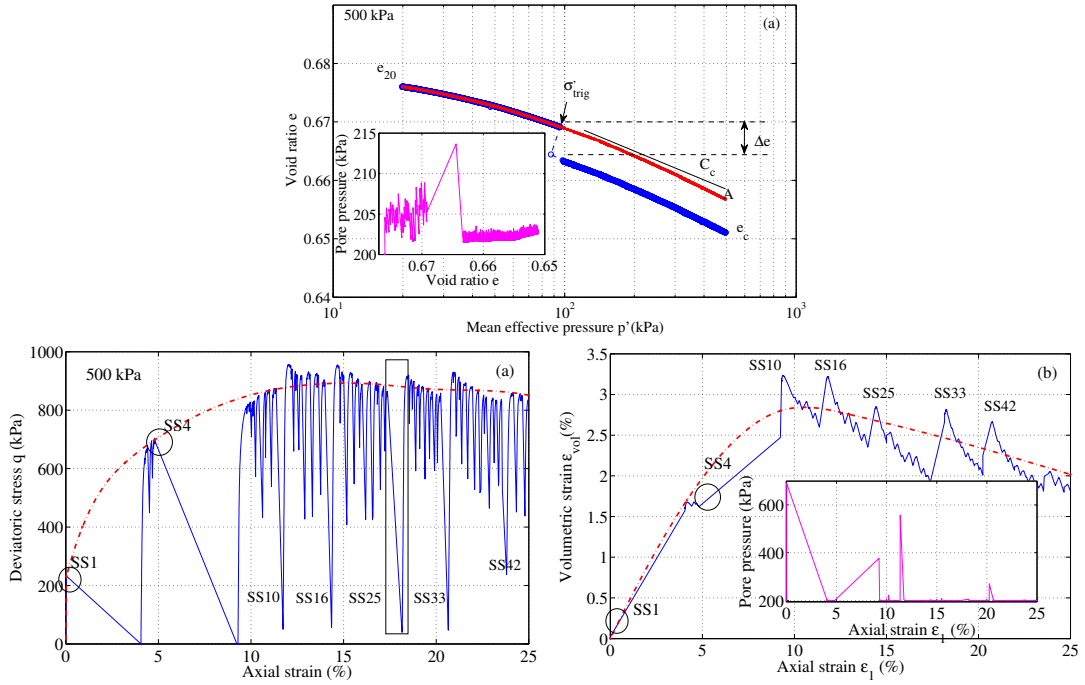

Figure E.1: Frottements saccadés en consolidation isotrope et en compression triaxiale drainée à 500 kPa.

La détermination de l'indice des vides e_c au départ de la compression triaxiale drainée nécessite des données précises de la compression isotrope précédant celle-ci. Ces données montrent l'incontrôllabilité de e_c à cause de nombreux effondrements isotropes et indiquent la non-répétabilité des frottements saccadés en compression triaxiale (figure E.1).

De nouvelles séries d'essais confirment l'existence de très larges frottements saccadés en compression triaxiale drainée, jusqu'à l'annulation du déviateur, ainsi que la présence inattendue des surpressions interstitielles au début de chaque frottement saccadé. Comme dans les effondrements isotropes ou dans les liquéfactions, cette surpression interstitielle n'est pas la première cause de ces instabilités, puisqu'elle apparaît systématiquement après la chute du déviateur. Néanmoins, elle amplifie fortement le développement des déformations axiales et volumiques en réduisant la contrainte effective. Le similarité du développement de cette surpression interstitielle dans les instabilités isotropes et déviatoriques suggère les mêmes mécanismes de déclenchement et **la phase de glissement peut être interprétée comme une consolidation dynamique à déviateur constant**.

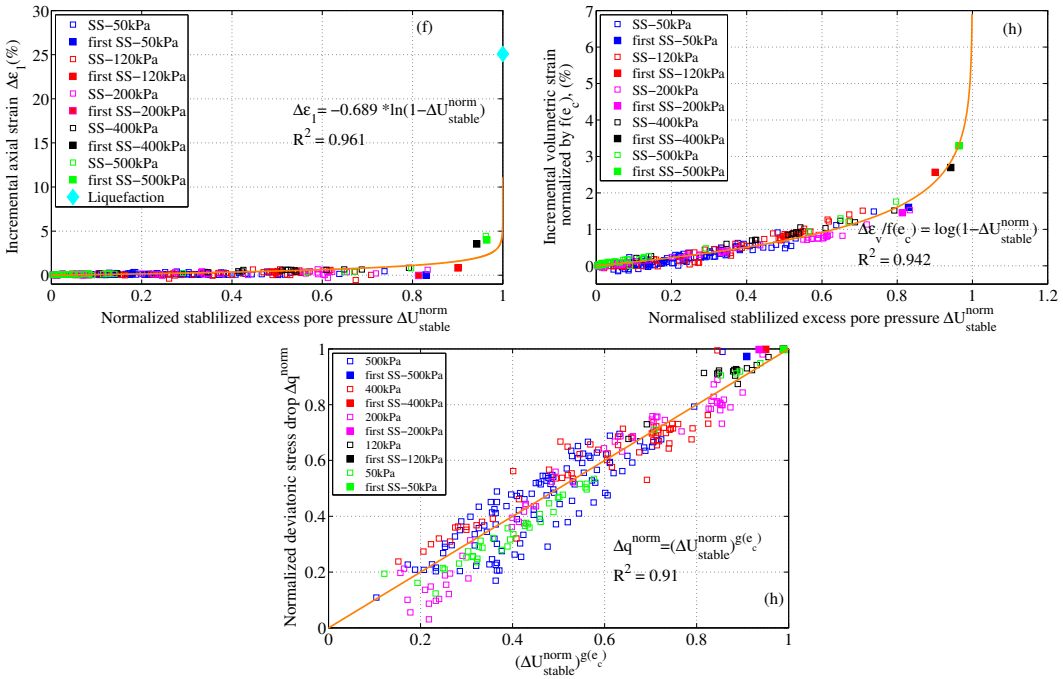

Figure E.2: Effets de surpression interstitielle stable et normalisée ΔU^{norm}_{stable} sur l'incrément des déformations axiales $\Delta\varepsilon_1$, l'incrément des déformations volumiques $\Delta\varepsilon_{vol}$ et la chute du déviateur normalisé Δq_{norm} en frottements saccadés.

Les mesures expérimentales minutieuses révèlent **le caractère non couplé entre la pression de confinement p'_0 et l'indice des vides** e_c sur le comportement mécanique de chaque frottement saccadé; ce qui amène à des corrélations empiriques unifiées entre les paramètres macroscopiques caractéristiques. Si la magnitude de la chute du déviateur Δq et la contrainte de déclenchement q_{trig} sont connues, alors

(i) la surpression interstitielle stable et normalisée ΔU^{norm}_{stable} peut être estimée à partir du déviateur normalisé $\Delta q_{norm} = \dfrac{\Delta q}{q_{trig}}$, (figure E.2),

(ii) l'incrément des déformations axiales $\Delta\varepsilon_1$ peut être déduit par ΔU^{norm}_{stable},

(iii) et l'incrément des déformations volumiques $\Delta\varepsilon_{vol}$ aussi par ΔU^{norm}_{stable}.

(iv) l'unique frontière des frottements saccadés dans le plan des contraintes effectives.

Les caractéristiques temporelles de la pression interstitielle dynamique dans le régime quasi-statique sont estimées par l'unique valeur de ΔU_{stable} :

(i) la durée de la phase transitoire oscillante I, t_{trans}, est estimée à partir de la contrainte moyenne stable normalisée $\dfrac{p'_{stable}}{p'_{crit}}$, qui est une fonction de l'excédent de la

pression interstitielle stabilisée ΔU_{stable} et de l'amplitude de la chute du déviateur Δq,

(ii) la durée de la phase intermédiate II, Δt_{05}, est estimée à partir de $\frac{p'_{stable}}{p'_{crit}}$,

(iii) la durée de la phase de dissipation III est caractérisée par C_v, variant non linéairement avec la pression de confinement p'_0. Toutes caractéristiques temporelles et ces effets couplés de surpression interstitielle avec les contraintes et les déformations montrent une évolution continue et fluide vers une liquéfaction finale.

De plus, la durée de la chute du déviateur t^q_{drop} est très courte et quasiment constante, environ 2.254 ms, quelles que soient les pressions de confinement entre 50 à 500 kPa.

Liquéfaction

La liquéfaction statique et la liquéfaction cyclique sont les deux seuls types de liquéfaction connus en mécanique des sols. La découverte surprenante d'un troisième type, la liquéfaction en consolidation isotrope ou en compression isotrope drainée sur les matériaux granulaires modèles très lâches pose de nouvelles questions, à la fois expérimentale, numériques et également théoriques. Pouvons-nous trouver d'autres membres inédits de cette nouvelle famille ? Avec de nouvelles mesures, pouvons-nous décrire les règles évolutionnelles capable de transformer les instabilités locales (effondrements isotropes et frottements saccadés en compression drainée) en liquéfaction globale ? Est-ce que les surpressions interstitielles, tout en n'étant pas une cause, peuvent être un composant clé contrôlant les paramètres mécaniques des nouvelles instabilités, par des corrélations empiriques ? Et surtout, pouvons-nous découvrir la signification physique cachée derrière les trois phases de la surpression interstitielle ?

Cette thèse montre une vue assez détaillée et globale des instabilités diffuses avec de nouveaux types de liquéfaction inédite et également des connections reliant les ruptures locales comme des frottements saccadés et des effondrements en isotrope et les ruptures globales de type liquéfaction. Nous avons découvert la liquéfaction en consolidation isotrope IL, puis la liquéfaction en frottement saccadé SL, la liquéfaction en phase de saturation par contre-pression BL, la liquéfaction en phase de saturation par circulation d'eau désaérée FL et même la liquéfaction par imbibition d'eau désaérée WL.

Les mesures de l'accélération verticale en tête de l'échantillon montrent définitivement que la surpression interstitielle n'est pas la cause des instabilités observées, puisqu'elle est systématiquement en retard de quelques milli-secondes par rapport à l'accélération verticale. La magnitude de l'accélération verticale et les trois phases de la surpression interstitielle sont des points importants de cette étude. La liquéfaction

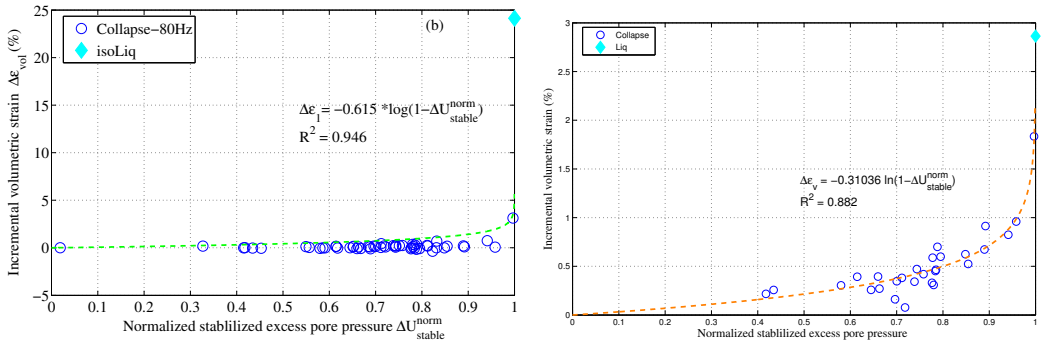

Figure E.3: Effets de surpression interstitielle stable et normalisée ΔU^{norm}_{stable} sur l'incrément des déformations axiales $\Delta\varepsilon_1$, l'incrément des déformations volumiques $\Delta\varepsilon_{vol}$ en consolidation isotrope.

en consolidation isotrope IL et celle en frottement saccadé SL ont la plus grande accélération verticale autour de 10 g, qui est trois ordres de grandeur plus élevé que celles des BL, SL et WL. Nous obtenons une distinction importante entre la liquéfaction dynamique et la liquéfaction statique puisque cette dernière n'a aucune accélération verticale et aucune vibration de surpression interstitielle.

Cette thèse montre également que la liquéfaction peut se produire dans des conditions de saturations imparfaites ou de quasi-saturation (coefficient de Skempton's B = 0.85-0.95). Pour des milieux totalement saturés, on obtient une fréquence dominante de 80 Hz avec la séries CIDNC et les caractéristiques temporelles de la pression interstitielle dynamique des effondrements en isotrope sont estimées par l'unique paramètre ΔU^{norm}_{stable}. La phase transitoire oscillante I est caractérisée par une constante $< t^{Coll}_{trans} >$. L'état stable t_{05} par ΔU^{norm}_{stable}. La durée de la phase de dissipation III est identifiée avec k^{norm}_{diss}. La magnitude de la surpression interstitielle ΔU^{norm}_{stable} est reliée à d'autres mesures mécaniques de déformations comme l'incrément des déformations axiales $\Delta\varepsilon_1$ et l'incrément des déformations volumiques $\Delta\varepsilon_{vol}$. Ce qui signifie que le paramètre ΔU^{norm}_{stable} contrôle les autres paramètres de déformations, (figure E.3).

Néanmoins, comme les précédents frottements saccadés avec les magnitudes inconnues de la chute du déviateur Δq et de la contrainte déviatorique de déclenchement q_{trig}, il reste à déterminer les magnitudes de la surpression interstitielle stabilisée ΔU_{stable} et de la contrainte isotrope de déclenchement σ'_{trig} pour avoir une compréhension totale de la liquéfaction dynamique.

Emission acoustique

Des bruits audibles sont systématiquement accompagnés de chaque instabilité, indépendamment des conditions de chargement (isotrope ou déviatorique), de drainage (drainé ou non drainé), de saturation (sec, mouillé ou saturé), de cisaillement (triaxial ou annulaire) et même de la granulométrie des particules (mono ou poly-disperse). Avec de nouveaux capteurs incluant l'émission acoustique passive (un accéléromètre piézoélectrique verticale, un microphone pré-polarisé horizontal) et un vibromètre horizontal par laser, les mesures de l'émission acoustique (AE) dans le domaine de faible fréquence, en-dessous de 5 kHz, complémentent les mesures mécaniques des instabilités diffuses dans l'environnement triaxial.

L'objectif est de relier quantitativement les paramètres macroscopiques de contrainte et de déformation de l'instabilité comme la chute des contraintes, la contrainte de déclenchement, la surpression interstitielle et les incréments des déformations axiales et volumiques à des mesures acoustiques passives comme l'énergie acoustique et la magnitude de G, M, V des événements.

L'analyse fréquentielle avec FFT est utilisée pour extraire le contenu fréquentiel en-dessous de 5 kHz. L'utilisation conjointe de trois techniques (l'accélération verticale, pression acoustique et vibration horizontales) permet d'obtenir et de vérifier le contenu fréquentiel des instabilités dynamiques. La **signature fréquentielle** des instabilités est ainsi obtenue. Des simulations numériques complémentaires avec Comsol utilisant une structure granulaire idéalisée, homogène et isotrope permettent d'obtenir des fréquences dominantes raisonnablement proches de celles de l'expérience. L'utilisation avancée des ondelettes de Cauchy permet d'identifier la durée, d'affiner la fréquence dominante des événements et de préciser l'évolution temporelle de ces fréquences dominantes, autour de 320, 640, 870, 1260 Hz dans la gamme des fréquences audibles. Le même groupe de fréquences identifiées pour la liquéfaction, les frottements saccadés et les effondrements isotropes fortement suggère que ces instabilités sont probablement créées par les mêmes mécanismes physiques de déclenchement. Ces fréquences dominantes sont donc des signatures d'un système en vibration. Par conséquence, les caractéristiques mécaniques élastiques (module K, coefficient de Poisson ν) peuvent être déduites rétroactivement.

On obtient ainsi des relations directes entre l'amplitude de l'accélération verticale en tête de l'échantillon G (de la vibration horizontale V et de la pression acoustique horizontale M) et les mesures mécaniques pour pouvoir prédire les paramètres manquants, (figure E.4):

(i) la contrainte déviatorique de déclenchement q_{trig} et la magnitude de la chute du déviateur Δq pour des frottements saccadés ;

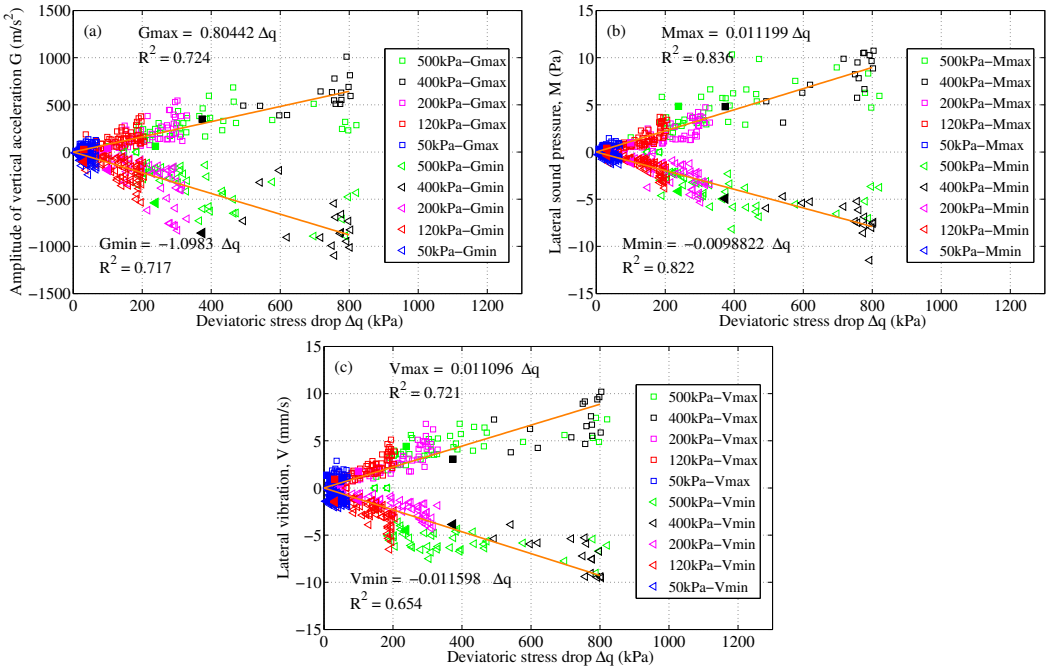

Figure E.4: Effets de l'accélération verticale G, pression acoustique horizontale M, vibration horizontale V sur la chute du déviateur Δq en frottements saccadés.

(ii) la contrainte effective isotrope de déclenchement σ'_{trig} et la surpression interstitielle stabilisée ΔU^{norm}_{stable} pour des effondrements en isotrope et des liquéfactions dynamiques.

Trois paramètres complémentaires et indispensables Δq, σ'_{trig}, ΔU_{stable} sont reliés par des relations empiriques à l'accélération verticale, spécialement son amplitude maximale tout au début de l'événement, y compris le cas d'une destruction complète de la structure granulaire lors d'une liquéfaction. Ces relations entre les mesures mécaniques et acoustiques révèlent **le caractère quasi-déterminisme des instabilités granulaires**.

Conclusions

Cette thèse étudie les instabilités dynamiques des milieux granulaires modèles saturés à l'aide d'un appareil triaxial classique. Les instabilités englobent la liquéfaction et les effondrements en compression isotrope drainée, les frottements saccadés en compression triaxiale drainée. Ces instabilités apparaissent spontanément à des contraintes

effectives de confinement impré-visibles. Elles sont accompagnées de très rapides et très fortes surpressions interstitielles, malgré un drainage approprié; ce que ne présentent pas les milieux granulaires naturels. En compression isotrope drainée (consolidation), des effondrements locaux naissent instantanément. En compression triaxiale drainée, on observe de larges frottements saccadés quasi-périodiques caractérisés par des déformations volumiques et axiales contractantes. De temps en temps, ces effondrements et frottements saccadés locaux peuvent se développer en liquéfaction menant à une destruction complète de la structure granulaire.

Les données à haute résolution temporelle issues de ce travail ont permis la découverte d'une nouvelle famille de liquéfaction dynamique et statique. L'étude des émissions acoustiques passives a permis l'identification de signature spectrale caractéristique. Pour les frottements saccadés, la phase de glissement peut être interprétée comme une consolidation dynamique, limitée par l'unique surface en dessous de la ligne critique de rupture dans le plan des contraintes effectives. La séquence temporelle précise des événements exclut que la pression interstitielle soit la cause principale des instabilités. Cependant, le rôle important de la surpression interstitielle est démontré dans des relations quantitatives entre les incréments de contraintes, et de déformations et l'éphémère surpression interstitielle stabilisée développée pendant la phase de glissement. Cela montre finalement la nature quasi-déterministique de ces instabilités dynamiques. Ces relations empiriques sont basées uniquement sur l'amplitude maximale de l'accélération verticale de très courte durée et sont gouvernées indépendamment par la pression de confinement et par l'indice des vides. La similarité de la surpression interstitielle entre différentes instabilités suggère fortement quelques mécanismes similaires de déclenchement, probablement à partir de ré-arrangements de la microstructure granulaire.

Appendix F

On the role of pore pressure in dynamic instabilities of saturated model granular materials

Noname manuscript No.
(will be inserted by the editor)

On the role of pore pressure in dynamic instabilities of saturated model granular materials

T.T.T. Nguyên · T. Doanh · A. Le Bot · D. Dalmas

Received: date / Accepted: date /

Abstract Drained triaxial axisymmetric isotropic and subsequently shear compression tests are performed on fully water-saturated short cylindrical samples of nearly monodisperse glass beads, initially assembled in a loose state by moist tamping and undercompaction technique. Both *fully drained* isotropic and shear tests are affected by dynamic instabilities triggered under uncontrolled isotropic or deviatoric stress. These dynamic instabilities encompass isotropic collapses, compression stick-slips and especially the unexpected isotropic liquefaction. The most reasonable but imprecise scenario points to a possible dynamical collapse of the granular structure triggered by a spontaneous failure of the force chains, generating an instantaneous surge of excess pore pressure in a fully saturated system. This paper aims in exploring the key role of pore pressure outburst on some global macroscopic parameters of these dynamic events. It focuses on the unforeseen, short-lived and stabilised excess dynamic pore pressure and proposes an in-depth assessment of the validity and the reliability of pore pressure measurements. Irrespective of loading condition (i.e. isotropic or drained compression shear) the ephemeral stabilised excess dynamic pore pressure controls the evolution of the axial and volumetric strains in an essentially dynamic consolidation process. Some appearance conditions for these unexpected dynamic instabilities are discussed.

Keywords Dynamic Instability · Liquefaction · Stick-slip · Model granular materials · Triaxial compression · Friction

T.T.T. Nguyen, T. Doanh
Ecole Nationale des Travaux Publics de l'Etat. LTDS (UMR CNRS 5513). 2 Rue M. Audin, 69518 Vaulx en Velin Cedex. France.

A. Le Bot, D. Dalmas
Ecole Centrale de Lyon. LTDS (UMR CNRS 5513). 36 avenue Guy-de-Collongue, 69134 Ecully Cedex. France.

1 Introduction

Granular matter is one of the most ubiquitous materials used in civil engineering, and one of the most difficult to model, theoretically or numerically, especially for earthquake engineering. Liquefaction often occurs in loose and saturated granular layers during earthquake with devastating consequences. This phenomenon can be easily explained by the lack of granular skeleton when the granular particles are separated from each other; resulting in a null effective contact stress $\sigma^{'}$ between grains. From the effective stress principle, $\sigma^{'} = \sigma - U$ formulated by Terzaghi [66] for totally saturated medium, σ being the total stress of the only two-phase (grains and water) element, and U the pore fluid pressure, liquefaction can be best understood as the vanishing of $\sigma^{'}$ or the equalisation of σ and U. Consequently, the measurement of the pore fluid pressure is of paramount importance to the understanding of this liquefaction phenomenon.

A large amount of experimental studies has been devoted to the measurement of U on site and in laboratory [55, 9,36]. Cyclic or pseudo-dynamic liquefaction was first investigated in laboratories using conventional and dynamic triaxial and torsional shear machines, due to the similarity with liquefaction induced by earthquakes. Static liquefaction has next been observed in undrained or partially drained loading conditions. The pore pressure evolution was investigated in these experiments with great precision; although it was slowly and progressively generated by quasi-static loading conditions. However, the physical significance behind the pore pressure generation is far from being fully understood, excepting by the soil dilatancy mechanism, Schofield et al. [58]. One simple scalar parameter, pore pressure ratio $r_u = U/\sigma^{'}_{ini}$ [61], was defined to identify the liquefaction level ($r_u = 1$), $\sigma^{'}_{ini}$ is the initial effective stress, often approximated in laboratory by the initial isotropic pressure in the triaxial chamber.

Centrifuge and 1-g shaking table testings complete the laboratory investigation as a useful step towards the understanding of the dynamic character of earthquakes. Recently, in-situ instrumentation has shed new light on the real time history of excess pore pressure on liquefied soils and shown the difficulty of measuring U on-site. These tests point out the dynamic aspect of U by measuring a sudden increase of pore pressure shortly after the beginning of shaking period, both in laboratory and on-site [9,54,69]. σ'_{ini} is taken as the initial vertical effective stress. However, many basic questions remains unanswered: What are the physical generating mechanisms and the associated controlling parameters of the pore fluid pressure?

In order to understand and explain the complexity of granular medium in laboratory testing, glass beads are frequently used as a simplified analogue material in soil mechanics [1], in physics [29] and geophysics [59].They served as a natural complement to the use of spherical grains in numerical discrete element modelling (DEM). These model materials lead to the discovery of the stick-slip phenomenon in triaxial compression and simple shear [47,2,10,18,76, 74]; and recently to the totally unexpected collapse and liquefaction during isotropic drained compression or consolidation [16,15]. These events, termed as dynamic instabilities, are probably different facets of the same physical phenomenon and are strongly related to the spontaneous generation of the pore fluid pressure. Excepting the rare case of destructuration on calcarenite in isotropic compression, with unknown dynamic features [38], and the case of liquefaction of Eniwetok sand happening during the first unloading under isotropic undrained cycle of high pressures [22], these dynamic instabilities were unknown to granular science prior to our works, especially the coupled volumetric stick-slip, the fast transition from solid-like to liquid-like behaviour and the isotropic liquefaction. To our knowledge, they have never been predicted theoretically, despite a large number of advanced constitutive models for geomaterials [12,27,40, 45,49,72,34], nor detected in numerous numerical DEM experiments with spherical particles [57,63,43,44,62], including a full solid-liquid coupling formulation [25,26,19], and instabilities [23].

Our previous studies also rule out the possibility of the dynamic pore fluid pressure being the primary cause of these events, and extend a step further the conjecture of dynamic pore pressure fluctuations formulated earlier in rapid shearing experiments [31].

Given the important place of pore fluid pressure in completely saturated materials, the objectives of this paper consist of a study of the unexpected effects of short-lived stabilised excess pore pressure on the axial and volumetric strains of these dynamic instabilities. It also includes an in-depth verification of the pore pressure measurements and stresses the importance of their accuracy, especially for dynamic events.

Table 1 Index properties of SLG 6-8 glass beads.

Property	Value
Density, ρ (kg/m^3)	2500
Mean size, D_{50} (mm)	0.723
Uniformity coefficient, C_u	1.463
Curvature coefficient, C_c	0.989
Maximum void ratio, e_{max}	0.686
Minimum void ratio, e_{min}	0.574

Section 2 describes the experimental setup designed for testing idealized granular materials and the sets of laboratory tests. The usual global behaviour under drained isotropic and vertically sheared compression is strongly affected by unexpected "stick-slip" like events. These remarkable dynamic instabilities are rapidly reported in Sec. 3, together with the assessment of the validity of the excess pore pressure measurements. The effects of the ephemeral stabilised pore pressure of these spontaneous dynamic events in compression loading, including the rare events in isotropic liquefaction and undrained compression stick-slip, are examined in Sec. 4. Finally, the paper discusses some conditions for the appearance of these unexpected dynamic instabilities and highlights some essential concluding remarks in the last section.

2 Experimental programme

Virgin monodisperse and spherical soda-lime glass beads (CVP Sil-glass) of mean diameter of 0.723 mm, commercialized by CVP, Linselles, France[1], are used in each experimental test to avoid possible wearing effects. These beads can be classified as clean and poorly graded fine-grained granular materials with usual index properties reported in table 1.

The classical experimental system is used in this study for triaxial testing on a short cylindrical specimen of initial height H_0 = 70 mm and diameter D_0 = 70 mm inside a triaxial cell [36]. The sample is a granular assembly enclosed inside a cylindrical and open-ended latex membrane of 0.3 mm thickness which is closed by a duralumin top cap when introduced in the loading cell. Loose and very loose model granular samples are created using modified moist tamping and under compaction method [8,35]. Predetermined quantities of moist glass beads, mixed with 2 % of distilled water by weight, are placed and gently compacted in five layers of prescribed thickness using a flat-bottom tamping circular stainless steel rod of 20 mm in diameter. A fully saturated state is obtained using CO_2 method [37] with de-aired

[1] www.Cvp-abrasif-broyage.com

distilled water, together with a high back pressure of 200 kPa. High Skempton's coefficient B = $\Delta U/\Delta\sigma \geqslant 0.95$ [64] assesses the fully saturated system. Additional information can be found in our previous works on sands [28, 17].

The initial structural anisotropy of model granular assembly created by moist-tamping method is one of the required conditions for the appearance of these instabilities [16].

In this study, Fig. 1 presents a special experimental setup to fully quantify the pore pressure evolution for the unexpected instabilities during the isotropic consolidation and compression shearing.

Constant back pressure U_0 needed for a full saturation is applied at the bottom of the sample. Since U_0 is imposed from the bottom drainage, the top pore-water pressure U_{top} is recorded close to the duralumin top cap of the granular sample to ensure a homogeneous stress state. Additionally, the bottom pore-water pressure U_{bottom} is measured to check the evolution of back pressure during dynamic instabilities. The data is synchronously acquired at 10 kHz with a dynamic data acquisition system NI 4472B of National Instruments. The static top pore-water pressure U_{top} is recorded by a piezoresistive transducer (Sedeme, MD20) with unknown resonant frequency. It is located outside the triaxial cell using a very thick plastic tube (Swagelok PFA) connected to the top cap of the granular sample, in a dead-end at a distance of about 60 cm. A dynamic piezoelectric pore pressure sensor (PCB S112A21) is also used in this experimental setup at 10 cm preceding the static one, having high resonant frequency (250 kHz). The bottom pore-water pressure U_{bottom} is measured by another transducer (Kistler, 4053A10) with natural frequency of about 120 kHz. It is also situated outside the triaxial cell at a distance of about 10 cm from the bottom platen and completed by another dynamic pore pressure sensor (PCB S112A21) in the same position.

Although miniature mid-plane pore pressure sensors can be an option in the triaxial experiment to assess these pore fluid responses [65]; unfortunately, their use is still problematic with very loose granular sample.

A classical triaxial test consists of two successive loading steps: isotropic consolidation or isotropic drained compression followed by drained vertical shearing in compression only if the sample is still geometrically stable. Compressed air under constant stress rate (1 kPa/s in our case) is used in the first isotropic step to bring the sample up to a desired cell pressure $\sigma_r^{'} = \sigma_3^{'}$, the minor principal stress. In the second step, the sample is subsequently sheared vertically under constant $\sigma_r^{'}$ and constant axial strain rate (0.0048 %/s) in drained or undrained condition. This second step adds an additional deviatoric shear stress $q = \sigma_a^{'} - \sigma_r^{'}$ to the first purely isotropic step; $\sigma_a^{'} = \sigma_1^{'}$ is the axial (major principal) stress. The excess pore pressure $\Delta U = U - U_0$

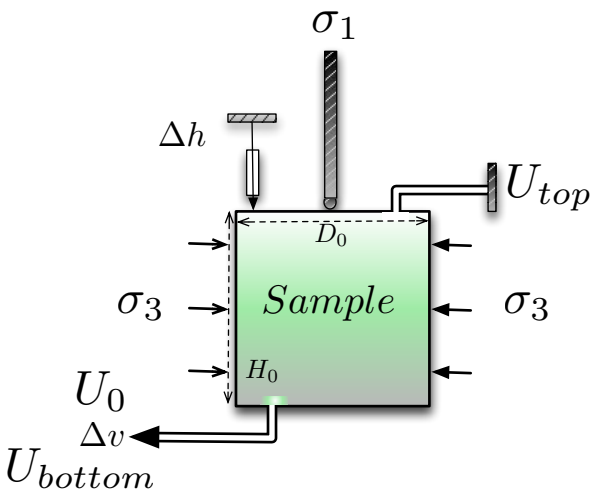

Fig. 1 Schematic view of the experimental setup for isotropic consolidation and drained triaxial compression.

is kept low - to a few kPa - to respect the requirement of full drainage for these two successive steps. The global axial strain $\varepsilon_a = \Delta h/H_0$ is estimated with the measurement of axial displacement Δh, using LVDT sensor, of the top platen inside the triaxial cell. The global volumetric strain is deduced from $\varepsilon_v = \Delta v/V_0$, where V_0 is the initial sample volume, and Δv the water volume expelled from or moved into the sample. The volumetric strain is usually translated into void ratio e in the first isotropic step. Following the usual convention in soil mechanics, volumetric and axial strains are positive (respt. negative) for compaction (respt. dilation).

Since the vertical loading ram is not physically connected to the top cap, the cylindrical sample is not kinematically constrained and it is free to deform, vertically and horizontally.

3 Experimental results

Since the temporal evolution of pore fluid pressure during the dynamic collapse and slip phase in triaxial testing is of particular interest, this paper is focused on the pore pressure measurements U_{top} and U_{bottom}, as well as the pore pressure difference $\Delta U_{tb} = U_{top} - U_{bottom}$.

Fig. 2 gives some essential notations of the temporal evolution of deviatoric stress q and pore pressure U during laboratory dynamic instabilities. The pore pressure changes from constant back-pressure U_0 to the first short-lived peak U^{peak}, then reduces to the stabilised U^{stable} before returning down to U_0. The deviatoric stress drops from q_{trig} towards the first minimum q_{vib} before returning to the steady-state q_{stable}. ΔU^{stable} is the brief stabilised excess pore pressure

Event	σ'_{trig}/q_{trig}	U_{top}			U_{bottom}			$\Delta\varepsilon_v$	$\Delta\varepsilon_a$	Δq
	kPa	Peak kPa	Stable kPa	Frequency Hz	Peak kPa	Stable kPa	Frequency Hz	Volume %	Axial %	Deviatoric stress drop kPa
Isotropic collapses from 20 to 500 kPa										
A	108	278	245	37	202	202	33,119	0.12	0.17	- -
B (double)	188	473	311	46	240	240	145	0.65	0.03	- -
C (double)	447	1032	500	61	437	437	145	0.82	0.14	- -
D	451	971	466	59	420	399	149	0.67	0.002	- -
Drained compression stick-slips at 500 kPa										
SS1	475	424	280	45	244	219	146	0.13	0.29	353
SS2	545	526	309	48	244	219	138	0.21	0.38	403
SS3	655	525	309	49	287	227	138	0.21	0.39	522
SS4	714	401	274	45	244	219	149	0.13	0.28	478
SS5	715	651	356	53	244	219	138	0.25	0.53	601
SS6	782	403	244	41	244	219	32,152	0.23	0.16	454
SS7	783	572	356	50	244	219	138	0.24	0.50	624
SS8	774	807	407	57	244	219	137	0.31	0.77	709
SS9	799	755	392	56	307	247	136	0.33	0.73	708
SS10	805	378	273	45	244	219	32,151	0.23	0.31	557
SS11	798	318	250	44	244	219	32,150	0.27	0.27	508
SS12	788	726	392	56	244	219	137	0.33	0.72	704
SS13	900	583	358	54	244	219	136	0.30	0.57	688

Table 2 Isotropic collapses from 20 to 500 kPa and drained compression stick-slips at 500 kPa of confining pressure on very loose model granular materials, $e_{20} = 0.707$ ($Dr_{20} = -19\%$), with 200 kPa of back pressure.

and Δq the deviatoric stress drop of the dynamic instability event.

In Fig. 3, we observed dynamic instabilities that occur in an isotropic consolidation from 20 up to 500 kPa and subsequently on a drained shear compression test at 500 kPa of confining pressure on very loose model granular materials. Four isotropic collapses, noted A to D, and 13 drained compression stick-slips, noted SS1 to SS13, are reported for this particular test.

Table 2 summarises different values measured to characterise the dynamic instabilities of this study. σ'_{trig}(respt. q_{trig}) is the uncontrolled triggering isotropic (respt. deviatoric) stress of the isotropic (shear) test. U_{top} (U_{bottom}) the interstitial pore water pressure at sample top (bottom) with the first peak U^{peak}, the stabilised value U^{stable} and the vibration frequency f_U; $\Delta\varepsilon_v$ ($\Delta\varepsilon_a$) the incremental volumetric (axial) strain produced during the instability event; Δq the deviatoric stress drop of the dynamical slip component of the stick-slip event and t_{50} the time for 50% of excess pore pressure dissipation. This very loose model granular sample has an initial void ratio (relative density $Dr = (e_{max} - e)/(e_{max} - e_{min})$) at the beginning of the isotropic consolidation at 20 kPa, $e_{20} = 0.707$ ($Dr_{20} = -19\%$).

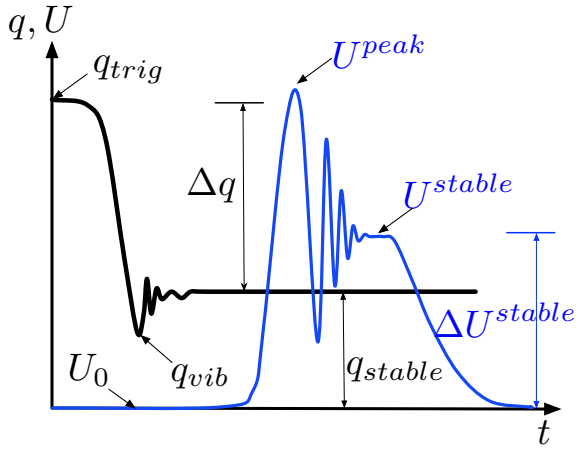

Fig. 2 Schematic view of the temporal evolution of deviatoric stress q and pore pressure U during laboratory dynamic instabilities.

3.1 Global behaviour

The isotropic compressibility from 20 to 500 kPa of Fig. 3a shows a very different compressibility behaviour of model granular materials from the traditional one of sands or powders [66,3]. Instead of the expected smooth and continuous decrease of void ratio $e = V_{void}/V_{grains}$ with increasing effective stress, four isotropic collapses at uncontrolled triggering stress σ'_{trig} of 108, 188, 447 and 451 kPa can be seen with a large unexpected drop Δe. Between two collapse events, classical continuous decrease of e is observed. Two large, nearly cascading events C and D, occur just before reaching the required 500 kPa of confining pressure of the drained triaxial compression. Double or cascading collapse is observed for the second and third collapses; however, no isotropic liquefaction is noticed. Dynamic isotropic collapse is defined

as spontaneous increase of axial and volumetric strains due to sudden pore pressure development at constant cell pressure, while preserving the initial cylindrical sample shape.

At the end of the isotropic consolidation at 500 kPa, Figs. 3b and c give the results of the subsequent drained compression shear. Again, instead of the expected smooth stress-strain relationship with continuous increase of q, without peak, with increasing ε_a for an initially loose granular assembly, stick-slip phenomenon is observed with quasi-periodic and large stick-slip events in Fig. 3b. Each event invariably has two phases. A first fast slip phase presents a very abrupt deviatoric stress drop Δq at also uncontrolled triggering stress q_{trig}; followed by a slow stick phase with a gradual hardening up to at least the previous deviatoric stress level, before the occurrence of the next stick-slip cycle. Quasi-regular stick-slips happen throughout the performed axial strain range, up to 25 %. The largest drop towards the isotropic stress state around 25 % of ε_a is a simple unloading-reloading cycle with no stick-slip in unloading. Some precursors with small Δq can be seen, as before SS4 and SS9 (open circles). On the nearly horizontal critical state plateau at q^{max}, the stick phase systematically presents a stress peak of an apparent dense behaviour, while a nearly smooth envelop curve is retrieved, conforming to the usual behaviour of loose granular materials.

The strongly coupled behaviour is noticed with the presence of large and quasi-periodic stick-slips in the evolution of volumetric strains in Fig. 3c and a constant critical state at 2.5 % of ε_v, confirming the loose character previously noted on the stress-strain relationship. The sawtooth volumetric profile seems to oscillate around this critical value. The loose model granular system constantly changes, and never reaches a steady state, in terms of stress and strain. Drained compression stick-slips always have a sudden volumetric compaction in the slip phase, and a gradual dilation in the stick phase.

Fig. 3 adds the isotropic collapses during the unavoidable isotropic consolidation phase prior to the drained compression shearing with stick-slips. The mobilized frictional angle at failure ($\varphi^{max} = 26°9$), at first stick-slip ($\varphi^{first} = 18°4$) and at the phase transformation ($\varphi_{PT} = 18°2$) strengthen previous findings [18].

The isotropic collapse and the drained compression stick-slip seem to share some common triggering mechanisms.

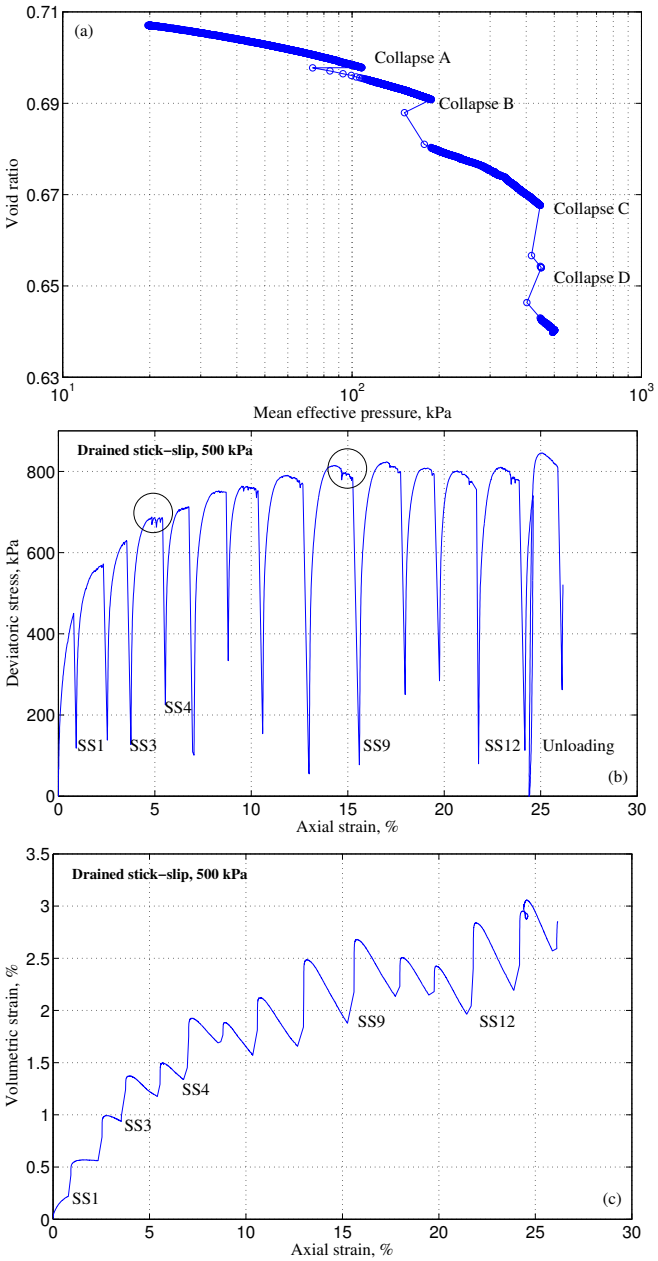

Fig. 3 (a) Isotropic instabilities from 20 to 500 kPa and (b) drained compression stick-slips with (c) coupled volumetric behaviour at 500 kPa of confining pressure on SLG 6-8 glass beads of 0.7 mm of diameter.

3.2 Isotropic collapses

Fig. 4a presents the temporal evolution of the pore pressure U concerning the fourth isotropic collapse D at 451 kPa, rapidly occurred after collapse C as a typical result for an isotropic collapse. The time origin is shifted to the beginning of the transient phase $\pm$ 0.1 ms, which is the current time resolution. A semi-logarithmic scale is used to emphasise the suddenness of the time-related variations of U. The static pore pressure at the sample top U_{top} (solid blue line) commences with a sudden surge up to 971 kPa, U_{top}^{peak}, from constant back-pressure U_0, followed by a rapid dissipation from a short-lived stable value of 466 kPa, U_{top}^{stable}, within a few seconds towards the equilibrium state of U_0. The static pore pressure U_{bottom} (solid green line) rises earlier, up to only 420 kPa at nearly 3 ms before U_{top}. A stabilised excess bottom pore pressure $\Delta U_{bottom} = U_{bottom} - U_0$ of 199 kPa is

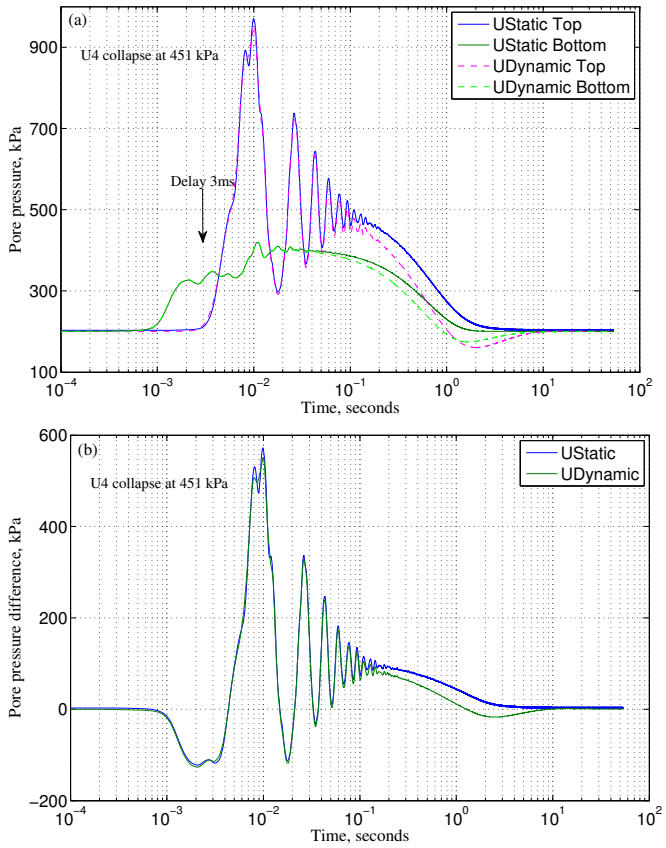

Fig. 4 (a) Temporal evolution of dynamic and static pore pressures at sample top and bottom, (b) dynamic and static pore pressure difference between top and bottom of isotropic collapse D at 451 kPa of confining pressure on 0.7 mm CVP beads.

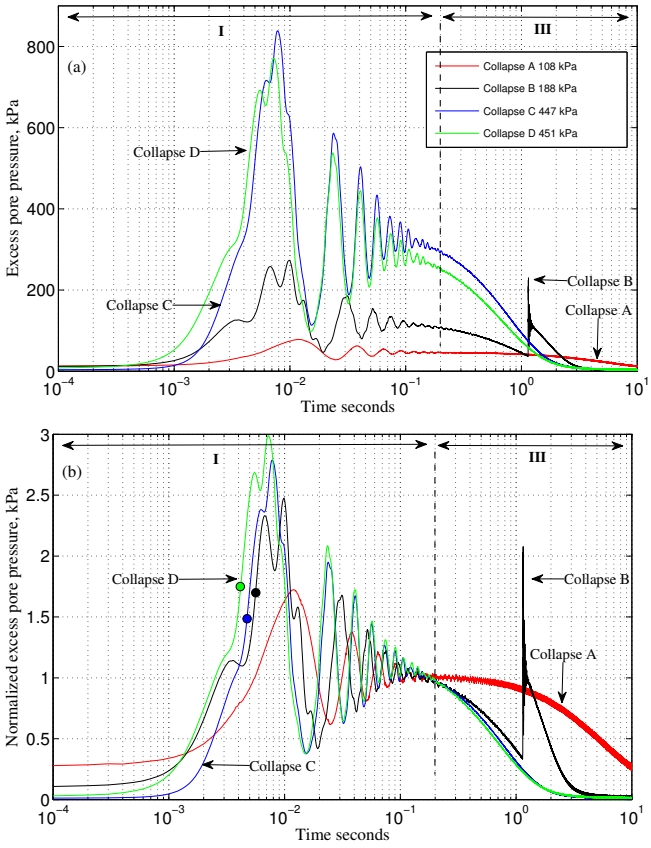

Fig. 5 (a) Temporal evolution of natural and (b) normalised static top excess pore pressures of isotropic collapses from 20 to 500 kPa of confining pressure on 0.7 mm CVP beads.

briefly obtained despite a completely open drainage system at the bottom platen and a slow increase of cell pressure to respect the isotropic consolidation condition with constant back-pressure U_0. U_{bottom} also mildly oscillates at higher frequency than U_{top}. The small variation of U_{bottom} is probably linked to the open end of the drainage system and the large oscillated phase of U_{top} to the top cap drainage end.

The complementary dynamic measurements of top and bottom pore pressures (dashed lines) exactly follow the static ones in the transient phase. Unfortunately, no explanation can be found for the discrepancies at the end of the dissipation phase, when the dynamic pore pressures go unexpectedly and briefly below the imposed constant back pressure U_0 of 200 kPa before returning to the steady state U_0.

The static and dynamic pore pressure difference is shown in Fig. 4b, confirming the briefly non-homogenous effective stress state within $\pm$ 100 kPa and the presence of the unexpected transient phase. These ephemeral signals from pore pressure measurement are ripples in time, probably created by powerful events such as the destruction of chain forces. They can even lead to cataclysmic liquefaction-like phenomenon [16]. Furthermore, the result shown in Fig. 4 is essentially a monochromatic audible signal, basically with only one frequency being emitted, Table 2.

3.3 Excess pore pressure development

Fig. 5a shows the spontaneous development of U_{top} for all four isotropic collapses, as the largest pore pressure inside the granular sample, due to the closed-ended (open-ended) of the top (bottom) drainage system. The second collapse is a rare event which presents a secondary collapse occurring during the dissipation phase. Large σ'_{trig} creates large U_{top}^{peak} and U_{top}^{stable}; however, U_{top}^{stable} occurs at constant time of 0.2 seconds.

After normalising the excess pore pressure by ΔU_{top}^{stable}, a more coherent picture of ΔU^{norm} is revealed in Fig. 5b with some discrepancies of U_{top}^{peak}. As usual for isotropic collapse case, the evolution of U_{top} and ΔU^{norm} can be reasonably broken-down into two phases. First a fast transient phase *I* occurred within 200 ms (vertical dashed line in Fig. 5). It is characterise by a damped oscillated behaviour of pore pressure which briefly stabilised after 200 ms at unity

level of ΔU^{norm}. The next long dissipation phase, termed phase *III*, is of about 5 seconds where the pore pressure gets back to its initial equilibrium value U_0. Contrary to isotropic liquefaction which will be discussed later in the paper, we do not observed any intermediate phase, termed phase *II*, of the pore pressure maintained at constant ΔU_{top}^{stable} in between those two phases.

The existence of constant pore pressure during intermediate phase *II* for at least 1 s above 95 % of ΔU_{top}^{stable} is one of three mandatory experimental conditions for isotropic and drained compression liquefaction [16]. The absence of this crucial phase leads to isotropic collapse and drained compression stick-slips.

Superimposed liquefaction points (solid circles) on the rising edge indicate the ΔU^{norm} levels close to unity ($r_u = 1$ or $\sigma = U$) in Fig. 5b. These levels correspond to a briefly null effective stress state for less than 5 ms or a short-lived local liquefaction with very limited deformation. They show a large contrast with the normal full global liquefaction always associated with runaway deformation and a total destruction of the granular skeleton [16]. The absence of a liquefaction point on the first collapse simply means a non-liquefaction event for the whole collapse. The very short duration of the stabilised phase *II* in the performed test is not long enough to bring local liquefaction to a global level of the whole granular sample.

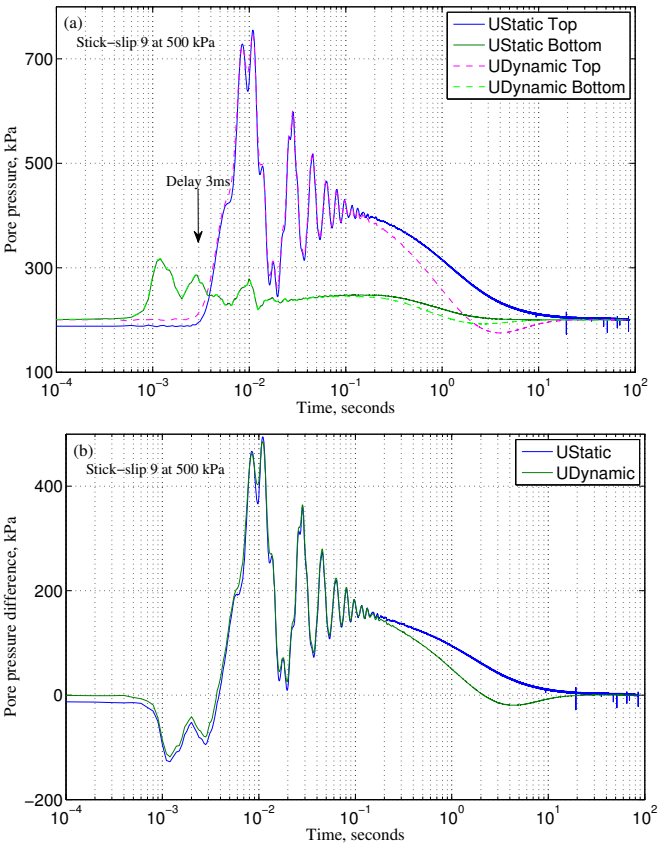

Fig. 6 (a) Temporal evolution of top and bottom dynamic and static pore pressures, (b) pore pressure difference between top and bottom of stick-slip SS9 at 500 kPa of confining pressure on 0.7 mm CVP beads.

3.4 Drained stick-slips

The large 9th stick-slip is chosen as a typical case of stick-slip behaviour in Fig. 6. The simultaneous static and dynamic measurement of top and bottom pore pressures give the impression of déjà vu despite the presence of deviatoric stress in this shearing phase. The decomposition of U in two transient and dissipated phases is very similar to isotropic collapse. A fast rise to U_{top}^{peak} within 10 ms, a brief presence of U_{top}^{stable} at 0.2 s before being dissipated, a small delay of 3 ms of U_{bottom} before U_{top} in Fig. 6a, a local liquefaction event with a short-lived pore pressure above 500 kPa, a resulting non-homogenous effective stress state in Fig. 6b and the validity of unanticipated U by two different measurement techniques.

Fig. 7a shows the temporal evolution of static excess top pore pressure for all stick-slips identified by their number on the right colorbar with increasing axial strain at the beginning of stick-slip event. This figure offers no pertinent analysis excepting the creation of large U_{top}^{peak} and U_{top}^{stable} as function of triggering deviatoric stress q_{trig}. The normalised ΔU^{norm} in Fig. 7b gives a more coherent picture with a single frequency during the transient phase and a possible classification of the dissipation phase as function of q_{trig}. However, no suitable analysis, such as normalised U_{bottom}^{norm}, can be found for U_{bottom} in Fig. 7c. Note the continuous increase of U_{bottom} towards the stabilised value long after the transient phase *I*.

So the pore pressure measurements always come up in pairs, counter-intuitive but measurable from sample top and bottom. Due to the bottom drainage condition, U_{bottom} is always smaller than U_{top}. Additionally U_{bottom} always happens earlier than U_{top} for about 3 ms. A pair of fluid pore pressures come up fast through the two opposite sides of the drainage system, then down again. According to the granular physics that we know for a consolidation condition, they should not be there; but they were, irrespective of the loading condition, isotropic or triaxial compression shear, and of fabrication procedure, moist tamping or even dry deposition. Note that no excess top and bottom pore pressures are detected during the unloading-reloading cycle.

This counter-intuitive surge of pore pressure is of paramount importance in understanding these newly observed dynamic instabilities. The simultaneous measurements of pore pressure at sample top and bottom by two complementary techniques rule out the possibility of their false detection, of their creation by artefacts and reduce the margin of experimental error.

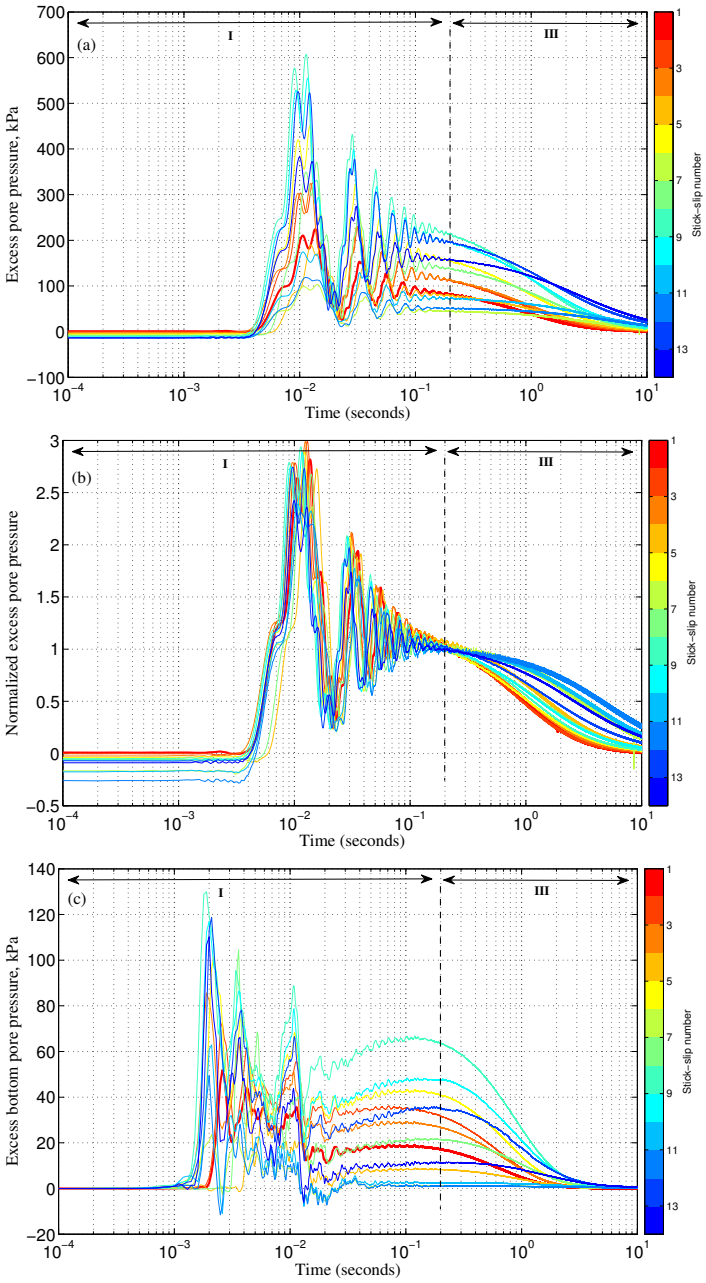

Fig. 7 Temporal evolution of (a) natural, (b) normalised static top and (c) natural bottom excess pore pressures of drained compression stick-slips at 500 kPa of confining pressure on 0.7 mm CVP beads. The stick-slip number is on the right colorbar.

The observed pore pressure evolution during and beyond the slip phase is qualitatively similar to that measured in double-direct shear experiment with saturated granular gouge [59], or under extreme conditions during earthquakes [7], impacts [33], or blast waves [30], without the regular oscillation of the transient phase *I*. However, the instabilities in our experiments, especially liquefaction (section 4.2), surprisingly occur at moderate overpressure ($\leqslant$ 1 MPa), low stress rate ($\leqslant$ 1 kPa/s), ambient temperature and without any known external blast-induced loadings.

For completeness, the complementary time evolution of ε_v, ε_a, ΔU^{norm} and the additional deviatoric stress for the first drained stick-slip (red) is given in Fig. 8 on the same logarithmic scale for the time axis. These temporal evolutions are quite similar to those of spontaneous collapse under isotropic consolidation (blue) with the exception of a suddenly large deviatoric stress drop Δq to a constant level in less than 2 ms, prior to the development of ΔU with 3 ms delay, with respect to Δq. Regardless of Δq, this constant slip duration is much shorter than that obtained from sheared granular layers of glass beads [48,2,59], indicating a more fragile behaviour. These figures reveal fast, although continuous, overall axial contraction and volumetric compaction from a steady-state to another, within only 2s, contrasting the axial and volumetric jumps of the literature [1,2,10,18,76,59]. Currently, no suitable explanation can be found for the unexpected small axial extension, although noticeable, during the transient phase. These observations strongly suggest a dynamic character of slip phase, and a dynamic regime for all observed granular instabilities. A complete time-resolved analysis of stick-slip phenomenon in triaxial compression of model granular media will be published elsewhere.

4 Analysis and discussions

After the assessment of the validity and the reliability of the excess pore pressure measurements, we will now focus on the effects of dynamic stabilised excess pore pressure on some global macroscopic parameters (incremental volumetric strain $\Delta\varepsilon_v$, incremental axial strain $\Delta\varepsilon_a$ and deviatoric stress drop Δq in the case of compression shear stick-slip). We also explore the rare case of isotropic liquefaction and measure the pore pressure responses under varying drainage condition as in undrained compression stick-slip.

4.1 Effects of dynamic stabilised excess pore pressure ΔU^{stable}

After checking the validity of pore pressure measurements, one logical question arises instantly: what are the effects of ΔU^{stable} on the other measuring macroscopic parameters?

Typical pore pressure and strain measurements in Fig. 8 for isotropic collapse and compression stick-slip paint a curious picture of a new type of dynamic instability of granular material, as the granular assembly has completely free drainage making collapses an unlikely condition.

For isotropic consolidation, the dynamic collapse triggered by uncontrolled σ'_{trig} creates a sudden increase of pore pressure up to a likely maximum ΔU^{stable}_{top} or a decrease of

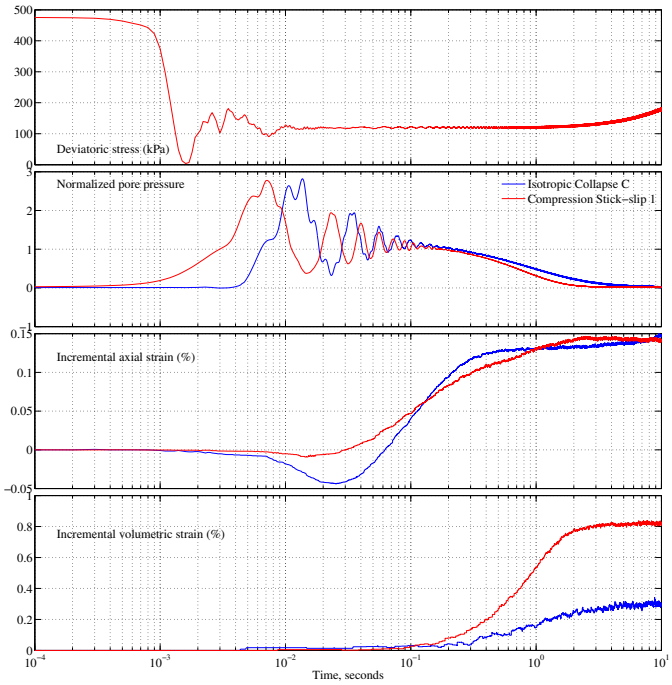

Fig. 8 Typical temporal evolution of isotropic collapse C (blue) and drained compression stick-slip SS1 (red) on 0.7 mm CVP beads : deviatoric stress, normalised excess pore pressure, axial and volumetric strain.

$\sigma^{'}$. Consequently, a dissipation phase follows in order to return to the previous level of σ'_{trig}. Similar reasoning applies for drained stick-slip with constant radial stress. As indicated in Fig. 8b, dynamic instability is essentially a consolidation process under constant deviatoric stress q.

Fig. 9a first explores the relationship between ΔU_{top}^{stable} and the incremental volumetric strain $\Delta\varepsilon_v$ during the isotropic collapse and during the slip component, in a usual semi-logarithmic scale in soil mechanics.

A power law relationship is obtained with high correlation, irrespective of different loading schemes: isotropic or compression shear. It means $\Delta\varepsilon_v$ is essentially controlled by the dynamic ΔU_{top}^{stable}. In the present case of constant radial stress at 500 kPa, this power law predicts 1.5 % of $\Delta\varepsilon_v$ for the liquefaction case when $U^{stable} \approx 500$ kPa, or $\sigma^{'} \approx 0$ kPa. This predicted value slightly underestimates the real isotropic liquefaction case [16].

Since an initial structural anisotropic state is one of the two basic required components in creating these dynamic instabilities, the effects of ΔU_{top}^{stable} on the complementary incremental axial strain $\Delta\varepsilon_a$ are examined in Fig. 9b. A linear relationship is only found for stick-slip event (i.e. without isotropic collapses) with medium correlation coefficient R, meaning ΔU_{top}^{stable} is still a meaningful parameter in controlling $\Delta\varepsilon_a$ in stick-slip experiment.

Concerning the mysterious transient phase I, ΔU_{top}^{peak} is strongly related to ΔU_{top}^{stable} in Fig. 9c with excellent corre-

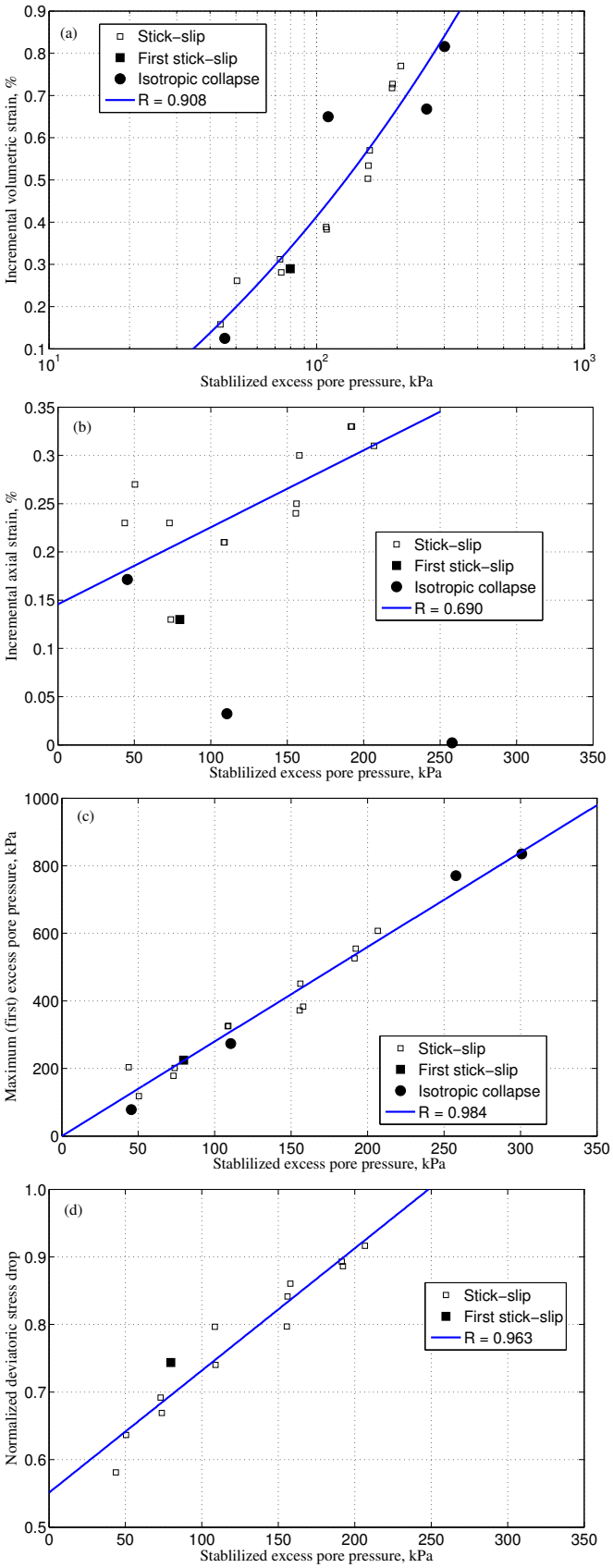

Fig. 9 Effects of dynamic stabilized excess pore pressure on (a) incremental volumetric strain $\Delta\varepsilon_v$, (b) incremental axial strain $\Delta\varepsilon_a$, (c) dynamic excess pore pressure peak ΔU_{top}^{peak} and (d) normalised deviatoric stress Δq^{norm}.

lation coefficient. It seems that the observed dynamic time evolution of ΔU during the oscillating transient phase I can be modelled by the classic second-order equation of vibrating system with only two parameters (damping factor ζ and natural frequency ω_n) [71].

These three phenomenological correlations point to the key role of dynamic pore pressure ΔU_{top}^{stable} in generating $\Delta\varepsilon_v$ and $\Delta\varepsilon_a$, even if ΔU is not the real primary cause [16]. It is even disturbing to note the control of the very short-lived ΔU_{top}^{peak} on ΔU_{top}^{stable}, $\Delta\varepsilon_v$ and $\Delta\varepsilon_a$, or in-summary, on the mechanical behaviour of the dynamic consolidation under constant q.

For stick-slip case, Fig. 9d investigates the links between ΔU_{top}^{stable} and the normalised deviatoric stress $\Delta q^{norm} = \Delta q/q_{trig}$. This normalisation eliminates the dependency on q_{trig} and enables the comparison of different stick-slip experiments. $\Delta q^{norm} = 1$ denotes largest stick-slip, transforming the solid-like state to liquid-like one with no shear stress ($q \approx 0$), and generating the largest ΔU_{top}^{stable}. Liquefaction state follows if this largest ΔU_{top}^{stable} can be maintained for some seconds.

Note that the synchronised measurements of U_{top} and U_{bottom} means an instantaneous reduction of effective stress σ', according to the effective stress principle, followed by a gradual recovery. These pore pressure measurements are visible indicators that the effective stress is out of balance. It means a very brief non-homogenous effective stress state inside the sample during the short-lived collapse for less than 4 s. U_{top} vibrates like an oscillating underdamped system with a dominant frequency using power spectral density. The systematic double check of U_{top} and U_{bottom} by dynamic and static sensors eliminates the instrumental artefacts of the measured pore fluid pressure.

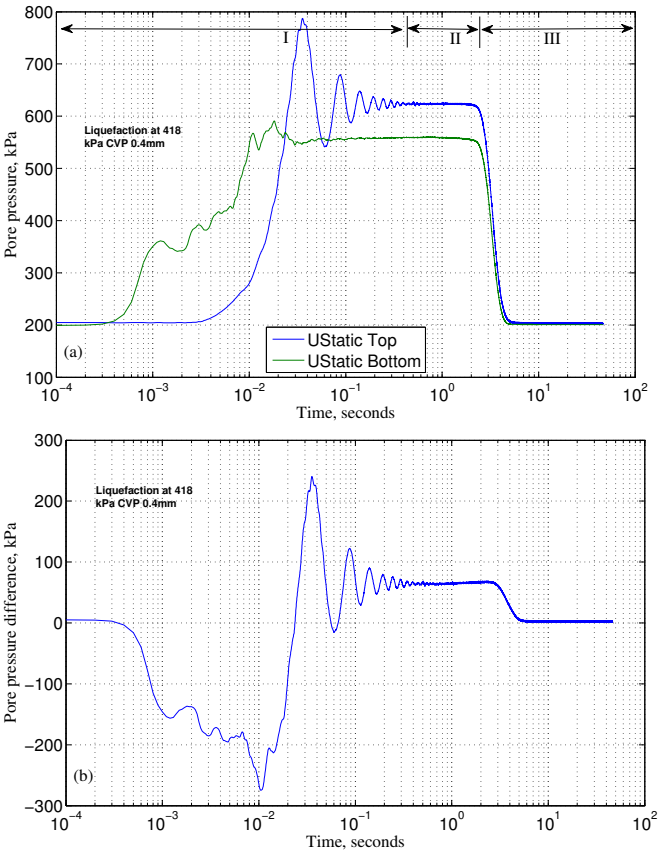

Fig. 10 (a) Temporal evolution of top and bottom static pore pressures, (b) pore pressure difference between top and bottom of isotropic liquefaction at 418 kPa of confining pressure on 0.4 mm CVP beads.

4.2 Isotropic liquefaction

Another question ensues: what are the static and dynamic pore pressure measurements in the special case of isotropic liquefaction with the presence of an additional phase II of constant ΔU^{stable} [16]?

Fig. 10a gives a very rare case of static top and bottom pore pressures of isotropic liquefaction occurring at 418 kPa on smaller 0.4 mm CVP beads. U_{top} confirms the three necessary conditions for instantaneous isotropic liquefaction on previous works [16]: a null effective stress during at least 1 s on a loose granular sample above a threshold void ratio e_{30}^{liq} at 30 kPa of confining pressure. U_{bottom} extends these same conditions for bottom pore pressure despite the full availability of the drainage system. The pore pressure difference in Fig. 10b stresses the non-homogenous effective stress state inside the sample for a liquefaction case. It also suggests the beginning of liquefaction within the upper part of the sample; then progressing downward to the lower end where the removal of the excess pore pressure is found.

This case paves the ways for the strong possibility of isotropic liquefaction in two-way drainage system on sample top and bottom, which has never been observed before in compression triaxial drained experiments.

Fig. 11a shows another rare case of full static and dynamic pore pressure measurements of isotropic liquefaction at low pressure of only 48 kPa on standard 0.7 mm CVP beads, confirming once again the three necessary conditions and the validity of pore pressure measurements. Since the dynamic pore pressure sensor can not capture the stabilised plateau of U^{stable}, the dynamic top pore pressure (dashed line) quickly returns to the steady level of U^{stable} given by the static top pore pressure sensor. For small σ'_{trig} of 48 kPa, U_{bottom} quickly dissipates. However, the non-homogenous effective stress state and the constant phase II in Fig. 11 lasts exceptionally longer than 30s.

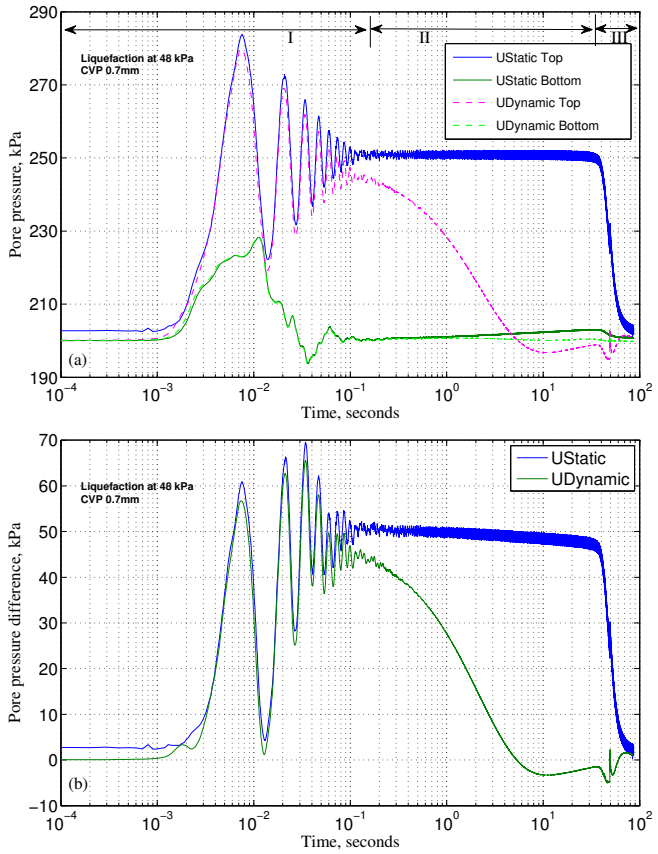

Fig. 11 (a) Temporal evolution of top and bottom dynamic and static pore pressures, (b) pore pressure difference between top and bottom of isotropic liquefaction at 48 kPa of confining pressure on 0.7 mm CVP beads.

4.3 Undrained compression stick-slip

One similar question emerges following the existence of unconventional top pore pressure, especially the vibrating phase *I*: what happens for a closed system when no drainage is permitted, as in undrained triaxial test?

The effective stress path of an undrained triaxial compression at 100 kPa of confining pressure on 0.7 mm CVP beads is in Fig. 12a, showing for the first time the existence of large undrained compression stick-slip and globally the static liquefaction behaviour on very loose model granular materials. No collapse was noticed during this short isotropic consolidation step of only 100 kPa.

Fig. 12b exposes the unusual case of the first undrained compression stick-slip SS1 (large hollow circle) with a very fast and large reduction (92.4 %) of effective confining pressure, reducing from 100 to only 7.6 kPa in one single step of a few seconds. As expected for a completely closed system, similar static top and bottom pore pressures are obtained with the indisputable presence of the first transient phase *I*, as detected simultaneously by the static and dynamic top and bottom pore pressure system. The stabilised U^{stable} after the

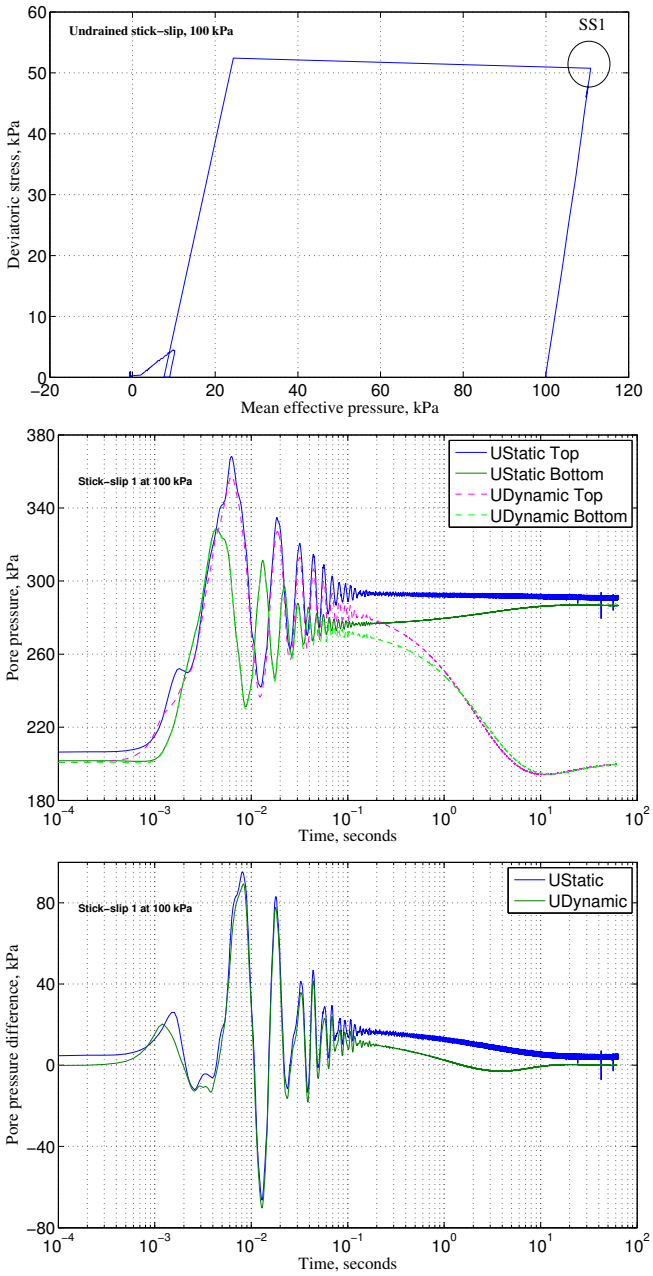

Fig. 12 (a) Effective stress path for undrained compression at 100 kPa of confining pressure, (b) temporal evolution of top and bottom dynamic and static pore pressures, (c) pore pressure difference between top and bottom of the first undrained stick-slip at 100 kPa on 0.7 mm CVP beads.

vibrating phase remains unchanged, as anticipated for undrained test on a fully saturated granular assembly. Note the systematically smaller value of bottom pore pressure during the transient phase *I*, and slightly out of phase with respect to top pore pressure.

The pore pressure difference in Fig. 12c gets progressively smaller during the transient phase *I* and an homogenous effective stress state is practically attained after 10 s.

Consequently, the unattended pore fluid pressure outburst seems to be an unambiguously signature of the observed instabilities. The top static pore pressure can be used as a proxy in explaining the isotropic liquefaction and the axial strain jump of drained and undrained stick-slip behaviour in triaxial compression [1,2,10,18,76] or in direct shear [59] .

4.4 Characteristic time

The characteristic time t for this dynamic pore pressure dissipation can be estimated approximatively using the normalized excess pore pressure from the classical one-dimensional consolidation theory of Terzaghi [66], while disregarding the transient and stabilised phases *I* and *II*:

$$t = \frac{T_v H^2}{C_v};\ C_v = \frac{k(1+e_0)}{\gamma_w} * \frac{\Delta\sigma'}{\Delta e} \tag{1}$$

with C_v the consolidation coefficient, k the permeability, γ_w the fluid unit weight, $\Delta\sigma'$ the incremental effective stress, Δe the incremental void ratio from the initial value e_0 in isotropic compression testing, T_v the time factor and H the drainage height. The permeability of loose granular assembly can be independently determined by traditional falling head permeameter, $k = 2.6{*}10^{-4}$ m/s.

Upon ignoring the local collapses from Fig. 3, C_v = 0.659 m/s^2 and the characteristic time t_{95} = 0.0084 seconds for 95% of pore pressure dissipation can be estimated. Unfortunately, this roughly approximated time t_{95} is of about three orders of magnitude smaller than the average experimental characteristic time of 10 seconds in Fig. 7. In this over-simplification, t_{95} depends on the sample geometry, but not on grain diameter.

Taking into account the effect of grain diameter on k, the empirical formula of Carman-Kozeny [39] and the two-dimensional consolidation of a homogeneous granular cylinder can be achieved. Regrettably, the same order of magnitude difference remains. The notoriously difficult Biot's dynamic consolidation [5,6] could be the next step to potentially overcome these difficulties.

4.5 Appearance conditions

What causes unusual isotropic collapses and drained compression stick-slips in model granular materials? In fact, the existence of these instabilities on model geomaterials was not predicted, neither theoretically nor numerically, and their origins are still not well understood. The experiments in this paper show many additional unknown details of these still mysterious instabilities.

Concerning the appearance conditions for these dynamic instabilities, in addition to an initially structural anisotropic state revealed by high anisotropic coefficient during isotropic consolidation [16], we have already identified a threshold fabric void ratio at 30 kPa of confining pressure $e_{30}^{col} \approx e_{min}$, having a collapse-free behaviour during isotropic consolidation on dense dry or saturated samples (Fig. 17 in [15]). We have also identified a velocity-weakening behaviour [14,1,42] associated with a critical axial strain rate $\dot{\varepsilon}_a^{crit}$ (critical velocity in [4], [47]), about 2.5 mm/min for 50 kPa of cell pressure, indicating a total disappearance of stick-slip instability beyond $\dot{\varepsilon}_a^{crit}$ (Fig. 18 in [18]). Unfortunately, the estimated $\dot{\varepsilon}_a^{crit}$ exceeds the possibilities of our current equipment.

When replacing the usual incompressible de-aired pore water by highly compressible fluid like air, isotropic collapses and compression stick-slips are still observable on medium dense dry sample created by dry deposition method. The isotropic collapses extend the presence of stick-slip instability in literature [1,18,11] into the too often neglected case of isotropic compression, and confirm the paramount role of pore fluid viscosity [10,60]. Two isotropic collapses are clearly detected at 62 and 197 kPa in Fig. 13a; and stick-slips with numerous precursors when sheared vertically at 500 kPa of confining pressure in Fig. 13b. The second collapse has a quite large incremental axial strain, of about 0.35%. Only axial strain was measured on this dry sample. Comparing to Fig. 4 on saturated samples, the striking feature still resides in the persistent presence of excess pore air pressure surge for all slip phases, however, very small value of about two orders of magnitude smaller with $\Delta U_{peak} \approx$ 0.5 kPa was detected in Fig. 13c. Small oscillations are even recorded in transient phase with dynamic pore pressure sensor (not shown). Consequently, the lateral effective stress remains virtually unchanged and the deviatoric stress drop unaffected by ΔU. This small magnitude of excess pore pressure can partially explain the large number of small stick-slips, the small incremental axial strain developed during slip phase and the highly reduced liquefaction potential with no deviatoric stress drop to isotropic stress level for dry materials. However, a full analysis of isotropic collapse and stick-slip phenomenon including specific appearance conditions on dry model granular materials using high resolution data is out of scope for this paper.

One logical question emerges : Can these instabilities appear on used beads? It turns out, as typical preliminary results, that the third run on the same beads, although from a different batch, still gives very similar isotropic collapses and drained compression stick-slips in Fig. 14 at the same 500 kPa of confining pressure, comparing to virgin beads on Fig. 4. Nevertheless, many details differ, especially the triggering stress for collapses and the first stick-slip, due to the unpredictability of these instabilities in addition to some un-

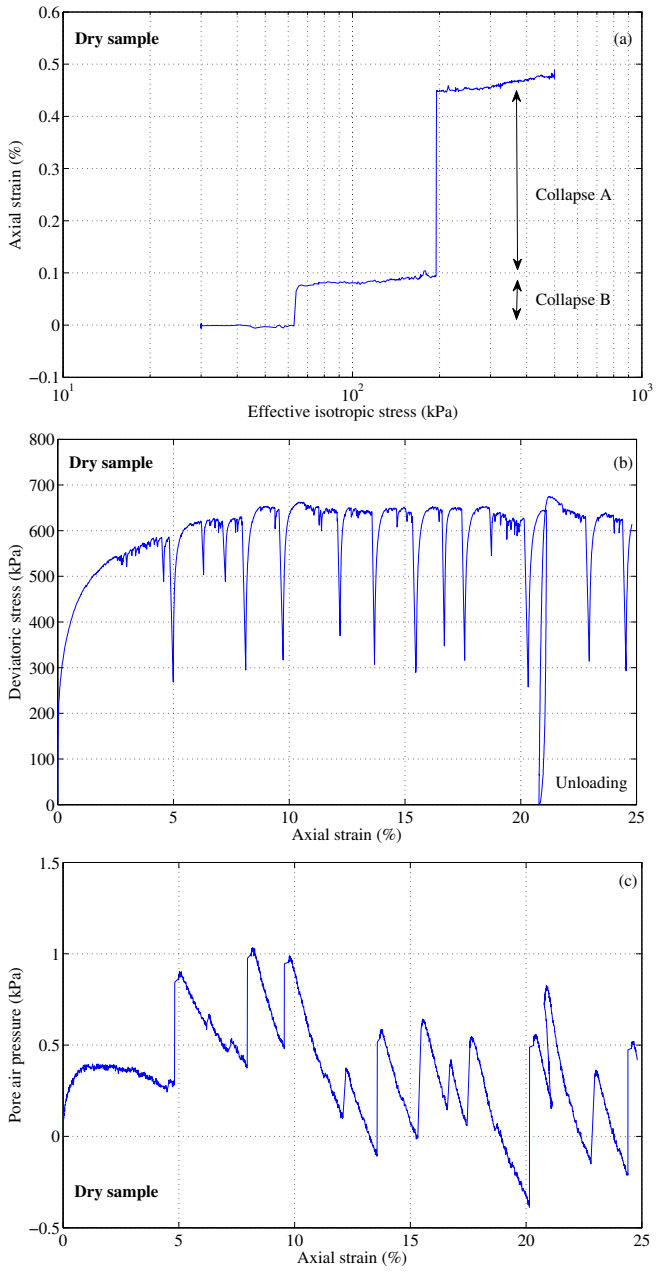

Fig. 13 (a) Isotropic consolidation with collapses at 62 and 197 kPa, (b) drained compression stick-slip behaviour with (c) pore air pressure at 500 kPa of confining pressure on dry medium dense specimen created by dry deposition method.

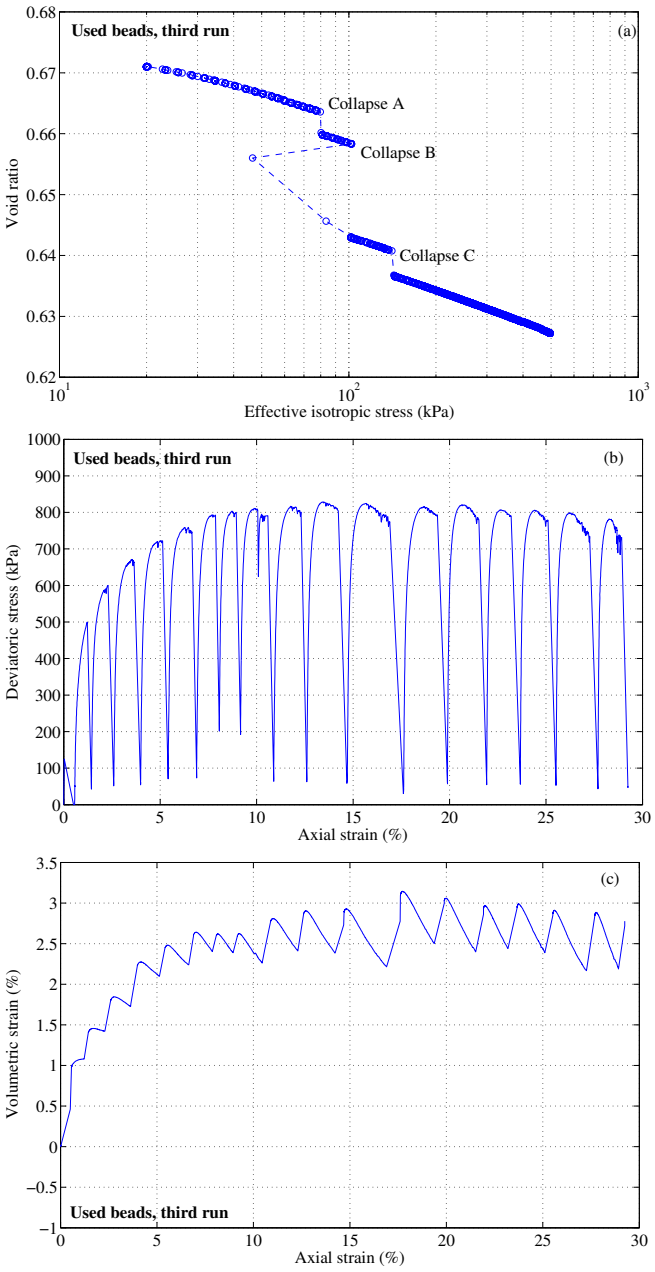

Fig. 14 (a) Isotropic consolidation with collapses at 80, 102 and 140 kPa, (b) drained compression stick-slip with (c) coupled volumetric behaviour at 500 kPa of confining pressure on the third run on saturated used glass beads.

known wearing effects. Since no plausible explanation can be found to explain these discrepancies, this paper uses only virgin glass beads following the precautionary principle. It seems that the reproducibility of these dynamic events cannot be achieved with exactly identical results, even for virgin beads. Again, a full study of this subject is beyond the framework of the current investigation.

Smooth bead surface coated with Teflon can reduce drastically the mechanical properties of dense glass beads [74]; unfortunately, surface roughness was not precisely determined in this study. Additionally, subtle initial conditions might strongly influence brittle failure phenomena [32,52]. We are planning to correlate the stick-slip behaviour with the bead's initial surface roughness measurements in future works.

Lastly, to our knowledge, these dynamic instabilities never happen for real granular materials (i.e. clean natural sands); and often soda-lime spherical glass beads were studied for having the same specific gravity as sands to facilitate the creation of very loose samples and to compare with

numerical DEM simulations using standard spherical particles. PMMA, steel and rigid polystyrene beads are rarely used [53,56,21]. Furthermore, the effects of particle shape, in approximating the irregular profile of real granular particle, on the global mechanical behaviour still remain an open question [24,76,75]. Additionally, recent X-ray imaging on dry granular assembly under low confining stress of only 20 kPa shows a surprising large stress drop for elongated artificial particles and small one for spherical shape in stick-slip experiments using triaxial machine [46].

4.6 Plausible triggering mechanisms

The systematic delay between the pore pressure development ΔU and the deviatoric stress drop Δq in slip phase, of about 3 ms, in Fig. 8 excludes ΔU as the primary cause of slip instability. The briefness of slip phase, of about 2 ms in the same figure, suggests the structural instability of metastable microstructure within the granular assembly. This structural hypothesis seems to be plausible for both isotropic collapse and shear stick-slip due to the similarity of pore pressure generation, with the support of force chains carrying most of the applied stress using photo elastic materials [20,41,73].

Numerical simulations using DEM technique can offer some insights into the complexities of these instabilities from the formation, breakage and buckling of force chains, often considered as quasi-linear short chains of granular particles. Force chains are among the driving forces for the micro-structural evolution of granular medium [68,67,78, 51]. However, much of past DEM studies intentionally omit the presence of pore fluid that can surge under dynamic phenomena since the physics of these processes were poorly understood. Recently, numerical explorations show a crucial role of full solid-liquid coupling formulation [25,26,19] in the understandings of the observed phenomena.

Together, even without any direct observation, physical and numerical experiments give some quantitative support to the hydromechanical coupling mechanisms involving first the breakage of force chains supposed to generate a strong overpressure of pore fluid, then, this excess pore pressure reduces the effective stress in fully saturated media. Finally, the effective stress recovers during the pore pressure dissipation with a consequence of increasing axial and and volumetric strains.

While the force chain buckling is a promising scheme for a causative mechanism, alternate approach of local negative second-work order is worth exploring within DEM simulations [49,50]. These approaches can provide some useful links to the possible microscopic origins of the instabilities. Additionally, strong fluid flow in small migration channel between grains can have a role in destabilising the meta-stable granular structure [70]. Furthermore, recent experiments on similar catastrophic phenomena point out the possibility of some global structural rearrangements of the weak-contact granular networks in the bulk of 3D granular assemblies, acting as reliable quasi-periodic precursors to final avalanche of increasingly inclined granular slope [32, 13,77]. Note that these avalanches have a quite well-defined triggering mechanism in the critical slope angle which is not our case.

Nevertheless, the key physical parameters that control this mechanical-induced pore pressure generation, either fluid or air, are still missing in these hypothetical scenarios, as well as the pore pressure evolution in the transient phase I and especially in the stable phase II leading to liquefaction case. Regardless of the adopted parameters, it will be a challenging task for DEM to consistently reproduce the observations during three distinct phases of the pore pressure evolution with different timescales and probably regulated by different physical processes.

5 Concluding remarks

The mechanical behaviour in drained isotropic and triaxial compression of loose, fully saturated monodisperse glass beads assembled by moist tamping and undercompaction method reveals the ubiquitous presence of dynamic instabilities, previously unknown in granular mechanics. These instabilities (i.e. isotropic collapse, compression stick-slip, and especially isotropic liquefaction) exhibit one common unexpected component in the sudden surge of excess pore pressure ΔU. This paper explores the key role of ΔU on the axial and volumetric strains of the dynamic collapse or slip component, following an in-depth verification of pore pressure measurement.

Three phases characterise each spontaneous instability occurring under uncontrolled isotropic or deviatoric triggering stress. A very fast ΔU is generated during the first short dynamic transient phase I, then oscillated like an underdamped system towards a stabilised top pore-water pressure ΔU^{stable}. The second phase II with a sustainable state of constant ΔU^{stable} can move the effective stress σ' downward to the null level of liquefaction if being maintained for some seconds. The sample deformation happens mostly in this phase, principally for the liquefaction case. The last dissipation phase III permits the recovery of σ' to the previous steady state before the instability event and resumes the instability cycle.

The unforeseen ΔU^{stable} is responsible for the development of the incremental axial and volumetric strains in an essentially dynamic consolidation process under constant deviatoric stress. Importantly, it can be linked to the evanescent first excess pore pressure peak ΔU^{peak}. The short-lived ΔU^{stable} is reliable, quadruple checked by top and bottom

dynamic and static measurements at the end of the oscillating phase *I* and irrespective of loading condition. It shows a briefly non-homogenous effective stress state for less than one second. A plausible corresponding non-homogenous strain state remains a relevant open question.

However, this sudden surge of interstitial pore fluid is not the primary cause of the observed instabilities. In stick-slip experiment, ΔU^{stable} is in turn controlled by the normalised deviatoric stress drop in a linear relationship with high correlation coefficient. Nevertheless, how this excess pore pressure is generated, oscillated, propagated and maintained for a prolonged period of time - some seconds in the case of isotropic liquefaction - is still a mystery, as well as the main triggering mechanisms. While many details remain unknown, these up-to-date pore pressure observations in this paper can provide new clues.

This paper provides the first experimental evidence of the link between dynamic instabilities and short-lived pore pressure bursts. It validates the dynamic pore pressure measurements on the sample top and bottom and demonstrates the necessity of measuring the ephemeral ΔU^{stable}_{top} in order to partly understand and explain these observed dynamic instabilities.

The test data of this paper can be downloaded from the journal website as supplementary materials.

Acknowledgements Partial financial support of the first author provided by the Viet Nam Ministry of Education and Training through the VIED excellence scholarship program is fully acknowledged. We are indebted to V. Vidal and J.C. Géminard for estimating the characteristic time using Carman-Kozeny equation, to D. Mawer for his kind proofreading service and to anonymous reviewers for helpful comments.

Compliance with ethical standards

Conflict of interest There is no conflict of interest.

References

1. Adjemian, F., Evesque, P. Experimental study of stick-slip behaviour. *Int. J. Num. Ana. Meth. in Geom.*, 28(6):501–530, 2004.
2. Alshibli, K.A., Roussel, L.E. Experimental investigation of stick-slip behaviour in granular materials. *Int. J. Num. Ana. Meth. in Geom.*, 30(14):1391–1407, 2006.
3. Andreotti, B., Forterre, Y., Pouliquen, O. *Granular Media: Between Fluid and Solid*. Cambridge University Press, 2013.
4. Berman, A. D., Ducker, W. A., Israelachvili, J. N. Experimental and theoretical investigations of stick-slip friction mechanisms. In E. Tosati B. Persson, editor, *Physics of Sliding Friction*, pages 51–67. Kluwer Academic Publishers, 1996.
5. Biot, M. A. Theory of propagation of elastic waves in a fluid-saturated porous solid. i. low frequency range. *The Journal of the Acoustical Society of America*, 28(2):168–178, 1956.
6. Biot, M. A. Theory of propagation of elastic waves in a fluid-saturated porous solid. ii. higher frequency range. *The Journal of the Acoustical Society of America*, 28(2):179–191, 1956.
7. Biswas, B., Ray, P., Chakrabarti, B.K. *Statistical Physics of Fracture, Breakdown and Earthquake*. Wiley, 2015.
8. Bjerrum, L., Krimgstad, S., Kummeneje, O. The shear strength of a fine sand. In *Proc. 5th Int. Conf. Soil. Mech. Found. Engrg.*, volume 1, pages 29–37, 1961.
9. Bradley, B. A. Strong ground motion characteristics observed in the 13 June 2011 M_w 6.0 Christchurch, New Zealand earthquake. *Soil Dynamic and Earthquake Engineering*, 91:23–38, 2016.
10. Çabalar, A.F., Clayton, C. R. I. Some observations of the effects of pore fluids on the triaxial behaviour of a sand. *Granular Matter*, 12(1):87–95, 2010.
11. Cui D., Wu, W., Xiang, W., Doanh, T., Chen, Q., Wang, S., Liu, Q., Wang, J. Stick-slip behaviours of dry glass beads in triaxial compression. *Granular Matter*, 19(1):1, 2017.
12. Daouadji, A., Darve, F., Al Gali, H., Hicher, P.Y., Laouafa, F., Lignon, S., Nicot, F., Nova, R., Pinheiro, M., Prunier, F., Sibille, L., Wan, R. Diffuse failure in geomaterials: Experiments, theory and modelling. *Int. J. Num. Ana. Meth. in Geom.*, 35(16):1731–1773, 2011.
13. Delannay, R., Duranteau, M., Tournat, V. Precursors and triggering mechanisms of granular avalanches. *Comptes Rendus Physiquee*, 16(1):45–50, 2015.
14. Dieterich, J. H. Time-dependent friction and the mechanics of stick-slip. *Pure and Applied Geophysics*, 116(4):790–806, 1978.
15. Doanh, T., Abdelmoula, N., Gribaa, L., Nguyên, T.T.T., Hans, S., Boutin, C., Le Bot, A. Dynamic instabilities under isotropic compression of idealized granular materials. *Acta Geotechnica*, 12(3):657–676, 2017.
16. Doanh, T., Abdelmoula, N., Nguyên, T.T.T., Hans, S., Boutin, C., Le Bot, A. Unexpected liquefaction under isotropic consolidation of idealized granular materials. *Granular Matter*, 18(3):67, 2016.
17. Doanh, T., Dubujet, Ph., Touron, T. Exploring the undrained induced anisotropy of Hostun RF loose sand. *Acta Geotechnica*, 5(4):239–256, 2010.
18. Doanh, T., Hoang, M.T., Roux, J.-N., Dequeker, C. Stick-slip behaviour of model granular materials in drained triaxial compression. *Granular Matter*, 15(1):1–23, 2013.
19. Dorostkar, O., Guyer, R.A., Johnson, P.A., Marone, C., Carmeliet, J. On the role of fluids in stick-slip dynamics of saturated granular fault gouge using a coupled computational fluid dynamics-discrete element approach. *J. Geophys. Res. Solid Earth*, 122(5):3689–3700, 2017.
20. Drescher, A., De Josselin de Jong, G. Photoelastic verification of a mechanical model for the flow of a granular material. *J. Mech. Phys. Solids*, 20:337–351, 1972.
21. Fall, A. , Ovarlez, G., Hautemayou, D., Mzire, C., Roux, J.-N., Chevoir, F. Dry granular flows : rheological measurements of the μ(I)-Rheology. *Journal of Rheology*, 59(4):1065–1080, 2015.
22. Fragaszy, R., Voss, M. Undrained compression behavior of sand. *J. Geotech. Engrg., ASCE*, 112(3):334347, 1986.
23. Gajo, A., Bigoni, D., Muir Wood, D. Multiple shear band development and related instabilities in granular materials. *J. of the Mechanics and Physics of Solids*, 52(22):2683–2724, 2004.
24. Garcia, X., Latham, J.-P., Xiang, J., Harrison, J.P. A clustered overlapping sphere algorithm to represent real particles indiscrete element modelling. *Géotechnique*, 59(9):779–784, 2009.
25. Goren, L., Aharonov, E., Sparks, D., Toussaint, R. Pore pressure evolution in deforming granular material: A general formulation and the infinitely stiff approximation. *J. Geophys. Research*, 115(B09216), 2010.
26. Goren, L., Aharonov, E., Sparks, D., Toussaint, R. The mechanical coupling of fluid-filled granular material under shear. *Pure and Applied Geophysics*, 168(12):2289–2323, 2011.
27. Gudehus, G., Jiang, Y., Liu, M. Seismo- and thermodynamics of granular solids. *Granular Matter*, 13(4):319–340, 2011.
28. Hareb, H., Doanh, T. Probing into the strain induced anisotropy of Hostun RF loose sand. *Granular Matter*, 14(5):589–605, 2012.

29. Heslot, F., Baumberger, T., Perrin, B., Caroli, B., Caroli, C. . Creep, stick-slip, and dry-friction dynamics: Experiments and a heuristic model. *Phys. Rev. E*, 49(6):4973–4988, 1994.
30. Igra, O., Seiler, F. *Experimental Methods of Shock Wave Research*. Springer, 2016.
31. Iverson, R.M., LaHusen, R.G. Dynamic pore-pressure fluctuations in rapidly shearing granular materials. *Science*, 246(4931):796–799, 1989.
32. Kiesgen de Richter, S., Le Caër, G., Delannay, R. Dynamics of rearrangements during inclination of granular packings: the avalanche precursor regime. *Journal of Statistical Mechanics*, page P04013, 2012.
33. Krehl, P. *History of Shock Waves, Explosions and Impact*. Springer, 2009.
34. Kumar, N., Luding, S. Memory of jamming - multiscale flow in soft and granular matter. *Granular Matter*, 18(3):58, 2016.
35. Ladd, R.S. Preparing test specimens using undercompaction. *Geotechnical Testing Journal*, 1(1):16–23, 1978.
36. Lade, P.V. *Triaxial Testing of Soils*. Wiley Blackwell, 2016.
37. Lade, P.V., Duncan, J.M. Cubical triaxial tests on cohesionless soil. *J. Soil Mech. and Found, ASCE*, 99(10):793–812, 1973.
38. Lagioia, R., Nova, R. An experimental and theoretical study of the behaviour of a calcarenite in triaxial compression. *Géotechnique*, 45(4):633–648, 1995.
39. Lambe, T.W., Whitman, R.V. . *Soil Mechanics*. Wiley, 1969.
40. Le Bouil, A., Amon, A., McNamara, S., Crassous, J. Emergence of cooperativity in plasticity of soft glassy materials. *Physical Review Letters*, 112:246001, 2014.
41. Liu, C. H., Nagel, S. R., Schecter, D. A., Coppersmith, S. N., Majmudar, S. Force fluctuations in bead packs. *Science*, 269(5223):513–515, 1995.
42. Marone, C. Laboratory-derived friction laws and their application to seismic faulting. *Annu. Rev. Earth Planet. Sci.*, 26:643–696, 1998.
43. Mašín, D. Asymptotic behaviour of granular materials. *Granular Matter*, 14(6):759–774, 2012.
44. Mcdowell, G. R., De Bono. On the micro mechanics of one-dimensional normal compression. *Géotechnique*, 63(11):895–908, 2013.
45. Michlmayr, G., Or, D. Mechanisms for acoustic emissions generation during granular shearing. *Granular Matter*, 16(5):627–640, 2014.
46. Murphy, K.A., Dahmen, K. A., Jaeger, H.M. Transforming mesoscale granular plasticity through particle shape. *Physical Review X*, 9:011014, 2019.
47. Nasuno, S., Kudrolli, A., Bak, A., Gollub, J.P. Time-resolved studies of stick-slip friction in sheared granular layers. *Phys. Rev. E*, 58(2):2161–2171, 1998.
48. Nasuno, S., Kudrolli, A., Gollub, J.P. Friction in granular layers: hysteresis and precursors. *Physical Review Letters*, 79(5):949–952, 1997.
49. Nicot, F., Daouadji, A., Laouafa, F., Darve, F. Second-order work, kinetic energy and diffuse failure in granular materials. *Granular Matter*, 13(1):19–28, 2011.
50. Nicot, F., Daouadji, A., Laouafa, F., Darve, F. Inertia effects as a possible missing link between micro and macro second-order work in granular media. *Int. J. of Solids and Structures*, 49(10):1252–1258, 2012.
51. Nicot, F., Xiong, H., Wautier, A., Lerbet, J., Darve, F. Force chain collapse as grain column buckling in granular materials. *Granular Matter*, 19(2):18, 2017.
52. Oger, L., Vidales, A., Uñac, R., Ippolito, I. Tilting process with humidity: DEM modeling and comparison with experiments. *Granular Matter*, 15(5):629–643, 2013.
53. Ovarlez, G. *Statique et rhéologie d'un milieu granulaire confiné*. Thèse de doctorat, Université Paris XI, U.F.R. Scientifique d'Orsay, 2002.
54. Popescu, R., Prevost, J. Centrifuge validation of a numerical model for dynamic soil liquefaction. *Soil Dynamic and Earthquake Engineering*, 12(2):93–90, 1993.
55. Popescu, R., Prevost, J. Comparison between VELACS Numerical "Class A" Predictions and Centrifuge Experimental Soil Test Results. *Soil Dynamic and Earthquake Engineering*, 14(2):79–92, 1995.
56. Pozo, O., Fraysse, N., Olivi-Tran, N. Ageing in the stick-slip motion for a humid granular medium. In S. McNamara R. Garcia-Rojo, H.J. Herrmann, editor, *Powders and grains*, pages 629–633. A.A. Balkema, Rotterdam, 2005.
57. Radjaï , F., Roux, S. Contact dynamics study of 2D granular media : critical states and relevant internal variables. In H. Hinrichsen and D. E. Wolf, editors, *The Physics of Granular Media*, pages 165–187, Berlin, 2004. Wiley-VCH.
58. Schofield, A., Wroth, P. *Critical state soil mechanics*. McGraw-Hill, 1968.
59. Scuderi, M. M., Carpenter, B. M., Johnson, P. A., Marone, C. Poromechanics of stick-slip frictional sliding and strength recovery on tectonic faults. *J. Geophys. Res. Solid Earth*, 120(10):6895–6912, 2015.
60. Scuderi, M. M., Carpenter, B. M., Marone, C. Physicochemical processes of frictional healing: effects of water on stick-slip stress drop and friction of granular fault gouge. *J. Geophys. Res. Solid Earth*, 119(5):4090–4105, 2014.
61. Seed, H.B., Martin, P.P., Lysmer, J. . Pore water pressure changes during soil liquefaction. *J. Geotech. Engrg., ASCE*, 102(4):323–346, 1976.
62. Sibille, L., Hadda, N., Nicot, F., Tordesillas, A., Darve, F. Granular plasticity, a contribution from discrete mechanics. *J. of the Mechanics and Physics of Solids*, 75(6):119–139, 2015.
63. Sitharam, T.G., Vinod, J. S. Critical state behaviour of granular materials from isotropic and rebounded paths: DEM simulations. *Granular Matter*, 11(1):33–42, 2009.
64. Skempton, A. W., Taylor, R.N. The pore pressure coefficients A and B. *Géotechnique*, 4(4):143–147, 1954.
65. Teng, F. C., Ou, C.Y., Hsieh, P.,G. Measurements and numerical simulations of inherent stiffness anisotropy in soft Taipei clay. *J. of Geotechnical and Geoenvironmental Engineering*, 140(1):237–250, 2014.
66. Terzaghi, K., Peck, R.P., Mesri, G. *Soil Mechanics in Engineering Practice, 3rd Edition*. John Wiley, 1996.
67. Tordesillas, A., Hilton, J. E., Tobin, S. T. Stick-slip and force chain evolution in a granular bed in response to a grain intruder. *Phys. Rev. E*, 89:042207, 2014.
68. Tordesillas, A., Zhang, J., Behringer, R. Buckling force chains in dense granular assemblies: physical and numerical experiments. *Geomechanics and Geoengineering: An International Journal*, 4(1):3–16, 2009.
69. Ueng, T-S., Lee, C-A. Pore pressure generation in saturated sand induced by one- and two-dimensional shakings. *Journal of Geo-Engineering*, 10(2):53–61, 2015.
70. Varas, G., Vidal, V., Géminard, J-C. Venting dynamics of an immersed granular layer. *Phys. Rev. E*, 83(1):011302, 2011.
71. Verruijt, A. *An Introduction to Soil Dynamics*. Springer, 2010.
72. Welker, P., McNamara, S. Precursors of failure and weakening in a biaxial test. *Granular Matter*, 13(1):93–105, 2011.
73. Wood, D. M., Lesniewska, D. Stresses in granular materials. *Granular Matter*, 13(4):395–415, 2011.
74. Wu, K., Abriak, N., Becquart, F., Pizette, P., Rémond, S., Liu, S. Shear mechanical behavior of model materials samples by experimental triaxial tests: case study of 4 mm diameter glass beads. *Granular Matter*, 19(4):65, 2017.
75. Yang, J., Luo, X.D. Exploring the relationship between critical state and particle shape for granular materials. *J. of the Mechanics and Physics of Solids*, 84(22):196–213, 2015.

76. Yang, J., Wei, L.M. Collapse of loose sand with the addition of fines : the role of particle shape. *Géotechnique*, 62(12):1111–1125, 2012.
77. Zaitsev, V., Richard, P., Delannay, R., Tournat, V., Gusev, V. E. Pre-avalanche structural rearrangements in the bulk of granular medium: experimental evidence. *Europhys. Lett.*, 83(6):64003, 2008.
78. Zhang, L., Nguyen, N.G.H., Lambert, S., Nicot, F., Prunier, F., Djeran-Maigre, I. The role of force chains in granular materials: from statics to dynamics. *European Journal of Environmental and Civil Engineering*, 21(7-8):874–895, 2017.

Notation :

ε_a	axial strain
ε_v	volumetric strain
$\Delta\varepsilon_a$	incremental axial strain
$\Delta\varepsilon_v$	incremental volumetric strain
Δh	axial displacement
Δq	deviatoric stress drop
Δq^{norm}	normalized deviatoric stress
Δv	volume displacement
ΔU	excess pore pressure
ΔU^{norm}	normalized excess pore pressure
ΔU^{peak}	maximum excess pore pressure in transient phase
ΔU^{stable}	stabilised excess pore pressure in transient phase
ΔU_{bottom}	bottom excess pore pressure
ΔU_{top}	top excess pore pressure
ΔU_{tb}	pore pressure difference between top and bottom
γ_w	fluid unit weight
φ^{first}	mobilized frictional angle at first stick-slip
φ^{max}	mobilized frictional angle at failure
φ^{PT}	mobilized frictional angle at phase transformation
ρ	density
σ	total stress
σ'	effective stress
σ'_{ini}	initial effective stress
σ'_{trig}	triggering effective stress
σ_a	axial stress
σ_r	radial stress
e	void ratio
e_{20}	void ratio at 20 kPa of confining pressure
e_c	void ratio at beginning of deviatoric shearing
e_{max}	maximum void ratio
e_{min}	minimum void ratio
e_{trig}	void ratio at σ'_{trig}
f_U	frequency of pore pressure at the transient phase
k	permeability
q	deviatoric stress
q_{trig}	triggering deviatoric stress of slip phase
q_{stable}	stabilised deviatoric stress
q_{vib}	minimum deviatoric stress in transient phase
r_u	pore pressure ratio
t_{50}	time for 50% of consolidation
B	Skempton's coefficient
C_c	curvature coefficient
C_u	uniformity coefficient
C_v	consolidation coefficient
D_0	initial diameter
D_{50}	average particle diameter
D_r	relative density
D_{r20}	relative density at 20 kPa of confining pressure
H_0	initial height
LVDT	linear variable differential transformer
T_v	time factor
U	pore pressure
U_{bottom}	bottom pore pressure
U_{top}	top pore pressure
U^{peak}	first peak of pore pressure
U^{stable}	stabilised pore pressure
U_0	back pressure
V_0	initial volume
V_{grains}	volume of grains
V_{void}	volume of void